Technische Universität München
TUM School of Engineering and Design

Data-Driven Models and Signaling Networks for Cardiac Growth

Christian Reinhard Bilas

Vollständiger Abdruck der von der TUM School of Engineering and Design der Technischen Universität München zur Erlangung eines

Doktors der Ingenieurwissenschaften (Dr.-Ing.)

genehmigten Dissertation.

Vorsitz: Prof. Dr. Oliver Lieleg

Prüfende der Dissertation:

1 Prof. Dr.-Ing. Michael W. Gee

2 Prof. Dr. Tim C. Lüth

3 Prof. Dr. Eckhard Wolf

Die Dissertation wurde am 11.03.2024 bei der Technischen Universität München eingereicht und durch die TUM School of Engineering and Design am 04.10.2024 angenommen.

Abstract

Cardiovascular diseases are the most common causes of death and impose a significant challenge in modern health care. These diseases are frequently associated with heart failure (HF). While the gold standard in HF therapy is heart transplantation, the availability of donor hearts is limited, especially in the case of pediatric HF. This critical limitation can be mitigated through early treatment in patients advancing towards HF. However, timely and suitable treatments require a detailed understanding of the many HF-associated compensatory mechanisms that are characterized by growth and remodeling. In this thesis, the knowledge about cardiac growth and remodeling is advanced by developing computational models of cardiac mechanics. These models can eventually support patient-specific therapies by in-silico predictions of long-term responses and, thereby, reduce the number of necessary heart transplantations.

This thesis presents a unique data set, which is derived from a growth hormone receptor knockout pig model designed to resemble the characteristics of healthy human pediatric heart development. The data set comprises motion-computer tomography (motion-CT) scans that capture the physiological motion and morphology over 40 days. This acquired data allows the calibration of beating heart and cardiac growth models as well as the construction of a representative heart shape.

The atlas construction method is employed on the acquired data set to derive a representative heart shape, which serves as a generic heart shape that can be used when patient-specific treatments are unfeasible.

The computational model of the beating heart combines a three-dimensional structural representation of the heart with a zero-dimensional model of the vascular system. Within the structural model of the heart, the contraction of heart muscle fibers is integrated through an active stress model. The active stress model is calibrated utilizing the model of the beating heart and an objective function that is derived from the segmentation of motion-CT scans. The vascular system model comprises Windkessel elements, whose calibration through scalar-valued optimization involves both the acquired data set and literature data.

The cardiac growth model is based on the kinematic growth framework. For its calibration, precise alignment of consecutive motion-CT images, despite potential variations in the position between scans, is guaranteed by applying a surface matching formulation with a rigid body mode-free projection. In addition, the calibration of the growth parameters is based on an image-based Bayesian inverse problem formulation. A novel signaling network that incorporates local insulin-like growth factor 1 production based on mechanical stimuli is introduced. Physiological ranges for the normalized input concentrations are defined. Moreover, a global sensitivity analysis is conducted to identify the most influential factors governing heart growth. Finally, a novel coupling between the signaling network and cardiac growth model is presented and analyzed.

Zusammenfassung

Kardiovaskuläre Erkrankungen sind die häufigste Todesursache und stellen eine bedeutende Herausforderung im modernen Gesundheitswesen dar. Diese Erkrankungen werden häufig mit Herzinsuffizienz in Verbindung gebracht. Der Goldstandard in der Therapie von Herzinsuffizienz ist die Herztransplantation. Allerdings begrenzt die eingeschränkte Verfügbarkeit von Spenderherzen den Zugang für alle bedürftigen Patienten, besonders wenn es um kindliche Herzinsuffizienz geht. Diese kritische Einschränkung kann gemildert werden durch eine frühzeitige Behandlung von Patienten, die sich der Herzinsuffizienz nähern. Allerdings benötigen rechtzeitige und geeignete Behandlungen ein detailliertes Verständnis der vielen kompensatorischen Mechanismen bei Herzinsuffizienz, die durch Wachstum und Anpassung (engl. 'growth and remodelling', G&R) charakterisiert werden. In dieser Arbeit wird das Verständnis von Wachstum und Anpassung weiterentwickelt durch die Entwicklung computerbasierter Modelle der kardialen Mechanik. Diese Modelle können letztendlich die patientenspezifische Therapie durch *in-silico* Vorhersagen langfristiger Reaktionen unterstützen und somit die Anzahl notwendiger Herztransplantationen reduzieren.

In dieser Arbeit wird ein einzigartiger Datensatz präsentiert, der aus einem Wachstumshormonrezeptor Knockout Schweinemodell abgeleitet ist und den Charakteristika der humanen kindlichen Herzentwicklung entspricht. Der Datensatz umfasst Bewegungs-Computertomographie (motioan-CT)-Scans, die die physiologische Bewegung und Morphologie über einen Zeitraum von 40 Tagen erfassen. Dieser erworbene Datensatz wird zur Kalibrierung des schlagenden Herzmodells und des kardialen Wachstumsmodells sowie für die Konstruktion einer repräsentativen Herzform verwendet.

Das computergestützte Modell des schlagenden Herzens kombiniert eine dreidimensionale strukturelle Darstellung des Herzens mit einem null-dimensionalen Modell des Kreislaufs. Das strukturelle Modell des Herzens enthält ein aktives Spannungsmodell, das die Kontraktion der Herzmuskelfasern steuert. Das aktive Spannungsmodell verwendet das computergestützte Modell des schlagenden Herzens und eine Zielfunktion, die auf der Segmentierung von motion-CT-Scans basiert, zur Kalibrierung. Das Kreislaufmodell besteht aus Windkessel-Elementen, welche durch skalare Optimierung kalibriert werden, wobei sowohl der erworbene Datensatz als auch Literaturdaten einbezogen werden.

Das kardiale Wachstumsmodell basiert auf dem kinematischen Wachstumsansatz. Für die Kalibrierung wird eine konsistente Ausrichtung aufeinanderfolgender Bilder trotz möglicher Variationen in der Position zwischen den Scans sichergestellt, indem die Oberflächenanpassung mit einer starrkörperfreien Projektion angewendet wird. Zusätzlich erfolgt die Kalibrierung der Wachstumsparameter auf Grundlage einer bildbasierten Bayesian inversen Problemformulierung. Ein neuartiges Signalnetzwerk, das die lokale Produktion von insulinähnlichem Wachstumsfaktor 1 basierend auf mechanischen Reizen integriert, wird eingeführt. Physiologische Bereiche für die normalisierten Eingangskonzentrationen werden definiert. Darüber hinaus wird eine globale Sensitivitätsanalyse durchgeführt, um die einflussreichsten Faktoren für das Wachs-

tum des Herzens zu identifizieren. Abschließend wird eine neuartige Kopplung zwischen dem Signalnetzwerk und dem kardialen Wachstumsmodell präsentiert und analysiert.

Danksagung

Diese Arbeit entstand während meiner Zeit als Doktorand am Lehrstuhl für Mechanik auf Höchstleistungsrechnern der Technischen Universität München sowie während meiner Tätigkeit bei der Firma AdjuCor GmbH. An dieser Stelle möchte ich allen danken, die mich während dieser Zeit sowohl im akademischen als auch im beruflichen Umfeld begleitet und unterstützt haben.
Der größte Dank gebührt meinem Doktorvater, Prof. Dr. Michael W. Gee, für die Möglichkeit, diese Arbeit zu realisieren. Sein Vertrauen in meine Fähigkeiten sowie seine Unterstützung waren von unschätzbarem Wert. Durch seine offene Art wurden stets neue Denkanstöße und Motivationsschübe vermittelt.
Ein besonderer Dank gilt auch dem industriellen Kooperationspartner, Prof. Dr. Stephen Wildhirt von der Firma AdjuCor GmbH, der mir sein Vertrauen entgegengebracht hat und jederzeit bereit war, medizinische Fragen zu beantworten. In diesem Zusammenhang möchte ich auch den anderen Mitarbeitern der Firma AdjuCor danken, deren Beiträge und Hilfsbereitschaft meine Arbeit bereichert haben. Besonders hervorheben möchte ich Dr. Andreas Maier, der nicht nur mein Mentor war, sondern mir während meiner gesamten Promotionszeit tatkräftig zur Seite stand. Sein Rat und seine Unterstützung waren für mich von großer Bedeutung. Zudem gilt mein Dank Michael Schmid, der während meiner Promotionszeit ein guter Freund geworden ist und mich in dieser Zeit begleitet sowie stets motiviert hat.
Darüber hinaus möchte ich meinen Kollegen am Lehrstuhl für Mechanik auf Höchstleistungsrechnern danken, die während meiner Promotionszeit eine angenehme und hilfsbereite Atmosphäre geschaffen haben. Die spannenden fachlichen Diskussionen und die entstandenen Freundschaften haben meinen Alltag bereichert. Ein besonderer Dank geht an Mikhail Zverlov, Tahar Arjoune, Lukas Rinderer, Ludwig Wagmüller, Willem Schüttler, Claus Kratzer, Dr. Lukas Bruder und Dr. Alexander Schein für den inspirierenden Austausch.
Zusätzlich danke ich meinen Freunden für ihre Unterstützung und die gemeinsamen Erlebnisse. Besonders hervorheben möchte meine engen Freunde Dr. Konstantin Key und Dr. Karsten Paul, die mich während meines Studiums und meiner gesamten Promotionszeit begleitet haben und entscheidend für meinen Weg waren. Ein ebenso großer Dank gilt meiner Freundin Rebecca, die mich während meiner Promotion entscheidend unterstützt und mein Leben bereichert hat.
Zudem möchte ich meiner Familie danken. Ohne meine Mutter, Sabine, und meine Schwester, Alina, wäre ich nicht der Mensch, der ich heute bin. Sie haben mir stets den Rückhalt gegeben, den ich brauchte, und mich in schwierigen Zeiten unermüdlich unterstützt. Ohne sie wäre dieser Weg erheblich herausfordernder gewesen.

München, im November 2024 Christian Bilas

Inhaltsverzeichnis

1. Introduction **1**
- 1.1. Motivation . . . 1
- 1.2. Cardiovascular system . . . 2
- 1.3. Research objectives . . . 5
- 1.4. Outline . . . 6

2. Mathematical fundamentals **9**
- 2.1. Continuum mechanics . . . 9
  - 2.1.1. Kinematics . . . 9
  - 2.1.2. Stresses and constitutive laws . . . 11
  - 2.1.3. Balance equations . . . 13
  - 2.1.4. Initial boundary value problem . . . 14
  - 2.1.5. Dimensionally-reduced fluid mechanics . . . 14
- 2.2. Finite element method . . . 16
  - 2.2.1. Weak formulation . . . 16
  - 2.2.2. Discretization in space . . . 17
  - 2.2.3. Discretization in time . . . 20
  - 2.2.4. Nonlinear solution techniques . . . 21
- 2.3. Parameter estimation . . . 22
  - 2.3.1. Parametrization and identification problem . . . 22
  - 2.3.2. Bayesian inverse problem . . . 23
  - 2.3.3. Lagrangian formulation and adjoint method . . . 24
  - 2.3.4. Regularization . . . 26
  - 2.3.5. Similarity measure . . . 26
- 2.4. Shape analysis . . . 29
  - 2.4.1. Surface matching problem . . . 29
  - 2.4.2. Atlas construction . . . 32
- 2.5. Sensitivity analysis . . . 33
  - 2.5.1. Global sensitivity analysis . . . 34
  - 2.5.2. Sobol indices . . . 34

3. Cardiac mechanics **37**
- 3.1. Computational cardiovascular mechanics . . . 37
  - 3.1.1. Segmentation and geometry construction . . . 37
  - 3.1.2. Constitutive model . . . 39
  - 3.1.3. Boundary conditions of the embedding tissue . . . 42
  - 3.1.4. Prestressing . . . 42
  - 3.1.5. 3D-0D coupled cardiovascular mechanics . . . 44

3.2. Computational cardiac growth mechanics . . . 51
3.2.1. Kinematics of growth . . . 53
3.2.2. Phenomenological growth model . . . 54
3.3. Signaling growth network . . . 56
3.3.1. Heart growth network . . . 56
3.3.2. Hill differential equation approach . . . 57
3.3.3. Signaling network evaluation . . . 61
3.3.4. Coupling the signaling network and cardiac mechanics . . . 63

4. Application **65**
4.1. Measurements . . . 65
4.1.1. Cardiac cycle calibration data . . . 66
4.1.2. Growth mechanics calibration data . . . 67
4.2. Atlas computation . . . 69
4.2.1. Problem setup and parameter setting . . . 69
4.2.2. Numerical results . . . 70
4.2.3. Discussion . . . 71
4.3. 3D-0D heartbeat model calibration . . . 72
4.3.1. Flow network calibration . . . 72
4.3.2. Numerical parameters . . . 76
4.3.3. Active stress calibration . . . 77
4.3.4. Patient-specific numerical results . . . 79
4.3.5. Discussion . . . 79
4.4. Surface matching problem for growth . . . 82
4.4.1. Problem setup and parameter setting . . . 82
4.4.2. Numerical results . . . 84
4.4.3. Discussion . . . 85
4.5. Cardiac growth model calibration . . . 86
4.5.1. Growth prediction for two consecutive images . . . 86
4.5.2. Numerical results . . . 87
4.5.3. Discussion . . . 88
4.6. Signaling network . . . 90
4.6.1. Global sensitivity analysis of signaling networks . . . 90
4.6.2. Coupling results . . . 91
4.6.3. Discussion . . . 93

5. Summary and outlook **97**

A. Mathematical model details **99**
A.1. Tensor notation and mathematical operators . . . 99
A.2. Windkessel model details . . . 99
A.3. Derivation of the weak form . . . 102
A.4. Probability space and random variables . . . 103
A.5. L-BFGS and optimization framework . . . 104
A.6. Surface matching linearization . . . 106

B. Cardiac mechanics model **111**
B.1. Active stress discretization 111
B.2. Growth material linearization 111

C. Signaling network **115**
C.1. Heart growth signaling network 115
C.2. Demonstrator network 118
C.3. Asymptotical stability 120
C.4. Signaling network model evaluation 120

D. Numerical results **123**
D.1. Measurements 123
D.2. Computational domain 124
D.3. Global sensitivity analysis of signaling network 125

Literaturverzeichnis **131**

Abbildungsverzeichnis

1.1. Simplified sketch of the cardiovascular system with the heart at its center. . . . 3
1.2. The left heart function during a cardiac cycle. 4

2.1. Nonlinear continuum mechanics setting. 10
2.2. 2-element windkessel model. 15
2.3. 4-element windkessel model. 15
2.4. Diode windkessel model. 16
2.5. Elastance windkessel model. 16

3.1. Exemplary CT image of the heart at the 80% diastolic state. 38
3.2. Exemplary lumina of the left and right ventricle and outer layer of the myocardium. 39
3.3. Exemplary computational domain of a porcine heart. 40
3.4. Exemplary visualization of fiber and sheet direction. 41
3.5. Time dependent active stress evolution. 42
3.6. Three-dimensional heart model coupled to the dimensionally reduced vascular system network. 46
3.7. Left and right atrial elastance evolution over a cardiac cycle. 48
3.8. Visualization of the multiplicative split of the deformation gradient. 54
3.9. Reduced and modified signaling network. 58
3.10. Different reaction types within a signaling network. 58
3.11. Nonlinear Hill activation function. 59
3.12. Ordinary differential equation solution of the heart growth signaling network. . 62
3.13. Reduced and modified signaling network output concentration *CellArea* over the input concentration of isoproterenol. 63

4.1. Left and right ventricular volume over a cardiac cycle. 66
4.2. Artificial pressure curves for the left and right heart. 67
4.3. Left and right ventricular end-diastolic volumes over time. 68
4.4. Segmented 80% diastolic state of the same heart over 40 days. 69
4.5. Epicardial surfaces for all six pigs. 70
4.6. Solution of the atlas construction problem. 71
4.7. Calibration of the systemic arterial windkessel model. 73
4.8. Calibration of the aortic valve. 75
4.9. Calibration of the active stress functions for the left and right ventricle. 78
4.10. Flow network state variables over one cardiac cycle. 80
4.11. Deformation of the heart over a cardiac cycle. 81
4.12. Initial configuration of the surface matching problem. 83
4.13. Final configuration of the surface matching problem. 84
4.14. Projected solution of the surface matching problem. 85

4.15. Objective function value during the growth calibration process. 87
4.16. Final distribution of the optimized growth parameter over the heart. 88
4.17. Comparison of the grown configuration with the measured data. 89
4.18. First- and total-order sensitivities for the REF and R&M network. 91
4.19. Convergence of Sobol indices. 92
4.20. Concentration of species *Stretch* over the heart. 93
4.21. CellArea concentration over the heart. 94

A.1. Resistance element. 100
A.2. Compliance element. 100
A.3. Inertance element. 100
A.4. 3-element windkessel model. 101

C.1. Reference signaling network. 115
C.2. Demonstrator signaling network. 119
C.3. Numerical solution of the demonstrator network. 119
C.4. Difference of DSS between the R&M and REF network. 122

D.1. Left and right ventricular stroke volume over time. 124
D.2. Visualization of the finite element mesh. 125
D.3. Visualization of boundary value problem. 126
D.4. Numerical solution of the spatial resolution study. 127
D.5. Sensitivity indices of *CellArea* with respect to the input concentrations for the reference and reduced and modified network. 128

Tabellenverzeichnis

2.1. First- and total-order sensitivity estimators. 36

3.1. Baseline constitutive model parameters. 43
3.2. Spring and dashpot boundary condition parameters. 43
3.3. Pressure states and flow rates within the flow network. 47
3.4. Baseline parameters for flow network. 48
3.5. Baseline values for the initial network state variables. 50

4.1. Overview of the atlas problem parameters. 71
4.2. Optimized flow network parameters. 76
4.3. Overview of the numerical parameters for the 3D-0D coupled problem. 77
4.4. Optimized active stress parameters for the 3D-0D coupled problem. 78
4.5. Overview of the surface matching parameters. 83
4.6. Overview of the growth identification problem parameters. 86
4.7. Initial, grown and measured volumes of the left and right ventricles. 88

C.1. List of all species within the reference and reduced and modified network. . . . 116

D.1. End-diastolic volumes for all pigs. 123
D.2. End-systolic volumes for all pigs. 124
D.3. Initial and final volumes of the left and right ventricles. 126
D.4. Global sensitivity estimators for *CellArea* with respect to the input species in the reference network. 127
D.5. Global sensitivity estimators for *CellArea* with respect to the input species in the reduced and modified network. 129

Acronyms

ANOVA	analysis of variance
AV	aortic valve point
AVP	atrioventricular plane
BSA	body surface area
CAE	computer-aided engineering
CER	cycle error criterion
CO	cardiac output
CT	computer tomography
DOF	degree of freedom
DSS	direct stationary solutions
EDV	end-diastolic volume
EF	ejection fraction
ESV	end-systolic volume
FD	finite difference
FEM	finite element method
FSI	fluid structure interaction
G&R	growth and remodeling
GHR	growth hormone receptor
GLS	global longitudinal strain
GMRES	generalized minimal residual method
HF	heart failure
HR	heart rate
HU	Hounsfield units
IBVP	initial boundary value problem
L-BFGS	limited-memory Broyden-Fletcher-Goldfarb-Shanno
LDDMM	large deformation diffeomorphic metric mapping
LV	left ventricle
LVB	left ventricular bottom point
MAP	maximum a posteriori
MC	monte carlo
MULF	modified updated Lagrangian formulation
MVP	mitral valve posterior point
OAT	one at a time
ODE	ordinary differential equation
PDF	probability density function
PTC	pseudo-transient continuation
R&M	reduced and modified network

REF	reference network
RKHS	reproducing kernel Hilbert space
RV	right ventricle
SIMPLE	semi-implicit method for pressure-linked equations
STL	stereolithographic
SV	stroke volume
TV	total variation

Nomenclature

Symbols	Description
Subscripts and superscripts	
$(\bullet)_{\mathrm{ar}}$	arterial circulation quantity
$(\bullet)_{\mathrm{at}}$	atrial quantity
$(\bullet)^{\mathrm{base}}$	heart base quantity
$(\bullet)^{\mathrm{c}}$	heart cavity quantity
$(\bullet)^{\mathrm{e}}$	element
$(\bullet)^{\mathrm{epi}}$	heart epicardium quantity
$(\bullet)_{\mathrm{ext}}$	external quantity
$(\bullet)_{\mathrm{in}}$	inlet quantity
$(\bullet)_{\mathrm{int}}$	internel quantity
$(\bullet)_{\mathrm{kin}}$	kinematic quantity
$(\bullet)_{\ell}$	left heart quantity
$(\bullet)^{\mathrm{lid}}$	lid quantity
$(\bullet)_{\mathrm{out}}$	outlet quantity
$(\bullet)^{\mathrm{pul}}$	pulmonary circulation quantity
$(\bullet)_{\mathrm{r}}$	right heart quantity
$(\bullet)^{\mathrm{sys}}$	systemic circulation quantity
$(\bullet)_{\mathrm{v}}$	ventricular quantity
$(\bullet)_{\mathrm{ven}}$	venous circulation quantity
Domains and surfaces	
Ω_0	reference configuration
Ω_{g}	intermediate growth configuration
Ω	current configuration
Γ	surface area
Γ_{u}	Dirichlet boundary
Γ_{n}	Neumann boundary
$\partial\Omega$	surface of the current configuration
Continuum physics	
$\boldsymbol{P}$	first Piola-Kirchhoff stress tensor
$\boldsymbol{S}$	second Piola-Kirchhoff stress tensor
$\mathbb{C}_{\mathrm{e}}$	elastic material tangent
Ψ_{e}	elastic strain energy function
$\boldsymbol{e}$	Euler-Almansi strain tensor

Symbols	Description
$\boldsymbol{E}$	Green-Lagrange strain tensor
$\mathbb{C}$	material tangent
$\boldsymbol{\varphi}$	mapping from reference to current configuration
$\boldsymbol{a}$	acceleration vector
$\boldsymbol{b}$	volumetric body force
$\boldsymbol{\sigma}$	Cauchy stress tensor
$\boldsymbol{n}$	outward surface normal in current configuration
$\boldsymbol{t}$	traction vector in current configuration
$\boldsymbol{x}$	position vector in current configuration
ρ	density in current configuration
$\boldsymbol{F}$	deformation gradient
J	determinat of the deformation gradient
$\boldsymbol{u}$	displacement vector
$\boldsymbol{I}$	identity matrix
$\bar{I}_1, \bar{I}_2, \bar{I}_3$	modified 1st, 2nd and 3rd invariant
I_1, I_2, I_3	1st, 2nd and 3rd invariant
$\boldsymbol{b}$	left Cauchy-Green deformation tensor
$\mathrm{d}\boldsymbol{x}$	line element in the current configuration
$\mathrm{d}\boldsymbol{X}$	line element in the reference configuration
m	mass
$\mathbb{R}^d$	coordinate space
$\boldsymbol{N}$	outward surface normal in reference configuration
$\boldsymbol{T}$	traction vector in reference configuration
$\boldsymbol{X}$	position vector in reference configuration
ρ_0	density in reference configuration
$\boldsymbol{C}$	right Cauchy-Green deformation tensor
Ψ	strain energy function
$\mathrm{d}\boldsymbol{a}$	surface element in the current configuration
$\mathrm{d}\boldsymbol{A}$	surface element in the reference configuration
T	end time
t_0	start time
t	time
$\boldsymbol{e}_\bullet$	unit vector
$\boldsymbol{v}$	velocity vector
$\mathrm{d}v$	volume element in the current configuration
$\mathrm{d}V$	volume element in the reference configuration

Dimensional reduced flow mechanics

y	atrial activation function
C	compliance parameter
V	volume of the compartment
E	elastance
q	flow rate
Z	impedance parameter

Symbols	Description
L	inertance parameter
p	pressure
R	resistance parameter
$\tilde{R}$	valve resistance parameter

Finite element analysis

β, γ	scalar parameter generalized-α method
α_f, α_m	time integration parameter of the generalized-α method
k_0^{ptc}	pseudo-transient continuation parameter
$\boldsymbol{a}$	acceleration degree of freedom
c_{M}	mass scaling in Rayleigh damping
$\boldsymbol{D}$	Rayleigh damping matrix
c_{f}	stiffness scaling in Rayleigh damping
$d_{i,j}$	displacement of node i in spatial direction j
$\boldsymbol{d}$	displacement degree of freedom
$\boldsymbol{u}_h$	approximation to displacement u
A	area of the domain
V	volume of the domain
ϵ_{inc}	tolerance for the displacement increment
ϵ_{res}	tolerance for the residual
$\boldsymbol{f}$	force vector
H	Sobolev space
$\boldsymbol{M}$	mass matrix
n_{dof}	number of degrees of freedom
n_{el}	number of elements
n_{n}	number of element nodes
$\tilde{\boldsymbol{X}}_h$	nodal coordinates
$\boldsymbol{X}_h$	approximation of the geometry
$\boldsymbol{r}$	residual
ρ_∞	spectral radius of the generalized-α method
N_i	shape functions
$\boldsymbol{N}$	shape function matrix
$\mathcal{U}$	solution function space
$\boldsymbol{K}_{\mathrm{eff}}$	dynamic effective tangential stiffness matrix
$\boldsymbol{K}_{\mathrm{T}}$	tangent stiffness matrix
θ	scalar parameter for the one-step-θ method
n	discrete time step
$\mathcal{V}$	trial function space
$\delta d_{i,j}$	virtual displacement of node i in spatial direction j
$\delta \boldsymbol{d}$	virtual displacement degree of freedom
$\delta \boldsymbol{u}_h$	approximation to test function δu
$\boldsymbol{v}$	velocity degree of freedom
$\delta \mathcal{W}$	variational form

Symbols	Description
$\delta \boldsymbol{u}$	weighting function

Parameter estimation

$\mathcal{B}$	Borel set
$\mathcal{F}$	set of events
A	specific event
E	expected value
p	probability density function
P	probability function
X	random variable
V	variance
Ω	sample space
$\varepsilon_{\mathrm{tv}}$	total variation parameter
w	total variation weight
α	regularization weight
$\hat{\boldsymbol{U}}$	current state of the system
D	distance measure
F	forward problem
$\mathcal{L}$	Lagrangian
$\boldsymbol{\lambda}$	Lagrange multiplier
C	observation operator
$\boldsymbol{Z}$	observation
$\mathcal{J}$	objective function
R	regularization
$\boldsymbol{\theta}$	optimization parameter
σ	variance of distance measure

Surface currents

$\mathcal{W}^*$	space of currents
$\mathcal{W}$	Hilbert space
$\boldsymbol{c}$	center point of surface element
σ_V	deformation kernel scale
$\boldsymbol{K_n}$	dual representation of a surface current
$k(\bullet, \bullet)$	kernel function
δ_{ij}	Kronecker delta
$\boldsymbol{n}$	normal vector
$n^{\mathcal{S}}$	number of surface elements
σ_W	spatial scale
$\mathcal{S}$	surface represented by surface currents
ω	surface current test function
S	surface current

Surface matching

Symbols	Description
θ	Lagrange multiplier for the flow function
ξ	Lagrange multiplier for the shoot function
$\mathcal{A}$	atlas or template surface
$\boldsymbol{c}$	control points
$\mathcal{S}$	matching shape
E_{kin}	kinetic energy
G	flow function
Φ	mapping function
$\boldsymbol{\alpha}$	momenta
n_{cp}	number of control points
n_{Sh}	number of surface shapes
n_{p}	number of surface points
$\mathcal{J}$	surface matching objective function
$\boldsymbol{x}$	particle position
F	shoot function
$\boldsymbol{S}$	state of the system of control points
$\mathcal{T}$	target shape
$\boldsymbol{v}$	particle velocity

Global sensitivity analysis

$\boldsymbol{A}, \boldsymbol{B}$	base sample matrices
E	expected model value
$n_{\mathcal{I}}$	number of inputs
n_S	number of samples
S	first-order sensitivity index
T	second-order sensitivity index
V_{tot}	total model variance
V	model variance
f_0	mean value
f	model function
N	number model evaluations
$\boldsymbol{x}$	model input
y	model output

Cardiac mechanics

$\varepsilon_{\mathrm{tol}}$	cardiac cycle error tolerance
$\varepsilon_{\mathrm{cycl}}$	cardiac cycle error
T_{cycl}	cardiac cycle time
$\boldsymbol{q}$	vector of unknown network variables
Δp	pressure pulse
c	dashpot parameter
k	spring stiffness
$\mathcal{H}$	Heaviside function
c_1, c_2, K	constant parameters in activation function

Symbols	Description
$\hat{f}$	activation function for the active stress
u	scaling function for the active stress
a_0, a_f, a_s, a_{fs}	material constant for passive strain energy law
b_0, b_f, b_s, b_{fs}	dimensionless material constant for passive strain energy law
κ	first Lamé constant or bulk modulus
μ	second Lamé constant or shear modulus
τ_{a}	active stress
$\alpha_{\max}$	active contraction upstroke rate
$\alpha_{\min}$	active contraction relaxation rate
σ_0	fiber contractility
$\boldsymbol{f}_0$	fiber direction in heart model
$\boldsymbol{r}_0$	radial direction in heart model
$\boldsymbol{s}_0$	sheet direction in heart model
t_{contr}	time of contraction
t_{relax}	time of relaxation

Cardiac growth mechanics

$\boldsymbol{S}_{\mathrm{e}}$	elastic second Piola-Kirchhoff stress tensor
$\boldsymbol{C}_{\mathrm{e}}$	elastic Cauchy-Green deformation tensor
T_{growth}	end time of the growth computation
c_ϑ	growth rate
t_0	start time of the growth computation
ϑ	growth stretch
$\boldsymbol{F}_{\mathrm{e}}$	elastic deformation gradient
$\boldsymbol{F}_{\mathrm{g}}$	growth deformation gradient

Signaling growth network

B, K, EC_{50}	Hill activation function parameter
τ	reaction time constant
w_{ij}	reaction weight
n	Hill activation function steepness parameter
$f_{\mathrm{act}}(\bullet)$	Hill activation function
$\mathrm{AND}(\bullet, \bullet)$	and activation function
$f_{\mathrm{inh}}(\bullet)$	Hill inhibition function
$f(\bullet)$	network evaluation function
$\mathrm{OR}(\bullet, \bullet)$	or activation function
$\boldsymbol{c}_{\mathcal{I}}$	input species concentration vector
$c_{\mathrm{s,max}}$	maximal species concentration
c_{s}	species concentration
s_i	network species
$\mathcal{I}$	set of input species
$\mathcal{S}$	set of species

1. Introduction

1.1. Motivation

Heart failure (HF) is a life-threatening clinical condition and affects more than 26 million people worldwide [117]. Despite improvements in medical care, heart diseases remain the leading cause of death in Europe and Northern America, contributing to 23% of all deaths in Germany and the United States [22, 110, 124].

HF is characterized by a complex clinical syndrome in which the heart is incapable of maintaining a cardiac output (CO) sufficient to meet metabolic requirements [82]. Symptoms of HF, such as fatigue, shortness of breath, and lower extremity edema, reveal the heart's struggle to pump blood effectively [154]. The outcome is ultimately fatal [135].

While the burden of HF is substantial across all age groups, it is a more pressing concern when it comes to pediatric cases. Considering the number of individuals affected, cases of adult HF significantly surpass the number of pediatric cases. However, pediatric HF emerges as a critical public health concern. When a child is hospitalized for HF, the costs are notably higher than those for adults due to the frequent need for surgical or catheter-based interventions. Beyond the financial burden, the emotional impact on the family is profound [67].

The etiology of HF in pediatric cases significantly differs from that observed in adults. The most prevalent factor contributing to pediatric heart failure is structural congenital heart disease, characterized by abnormalities in the heart's structure present from birth [30]. Cardiomyopathies, which lead to impaired pumping function, are the primary cause of heart failure in children with a structurally normal heart [97].

Understanding and treating HF in children leads to distinctive challenges. The overall treatment goals are similar to HF in adults, which are correcting underlying problems, minimizing morbidity and mortality, and improving functional status and quality of life [68]. However, a fundamental difference emerges since only a few drugs that have proven effective in adults with HF have gained regulatory approval for use in children [112]. Surgical and interventional advancements have significantly reduced morbidity and mortality associated with structural heart disease. However, when it comes to cardiomyopathy, only little progress has been made in improving the significant mortality and morbidity. Heart transplantation stands as the preferred therapy for end-stage HF in children resistant to surgical and medical interventions. Yet, after one year post-transplantation, the survival chances reach up to 85%, and the overall survival after 20 years post-transplantation is even only 40% [68].

To increase these numbers, the early identification of patients advancing toward HF is essential for implementing timely and suitable treatments. Additionally, integrating predictions of long-term response to treatments supports clinical decision-making, enhancing the overall effectiveness of patient care. Computational models of cardiac mechanics have the potential to support patient-specific therapies by *in-silico*. In this context, biophysical models of organs provide the

opportunity to non-invasively estimate clinical quantities of interest. The value of computer-aided engineering (CAE) is linked to the dynamic progressions, which are the ever-increasing speed of computing hardware and, the continuous refinement of computational approaches concerning physical models, and the robustness of predictions. To complement these hardware advancements, the evolution of software is equally imperative, ensuring a seamless transition and optimizing the overall efficiency in engineering problem-solving.

This work advances the knowledge about cardiac growth and remodeling. Therefore, a unique data set, which resembles the characteristics of healthy pediatric heart development, is presented. This data set is employed for the calibration of a beating heart and cardiac growth model as well as to construct a representative heart shape. This representative heart shape can be used when patient-specific treatments are unfeasible. As a foundation for the development of cardiac growth models, the beating heart model is calibrated to the acquired data set. Subsequently, the patient-specific cardiac growth model is derived based on the data set. Another cardiac growth model employs signaling cascades on a cellular level as a growth measure.

In the remainder of this section, the medical background is explored to provide the necessary foundation. For a more profound overview, the reader is referred to [13, 72]. Subsequently, the particular research objectives are outlined.

1.2. Cardiovascular system

The cardiovascular system is an intricate network of veins and arteries, forming a closed circulatory system. Its primary function is to serve as the central transport system for blood, ensuring the circulation of oxygen, nutrients, and waste products throughout the body. At its center, the heart, which is a muscular organ situated in the thoracic cavity, is located and is responsible for driving the circulatory process.

The heart is suspended by its attachment to the major vessels within a fibrous sac called the *pericardium*. It is composed of three types of cardiac muscle fibers: The atrial muscle fibers, the ventricular muscle fibers, and the conductive muscle fibers. The atrial and ventricular muscles are similar to skeletal muscles, while the conductive muscles consist of specialized fibers that can be stimulated and contracted. This unique combination allows electrical signals to travel, leading to the contraction of individual cells within the fibers. Simplified, the cardiac muscle can be thought of as a network formed by many cardiac muscle cells [78].

The heart is divided into four chambers, forming two separate pumps organized in series: the right heart, which transports blood into the lungs, and the left heart, which is responsible for pumping blood throughout the peripheral or systemic organs into the rest of the body. Each pump is subdivided into an atrium as the receiving chamber and a ventricle as the discharging chamber. The atrium serves as a weak first pump, supplying the ventricle with a continuous blood flow. The primary pumping force results from the ventricle. The pathway of blood flow through the circulatory system and the four-chambered heart is depicted in Fig. 1.1.

Deoxygenated blood returns from the systemic organs through the superior and inferior vena cavae to the right atrium. Subsequently, it travels through the tricuspid valve into the right ventricle and is pumped through the pulmonary valve into the pulmonary artery. After traversing the pulmonary capillary beds, the now-oxygenated blood returns to the left atrium through the

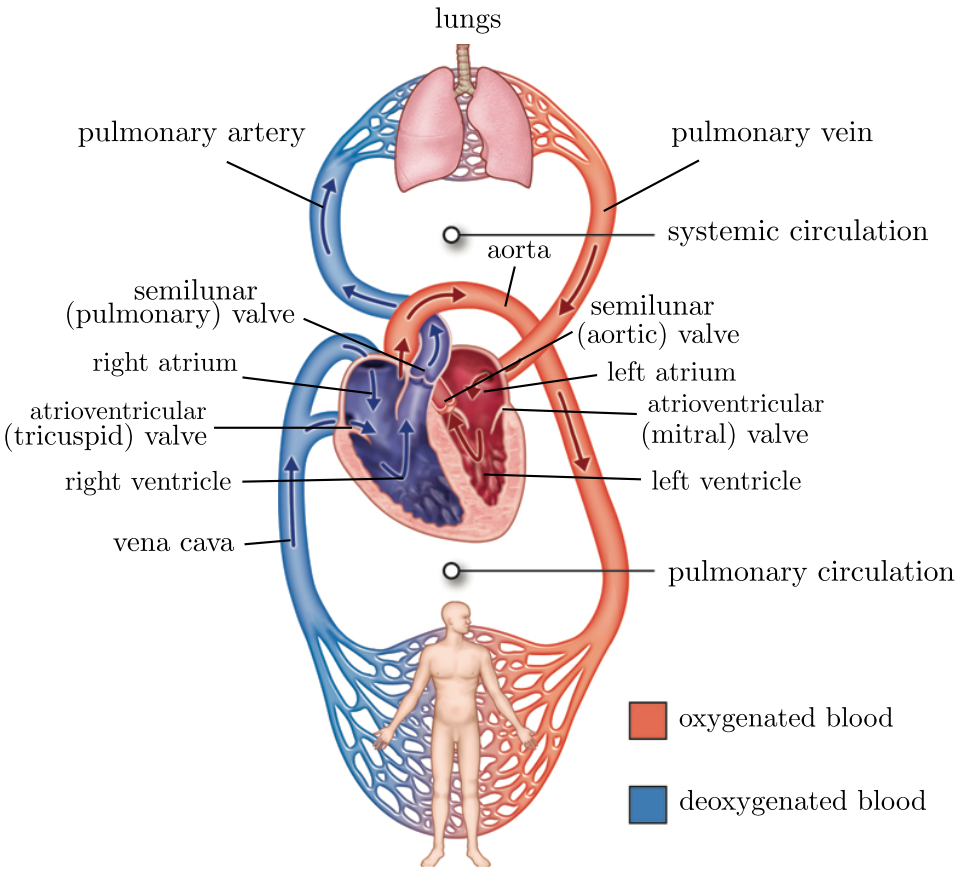

Abbildung 1.1.: Simplified sketch of the cardiovascular system with the heart at its center. First, oxygenated blood is ejected from the left ventricle through the aortic valve into systemic circulation via the aorta. Simultaneously, deoxygenated blood is delivered to the pulmonary circulation via the pulmonary artery into the lungs. Within the capillary networks, oxygen consumption and re-oxygenation take place. Subsequently, the ventricles relax, and filling through the left and right atria starts. The figure is reprinted and modified with permission under a Creative Commons license [26].

pulmonary veins. The blood flow then proceeds through the mitral valve into the left ventricle and is pumped through the aortic valve into the aorta.

The cardiac events occurring within one heartbeat are called the cardiac cycle. The resulting blood pressure and volume curves during a cardiac cycle are exemplary shown in Fig. 1.2. Furthermore, a single heartbeat is divided into five phases [54].

- **Phase 1: Atrial contraction** initiates the cardiac cycle as the atrioventricular valves open while the semilunar valves remain closed. During this phase, the atria contract to actively support the filling of the ventricles, which results in an increase in the ventricular volume.

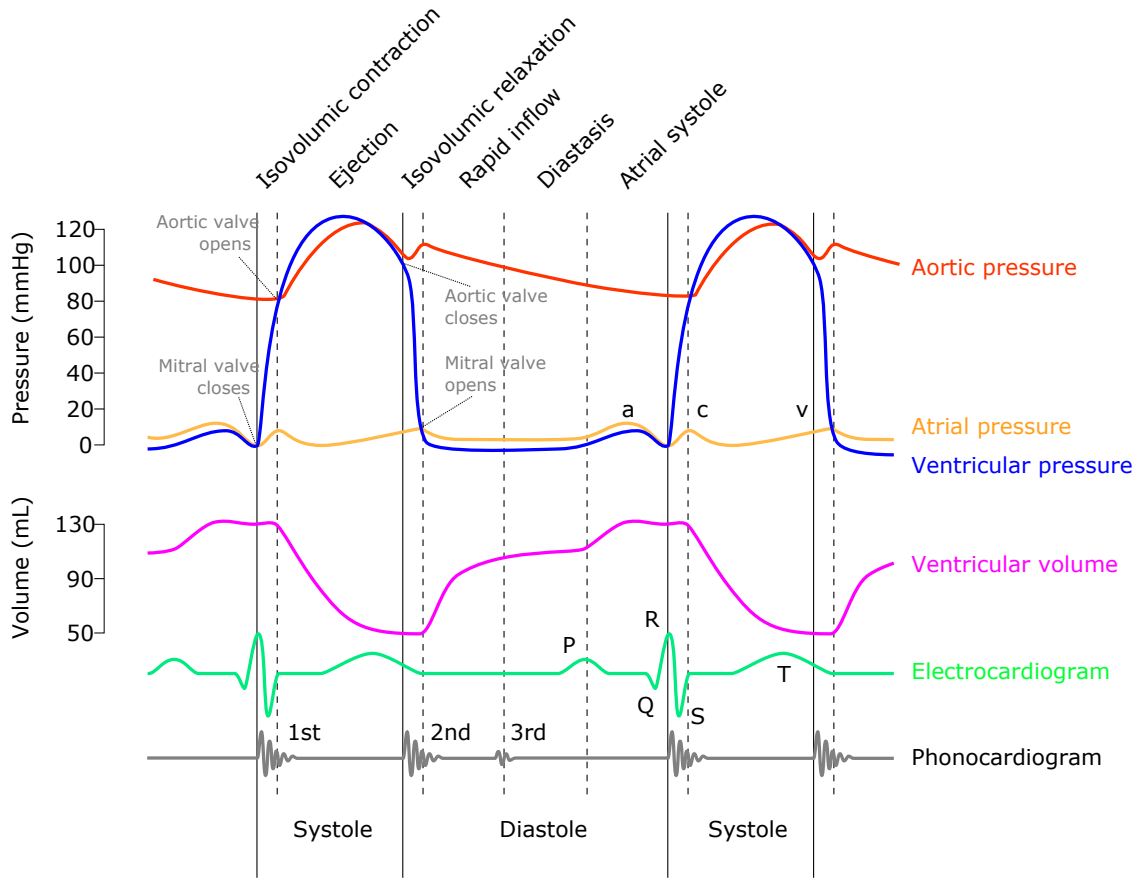

Abbildung 1.2.: The left heart function during a cardiac cycle. The figure is published under a Creative Commons license [18].

- **Phase 2: Isovolumetric contraction** is characterized by the closure of both the atrioventricular and semilunar valves. Here, the ventricular myocytes, primarily aligned in a circumferential orientation, start to contract. This contraction generates tension within the ventricular walls, leading to an increase in chamber pressure while keeping the volume constant.

- **Phase 3: Ejection** of blood from the ventricular chambers starts when the ventricular pressures exceed the pressures within the aorta (on the left side) and the pulmonary artery (on the right side). This phase of the cardiac cycle is known as *systole*. During systole, the tricuspid and mitral (atrioventricular) valves remain closed due to the higher pressures within the ventricles. Consequently, ventricular volume and pressure decrease.

- **Phase 4: Isovolumetric relaxation** begins as soon as the ventricular pressure falls below the aortic or pulmonary artery pressure, leading to the closure of the aortic and pulmonary valves. Further, when the pressures in the ventricles fall below those in the atria, the atrioventricular valves open. This phase of the cardiac cycle is known as *diastole*.

- **Phase 5: Ventricular filling** marks the start of the last phase, where the ventricular volume increases while the pressure remains constant.

Subsequently, atrial contraction initiates the next cardiac cycle. Under normal *in-vivo* conditions, the heart rate (HR) determines the number of cardiac cycles per minute and typically averages around 70 beats per minute.
Further crucial parameters in this context are the *end-diastolic volume* (EDV), which is measured at the end of phase 1, and the *end-systolic volume* (ESV), determined at the end of phase 3. The difference between EDV and ESV is called stroke volume (SV)

$$\mathrm{SV} = \mathrm{EDV} - \mathrm{ESV}. \tag{1.1}$$

The cardiac output (CO) relates the SV and HR

$$\mathrm{CO} = \mathrm{SV} * \mathrm{HR}. \tag{1.2}$$

The ejection fraction (EF) acts as a standard parameter to assess the severity of HF and is defined as

$$\mathrm{EF} = \frac{\mathrm{SV}}{\mathrm{EDV}}. \tag{1.3}$$

In a resting, healthy individual, the left ventricular EF is typically around 60%, and the right ventricular EF is approximately 50% [114]. The CO is roughly 5 liters per minute. For children, it is around $100 - 250\ \mathrm{mL}/(\mathrm{min\,kg})$ [32]. In heart failure, where the ventricles cannot pump blood effectively, the CO is reduced. This leads to a diminished circulation of blood throughout the body, impairing the delivery of oxygen and nutrients to vital organs and tissues. Subsequently leading to limitations in physical activity.

1.3. Research objectives

As outlined in Sec. 1.1, the potential value of computational biomedical models in supporting clinical analysis, decision-making, and predicting long-term responses is substantial. The primary objective of this thesis is to advance models in the field of computational cardiac mechanics, focusing on patient-specific calibration.
The specific research contributions are as follows:

- **Data acquisition:** The initial step toward developing patient-specific computational cardiac mechanics models is to acquire a data set that captures the physiological motion and morphology of the heart. This involves taking motion-computer tomography (motion-CT) scans on porcine hearts, ensuring that the heartbeat is covered in multiple images. To account for growth-related changes, these CT scans are repeated over time. The data set is specifically designed to resemble the heart size of children, which leads to the choice of growth hormone receptor (GHR) knockout pigs [60, 61].

- **Identification of a representative heart shape:** In various engineering tasks, the representation of a data set by a single shape that captures the essential morphological and geometrical features is crucial. The atlas construction method [37] is employed to create a representative heart shape, which acts as a generic heart shape of the acquired data set.

- **Calibration of the beating heart:** The evaluation of the cardiac heartbeat model contains the solution of a nonlinear elastodynamic boundary value problem, which returns the material deformation throughout the heartbeat and temporally resolved pressure and flow values within the cardiovascular system [62]. The objective is to calibrate the model parameters using the acquired data set based on an inverse problem formulation [63].

- **Patient-specific computational cardiac growth model:** To ensure consistent alignment of consecutive images, the objective is to employ a method based on the surface matching formulation [51]. This method guarantees accurate image alignment despite potential variations in the patient's position between scans. Subsequently, the objective is to use an image-based inverse analysis framework [80] to calibrate the computational cardiac growth model. The overall application of this model is to predict heart growth and potential individual disease-related deviations, aiding doctors in their treatment decisions and the selection of suitable implants and prostheses.

- **Identification and modeling the cardiac growth signaling cascades:** Signaling networks capture the complex interplay of mechanical and biochemical stimuli for heart growth on a cellular level [45, 55, 56, 153]. The goal is to identify a network that, first, is capable of modeling the local insulin-like growth factor 1 (*IGF1*) production in response to mechanical stimuli and, second, can be used to predict a quantity to drive heart growth. Furthermore, the aim is to use global sensitivity analysis, based on Sobol indices [132], to identify the most influential factors governing heart growth within this novel network. Subsequently, the objective is to couple this network with computational cardiac mechanics models, utilizing inputs from the cardiac heartbeat model to predict heart growth.

Parts of these objectives were developed in cooperation with an industrial partner. Therefore, some applications may not be fully explicated within this thesis. The primary focus remains on methodological advancements. For example, the atlas construction method has been utilized to identify a representative heart shape, while its application is not detailed.

1.4. Outline

The remainder of this thesis is structured as follows:

Chapter 2 outlines the mathematical fundamentals. In Sec. 2.1, the fundamentals of nonlinear continuum mechanics are derived. Sec. 2.2 summarizes the spatial and temporal discretization methods as well as the iterative solution techniques for nonlinear systems of equations. Sec. 2.3 introduces the parametrization framework to the nonlinear systems of equations. The surface matching framework based on the surface currents is presented in Sec. 2.4. Finally, in Sec. 2.5, the global sensitivity analysis based on Sobol's indices is derived.

The formulation of the computational cardiovascular mechanics models is given in Chapter 3. Sec. 3.1 focuses on the segmentation, geometry construction, and computational formulation of the beating heart, as well as the coupling with the vascular system. Sec. 3.2 describes the kinematic growth framework and the corresponding parametrization. In Sec. 3.3, the signaling

network, which describes the heart growth signaling cascades, is outlined.

Chapter 4 presents numerical examples for the proposed frameworks. In Sec. 4.1, the data collection process and evaluation are discussed. In Sec. 4.2, the representative shape of the acquired data set is shown. Subsequently, Sec. 4.3 presents the calibration of the computational model of the beating heart. The alignment of consecutive CT images using the surface matching framework is shown in Sec. 4.4. In Sec. 4.5, the calibration of the kinematic growth framework is outlined. Sec. 4.6 presents the results of the global sensitivity analysis and the coupling between the cardiac mechanics models and the signaling networks.

Chapter 5 concludes this thesis and describes possible extensions for future work.

2. Mathematical fundamentals

This chapter summarizes the mathematical fundamentals used within the computational models of this work. Sec. 2.1 introduces the fundamental governing equations of nonlinear continuum mechanics. Subsequently, Sec. 2.2 provides the concepts to approximate the solution of the resulting nonlinear initial boundary value problem using the finite element method. Sec. 2.3 discusses the inverse analysis framework for parameter optimization. Thereafter, in Sec. 2.4, the computational method of shape analysis is outlined. Finally, in Sec. 2.5, global sensitivity analysis is presented.

2.1. Continuum mechanics

This section presents a brief overview of the governing equations of continuum mechanics, including crucial aspects such as kinematics, stress principles, balance laws, and constitutive relations. Subsequently, the initial boundary value problem for dynamical problems is derived. For a more profound introduction to continuum mechanics, the reader is referred to [64]. Note that in this work, all higher-order tensors are denoted by bold symbols, and a general overview of tensorial notation and mathematical operations is given in App A.1.

2.1.1. Kinematics

The general geometrical setup of nonlinear continuum mechanics is depicted in Fig. 2.1.
Let $\Omega_0 \in \mathbb{R}^3$ denote the *reference* or *material configuration* of a continuous body with particle position $\boldsymbol{X}$ at time $t = 0$. Correspondingly, the *spatial* or *current configuration* Ω_t of the same body with particle position $\boldsymbol{x}$ is introduced. The deformation of the body is characterized by the bijective nonlinear *deformation map* $\boldsymbol{\varphi}$ that transforms the material position $\boldsymbol{X}$ into the spatial position $\boldsymbol{x}$ for all times t,

$$\boldsymbol{\varphi}(\boldsymbol{X}, t) = \begin{cases} \Omega_0 \to \Omega_t, \\ \boldsymbol{X} \to \boldsymbol{x}(\boldsymbol{X}, t). \end{cases} \tag{2.1}$$

The finite *displacement field* between the two configurations is defined as

$$\boldsymbol{u}(\boldsymbol{X}, t) = \boldsymbol{x}(\boldsymbol{X}, t) - \boldsymbol{X}. \tag{2.2}$$

The *material time derivative* is denoted by

$$\dot{(\bullet)} = \frac{\mathrm{d}}{\mathrm{d}t}(\bullet). \tag{2.3}$$

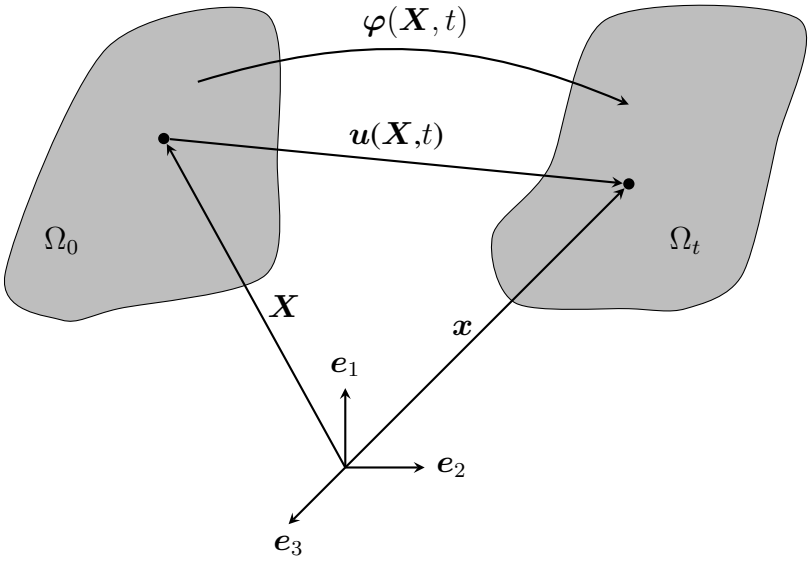

Abbildung 2.1.: Nonlinear continuum mechanics setting with reference configuration Ω_0 and current configuration Ω_t of a continuum body.

The first- and second-time derivatives of the displacement field result in the *velocity* and *acceleration field*,

$$\boldsymbol{v}(\boldsymbol{X},t) = \dot{\boldsymbol{u}}(\boldsymbol{X},t), \tag{2.4}$$

$$\boldsymbol{a}(\boldsymbol{X},t) = \dot{\boldsymbol{v}}(\boldsymbol{X},t) = \ddot{\boldsymbol{u}}(\boldsymbol{X},t). \tag{2.5}$$

The material gradient of the deformation mapping is called the *deformation gradient* $\boldsymbol{F}$ and is defined as

$$\boldsymbol{F}(\boldsymbol{X},t) = \frac{\partial \boldsymbol{\varphi}(\boldsymbol{X},t)}{\partial \boldsymbol{X}}. \tag{2.6}$$

For the sake of simplicity and readability, in the following, the dependency of kinematic quantities on time t and space $\boldsymbol{X}$ is omitted.
The second-order tensor field $\boldsymbol{F}$ is used to transform an infinitesimal line segment $\mathrm{d}\boldsymbol{X}$ from the reference configuration into the current configuration $\mathrm{d}\boldsymbol{x}$, which is called a *push-forward* operation,

$$\mathrm{d}\boldsymbol{x} = \boldsymbol{F}\mathrm{d}\boldsymbol{X}. \tag{2.7}$$

Its inverse defines the *pull-back* operation

$$\mathrm{d}\boldsymbol{X} = \boldsymbol{F}^{-1}\mathrm{d}\boldsymbol{x}. \tag{2.8}$$

The determinant J of the deformation gradient

$$J = \det(\boldsymbol{F}) > 0, \tag{2.9}$$

serves as a measure of the change of the infinitesimal volume element $\mathrm{d}v$ and $\mathrm{d}V$ in the current and reference configuration, respectively and it reads

$$\mathrm{d}v = J\mathrm{d}V. \tag{2.10}$$

Similarly, using Nanson's formula, the deformation of an infinitesimal surface element is given by

$$\mathrm{d}\boldsymbol{a} = J\boldsymbol{F}^{-T}\mathrm{d}\boldsymbol{A}, \tag{2.11}$$

where $\mathrm{d}\boldsymbol{a}$ and $\mathrm{d}\boldsymbol{A}$ are the infinitesimal surface elements in the current and reference configuration, respectively.
Defining metrics of strain is essential for characterizing the material's behavior. Two commonly used definitions of strain are the material *Green-Lagrange* strain tensor

$$\boldsymbol{E} = \frac{1}{2}\left(\boldsymbol{C} - \boldsymbol{I}\right), \tag{2.12}$$

and the spatial *Euler-Almansi* strain tensor

$$\boldsymbol{e} = \frac{1}{2}\left(\boldsymbol{I} - \boldsymbol{b}^{-1}\right), \tag{2.13}$$

where

$$\boldsymbol{C} = \boldsymbol{F}^T\boldsymbol{F}, \tag{2.14}$$

is the *right Cauchy-Green deformation tensor*, which is invariant to rigid body motion and

$$\boldsymbol{b} = \boldsymbol{F}\boldsymbol{F}^T, \tag{2.15}$$

is the *left Cauchy-Green deformation tensor* associated with the spatial configuration.

2.1.2. Stresses and constitutive laws

The relationship between stress and strain is a fundamental aspect of describing the behavior of deformable materials. In this context, stress can be thought of as the force responsible for deformation, while strain quantifies the resulting deformation. According to Cauchy's stress theorem, the relationship between the spatial surface traction $\boldsymbol{t}$ and the spatial outward surface normal $\boldsymbol{n}$ at an arbitrary point $\boldsymbol{x}$ on a cut through a body is linear. This relationship is described by the symmetric second-order *Cauchy stress tensor* $\boldsymbol{\sigma}$,

$$\boldsymbol{t}(\boldsymbol{x}, \boldsymbol{n}) = \boldsymbol{\sigma}(\boldsymbol{x})\boldsymbol{n}. \tag{2.16}$$

This theorem can also be formulated in terms of the reference outward normal $\boldsymbol{N}$, and the reference coordinate $\boldsymbol{X}$, resulting in

$$\boldsymbol{t}_0 = \boldsymbol{t}(\boldsymbol{X}, \boldsymbol{N}) = \boldsymbol{P}(\boldsymbol{X})\boldsymbol{N}. \tag{2.17}$$

Here, $\boldsymbol{P}$ represents the non-symmetric *first Piola-Kirchhoff stress tensor*, which is obtained from the Cauchy stress tensor by a pull-back operation

$$\boldsymbol{P} = J\boldsymbol{\sigma}\boldsymbol{F}^{-T}. \tag{2.18}$$

Given that the first Piola-Kirchhoff stress tensor is a two-point tensor defined in the reference and current configuration, an alternative stress measure is introduced. This alternative measure, known as the *second Piola-Kirchhoff stress tensor* $\boldsymbol{S}$, is defined only in the material configuration, and it reads

$$\boldsymbol{S} = \boldsymbol{F}^{-1}\boldsymbol{P}. \tag{2.19}$$

The second Piola-Kirchhoff stress tensor is symmetric, making it a suitable quantity for formulating constitutive laws in the context of total Lagrangian solid mechanics. This symmetry is crucial for *objectivity*, ensuring that the stress measures are independent of the choice of coordinate systems or observers and remain invariant under arbitrary rigid body motions, thereby providing a consistent description of material behavior. Using the second Piola-Kirchhoff stress tensor, the reference traction force $\boldsymbol{T}$ is defined as

$$\boldsymbol{T}(\boldsymbol{X}, \boldsymbol{N}) = \boldsymbol{S}(\boldsymbol{X})\boldsymbol{N}. \tag{2.20}$$

Constitutive theories aim to mathematically model the behavior of materials and link the stress response of a material to strain measures. Within this thesis, models with homogeneous hyperelasticity are used. These materials postulate the existence of a so-called strain energy function $\Psi(\boldsymbol{F})$, which maps a second-order tensor to a scalar with units of energy per volume [J/m^3]. Under the assumption of isotropic material behavior, Ψ can be represented using the three principal invariants of the right Cauchy-Green tensor $\boldsymbol{C}$,

$$\Psi = \Psi(\boldsymbol{C}) = \Psi(I_1(\boldsymbol{C}), I_2(\boldsymbol{C}), I_3(\boldsymbol{C})), \tag{2.21}$$

with

$$I_1(\boldsymbol{C}) = tr(\boldsymbol{C}), \tag{2.22}$$

$$I_2(\boldsymbol{C}) = \frac{1}{2}\left[(tr(\boldsymbol{C}))^2 - tr(\boldsymbol{C}^2)\right], \tag{2.23}$$

$$I_3(\boldsymbol{C}) = \det(\boldsymbol{C}) = J^2. \tag{2.24}$$

Recalling Eq. (2.14) and Eq. (2.12), the strain energy function can also be written as

$$\Psi(\boldsymbol{C}) = \Psi(\boldsymbol{F}) = \Psi(\boldsymbol{E}). \tag{2.25}$$

Within compressible isotropic hyperelasticity, the deformation can be split into an isochoric and volumetric part, adopting a penalty-based approach. This allows for practical handling of near-incompressible behavior and provides flexibility in addressing various degrees of volume changes, and it reads

$$\Psi(I_1(\boldsymbol{C}), I_2(\boldsymbol{C}), I_3(\boldsymbol{C})) = \Psi_{\text{iso}}(\bar{I}_1(\boldsymbol{C}), \bar{I}_2(\boldsymbol{C})) + \Psi_{\text{vol}}(J) \tag{2.26}$$

with the modified invariants

$$\bar{I}_1(\boldsymbol{C}) = J^{-2/3} I_1(\boldsymbol{C}), \tag{2.27}$$

$$\bar{I}_2(\boldsymbol{C}) = J^{-4/3} I_2(\boldsymbol{C}), \tag{2.28}$$

$$\bar{I}_3(\boldsymbol{C}) = 1. \tag{2.29}$$

By differentiating a given strain energy function Ψ, the first Piola-Kirchhoff stress tensor can be computed as

$$\boldsymbol{P} = \frac{\partial \Psi}{\partial \boldsymbol{F}}, \tag{2.30}$$

and the second Piola-Kirchhoff stress tensor is given by

$$\boldsymbol{S} = 2\frac{\partial \Psi}{\partial \boldsymbol{C}} = \frac{\partial \Psi}{\partial \boldsymbol{E}}. \tag{2.31}$$

Further, the material tangent to the stress-strain relationship is computed via

$$\mathbb{C} = 2\frac{\partial \boldsymbol{S}}{\partial \boldsymbol{C}} = 4\frac{\partial^2 \Psi}{\partial \boldsymbol{C}^2}. \tag{2.32}$$

This fourth-order tensor will be used in nonlinear continuum mechanic problems, see Sec. 2.2.4.

2.1.3. Balance equations

Conservation of mass In a closed mechanical system, i.e., without growth or remodeling, the total mass m of the body is conserved. With respect to the reference configuration, this yields

$$\frac{\mathrm{d}m}{\mathrm{d}t} = \frac{\mathrm{d}}{\mathrm{d}t} \int_{\Omega_0} \rho_0 \, \mathrm{d}V = \int_{\Omega_0} \dot{\rho}_0 \, \mathrm{d}V = 0, \tag{2.33}$$

and thus, in local form

$$\dot{\rho}_0 = 0, \qquad \text{in } \Omega_0. \tag{2.34}$$

The local form in the current configuration can be derived using Reynold's transport theorem [12] and is given by

$$\dot{\rho} + \rho \nabla_{\boldsymbol{x}} \cdot \dot{\boldsymbol{u}} = 0, \qquad \text{in } \Omega_t. \tag{2.35}$$

The densites ρ and ρ_0 are defined as the ratio of a material element mass $\mathrm{d}m$ over its deformed or undeformed volume, respectively.

Balance of linear momentum As a generalized version of Newton's first law of motion, the balance of linear momentum states that changes in linear momentum must correspond to all external forces acting on a body. In reference configuration, it is given by

$$\rho_0 \ddot{\boldsymbol{u}} = \nabla_{\boldsymbol{X}} \cdot \boldsymbol{P} + \boldsymbol{b}_0, \tag{2.36}$$

while in the current configuration, it reads

$$\rho \ddot{\boldsymbol{u}} = \nabla_{\boldsymbol{x}} \cdot \boldsymbol{\sigma} + \boldsymbol{b}, \tag{2.37}$$

where $\boldsymbol{b}$ and $\boldsymbol{b}_0$ are volumetric forces defined as the ratio of the material element force $\mathrm{d}\boldsymbol{b}$ over its deformed or undeformed volume, respectively.

Balance of angular momentum The balance of angular momentum states that the change in angular momentum must equal all external moments acting on the body. It can be demonstrated that for both the reference and current configuration, the angular momentum imposes the condition that both the Cauchy stress tensor $\boldsymbol{\sigma}$ and the second Piola-Kirchhoff stress tensor $\boldsymbol{S}$ must be symmetric

$$\boldsymbol{\sigma} = \boldsymbol{\sigma}^T, \tag{2.38}$$

$$\boldsymbol{S} = \boldsymbol{S}^T. \tag{2.39}$$

2.1.4. Initial boundary value problem

The equations presented above fully describe the kinematics and stress-strain relations in a continuum. Generally, problems in nonlinear continuum mechanics can be addressed by an initial boundary value problem (IBVP) in a given time span $t \in [t_0, T]$. In material description, the IBVP reads

$$\nabla_{\boldsymbol{X}} \cdot \boldsymbol{P} + \boldsymbol{b}_0 = \rho_0 \ddot{\boldsymbol{u}} \quad \text{in } \Omega \times [t_0, T], \tag{2.40}$$

$$\boldsymbol{u} = \hat{\boldsymbol{u}} \quad \text{on } \Gamma_{\mathrm{u}} \times [t_0, T], \tag{2.41}$$

$$\boldsymbol{P} \cdot \boldsymbol{N} = \boldsymbol{t}_0 \quad \text{on } \Gamma_{\mathrm{n}} \times [t_0, T], \tag{2.42}$$

$$\boldsymbol{u}(\boldsymbol{X}, t_0) = \hat{\boldsymbol{u}}(\boldsymbol{X}) \quad \text{in } \Omega_0, \tag{2.43}$$

$$\dot{\boldsymbol{u}}(\boldsymbol{X}, t_0) = \hat{\boldsymbol{v}}(\boldsymbol{X}) \quad \text{in } \Omega_0. \tag{2.44}$$

The Dirichlet and Neumann boundaries in the reference configuration Γ_{u} and Γ_{n}, respectively, are disjunct sets and form the surface $\partial\Omega$ of the reference domain. Dirichlet boundary conditions specify values of the displacements $\boldsymbol{u}$, whereas Neumann boundary conditions specify a traction force $\boldsymbol{t}_0$. Equations (2.43) and (2.44) are the initial conditions at time $t = t_0$ for the displacement and the velocity field, respectively. The set of equations (2.40)-(2.44) are also called the local or strong form since they describe the local mechanical behavior at every material point and at every time.

2.1.5. Dimensionally-reduced fluid mechanics

As discussed in Sec. 1.2, the heart operates in a closed-loop system, where blood flows continuously through the circulatory system. Hence, when modeling cardiac mechanics, it is essential to account for the circulatory system and blood flow. This can be achieved in various ways, such as employing complex Fluid-Structure Interaction (FSI) methods, as discussed in [91]. However, in this thesis, a simplified dimensional reduced mechanical model is used to approximate the vascular system. Here, so-called *0-dimensional (0D) lumped parameter Windkessel* models are employed.
Within these models, the relationship between the quantities of interest, the pressure p, and flow rate q is modeled. For a comprehensive overview, the reader is referred to [158]. The following section provides an overview of all necessary components based on the insights from [62]. These components are motivated by principles found in electrical circuits. A detailed description of each component and the derivation of all windkessel model equations can be found in App. A.2.

2-element windkessel The 2-element windkessel model describes the circulatory system's venous behavior and is depicted in Fig. 2.2. In analogy, this model operates as a low-pass filter element. The model equation reads

$$C\frac{\mathrm{d}p_{\text{in}}}{\mathrm{d}t} + \frac{p_{\text{in}} - p_{\text{out}}}{R} = q_{\text{in}}. \tag{2.45}$$

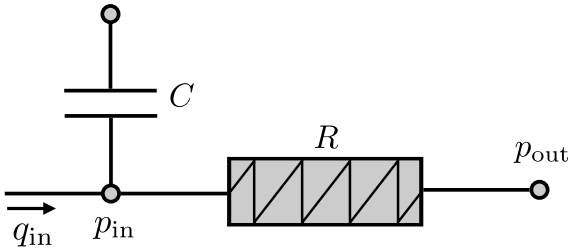

Abbildung 2.2.: 2-element windkessel model.

4-element windkessel The 4-element windkessel model is used to describe the arterial circulation and is presented in Fig. 2.3. Its model equation is given by [144]

$$C\frac{\mathrm{d}p_{\text{in}}}{\mathrm{d}t} + \frac{p_{\text{in}} - p_{\text{out}}}{R} + \frac{LC}{R}\frac{\mathrm{d}^2 p_{\text{in}}}{\mathrm{d}t^2} = \left(1 + \frac{Z}{R}\right) q_{\text{in}} + \left(CZ + \frac{L}{R}\right)\frac{\mathrm{d}q_{\text{in}}}{\mathrm{d}t} + \frac{LCZ}{R}\frac{\mathrm{d}^2 q_{\text{in}}}{\mathrm{d}t^2}. \tag{2.46}$$

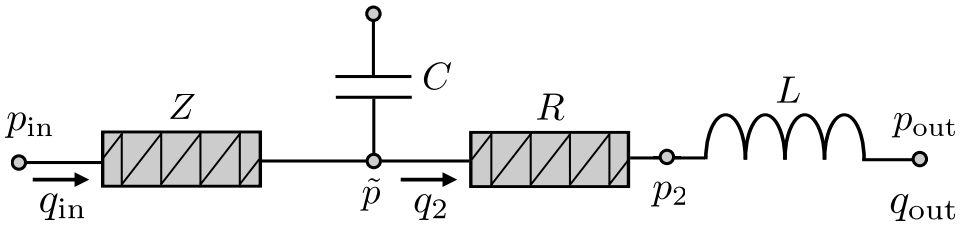

Abbildung 2.3.: 4-element windkessel model.

Diode element The diode element models the heart valves and is shown in Fig. 2.4. It induces a pressure drop in the presence of flow. Unlike the resistance, the proportionality constant $\tilde{R}$ varies with the direction of the pressure gradient across the valve. The model equations read

$$\tilde{R}q = p_{\text{in}} - p_{\text{out}}, \tag{2.47}$$

$$\tilde{R} = \begin{cases} R^{\text{max}} & \text{for } p_{\text{in}} < p_{\text{out}}, \\ R^{\text{min}} & \text{for } p_{\text{in}} \geqslant p_{\text{out}}. \end{cases} \tag{2.48}$$

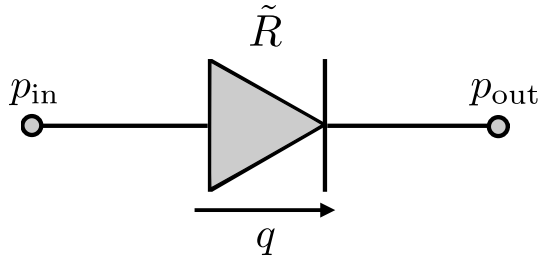

Abbildung 2.4.: Diode windkessel model.

Elastance model The Elastance model is used to model the atrial compartments and is depicted in Fig.2.5. It represents a capacity to store and release fluid. Consequently, the rate of change in a compartment volume describes the reduction in flow rate. The model equations read

$$\frac{\mathrm{d}V}{\mathrm{d}t} - q_{\text{in}} + q_{\text{out}} = 0, \tag{2.49}$$

$$p_{\text{in}} = [(E_{\text{max}} - E_{\text{min}})y(t) + E_{\text{min}}](V - V_0). \tag{2.50}$$

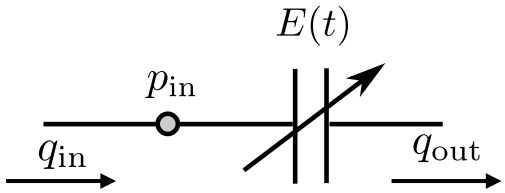

Abbildung 2.5.: Elastance windkessel model.

2.2. Finite element method

The finite element method (FEM) [70, 165] is based on variational formulations of differential problems, like the ones introduced in Sec. 2.1.4. The corresponding variational problems, assuming sufficient regularity of the solutions, share identical solutions with their differential counterparts. Specifically, it is possible to analyze differential problems using functional analysis by first obtaining their linear variational forms, see Sec. 2.2.1. After obtaining the weak form, the computational domain is approximated by so-called finite elements, see Sec. 2.2.2. Sec. 2.2.3 explains temporal discretization needed for dynamic problems. Finally, in Sec. 2.2.4, iterative solution techniques for nonlinear systems of equations are presented.

2.2.1. Weak formulation

To derive the weak form, the balance law in Eq. (2.40) is multiplied with a so-called *weighting* or *test* function[1] $\delta\boldsymbol{u}$ from an appropriate vector space $\mathcal{V}$ and afterward integrated over the reference

[1] In the context of structural mechanics, the test function is also referred to as the virtual displacement.

computational domain and it reads

$$\int_{\Omega_0} [\rho_0 \ddot{\boldsymbol{u}} - \nabla_{\boldsymbol{X}} \cdot \boldsymbol{P} - \boldsymbol{b}_0] \, \delta \boldsymbol{u} \, \mathrm{d}V = 0 \quad \forall \delta \boldsymbol{u} \in \mathcal{V}. \tag{2.51}$$

Subsequently, suitable infinite-dimensional solution manifolds and spaces for the solutions $\boldsymbol{u}$ and the test function $\delta \boldsymbol{u}$ are defined, respectively,

$$\boldsymbol{u} \in \mathcal{U} = \{\boldsymbol{u} \in [H^1(\Omega_0)]^3 | \; \boldsymbol{u} = \hat{\boldsymbol{u}} \text{ on } \Gamma_\mathrm{u}\}, \tag{2.52}$$

$$\delta \boldsymbol{u} \in \mathcal{V} = \{\delta \boldsymbol{u} \in [H^1(\Omega_0)]^3 | \; \delta \boldsymbol{u} = 0 \text{ on } \Gamma_\mathrm{u}\}. \tag{2.53}$$

Here, $\mathcal{U}$ denotes the solution space, $\mathcal{V}$ the trial function space, and $H^1(\Omega_0)$ is a Sobolev space on Ω_0. The Dirichlet boundary conditions are consistently imposed by selecting appropriate function spaces.
Using the divergence theorem, the boundary conditions of the IBVP and the transformation from the first to the second Piola-Kirchhoff stress tensor yields the well-known *principle of virtual work* in the material description. A more detailed derivation is given in App. A.3. The final form of the weak form reads

$$\delta \mathcal{W} = \delta \mathcal{W}_\text{kin} + \delta \mathcal{W}_\text{int} - \delta \mathcal{W}_\text{ext} = 0 \quad \forall \delta \boldsymbol{u} \in \mathcal{V}, \tag{2.54}$$

with the kinematic virtual work

$$\delta \mathcal{W}_\text{kin} = \int_{\Omega_0} \rho_0 \ddot{\boldsymbol{u}} \cdot \delta \boldsymbol{u} \, \mathrm{d}V, \tag{2.55}$$

the internal virtual work

$$\delta \mathcal{W}_\text{int} = \int_{\Omega_0} \boldsymbol{S} : \delta \boldsymbol{E} \, \mathrm{d}V, \tag{2.56}$$

and the external virtual work

$$\delta \mathcal{W}_\text{ext} = \int_{\Omega_0} \boldsymbol{b}_0 \cdot \delta \boldsymbol{u} \, \mathrm{d}V + \int_{\Gamma_\mathrm{n}} \boldsymbol{t}_0 \cdot \delta \boldsymbol{u} \, \mathrm{d}A. \tag{2.57}$$

2.2.2. Discretization in space

The weak form of the IBVP (2.54) is the starting point for the finite element method. First, the computational domain is divided into finite elements, which are a set of geometrically simple shapes, e.g., tetrahedra,

$$\Omega_0 \approx \tilde{\Omega}_0 = \bigcup_{e=1}^{n_\mathrm{el}} \Omega_0^e, \tag{2.58}$$

where n_el is the total number of elements that are used to approximate the domain Ω_0. Second, the continuous problem is reformulated as a discrete problem. Therefore, the global continuous function $\boldsymbol{u}$ is substituted with the discrete solution $\boldsymbol{u}_h \in \mathcal{U}_h \subset \mathcal{U}$ and the test function $\delta \boldsymbol{u}$ is substituted with the virtual displacement $\delta \boldsymbol{u}_h \in \mathcal{V}_h \subset \mathcal{V}$. Given a finite element with a total of n_n

element nodes, each of these nodes is associated with a *shape function* $N_i(\boldsymbol{X}), i \in \{1, \ldots, n_\mathrm{n}\}$. The set of all shape functions within one finite element is denoted as $\boldsymbol{N}^e(\boldsymbol{X})$. The displacement vector $\boldsymbol{u}_h$ for each finite element is defined as the linear combination of the *nodal displacements* $\boldsymbol{d}^e$ and its shape functions $\boldsymbol{N}^e(\boldsymbol{X})$,

$$\boldsymbol{u}_h\Big|_{\Omega_0^e} \approx \boldsymbol{u}_h^e(\boldsymbol{X}, t) = \boldsymbol{N}^e(\boldsymbol{X})\, \boldsymbol{d}^e(t). \tag{2.59}$$

Similarly, the virtual displacement $\delta\boldsymbol{u}_h$ is approximated as

$$\delta\boldsymbol{u}_h\Big|_{\Omega_0^e} \approx \delta\boldsymbol{u}_h^e(\boldsymbol{X}, t) = \boldsymbol{N}^e(\boldsymbol{X})\, \delta\boldsymbol{d}^e(t), \tag{2.60}$$

where $\delta\boldsymbol{d}^e$ is the virtual displacement vector. Using the same shape functions for the solution $\boldsymbol{u}_h$ and the weighting function $\delta\boldsymbol{u}_h$ is called the *Bubnov-Galerkin method*[2] [148].
For the sake of simplicity and readability, the dependencies of Eq. (2.59) and Eq. (2.60) on position $\boldsymbol{X}$ and time t are omitted. In this work, the finite element method is based on the isoparametric concept, i.e., the chosen basis functions are also used to represent the geometry

$$\boldsymbol{X}_h\Big|_{\Omega_0^e} \approx \boldsymbol{X}_h^e = \boldsymbol{N}^e\, \tilde{\boldsymbol{X}}_h^e, \tag{2.61}$$

where $\tilde{\boldsymbol{X}}_h^e$ are the nodal coordinates. For a given finite element with n_n element nodes, the shape function matrix $\boldsymbol{N}^e \in \mathbb{R}^{3\times n_\mathrm{el}}$ reads

$$\boldsymbol{N}^e = \begin{bmatrix} N_1 & 0 & 0 & \ldots & N_{n_\mathrm{n}} & 0 & 0 \\ 0 & N_1 & 0 & \ldots & 0 & N_{n_\mathrm{n}} & 0 \\ 0 & 0 & N_1 & \ldots & 0 & 0 & N_{n_\mathrm{n}} \end{bmatrix}. \tag{2.62}$$

The basic idea for shape functions is to choose a set of simple polynomials, where the i^{th} shape function takes the value of 1 at the i^{th} node and 0 at every other node. Furthermore, they sum up to 1 at every location inside the finite element, which is the so-called *partition of unity*. The most common shape functions are Lagrange polynomials.
The element displacement vector $\boldsymbol{d}^e \in \mathbb{R}^{3n_\mathrm{n}}$ and the virtual displacement vector $\delta\boldsymbol{d}^e \in \mathbb{R}^{3n_\mathrm{n}}$ are given as

$$\boldsymbol{d}^e = \begin{bmatrix} d_{1,1}^e \\ d_{1,2}^e \\ d_{1,3}^e \\ \vdots \\ d_{n_\mathrm{n},1}^e \\ d_{n_\mathrm{n},2}^e \\ d_{n_\mathrm{n},3}^e \end{bmatrix}, \quad \delta\boldsymbol{d}^e = \begin{bmatrix} \delta d_{1,1}^e \\ \delta d_{1,2}^e \\ \delta d_{1,3}^e \\ \vdots \\ \delta d_{n_\mathrm{n},1}^e \\ \delta d_{n_\mathrm{n},2}^e \\ \delta d_{n_\mathrm{n},3}^e \end{bmatrix}, \tag{2.63}$$

where $d_{i,j}$ and $\delta d_{i,j}$ of element e are the displacement and virtual displacement of node i in spatial direction j, respectively.

[2] Choosing different basis functions yields the so-called the *Petrov-Galerkin method*.

With all the necessary tools available, the weak from Eq. (2.54) can now be approximated as the sum over all finite elements

$$\delta \mathcal{W} \approx \sum_{e=1}^{n_{\mathrm{el}}} \left[\boldsymbol{M}^e \ddot{\boldsymbol{d}}^e + \boldsymbol{f}_{\mathrm{int}}^e - \boldsymbol{f}_{\mathrm{ext}}^e \right] \cdot \delta \boldsymbol{d}^e = \boldsymbol{0}, \quad \forall \delta \boldsymbol{d}^e. \tag{2.64}$$

The element mass matrix $\boldsymbol{M}^e$ fulfills

$$\boldsymbol{M}^e \ddot{\boldsymbol{d}}^e \cdot \delta \boldsymbol{d}^e = \int_{\Omega_0} {\rho_0}^e \ddot{\boldsymbol{u}}_h^e \cdot \delta \boldsymbol{u}_h^e \, \mathrm{d}V. \tag{2.65}$$

The nonlinear element internal force vector $\boldsymbol{f}_{\mathrm{int}}^e$ includes all kinematic and constitutive contributions and fulfills

$$\boldsymbol{f}_{\mathrm{int}}^e \cdot \delta \boldsymbol{d}^e = \int_{\Omega_0} \boldsymbol{S}^e : \delta \boldsymbol{E}^e \, \mathrm{d}V. \tag{2.66}$$

The element external force vector $\boldsymbol{f}_{\mathrm{ext}}^e$ includes contributions of prescribed body forces and boundary tractions and fulfills

$$\boldsymbol{f}_{\mathrm{ext}}^e \cdot \delta \boldsymbol{d}^e = \int_{\Omega_0} \boldsymbol{b}_0^e \cdot \delta \boldsymbol{u}_h^e \, \mathrm{d}V + \int_{\Gamma_{\mathrm{n}}} \boldsymbol{T}^e \cdot \delta \boldsymbol{u}_h^e \, \mathrm{d}A. \tag{2.67}$$

According to the fundamental lemma of variational calculus, the discretized global principle of virtual work (2.64) has to be satisfied for arbitrary virtual displacements $\delta \boldsymbol{d}^e$. Thus, the final global balance of linear momentum yields

$$\boldsymbol{M} \ddot{\boldsymbol{d}} + \boldsymbol{f}_{\mathrm{int}} - \boldsymbol{f}_{\mathrm{ext}} = \boldsymbol{0}, \tag{2.68}$$

with the global mass matrix $\boldsymbol{M} \in \mathbb{R}^{n_{\mathrm{dof}} \times n_{\mathrm{dof}}}$, the global internal force vector $\boldsymbol{f}_{\mathrm{int}} \in \mathbb{R}^{n_{\mathrm{dof}}}$, the global external force vector $\boldsymbol{f}_{\mathrm{ext}} \in \mathbb{R}^{n_{\mathrm{dof}}}$, the global displacement vector $\boldsymbol{d} \in \mathbb{R}^{n_{\mathrm{dof}}}$, the global virtual displacement vector $\delta \boldsymbol{d} \in \mathbb{R}^{n_{\mathrm{dof}}}$ and n_{dof} as the global number of degrees of freedom. Note that to obtain the global mass matrix, internal force and external force vector, assembly procedures are required. These procedures involve aggregating the contributions from individual elements into the corresponding global quantities, accounting for the connectivity and boundary conditions of the finite element model [165].
While damping is prevalent in nearly all engineering applications, the global balance equation (2.68) does not account for damping. To address this, it is common practice to introduce the *Rayleigh damping* matrix $\boldsymbol{D} \in \mathbb{R}^{n_{\mathrm{dof}} \times n_{\mathrm{dof}}}$ as

$$\boldsymbol{D} = c_{\mathrm{M}} \boldsymbol{M} + c_{\mathrm{f}} \frac{\partial \boldsymbol{f}_{\mathrm{int}}}{\partial \boldsymbol{d}}, \tag{2.69}$$

with c_{M} $[1/\mathrm{s}]$ being the constant scale factor for the mass matrix and c_{f} $[\mathrm{s}]$ as the scale factor of the so-called tangent stiffness matrix.
Finally, the spatially discretized computational model reads

$$\boldsymbol{M} \ddot{\boldsymbol{d}} + \boldsymbol{D} \dot{\boldsymbol{d}} + \boldsymbol{f}_{\mathrm{int}} - \boldsymbol{f}_{\mathrm{ext}} = \boldsymbol{0}. \tag{2.70}$$

Note that the displacements $\boldsymbol{d} = \boldsymbol{d}(t)$ and the forces $\boldsymbol{f}_{\mathrm{int}} = \boldsymbol{f}_{\mathrm{int}}(\boldsymbol{d}, t)$ and $\boldsymbol{f}_{\mathrm{ext}} = \boldsymbol{f}_{\mathrm{ext}}(\boldsymbol{d}, t)$ are time-dependent functions. Therefore, discretization in time is explained in the following section. For steady-state problems, i.e., problems with no temporal dependency, Eq. (2.70) simplifies to

$$\boldsymbol{f}_{\mathrm{int}} - \boldsymbol{f}_{\mathrm{ext}} = \boldsymbol{0}. \tag{2.71}$$

2.2.3. Discretization in time

This section presents time integration schemes for solving first- and second-order ordinary differential equations (ODEs). In contrast to spatial discretization, time discretization in this work is achieved through the finite difference (FD) method.
For first-order ODEs, the one-step-θ scheme is used

$$\frac{(\bullet)^n - (\bullet)^{n-1}}{\Delta t} = \theta f((\bullet)^n) + [1-\theta] f((\bullet)^{n-1}), \tag{2.72}$$

with the scalar parameter $\theta \in [0,1]$ and time step n. For $\theta = 0$ the explicit time integration scheme called *Forward-Euler scheme* is obtained, wheres $\theta = 1$ yields the fully implicit method called *Backward-Euler scheme*.
For second-order ODE's like Eq. (2.70), the generalized-α scheme is applied [25]. Therein, the discretized equation of motion in residual form reads

$$\boldsymbol{r} = \boldsymbol{M}\boldsymbol{a}^{n+1-\alpha_m} + \boldsymbol{D}\boldsymbol{v}^{n+1-\alpha_f} + \boldsymbol{f}_{\text{int}}^{n+1-\alpha_f} - \boldsymbol{f}_{\text{ext}}^{n+1-\alpha_f}, \tag{2.73}$$

where $\alpha_m \in [0,1]$ and $\alpha_f \in [0,1]$ are scalar constants defined as

$$\alpha_m = \frac{2\rho_\infty - 1}{\rho_\infty + 1}, \tag{2.74}$$

$$\alpha_f = \frac{\rho_\infty}{\rho_\infty + 1}, \tag{2.75}$$

with constant parameter $\rho_\infty \in [0,1]$ which adjusts the numerical dissipation of the time integration. The midpoint accelerations, velocities, displacements, and forces are defined as linear combinations of their respective current and previous time step values

$$\boldsymbol{a}^{n+1-\alpha_m} = [1-\alpha_m]\boldsymbol{a}^{n+1} + \alpha_m \boldsymbol{a}^n, \tag{2.76}$$

$$\boldsymbol{v}^{n+1-\alpha_f} = [1-\alpha_f]\boldsymbol{v}^{n+1} + \alpha_f \boldsymbol{v}^n, \tag{2.77}$$

$$\boldsymbol{d}^{n+1-\alpha_f} = [1-\alpha_f]\boldsymbol{d}^{n+1} + \alpha_f \boldsymbol{d}^n, \tag{2.78}$$

$$\boldsymbol{f}_{\text{int}}^{n+1-\alpha_f} = [1-\alpha_f]\boldsymbol{f}_{\text{int}}^{n+1} + \alpha_f \boldsymbol{f}_{\text{int}}^n, \tag{2.79}$$

$$\boldsymbol{f}_{\text{ext}}^{n+1-\alpha_f} = [1-\alpha_f]\boldsymbol{f}_{\text{ext}}^{n+1} + \alpha_f \boldsymbol{f}_{\text{ext}}^n. \tag{2.80}$$

As the displacement field $\boldsymbol{d}$ is the only primary variable, the reconstruction of the velocity and acceleration is introduced as

$$\boldsymbol{a}^{n+1} = \frac{1}{\beta \Delta t^2}[\boldsymbol{d}^{n+1} - \boldsymbol{d}^n] - \frac{1}{\beta \Delta t}\boldsymbol{v}^n - \frac{1-2\beta}{2\beta}\boldsymbol{a}^n, \tag{2.81}$$

$$\boldsymbol{v}^{n+1} = \frac{\gamma}{\beta \Delta t}[\boldsymbol{d}^{n+1} - \boldsymbol{d}^n] - \frac{\gamma - \beta}{\beta}\boldsymbol{v}^n - \frac{\gamma - 2\beta}{2\beta}\Delta t \boldsymbol{a}^n, \tag{2.82}$$

with the scalar constants $\beta \in [0, \frac{1}{2}]$ and $\gamma \in [0,1]$ as

$$\beta = \frac{1}{4}(1 - \alpha_m + \alpha_f)^2, \tag{2.83}$$

$$\gamma = \frac{1}{2} - \alpha_m + \alpha_f. \tag{2.84}$$

2.2.4. Nonlinear solution techniques

To solve the nonlinear equation (2.73) for the discrete vector of unknowns $\boldsymbol{d}^{n+1}$, an iterative solution technique is used. Here, the Newton-Raphson method [163] is chosen. It requires a linearization of Eq. (2.73) at the end of the time step, which reads

$$\text{Lin}\, \boldsymbol{r}(\boldsymbol{d}_i^{n+1}) = \boldsymbol{r}(\boldsymbol{d}_i^{n+1}) + \boldsymbol{K}_{\text{eff}}(\boldsymbol{d}_i^{n+1})\Delta\boldsymbol{d}_{i+1}^{n+1}, \tag{2.85}$$

where the index i is the step of the Newton-Raphson algorithm and $\boldsymbol{K}_{\text{eff}}$ denotes the *dynamic effective tangential stiffness* matrix given as

$$\boldsymbol{K}_{\text{eff}}(\boldsymbol{d}_i^{n+1-\alpha_f}) = \left[\frac{1-\alpha_m}{\beta\Delta t^2}\boldsymbol{M} + \frac{(1-\alpha_f)\gamma}{\beta\Delta t}\boldsymbol{D}(\boldsymbol{d}^{n+1-\alpha_f}) + (1-\alpha_f)\boldsymbol{K}_{\text{T}}(\boldsymbol{d}^{n+1-\alpha_f})\right]_i, \tag{2.86}$$

where

$$\boldsymbol{K}_{\text{T}}(\boldsymbol{d}^{n+1-\alpha_f}) = \frac{\partial \boldsymbol{f}_{\text{int}}(\boldsymbol{d}^{n+1-\alpha_f})}{\partial \boldsymbol{d}^{n+1}} - \frac{\partial \boldsymbol{f}_{\text{ext}}(\boldsymbol{d}^{n+1-\alpha_f})}{\partial \boldsymbol{d}^{n+1}}. \tag{2.87}$$

is the *tangential stiffness* matrix $\boldsymbol{K}_{\text{T}}$, including geometrical and material stiffness contributions from the finite elements. Furthermore, this stiffness matrix is the discrete representation of the material tangent in Eq. (2.32).

The update for a new displacement field reads

$$\boldsymbol{d}_{i+1}^{n+1} = \boldsymbol{d}_i^{n+1} + \Delta\boldsymbol{d}_{i+1}^{n+1}, \tag{2.88}$$

where the displacement increment $\Delta\boldsymbol{d}_{i+1}^{n+1}$ results from the solution of the linear equation system in Eq. (2.85) and is given by

$$\boldsymbol{K}_{\text{eff}}(\boldsymbol{d}_i^{n+1-\alpha_f})\Delta\boldsymbol{d}_{i+1}^{n+1} = -\boldsymbol{r}(\boldsymbol{d}_i^{n+1}). \tag{2.89}$$

The iteration process is continued until convergence is reached, i.e., the residual and displacement increment 2-norms are below a certain tolerance.

$$||\boldsymbol{r}(\boldsymbol{d}_i^{n+1})||_2 \leq \epsilon_{\text{res}}, \tag{2.90}$$

$$||\Delta\boldsymbol{d}_{i+1}^{n+1}||_2 \leq \epsilon_{\text{inc}}. \tag{2.91}$$

Although the Newton-Raphson scheme typically exhibits quadratic convergence, it can encounter issues at critical points like bifurcation problems, snap-through phenomena, or abrupt load changes. To address these challenges, it is common practice to complement it with a line search algorithm or other regularization techniques such as pseudo-transient continuation (PTC) scheme [44].
Solving a large linear system, as the one in Eq. (2.89), can be computationally expensive. These systems can be solved efficiently if the condition number of the matrix $\boldsymbol{K}_{\text{eff}}$ is close to 1, indicating a well-conditioned problem. Preconditioning techniques can be employed to reduce the condition number and enhance the overall numerical stability of the system [23].

2.3. Parameter estimation

Numerous parameters in cardiac mechanics models, such as the myocardial tissue contractility or the muscle growth rate, are intricately linked to a patient's unique physiology and anatomy, making their determination through *in-vivo* experiments impossible. Consequently, developing patient-specific models involves an iterative procedure called *inverse analysis*. In this context, the weak form of the IBVP in Eq. (2.54) is called the *forward problem*. The task of finding the matching parameters is known as the so-called *parameter identification* or *inverse problem*.
In Sec. 2.3.1, the parametrization of the IBVP is outlined. Subsequently, in Sec. 2.3.2, the statistical formulation of the identification problem is presented. In Sec. 2.3.3, the Lagrangian formulation and the corresponding adjoint equations are derived. In Sec. 2.3.4, the regularization of the parametrization is briefly discussed. Finally, in Sec. 2.3.5, the similarity measure between two surfaces is presented. For a more detailed overview of the following framework, the reader is referred to [16, 79, 80].

2.3.1. Parametrization and identification problem

To establish the parameter identification framework and define the inverse problem, the parametrization $\boldsymbol{\theta}$ is introduced. These parameters are assumed to vary in space and are therefore represented as

$$\boldsymbol{\theta} = \boldsymbol{\theta}(\boldsymbol{X}). \tag{2.92}$$

The parameters $\boldsymbol{\theta}$ can be incorporated into the equations in two ways: One option is to integrate them within the parametrized strain energy function, which reads

$$\Psi(\boldsymbol{C}) = \Psi_{\boldsymbol{\theta}}(\boldsymbol{C}, \boldsymbol{\theta}). \tag{2.93}$$

Another option is to integrate these parameters into the deformation gradient, which results in a modified version of the weak formulation Eq. (2.54) of the nonlinear solid mechanics problem

$$\delta\mathcal{W}(\boldsymbol{u}(\boldsymbol{\theta}), \delta\boldsymbol{u}, \boldsymbol{\theta}) = 0 \quad \forall \delta\boldsymbol{u} \in \mathcal{V}. \tag{2.94}$$

Within this thesis, the latter formulation is used, and the modified weak form in Eq. (2.94) acts as the forward problem $F(\boldsymbol{u}(\boldsymbol{\theta}), \boldsymbol{\theta})$.
To complete the terminology, the system's current state is defined as $\hat{\boldsymbol{U}}$, while the observation $\boldsymbol{Z}$ represents the given measurements. In the case of cardiac mechanics models, measurements are, for example, computed tomography (CT) images. The observation operator C establishes the relationship between the current state of the system and the observations.
The overall objective of the identification problem is to find a parametrization $\boldsymbol{\theta}$ such that

$$\boldsymbol{Z} = C(F(\boldsymbol{u}(\boldsymbol{\theta}), \boldsymbol{\theta})). \tag{2.95}$$

However, the direct solution approach to this identification problem via inversion suffers from severe shortcomings [79]. More precisely, given an exact distribution $\boldsymbol{\theta}^*$, the solution of the weak form causes a potential discrepancy between the model output and the real system state.

Furthermore, errors in the measurements can increase this discrepancy. Therefore, the identification problem is typically formulated as an optimization problem to minimize an objective function $\mathcal{J}$.
In this context, regularization of the output least-squares formulation is employed

$$\boldsymbol{\theta}^* = \underset{\boldsymbol{\theta}}{\operatorname{argmin}}\, \mathcal{J}(\boldsymbol{\theta}) = \underset{\boldsymbol{\theta}}{\operatorname{argmin}} \left(||\boldsymbol{Z} - C(F(\boldsymbol{u}(\boldsymbol{\theta}), \boldsymbol{\theta}))||_{\boldsymbol{Z}}^2 + R(\boldsymbol{\theta}) \right), \tag{2.96}$$

where R is the regularization functional controlling the norm of the solution $\boldsymbol{\theta}^*$. Regularization of the parameters is essential as the optimization problem can become ill-conditioned, i.e., the solution can become non-unique, non-convex, or could have multiple minimum, and a minor alteration in the observations can result in significant variations in the optimal parameters $\boldsymbol{\theta}^*$. The observation norm $||\bullet||_{\boldsymbol{Z}}$ depends on the specific choice of the measurements. For example, for scalar-valued measurements, the 2-norm could be used, and in the case of CT images, this norm could compare surfaces to each other.
This deterministic solution approach, however, is unable to account for variability in the optimal solution induced by the noise of the measurements. Therefore, the identification problem has to be formulated in a probabilistic manner. This probabilistic framework is based on the Bayesian paradigm, which is explained in the following section.

2.3.2. Bayesian inverse problem

The theoretical background of the concepts of probability theory, random variables, expected values, and variance is briefly summarized in App. A.4 and is based on [10].
To transform the identification problem into a statistical setting, the observations $\boldsymbol{Z}$ and the parameters $\boldsymbol{\theta}$ are interpreted as random variables

$$\boldsymbol{Z} \sim p(\boldsymbol{Z}), \tag{2.97}$$

$$\boldsymbol{\theta} \sim p(\boldsymbol{\theta}), \tag{2.98}$$

with $p(\boldsymbol{Z})$ and $p(\boldsymbol{\theta})$ being the *prior probability densities* of $\boldsymbol{Z}$ and $\boldsymbol{\theta}$, respectively. The conditional probability of $\boldsymbol{\theta}$, while knowing $\boldsymbol{Z}$, is called *posterior density* and is defined by the application of Bayes' theorem and reads

$$p(\boldsymbol{\theta}|\boldsymbol{Z}) = \frac{p(\boldsymbol{Z}|\boldsymbol{\theta})p(\boldsymbol{\theta})}{p(\boldsymbol{Z})}, \tag{2.99}$$

where the conditional probability $p(\boldsymbol{Z}|\boldsymbol{\theta})$ is referred to as the *likelihood* of the observations for given parameters. To establish a concept of optimality, the constant model evidence $p(\boldsymbol{Z})$ with respect to $\boldsymbol{\theta}$ is omitted, and it is sufficient to observe the proportionality

$$p(\boldsymbol{\theta}|\boldsymbol{Z}) \propto p(\boldsymbol{Z}|\boldsymbol{\theta})p(\boldsymbol{\theta}). \tag{2.100}$$

The Bayesian reinterpretation of the identification problem is similar to the optimization problem presented in Eq. (2.96). However, the outcome is a probability density function instead of yielding a single-point estimate. The objective is to maximize the posterior density $p(\boldsymbol{\theta}|\boldsymbol{Z})$, which leads to the application of the *maximum a posteriori* (MAP) estimation.
The remainder of this section is used to derive the formulation of the statistical identification problem and to provide definitions of the likelihood function $p(\boldsymbol{Z}|\boldsymbol{\theta})$ and the prior $p(\boldsymbol{\theta})$.

2.3.3. Lagrangian formulation and adjoint method

It is often challenging to directly discretize the MAP estimation and solve for a maximum posterior density. Therefore, a common approach is to transform the statistical identification problem in Eq. (2.100) into a minimization problem similar to Eq. (2.96). This is achieved by redefining the objective function as

$$\mathcal{J}(\boldsymbol{u}(\boldsymbol{\theta}), \boldsymbol{\theta}) := \frac{1}{2\sigma^2} D(\boldsymbol{Z}, F(\boldsymbol{u}(\boldsymbol{\theta}), \boldsymbol{\theta})) + \alpha R(\boldsymbol{\theta}), \tag{2.101}$$

where σ is the variance of the distance measure, $D(\bullet, \bullet)$ is called the similarity measure between two surfaces explained in Sec. 2.3.5, and α is the regularization weight associated with the regularization function $R(\boldsymbol{\theta})$ explained in Sec. 2.3.4. For a specific choice of the function $p(\bullet)$, maximizing the posterior in Eq. (2.100) becomes [80]

$$\underset{\boldsymbol{\theta}}{\operatorname{argmax}}\, p(\boldsymbol{Z}|\boldsymbol{\theta}) p(\boldsymbol{\theta}) = \underset{\boldsymbol{\theta}}{\operatorname{argmin}}\, \mathcal{J}(\boldsymbol{u}(\boldsymbol{\theta}), \boldsymbol{\theta}). \tag{2.102}$$

To solve this minimization problem using gradient-based optimization, the gradient of the objective function $\mathcal{J}$ with respect to the parameter $\boldsymbol{\theta}$ has to be evaluated. The gradient is obtained using the chain rule and reads

$$\frac{\mathrm{d}\mathcal{J}}{\mathrm{d}\boldsymbol{\theta}} = \frac{\partial \mathcal{J}}{\partial \boldsymbol{u}} \frac{\partial \boldsymbol{u}}{\partial \boldsymbol{\theta}} + \frac{\partial \mathcal{J}}{\partial \boldsymbol{\theta}}. \tag{2.103}$$

Note that evaluating the gradient using FD is not feasible due to the high computational cost in the case of large mechanical models, as the number of model evaluations scales with the number of optimization parameters. Therefore, the adjoint method is selected to compute the gradient, as the number of model evaluations is independent of the parameter dimension [49].

Gradient computation

Starting from a continuous formulation, the Lagrangian $\mathcal{L}$ is introduced as a function of the objective functional $\mathcal{J}$ from Eq. (2.101) and the weak form in Eq. (2.54) and it reads

$$\begin{aligned} \mathcal{L}(\boldsymbol{u}(\boldsymbol{\theta}), \boldsymbol{\lambda}, \boldsymbol{\theta}) : &= \mathcal{J}(\boldsymbol{u}(\boldsymbol{\theta}), \boldsymbol{\theta}) + \delta \mathcal{W}(\boldsymbol{u}(\boldsymbol{\theta}), \boldsymbol{\lambda}, \boldsymbol{\theta}), && (2.104) \\ &= \frac{1}{2\sigma^2} D(\boldsymbol{Z}, F(\boldsymbol{u}(\boldsymbol{\theta}), \boldsymbol{\theta})) + \alpha R(\boldsymbol{\theta}) + \boldsymbol{\lambda}^T \delta \mathcal{W}(\boldsymbol{u}(\boldsymbol{\theta}), \boldsymbol{\theta}), && (2.105) \end{aligned}$$

where $\boldsymbol{\lambda}$ is the vector of Lagrange multipliers. Note that $\boldsymbol{\lambda}$ replaces the test functions $\delta \boldsymbol{d}^e$ in Eq. (2.64). Furthermore, the residual $\delta \mathcal{W}$ evaluated at the solution $\boldsymbol{u}^*$ for an arbitrary $\boldsymbol{\theta}$ has to vanish, and therefore, the following equivalence is enforced

$$\underset{\boldsymbol{\theta}}{\operatorname{argmin}}\, \mathcal{J}(\boldsymbol{u}(\boldsymbol{\theta}), \boldsymbol{\theta}) \equiv \underset{\boldsymbol{\theta}}{\operatorname{argmin}}\, \mathcal{L}(\boldsymbol{u}(\boldsymbol{\theta}), \boldsymbol{\lambda}, \boldsymbol{\theta}). \tag{2.106}$$

Now, the gradient from Eq. (2.103) can be rewritten as

$$\frac{\mathrm{d}\mathcal{J}}{\mathrm{d}\boldsymbol{\theta}} = \frac{\mathrm{d}\mathcal{L}(\boldsymbol{u}(\boldsymbol{\theta}), \boldsymbol{\lambda}, \boldsymbol{\theta})}{\mathrm{d}\boldsymbol{\theta}} = \frac{\partial \mathcal{J}}{\partial \boldsymbol{u}} \frac{\partial \boldsymbol{u}}{\partial \boldsymbol{\theta}} + \frac{\partial \mathcal{J}}{\partial \boldsymbol{\theta}} + \boldsymbol{\lambda}^T \left[\frac{\partial \delta \mathcal{W}}{\partial \boldsymbol{u}} \frac{\partial \boldsymbol{u}}{\partial \boldsymbol{\theta}} + \frac{\partial \delta \mathcal{W}}{\partial \boldsymbol{\theta}} \right]. \tag{2.107}$$

Rearranging Eq. (2.107) yields

$$\frac{\mathrm{d}\mathcal{L}(\boldsymbol{u}(\boldsymbol{\theta}),\boldsymbol{\lambda},\boldsymbol{\theta})}{\mathrm{d}\boldsymbol{\theta}} = \left[\frac{\partial\mathcal{J}}{\partial\boldsymbol{u}} + \boldsymbol{\lambda}^T\frac{\partial\delta\mathcal{W}}{\partial\boldsymbol{u}}\right]\frac{\partial\boldsymbol{u}}{\partial\boldsymbol{\theta}} + \frac{\partial\mathcal{J}}{\partial\boldsymbol{\theta}} + \boldsymbol{\lambda}^T\frac{\partial\delta\mathcal{W}}{\partial\boldsymbol{\theta}}. \tag{2.108}$$

Since the gradient $\partial\boldsymbol{u}/\partial\boldsymbol{\theta}$ can only be computed through the nonlinear solution, a straightforward computation of this gradient is complex. Hence, the free-choice Lagrange parameter $\boldsymbol{\lambda}$ is chosen such that the first term in Eq. (2.108) vanishes. This equation is referred to as the *adjoint equation*, and it reads

$$\frac{\partial\mathcal{J}}{\partial\boldsymbol{u}} + \boldsymbol{\lambda}^T\frac{\partial\delta\mathcal{W}}{\partial\boldsymbol{u}} = \boldsymbol{0}. \tag{2.109}$$

Note that the gradient of the residual $\delta\mathcal{W}$ with respect to the displacement field $\boldsymbol{u}$ is the tangent stiffness matrix $\boldsymbol{K}_{\mathrm{T}}$, see Eq. (2.87). The first term of the adjoint equation (2.109) solely depends on the choice of the similarity measure D, since the regularization function R is independent of the displacement field $\boldsymbol{u}$. Their definition and gradient computation are discussed in Sec. 2.3.4 and Sec. 2.3.5.
Inserting the solution of the adjoint equation (2.109) into Eq. (2.108), the gradient becomes

$$\frac{\mathrm{d}\mathcal{L}(\boldsymbol{u}(\boldsymbol{\theta}),\boldsymbol{\lambda},\boldsymbol{\theta})}{\mathrm{d}\boldsymbol{\theta}} = \frac{\partial\mathcal{J}}{\partial\boldsymbol{\theta}} + \boldsymbol{\lambda}^T\frac{\partial\delta\mathcal{W}}{\partial\boldsymbol{\theta}}. \tag{2.110}$$

Therein, the first term solely depends on the choice of the regularization function R, whereas the second term depends on the mechanical problem. For steady-state problems, see Eq. (2.71), the gradient of the weak form with respect to the parameters $\boldsymbol{\theta}$ is given by

$$\frac{\partial\delta\mathcal{W}}{\partial\boldsymbol{\theta}} = \frac{\partial(\boldsymbol{f}_{\text{int}} - \boldsymbol{f}_{\text{ext}})}{\partial\boldsymbol{\theta}}. \tag{2.111}$$

The external force vector $\boldsymbol{f}_{\text{ext}}$ does not depend on the parameters $\boldsymbol{\theta}$ and thus, from Eq. (2.56) it follows

$$\frac{\partial(\boldsymbol{S}:\delta\boldsymbol{E})}{\partial\boldsymbol{\theta}} = \frac{\partial\boldsymbol{S}}{\partial\boldsymbol{\theta}}:\delta\boldsymbol{E} + \boldsymbol{S}:\underbrace{\frac{\partial\delta\boldsymbol{E}}{\partial\boldsymbol{\theta}}}_{=0}. \tag{2.112}$$

The gradient of the second Piola-Kirchhoff stress tensor with respect to the parameters $\boldsymbol{\theta}$ depends on the choice of the strain energy function and the corresponding mechanical problem, and this is discussed in Sec. 3.2.

Rewriting Eq. (2.109) and Eq. (2.110) yield

$$\frac{1}{2\sigma^2}\frac{\partial D(\boldsymbol{Z},F(\boldsymbol{u}(\boldsymbol{\theta}),\boldsymbol{\theta}))}{\partial\boldsymbol{u}} + \boldsymbol{\lambda}^T\boldsymbol{K}_{\mathrm{T}} = \boldsymbol{0}, \tag{2.113}$$

$$\frac{\mathrm{d}\mathcal{L}(\boldsymbol{u}(\boldsymbol{\theta}),\boldsymbol{\lambda},\boldsymbol{\theta})}{\mathrm{d}\boldsymbol{\theta}} = \alpha\frac{\partial R}{\partial\boldsymbol{\theta}} + \boldsymbol{\lambda}^T\frac{\partial\boldsymbol{S}}{\partial\boldsymbol{\theta}}:\delta\boldsymbol{E}. \tag{2.114}$$

In summary, the identification problem starts with evaluating the forward problem $F(\boldsymbol{u}(\boldsymbol{\theta}),\boldsymbol{\theta})$. Subsequently, the objective function in Eq. (2.101) is computed. Thereafter, the adjoint equation (2.113) is solved, and then it is used to evaluate the gradient in Eq. (2.114). To solve the

optimization problem, the limited-memory BFGS (L-BFGS) method is used [15, 109]. This method is part of the quasi-Newton method, which approximates the Hessian of the objective function by using gradient information. An outline of the L-BFGS method and the optimization framework can be found in App. A.5.
In the following, the regularization function $R(\boldsymbol{\theta})$, the similarity measure $D(\boldsymbol{Z}, F(\boldsymbol{u}(\boldsymbol{\theta}), \boldsymbol{\theta}))$ and their corresponding gradient computation are discussed.

2.3.4. Regularization

Here, the regularization of the identification problem is achieved by employing the *total variation* (TV) functional [126]. It measures the total variation or total change in a measurement. As a regularization term, it penalizes rapid changes in the identified parameters, favoring solutions with smoother variations. Unlike classical Tikhonov regularization, total variation regularization has proven effective in handling discontinuous parameters [155]. Another advantage of TV is that it suppresses noise in the identified parameters and helps to find stable and robust solutions. Within this thesis, the graph based-version of the TV functional is used [58], which reads

$$R(\boldsymbol{\theta}) = \sum_{i=1}^{n_{\mathrm{el}}} \left(\sum_{j=1}^{n_i} w_{ij} (\theta_j - \theta_i)^2 + {\varepsilon_{\mathrm{tv}}}^2 \right)^{1/2}, \tag{2.115}$$

where n_i is the number of parameters adjacent to θ_i, w_{ij} are the weights associated with the parameter θ_j and θ_i and $\varepsilon_{\mathrm{tv}} \geq 0$ is a hyperparameter maintaining the functional's differentiability. As shown in the previous section, the gradient of the regularization with respect to the optimization parameter $\boldsymbol{\theta}$ is needed, see Eq. (2.114). For its derivation, the reader is referred to [79].

2.3.5. Similarity measure

The comparison between two geometries based on their surfaces is achieved by the distance measure. In this thesis, the so-called *surface currents* are used to define the distance measure. They were first introduced within the framework of *large deformation diffeomorphic metric mapping* (LDDMM) [35]. Within this framework, the aim is to find an optimal mapping between two shapes or geometries, allowing for large deformations and preserving geometric features. This framework is discussed in Sec. 2.4. A thorough mathematical description of surface currents can be found in [36, 50].

A surface current, denoted as $S(\omega) \in \mathcal{W}^*$ on a surface $\mathcal{S}$, is a linear functional acting upon the space of test functions $\boldsymbol{w} \in \mathcal{W}$, defining the differential 2-form ω given by

$$S(\omega) := \int_{\mathcal{S}} \boldsymbol{w} \cdot \boldsymbol{n} \, \mathrm{d}\Gamma, \tag{2.116}$$

where $\boldsymbol{n}$ is the surface normal vector, $\mathcal{W}$ is a Hilbert space and $\mathcal{W}^*$ its corresponding dual space. The Hilbert space is a mathematical space equipped with an inner product $\langle \bullet, \bullet \rangle_{\mathcal{W}}$, for studying functions and sequences. Its dual space consists of continuous linear functionals, providing a

natural extension for linear algebra. Following the Riesz representation theorem [51], for every surface current a dual representation $\boldsymbol{K}_{\boldsymbol{n}}^{S} \in \mathcal{W}$ is given by

$$S(\omega) = \langle \boldsymbol{K}_{\boldsymbol{n}}^{S}, \boldsymbol{w} \rangle_{\mathcal{W}}, \quad \forall \boldsymbol{w} \in \mathcal{W}. \tag{2.117}$$

The dual space norm $||\boldsymbol{K}_{\boldsymbol{n}}^{S}||$ allows the definition of a norm in the space of currents $\mathcal{W}^*$ as

$$||S||_{\mathcal{W}^*}^2 = \langle \boldsymbol{K}_{\boldsymbol{n}}^{S}, \boldsymbol{K}_{\boldsymbol{n}}^{S} \rangle_{\mathcal{W}} = \int_{\mathcal{S}} \boldsymbol{K}_{\boldsymbol{n}}^{S} \cdot \boldsymbol{n} \, \mathrm{d}\Gamma, \tag{2.118}$$

Based on this norm, a distance measure between two surfaces can be defined as

$$D(\boldsymbol{Z}, \mathcal{S}) = \frac{1}{2} ||\boldsymbol{Z} - \mathcal{S}||_{\mathcal{W}^*}^2, \tag{2.119}$$

where $\boldsymbol{Z}$ is the observation or measured surface and $\mathcal{S}$ is the surface representation resulting from the forward model $F(\boldsymbol{u}(\boldsymbol{\theta}), \boldsymbol{\theta})$.
To compute the integral in Eq. (2.118), the Hilbert space $\mathcal{W}$ is formulated as a *reproducing kernel Hilbert space* (RKHS) [5]. In a RKHS, each point in space corresponds to a function, and the inner product between functions can be computed using a *reproducing kernel*, which simplifies the computation of integrals. The inner product between two surfaces $\boldsymbol{Z}$ and $\mathcal{S}$ is given by

$$\langle \boldsymbol{Z}, \mathcal{S} \rangle_{\mathcal{W}^*} = \int_{\boldsymbol{Z}} \int_{\mathcal{S}} \boldsymbol{n}^{\boldsymbol{Z}}(x) \cdot k(x, y) \cdot \boldsymbol{n}^{\mathcal{S}}(y) \, \mathrm{d}\Gamma \mathrm{d}\Gamma, \tag{2.120}$$

where $\boldsymbol{n}^{\boldsymbol{Z}}$ and $\boldsymbol{n}^{\mathcal{S}}$ are the basis representations of surface $\boldsymbol{Z}$ and $\mathcal{S}$, respectively. The function $k(\bullet, \bullet) : \mathbb{R}^3 \mapsto \mathbb{R}$ represents the kernel functional. In this work, the *Gaussian kernel* is used, which is defined as

$$k(x, y) = \exp\left(-\frac{||x - y||^2}{{\sigma_W}^2} \right), \tag{2.121}$$

with the spatial scale of the covariance σ_W [79].
The distance measure between two surfaces in the space of currents can then be written as

$$\begin{aligned} ||\boldsymbol{Z} - \mathcal{S}||_{\mathcal{W}^*}^2 =& \langle \boldsymbol{Z}, \boldsymbol{Z} \rangle_{\mathcal{W}^*} - 2\langle \boldsymbol{Z}, \mathcal{S} \rangle_{\mathcal{W}^*} + \langle \mathcal{S}, \mathcal{S} \rangle_{\mathcal{W}^*} \\ =& \int_{\boldsymbol{Z}} \int_{\boldsymbol{Z}} \boldsymbol{n}^{\boldsymbol{Z}}(x) \cdot k(x, y) \cdot \boldsymbol{n}^{\boldsymbol{Z}}(y) \, \mathrm{d}\Gamma \mathrm{d}\Gamma \\ & - 2 \int_{\boldsymbol{Z}} \int_{\mathcal{S}} \boldsymbol{n}^{\boldsymbol{Z}}(x) \cdot k(x, y) \cdot \boldsymbol{n}^{\mathcal{S}}(y) \, \mathrm{d}\Gamma \mathrm{d}\Gamma \\ & + \int_{\mathcal{S}} \int_{\mathcal{S}} \boldsymbol{n}^{\mathcal{S}}(x) \cdot k(x, y) \cdot \boldsymbol{n}^{\mathcal{S}}(y) \, \mathrm{d}\Gamma \mathrm{d}\Gamma. \end{aligned} \tag{2.122}$$

For a more detailed derivation, the reader is referred to [152].

Discretization in space

Similar to the finite element discretization in Sec. 2.2.2, a discretization for the surfaces in space is needed to numerically compute Eq. (2.122). The surfaces are obtained from the volume discretization outlined in Sec. 2.2.2. In this thesis, each surface is discretized using triangles, where each triangle consists of a normal vector $\boldsymbol{n} \in \mathbb{R}^3$ and a center point $\boldsymbol{c} \in \mathbb{R}^3$.
Using this discretization, the distance measure in Eq. (2.122) becomes

$$\begin{aligned} D(\boldsymbol{Z}, \mathcal{S}) = ||\boldsymbol{Z} - \mathcal{S}||^2_{\mathcal{W}^*} \approx &\sum_{i}^{n^{\boldsymbol{Z}}} \sum_{j}^{n^{\boldsymbol{Z}}} \boldsymbol{n}_i^{\boldsymbol{Z}} \cdot k(\boldsymbol{c}_i^{\boldsymbol{Z}}, \boldsymbol{c}_j^{\boldsymbol{Z}}) \cdot \boldsymbol{n}_j^{\boldsymbol{Z}} \\ &- 2 \sum_{i}^{n^{\boldsymbol{Z}}} \sum_{j}^{n^{\mathcal{S}}} \boldsymbol{n}_i^{\boldsymbol{Z}} \cdot k(\boldsymbol{c}_i^{\boldsymbol{Z}}, \boldsymbol{c}_j^{\mathcal{S}}) \cdot \boldsymbol{n}_j^{\mathcal{S}} \\ &+ \sum_{i}^{n^{\mathcal{S}}} \sum_{j}^{n^{\mathcal{S}}} \boldsymbol{n}_i^{\mathcal{S}} \cdot k(\boldsymbol{c}_i^{\mathcal{S}}, \boldsymbol{c}_j^{\mathcal{S}}) \cdot \boldsymbol{n}_j^{\mathcal{S}}, \end{aligned} \tag{2.123}$$

where $\boldsymbol{c}_i^{\boldsymbol{Z}}$, $\boldsymbol{c}_i^{\mathcal{S}}$, $\boldsymbol{n}_i^{\boldsymbol{Z}}$ and $\boldsymbol{n}_i^{\mathcal{S}}$ are the center points and normal vectors of the i-th triangle for the measured surface $\boldsymbol{Z}$ and the current surface $\mathcal{S}$, respectively. The number of triangles in each discretization is given by $n^{\boldsymbol{Z}}$ and $n^{\mathcal{S}}$. Note that the kernel function can also be interpreted as a matrix. For example, for surfaces $\boldsymbol{Z}$ and $\mathcal{S}$ it results in $\boldsymbol{K} \in \mathbb{R}^{n^{\boldsymbol{Z}} \times n^{\mathcal{S}}}$. The computational complexity of Eq. (2.123) is $\mathcal{O}\left(n^{\boldsymbol{Z}} n^{\mathcal{S}} + \left(n^{\mathcal{S}}\right)^2\right)$. The first scalar product of the observation $\boldsymbol{Z}$ with itself does not change and can thus be evaluated once, whereas, for a new surface $\mathcal{S}$, the second and third scalar products have to be re-evaluated.

Gradient computation

The gradient of the distance measure with respect to the displacement field $\boldsymbol{u}$ is required, see Eq. (2.113). Using the definition of D, this gradient can be written as

$$\frac{\partial D(\boldsymbol{Z}, \mathcal{S})}{\partial \boldsymbol{u}} = \underbrace{\frac{\partial}{\partial \boldsymbol{u}} \langle \boldsymbol{Z}, \boldsymbol{Z} \rangle_{\mathcal{W}^*}}_{=0} - 2 \frac{\partial}{\partial \boldsymbol{u}} \langle \boldsymbol{Z}, \mathcal{S} \rangle_{\mathcal{W}^*} + \frac{\partial}{\partial \boldsymbol{u}} \langle \mathcal{S}, \mathcal{S} \rangle_{\mathcal{W}^*}. \tag{2.124}$$

The derivative of the first scalar product vanishes since the observation $\boldsymbol{Z}$ does not depend on the displacement field $\boldsymbol{u}$. Specifically, only the normal vectors $\boldsymbol{n}^{\mathcal{S}}$ and the center point $\boldsymbol{c}^{\mathcal{S}}$ are a function of the displacement field. Hence, using the chain rule, the gradient of the second scalar product in Eq. (2.123) is given by

$$\frac{\partial}{\partial \boldsymbol{u}} \langle \boldsymbol{Z}, \mathcal{S} \rangle_{\mathcal{W}^*} = \sum_{i}^{n^{\boldsymbol{Z}}} \sum_{j}^{n^{\mathcal{S}}} \boldsymbol{n}_i^{\boldsymbol{Z}} \cdot \frac{\partial k(\boldsymbol{c}_i^{\boldsymbol{Z}}, \boldsymbol{c}_j^{\mathcal{S}})}{\partial \boldsymbol{c}_k^{\mathcal{S}}} \frac{\partial \boldsymbol{c}_k^{\mathcal{S}}}{\partial \boldsymbol{u}} \boldsymbol{n}_j^{\mathcal{S}} + \sum_{i}^{n^{\boldsymbol{Z}}} \sum_{j}^{n^{\mathcal{S}}} \boldsymbol{n}_i^{\boldsymbol{Z}} \cdot k(\boldsymbol{c}_i^{\boldsymbol{Z}}, \boldsymbol{c}_j^{\mathcal{S}}) \frac{\partial \boldsymbol{n}_j^{\mathcal{S}}}{\partial \boldsymbol{u}}. \tag{2.125}$$

The gradient of the last scalar product results in

$$\begin{aligned}\frac{\partial}{\partial \boldsymbol{u}}\langle \mathcal{S}, \mathcal{S}\rangle_{\mathcal{W}^*} = &\sum_i^{n^{\mathcal{S}}}\sum_j^{n^{\mathcal{S}}} \frac{\partial \boldsymbol{n}_i^{\mathcal{S}}}{\partial \boldsymbol{u}} \cdot k(\boldsymbol{c}_i^{\mathcal{S}}, \boldsymbol{c}_j^{\mathcal{S}})\boldsymbol{n}_j^{\mathcal{S}} \\ &+ \sum_i^{n^{\mathcal{S}}}\sum_j^{n^{\mathcal{S}}} \boldsymbol{n}_i^{\mathcal{S}} \cdot \frac{\partial k(\boldsymbol{c}_i^{\mathcal{S}}, \boldsymbol{c}_j^{\mathcal{S}})}{\partial \boldsymbol{c}_k^{\mathcal{S}}} \frac{\partial \boldsymbol{c}_k^{\mathcal{S}}}{\partial \boldsymbol{u}} \boldsymbol{n}_j^{\mathcal{S}} \\ &+ \sum_i^{n^{\mathcal{S}}}\sum_j^{n^{\mathcal{S}}} \boldsymbol{n}_i^{\mathcal{S}} \cdot k(\boldsymbol{c}_i^{\mathcal{S}}, \boldsymbol{c}_j^{\mathcal{S}}) \frac{\partial \boldsymbol{n}_j^{\mathcal{S}}}{\partial \boldsymbol{u}}.\end{aligned} \tag{2.126}$$

The derivative of the Gaussian kernel is given by

$$\frac{\partial k(\boldsymbol{c}_i, \boldsymbol{c}_j)}{\partial \boldsymbol{c}_k} = \left(\frac{-2}{{\sigma_W}^2} k(\boldsymbol{c}_i, \boldsymbol{c}_j)(\boldsymbol{c}_i - \boldsymbol{c}_j)\right)(\delta_{ik} - \delta_{jk}), \tag{2.127}$$

where δ_{ij} is the Kronecker-delta function, defined as

$$\delta_{ij} = \begin{cases} 1 & \text{for } i = j, \\ 0 & \text{for } i \neq j. \end{cases} \tag{2.128}$$

Note that $k(\boldsymbol{c}_i, \boldsymbol{c}_i) = 1$ holds and thus, the kernel gradient vanishes at $i = j$.
The derivative of normal vectors $\boldsymbol{n}^{\mathcal{S}}$ and center points $\boldsymbol{c}^{\mathcal{S}}$ with respect to the displacement field $\boldsymbol{u}$ are given by the push-forward operation of the surface currents based on the solution of the nonlinear problem in Eq. (2.70), see [79] for an explicit derivation.

2.4. Shape analysis

The large deformation diffeomorphic metric mapping framework presented in [35, 102, 104] aims to find a mapping between two geometries. The term *diffeomorphic* emphasizes that the transformations involved are smooth and invertible, ensuring a one-to-one correspondence between points in the original and transformed shapes. LDDMM is particularly valuable for analyzing and comparing shapes undergoing significant deformations. It provides a robust method for capturing complex spatial variations in structures. Furthermore, this framework provides an estimation of an average model of the given shapes, which is called *template* or *atlas* shape. For a more detailed derivation, the reader is referred to [38, 152] and further examples are given in [76, 98].
In Sec. 2.4.1, the surface matching algorithm is presented, and subsequently, the framework to compute the atlas shape is outlined in Sec. 2.4.2.

2.4.1. Surface matching problem

Surface matching is a registration method that allows matching an object $\mathcal{S}$ to another object $\mathcal{T}$. Starting from an initial shape configuration $\mathcal{S}_0$ with a finite number of surface points $\boldsymbol{x}_0 \in \mathbb{R}^{3n_{\mathrm{P}}}$,

the idea is to find a time-dependent mapping function $\Phi_t(\boldsymbol{x}_0)$ with $t \in [0, 1]$ such that

$$\mathcal{S}_0 = \Phi_0(\boldsymbol{x}_0) = \boldsymbol{x}(t = 0) = \boldsymbol{x}_0, \tag{2.129}$$

$$\mathcal{S}_1 = \Phi_1(\boldsymbol{x}_0) = \boldsymbol{x}(t = 1) = \boldsymbol{x}_1. \tag{2.130}$$

The surface $\mathcal{S}_1$ represented by the surface points $\boldsymbol{x}_1$ then leads to the deformation of interest given by $\mathcal{S}_1 \approx \mathcal{T}$. For any time $t > 0$, this mapping defines a path and is a *diffeomorphism*.
In addition to the time-dependent surface points $\boldsymbol{x}(t)$, the so-called *control points* $\boldsymbol{c}(t) \in \mathbb{R}^{3n_{\text{cp}}}$ and parameter weights *momenta* $\boldsymbol{\alpha}(t) \in \mathbb{R}^{3n_{\text{cp}}}$ are introduced. The control points offer flexibility in the surface representation. They can either coincide with the surface points such that $\boldsymbol{c}(t) = \boldsymbol{x}(t)$, which is referred to as *dense mode* or they can be strategically chosen to optimize specific characteristics. Notably, the dimensionality of the control points is typically much smaller than that of the surface points, making it computationally efficient. Further, the velocity field $\boldsymbol{v}(t, \boldsymbol{x}_i(t)) \in \mathbb{R}^3$ at any time t at space location $\boldsymbol{x}_i \in \mathbb{R}^3$ is defined as

$$\boldsymbol{v}(t, \boldsymbol{x}_i(t)) = \dot{\boldsymbol{x}}_i(t) = \sum_{k=1}^{n_{\text{cp}}} k(\boldsymbol{x}_i(t), \boldsymbol{c}_k(t))\boldsymbol{\alpha}_k(t), \tag{2.131}$$

with $\boldsymbol{\alpha}_k(t), \boldsymbol{c}_k(t) \in \mathbb{R}^3$ and initial condition $\boldsymbol{x}(0) = \boldsymbol{x}_0$. This equation of motion is called *flow* of diffeomorphisms. Note that the kernel function $k(\bullet, \bullet)$ is defined as the Gaussian kernel, see Eq. (2.121) with kernel width parameter σ_V.
Similarly, the equation of motion applies to the control points and is given in matrix notation as

$$\dot{\boldsymbol{c}}(t) = \boldsymbol{K}(\boldsymbol{c}(t), \boldsymbol{c}(t))\boldsymbol{\alpha}(t), \tag{2.132}$$

with $\boldsymbol{K} \in \mathbb{R}^{n_{\text{cp}} \times n_{\text{cp}}}$ and initial condition $\boldsymbol{c}(0) = \boldsymbol{c}_0$.
For the sake of simplicity and readability, the time dependency of the velocity $\boldsymbol{v}(t)$, control points $\boldsymbol{c}(t)$, and the momenta $\boldsymbol{\alpha}(t)$ is omitted.
With a fixed set of initial control points $\boldsymbol{c}_0$, the time-varying vectors $\boldsymbol{\alpha}$ define a path $\Phi_t(\boldsymbol{x}_0)$ leading to a deformation of the initial shape $\mathcal{S}_0$. However, the vectors defining a specific deformation are not unique. A unique set of vectors $\boldsymbol{\alpha}$ is obtained by minimizing the integral of the kinetic energy $E_{\text{kin}} \in \mathbb{R}$ given by

$$E_{\text{kin}} = \frac{1}{2} \int_0^1 ||\boldsymbol{v}||^2 \mathrm{d}t = \frac{1}{2} \int_0^1 \boldsymbol{\alpha}^T \boldsymbol{K}(\boldsymbol{c}, \boldsymbol{c})\boldsymbol{\alpha} \, \mathrm{d}t. \tag{2.133}$$

It can be shown that minimizing the kinetic energy leads to a specific set of differential equations [38] and together with Eq. (2.132), the system of differential equations called *shoot* is given by

$$\begin{cases} \dot{\boldsymbol{c}}_k = \displaystyle\sum_{p=1}^{n_{\text{cp}}} k(\boldsymbol{c}_k, \boldsymbol{c}_p)\boldsymbol{\alpha}_p, \\ \dot{\boldsymbol{\alpha}}_k = -\displaystyle\sum_{p=1}^{n_{\text{cp}}} \boldsymbol{\alpha}_k^T \boldsymbol{\alpha}_p \nabla_1 k(\boldsymbol{c}_k, \boldsymbol{c}_p), \end{cases} \tag{2.134}$$

with initial condition $\boldsymbol{\alpha}(0) = \boldsymbol{\alpha}_0$. The operator ∇_1 denotes the derivative with respect to the first input argument and $\nabla_1 k(\boldsymbol{c}_k, \boldsymbol{c}_p) = \nabla_2 k(\boldsymbol{c}_k, \boldsymbol{c}_p)$ holds due to the symmetry of the kernel operator, see Eq. (2.127). This system is parameterized by initial positions of the control points $\boldsymbol{c}_0$ and

initial momenta $\boldsymbol{\alpha}_0$. The positions of control points $\boldsymbol{c}$ and momenta $\boldsymbol{\alpha}$ at any time t is computed by integrating Eq. (2.134) from initial conditions. Integrating Eq. (2.131) with the new control points $\boldsymbol{c}$ and momenta $\boldsymbol{\alpha}$ yields a trajectory of the surface points $\boldsymbol{x}$ and a new surface $\mathcal{S}_1$ at time $t = 1$.

Within the optimization framework for the surface matching problem, the parameter $\boldsymbol{\alpha}_0$ is estimated such that the mapping $\Phi_t(\boldsymbol{x}_0)$ results in the deformation of interest $\mathcal{T}$. Therefore, a varifold metric between two surfaces is needed. In this case, the surface norm from Eq. (2.122) is chosen.
Finally, the optimization problem with objective function $\mathcal{J} \in \mathbb{R}$ of the surface matching problem reads

$$\min_{\boldsymbol{\alpha}_0} \mathcal{J} = \min_{\boldsymbol{\alpha}_0} \left(\frac{1}{\sigma^2} \underbrace{||\mathcal{T} - \mathcal{S}_1||^2_{\mathcal{W}^*}}_{D(\mathcal{T},\mathcal{S}_1)} + E_{\text{kin}} \right), \tag{2.135}$$

where σ acts as a regularization term similar to Eq. (2.101)

Gradient computation

Similar to Sec. 2.3.3, the gradient of the objective function is needed to solve the optimization problem. In this case, the surface distance measure is only evaluated at time $t = 1$. In contrast, the kinetic energy E_{kin} is a time-dependent function evaluated at any point in time. However, the optimization parameter $\boldsymbol{\alpha}_0$ is solely defined at time $t = 0$. Hence, a straightforward gradient computation is not possible. Therefore, an adjoint-based approach is used to compute the gradient.

First, the system of differential equations (2.134) is rewritten in short notation as

$$\dot{\boldsymbol{S}} = F(\boldsymbol{S}) = \begin{bmatrix} F^c(\boldsymbol{S}) \\ F^\alpha(\boldsymbol{S}) \end{bmatrix}, \quad \text{with } \boldsymbol{S} = \begin{bmatrix} \boldsymbol{c} \\ \boldsymbol{\alpha} \end{bmatrix}, \text{ and } \boldsymbol{S}_0 = \begin{bmatrix} \boldsymbol{c}_0 \\ \boldsymbol{\alpha}_0 \end{bmatrix}, \tag{2.136}$$

where $\boldsymbol{S}$ represents the state of the system and F is the shoot function defined by Eq. (2.134). Similarly, a short notation for Eq. (2.131) is given by the flow function G and reads

$$\dot{\boldsymbol{x}} = G(\boldsymbol{x}, \boldsymbol{S}), \quad \text{with } \boldsymbol{x}(0) = \boldsymbol{x}_0. \tag{2.137}$$

Similar to the identification problem, the objective function is extended by the residual formulation of Eq. (2.136) and Eq. (2.137). Introducing the Lagrange multipliers ξ and θ, the Lagrangian formulation of the objective function reads

$$\begin{aligned} \mathcal{L}(\boldsymbol{x}_0, \boldsymbol{S}_0, \xi, \theta) = \frac{1}{\sigma^2} D(\mathcal{T}, \mathcal{S}_1) + E_{\text{kin}}\Big|_{t=0} \\ + \int_0^1 (F(\boldsymbol{S}) - \dot{\boldsymbol{S}})\xi \, \mathrm{d}t + \int_0^1 (G(\boldsymbol{x}, \boldsymbol{S}) - \dot{\boldsymbol{x}})\theta \, \mathrm{d}t. \end{aligned} \tag{2.138}$$

The gradients of the objective function $\mathcal{L}$ with respect to the initial position $\boldsymbol{x}_0$ and the initial state $\boldsymbol{S}_0$ are given by

$$\frac{\partial \mathcal{L}}{\partial \boldsymbol{x}_0} = \theta_0, \tag{2.139}$$

$$\frac{\partial \mathcal{L}}{\partial \boldsymbol{S}_0} = \left.\frac{\partial E_{\text{kin}}}{\partial \boldsymbol{S}_0}\right|_{t=0} + \xi_0. \tag{2.140}$$

Further, the corresponding adjoint equations are

$$\dot{\theta} = \frac{\partial G(\boldsymbol{x}, \boldsymbol{S})}{\partial \boldsymbol{x}}\theta, \qquad \text{with } \theta_1 = \frac{1}{\sigma^2}\frac{\partial D(\mathcal{T}, \mathcal{S}_1)}{\partial \boldsymbol{x}_1}, \tag{2.141}$$

$$\dot{\xi} = \frac{\partial F(\boldsymbol{S})}{\partial \boldsymbol{S}}\xi + \frac{\partial G(\boldsymbol{x}, \boldsymbol{S})}{\partial \boldsymbol{S}}\theta, \qquad \text{with } \xi_1 = 0. \tag{2.142}$$

The explicit derivation of these gradients is presented in App. A.6. Note that the gradient of the distance measure in Eq. (2.141) in case of surface currents is explicitly given in Eq. (2.124).

Numerical solution

Given an initial surface $\mathcal{S}_0$ with surface points $\boldsymbol{x}_0$, control points $\boldsymbol{c}_0$, and initial conditions $\boldsymbol{\alpha}_0$, the surface matching framework starts with evaluating the forward problem in Eq. (2.134) and Eq. (2.131). Subsequently, the objective function in Eq. (2.135) is computed. Thereafter, the first-order ordinary differential adjoint equations Eq. (2.141) and Eq. (2.142) are solved backward in time for θ_0 and ξ_0 using the one-step-θ method with $\theta = 1$, see Sec. 2.2.3. Afterward, the solutions are used to compute the gradient with respect to the initial momenta α_0 in Eq. (2.140). To update the initial state parameter α_0, the L-BFGS is used, see App. A.5. This iterative process to compute the optimal path to match one surface to another is shown in Alg. 1.

Algorithm 1 Surface matching computation

Require: $\boldsymbol{x}(t=0), \boldsymbol{c}(t=0), \boldsymbol{\alpha}(t=0)$ ▷ initial conditions

1: **while** not converged **do**
2: solve forward problem Eq. (2.134) and Eq. (2.131).
3: evaluate objective function Eq. (2.135)
4: solve adjoint equations Eq. (2.141) and Eq. (2.142)
5: compute gradient Eq. (2.140)
6: update α_0 ▷ using L-BFGS
7: **end while**

2.4.2. Atlas construction

The atlas shape $\mathcal{A}$ refers to a set of initial surface and control points derived from a set of provided measurements and serves as a Fréchet mean, defined as the minimizer of the sample

variance [37, 38, 75]. Given a set of initial shapes $\{\mathcal{S}^1, \mathcal{S}^2, ..., \mathcal{S}^{n_{\text{Sh}}}\}$, the minimization problem reads

$$\min_{\boldsymbol{x}_0^{\mathcal{A}}, \boldsymbol{c}_0^{\mathcal{A}}} \mathcal{J}_{\mathcal{A}} = \min_{\boldsymbol{x}_0^{\mathcal{A}}, \boldsymbol{c}_0^{\mathcal{A}}} \sum_{i=1}^{n_{\text{Sh}}} \left(\underbrace{\frac{1}{\sigma^2} ||\mathcal{A} - \mathcal{S}^i||^2_{\mathcal{W}^*} + E^i_{\text{kin}}}_{\text{see (2.135)}} \right), \tag{2.143}$$

where n_{Sh} is the number of provided surfaces, $\boldsymbol{x}_0^{\mathcal{A}}$ and $\boldsymbol{c}_0^{\mathcal{A}}$ are the initial surface and control points of the atlas shape $\mathcal{A}$, respectively. The first component operates on the deformation parameters to optimize the alignment between the atlas $\mathcal{A}$ and each provided measurement $\mathcal{S}^i$. The kinetic energy E^i_{kin} of the i^{th} observation characterizes the sample variance required to establish a mean for all observations and is given by

$$E^i_{\text{kin}} = \left(\boldsymbol{\alpha}_0^i\right)^T \boldsymbol{K}(\boldsymbol{c}_0^{\mathcal{A}}, \boldsymbol{c}_0^{\mathcal{A}}) \boldsymbol{\alpha}_0^i. \tag{2.144}$$

Starting from an initial topology with a set of surface points $\boldsymbol{x}_0^{\mathcal{A}}$ and control points $\boldsymbol{c}_0^{\mathcal{A}}$, the surface matching problem is solved between the atlas and each observation individually to find the optimal initial moments $\boldsymbol{\alpha}_0^i$. Thereafter, the surface points $\boldsymbol{x}_0^{\mathcal{A}}$ and control points $\boldsymbol{c}_0^{\mathcal{A}}$ are updated using their gradients, which are defined as

$$\frac{\partial \mathcal{J}_{\mathcal{A}}}{\partial \boldsymbol{x}_0^{\mathcal{A}}} = \sum_{i=1}^{n_{\text{Sh}}} \theta_0^i, \tag{2.145}$$

$$\frac{\partial \mathcal{J}_{\mathcal{A}}}{\partial \boldsymbol{c}_0^{\mathcal{A}}} = \sum_{i=1}^{n_{\text{Sh}}} \xi_0^i + \left. \frac{\partial E^i_{\text{kin}}}{\partial \boldsymbol{c}_0^i} \right|_{t=0}, \tag{2.146}$$

where the individual summands result from the surface matching problems and the gradients therein. The iterative process to compute the atlas shape is shown in Alg. 2.

Algorithm 2 Atlas construction computation

Require: $\boldsymbol{x}_0^{\mathcal{A}}, \boldsymbol{c}_0^{\mathcal{A}}$ ▷ initial conditions

while not converged **do**
  for $i = 1 : n_{\text{Sh}}$ **do**
    match atlas $\mathcal{A}$ to $\mathcal{S}^i$ Eq. (2.135) ▷ surface matching problem
  end for
  compute gradient Eq. (2.145) and Eq. (2.146)
  update $\boldsymbol{x}_0^{\mathcal{A}}$ and $\boldsymbol{c}_0^{\mathcal{A}}$ ▷ using L-BFGS
  evaluate objective function Eq. (2.143)
end while

2.5. Sensitivity analysis

Sensitivity analysis can be used to identify the uncertainty the model inputs convey to the model outputs. In general, it is differentiated between local and global sensitivity analysis. In local

sensitivity analysis, the change in the model output for a fixed set of input values is investigated. In contrast, in global sensitivity analysis, the change in the model output over a range of inputs is described. Furthermore, nonlinear effects and interactions between inputs can be analyzed. For a more detailed overview of sensitivity analysis, the reader is referred to [133, 139, 141].
In the following, in Sec.2.5.1, a brief summary of global sensitivity analysis is outlined. Subsequently, in Sec. 2.5.2, the computation of global sensitivity measures is presented.

2.5.1. Global sensitivity analysis

Given a model of the form $y = f(\boldsymbol{x})$, where $\boldsymbol{x} = (x_1, x_1, ..., x_k) \in \mathbb{R}^k$ represent the independent model inputs and y is the scalar model output. Assuming a finite mean value f_0 and variance V, the model output y can be decomposed into first-order effects and higher-order interactions [74, 132]. The decomposition reads

$$y = f_0 + \underbrace{\sum_i f_i(x_i)}_{\text{first order}} + \underbrace{\sum_{i<j} f_{ij}(x_i, x_j)}_{\text{second order}} + \cdots + \underbrace{f_{1\ldots k}(x_1, \ldots, x_k)}_{k^{\text{th}}\text{order}}, \tag{2.147}$$

where f_i depends solely on x_i, f_{ij} on x_i and x_j, etc. [74]. In case the summands of Eq. (2.147) are uncorrelated, the total variance V_{tot} of the model output can be decomposed into

$$V_{\text{tot}}(y) = \sum_i V_i(f_i(x_i)) + \sum_{i<j} V_{ij}(f_{ij}(x_i, x_j)) + \cdots + V_{1\ldots k}(f_{1\ldots k}(x_1, \ldots, x_k)), \tag{2.148}$$

where the variances are defined as [140]

$$V_i(f_i(x_i)) = V_{x_i}(E_{\boldsymbol{x}\sim_i}(y|x_i)), \tag{2.149}$$

$$V_{ij}(f_{ij}(x_i, x_j)) = V_{x_i,x_j}(E_{\boldsymbol{x}\sim_{i,j}}(y|x_i, x_j)) - V_i(f_i(x_i)) - V_j(f_j(x_j)), \tag{2.150}$$

and analogously for higher-order terms. Here, $E_{\boldsymbol{x}\sim_i}(y|x_i)$ is the expectation of y when x_i is distributed and observed and V_{x_i} is the variance of y for the input x_i [133]. The expression $\boldsymbol{x}_{\sim i}$ denotes that all model inputs expect the i^{th} are varied to compute the mean value [118].
The decomposition in Eq. (2.147) and Eq. (2.148) is called *analysis of variance* (ANOVA) decomposition [14, 133]. Based on this decomposition, so-called *Sobol indices* as global sensitivity estimators can be defined [140]. The remainder of this section is used to outline the computation of Sobol indices.

2.5.2. Sobol indices

The first-order sensitivity index S_i for an input is obtained by dividing each term in Eq. (2.148) by the unconditional model output variance $V_{\text{tot}}(y)$ [118] and they read

$$S_i = \frac{V_{x_i}(E_{\boldsymbol{x}\sim_i}(y|x_i))}{V_{\text{tot}}(y)}, \tag{2.151}$$

It measures the first-order contributions of x_i to the model output variance, and they are used to rank model inputs according to their contribution to the model output uncertainty, which is called *factor prioritization* [131].

The total-order indices

$$T_i = \frac{E_{\boldsymbol{x}_{\sim i}}(V_{x_i}(y|\boldsymbol{x}_{\sim i}))}{V_{\text{tot}}(y)} = 1 - \frac{V_{\boldsymbol{x}_{\sim i}}(E_{x_i}(y|\boldsymbol{x}_{\sim i}))}{V_{\text{tot}}(y)}. \tag{2.152}$$

measure the first-order effects of the model together with interaction terms between other parameters up to the k^{th} order [66]. If $T_i \approx 0$, x_i has a negligible contribution to the variance of y. Further, it describes the expected variance when all inputs except x_i are fixed. Therefore, total-order indices are applied to distinguish influential from non-influential model inputs and reduce the dimensionality of the uncertainty space, which is called *factor fixing* [118].

Computation of Sobol Indicies

In case of many model inputs, the evaluation of the variances in Eq. (2.151) and Eq. (2.152) is computationally expensive [132]. Therefore, the variances are computed using the *Monte Carlo* (MC) method [145], which avoids imposing any assumptions on the functional form of the response function [130]. Here, MC sampling can be performed using random or quasi-random numbers, e.g., Latin Hypercube Sampling [142] or Sobol' quasi-random numbers [139]. For that, the so-called *base sample matrices* $\boldsymbol{A}$ and $\boldsymbol{B} \in \mathbb{R}^{n_\mathcal{I} \times n_S}$ are introduced and each matrix is sampled individually and independent of each other [118]. Exemplary, the matrix $\boldsymbol{A}$ reads

$$\boldsymbol{A} = \begin{bmatrix} x_{11} & \cdots & x_{1i} & \cdots & x_{1n_\mathcal{I}} \\ \vdots & & \vdots & & \vdots \\ x_{s1} & \cdots & x_{si} & \cdots & x_{sn_\mathcal{I}} \\ \vdots & & \vdots & & \vdots \\ x_{n_S 1} & \cdots & \underbrace{x_{N_S i}}_{i^{\text{th}}\text{ input}} & \cdots & x_{n_S n_\mathcal{I}} \end{bmatrix} \Big\} s^{\text{th}}\text{ sample} \ . \tag{2.153}$$

where $n_\mathcal{I}$ is the number of inputs, and n_S is the number of samples. Furthermore, the matrix $\boldsymbol{A}_{\boldsymbol{B}}^{(i)}$ is introduced, where all columns are from $\boldsymbol{A}$ except the i^{th} which is used from $\boldsymbol{B}$ and similarly the matrix $\boldsymbol{B}_{\boldsymbol{A}}^{(i)}$ is formed. With these matrices, sensitivity estimators to compute S_i and T_i are defined and are listed in Tab. 2.1. These estimators are based on the work of Sobol [73, 140] (Sob), Saltelli [132] (Sat), Jansen [74, 132] (Jan), and Homma [66] (Hom). Therein, the term $f(\boldsymbol{A})_j$ denotes a function evaluation, where the j^{th} column of $\boldsymbol{A}$ serves as model input. Accordingly, the terms $f(\boldsymbol{B})_j$, $f(\boldsymbol{A}_{\boldsymbol{B}}^{(i)})_j$ and $f(\boldsymbol{B}_{\boldsymbol{A}}^{(i)})_j$ are defined.
The computational cost to evaluate the function f for all samples in $\boldsymbol{A}$ or $\boldsymbol{B}$ scales with n_S. To evaluate all samples from the matrices $\boldsymbol{A}_{\boldsymbol{B}}^{(i)}$ or $\boldsymbol{B}_{\boldsymbol{A}}^{(i)}$ with $i = 1, ..., n_\mathcal{I}$, the computational cost scales with $n_\mathcal{I} \cdot n_S$.

Tabelle 2.1.: First- and total-order sensitivity estimators.

S_i, see Eq. (2.151)	Reference
$S_i^{\text{Sob}} = \frac{1}{n_S}\sum_{j=1}^{n_S}[f(\boldsymbol{A})_j f(\boldsymbol{A}_{\boldsymbol{B}}^{(i)})_j - {f_0}^2]$	[140]
$S_i^{\text{Sat}} = \frac{1}{n_S}\sum_{j=1}^{n_S}[f(\boldsymbol{B})_j (f(\boldsymbol{A}_{\boldsymbol{B}}^{(i)})_j - f(\boldsymbol{A})_j)]$	[132]
$S_i^{\text{Jan}} = V_{\text{tot}}(y) - \frac{1}{2n_S}\sum_{j=1}^{n_S}[f(\boldsymbol{A})_j - f(\boldsymbol{B}_{\boldsymbol{A}}^{(i)})_j]^2$	[74]
T_i, see Eq. (2.152)	
$T_i^{\text{Hom}} = \frac{1}{n_S}\sum_{j=1}^{n_S}[f(\boldsymbol{A})_j (f(\boldsymbol{A})_j - f(\boldsymbol{A}_{\boldsymbol{B}}^{(i)})_j)]$	[66]
$T_i^{\text{Sob}} = \frac{1}{n_S}\sum_{j=1}^{n_S}[f(\boldsymbol{A})_j (f(\boldsymbol{A})_j - f(\boldsymbol{A}_{\boldsymbol{B}}^{(i)})_j)]$	[73]
$T_i^{\text{Jan}} = \frac{1}{2n_S}\sum_{j=1}^{n_S}[f(\boldsymbol{A})_j - f(\boldsymbol{A}_{\boldsymbol{B}}^{(i)})_j]^2$	[74, 132]

3. Cardiac mechanics

This chapter summarizes the mathematical concepts used within the cardiac mechanics models of this work. Sec. 3.1 presents the computational model of the contracting heart coupled to the vascular system. Subsequently, Sec. 3.2 outlines the kinematic heart growth framework. Finally, in Sec. 3.3, signaling networks used to represent the complex interplay of mechanical and biochemical stimuli for heart growth on a cellular level are discussed.

3.1. Computational cardiovascular mechanics

In this section, the computational cardiac mechanics of the beating heart are explained, starting with the identification of the computational domain and its meshing, see Sec. 3.1.1. Subsequently, the constitutive laws for the myocardium are presented in Sec. 3.1.2. In Sec. 3.1.3, the boundary conditions of the embedding tissue are discussed. In Sec. 3.1.4, models that address the impact of blood pressure acting on the geometry of the heart are outlined. Finally, Sec. 3.1.5 presents the governing equations, coupling conditions between the structural part and the vascular system, and the corresponding IBVP.

3.1.1. Segmentation and geometry construction

Within this thesis, computed tomography (CT) was used to monitor the heart geometry and was provided by the university hospital Rechts der Isar of the Technische Universität München.
In CT images, the differentiation of regions and organs within the human body is achieved using *Hounsfield Units* (HU). HU serves as a measure of X-ray attenuation, also known as radiodensity, of the imaged material. Radiodensity, a physical property of the material, ensures consistent image information regardless of the specific CT scanner used. In the human body, the HU vary from -1000 HU (air) to approximately 3000 HU [121]. Here, a low value is displayed in a darker gray, whereas high values appear in a brighter gray.
The heart is segmented using the software Simpleware™ ScanIP (Version S-2021.06; Synopsys, Inc., Mountain View, USA). For the mechanical heartbeat model, see Sec. 3.1.5, and for the growth model, see Sec. 3.2, the heart is segmented at its 80% diastolic state, which corresponds to the time right before the atria start to contract. The choice of this specific moment is due to the heart's minimal motion at this stage, making it an optimal choice for segmentation.
The heart model generation is based on the work in [62]. Within the segmentation process, the lumina of the left and right ventricles, as well as the outer layer of the myocardium, are segmented, see Fig. 3.1. The atria and valves are not part of the computational domain, and hence, they are not segmented. Furthermore, three characteristic points are identified for a unique alignment. These points are the lowest left ventricular point (LVB), the posterior mitral valve point (MVP), and the aortic valve point (AV). Within the alignment process, the LVB to AV line

is interpreted as a z-axis, and AV, LVB and MVP define the y-z plane. Following segmentation and smoothing, the three geometries are exported in the form of *stereolithographic* (STL) files, see Fig.3.2.

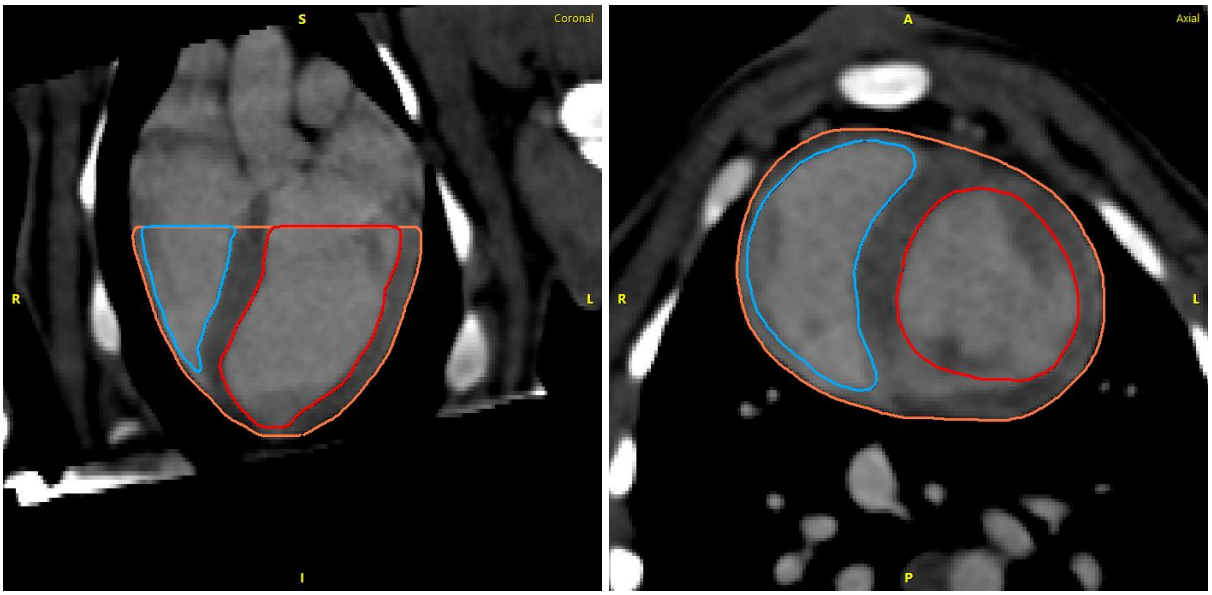

Abbildung 3.1.: Exemplary CT image of the heart at the 80% diastolic state. On the left side is the coronal view, and on the right side is the axial view. The left ventricle is marked in red, the right ventricle in blue, and the outer layer of the myocardium in orange.

The finite element mesh of the exported STL files is created using the Trelis® software. A Python interface allows for the automation of the heart mesh construction. Starting with the imported surfaces, the lumina of the left and right ventricles are subtracted from the heart contour. Afterwards, all three volumes are intersected at the atrioventricular plane (AVP). This plane intersects the posterior mitral valve leaflet and is perpendicular to the line between the LVB and AV. Since valves are not explicitly segmented, two artificial lids are introduced to close the ventricular volumes. The resulting five surfaces are then meshed using the built-in tetrahedral meshing scheme *TetMesh*. In Fig. 3.3(a), the final computational domain of the heart is shown. Fig. 3.3(b) depicts a cut-through of the heart exposing the ventricle lumina. Furthermore, the computational domain is represented by five surfaces, Γ^{lid} as the abluminal surface of the covering lids, Γ^{base} refers to the heart base, Γ^{epi} as the the epicardial surface, and Γ_{v}^{ℓ} and Γ_{v}^{r} are the left and right ventricular surfaces, respectively. In Fig. 3.3(c-d), an example mesh of the computational domain is presented.

Since myocardial tissue has orthotropic material behavior [65], it is essential to incorporate its anisotropy into the model. Therefore, the two fiber directions $\boldsymbol{f}_0$ as the muscle fiber direction and $\boldsymbol{s}_0$ as the sheet direction are introduced. On the epicardium, the muscle fiber inclines $-60°$ with respect to the circumference of the ventricles and is responsible for generating the active contraction force. It rotates its orientation to $60°$ on the endocardial wall. The sheet direction $\boldsymbol{s}_0$ is orthogonal to the fiber direction $\boldsymbol{f}_0$. Both directions are in plane and orthogonal to the surface

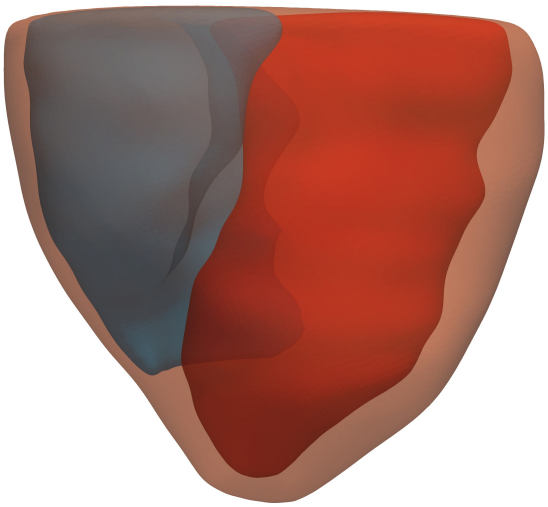

Abbildung 3.2.: Exemplary lumina of the left and right ventricle, as well as the outer layer of the myocardium exported as STL. The inner surface of the left ventricle is represented in red, the inner surface of the right ventricle in blue, and the outer layer of the myocardium in orange.

normal direction $\boldsymbol{r}_0$. The fiber and sheet direction are constructed based on the work in [107] and are depicted in Fig. 3.4.

3.1.2. Constitutive model

To model the passive-active material behavior, a constitutive equation for the second Piola-Kirchhoff stress $\boldsymbol{S}$ is needed, see Sec. 2.1.2. For the myocardial tissue, the constitutive model is based on an additive decomposition of the stress into a hyperelastic passive part and an active stress contribution [4] and reads

$$\boldsymbol{S} = \frac{\partial \Psi}{\partial \boldsymbol{E}} + \tau_{\mathrm{a}}(t)\boldsymbol{f}_0 \otimes \boldsymbol{f}_0. \tag{3.1}$$

For the passive material, the strain energy density proposed in [65] is given by

$$\begin{aligned}\Psi = &\frac{a_0}{2b_0}\left[\exp\left(b_0(\bar{I}_1 - 3)\right) - 1\right] + \frac{\kappa}{2}[J-1]^2 + \frac{a_f}{2b_f}\left[\exp\left(b_f({\boldsymbol{f}_0}^T\boldsymbol{C}\boldsymbol{f}_0 - 1)^2\right) - 1\right] \\ &+ \frac{a_s}{2b_s}\left[\exp\left(b_s({\boldsymbol{s}_0}^T\boldsymbol{C}\boldsymbol{s}_0 - 1)^2\right) - 1\right] + \frac{a_{fs}}{2b_{fs}}\left[\exp\left(b_{fs}({\boldsymbol{f}_0}^T\boldsymbol{C}\boldsymbol{s}_0)^2\right) - 1\right],\end{aligned} \tag{3.2}$$

where a_0, b_0, κ, a_f, b_f, a_s, b_s, a_{fs}, and b_{fs} are positive material constants. The first two summands model the isotropic part of material response under an isochoric-volumetric split, whereas the remaining three summands model an anisotropic, passive material response. Since the myocardium is assumed to be incompressible, the bulk modulus κ is chosen to be large, see Tab. 3.1.

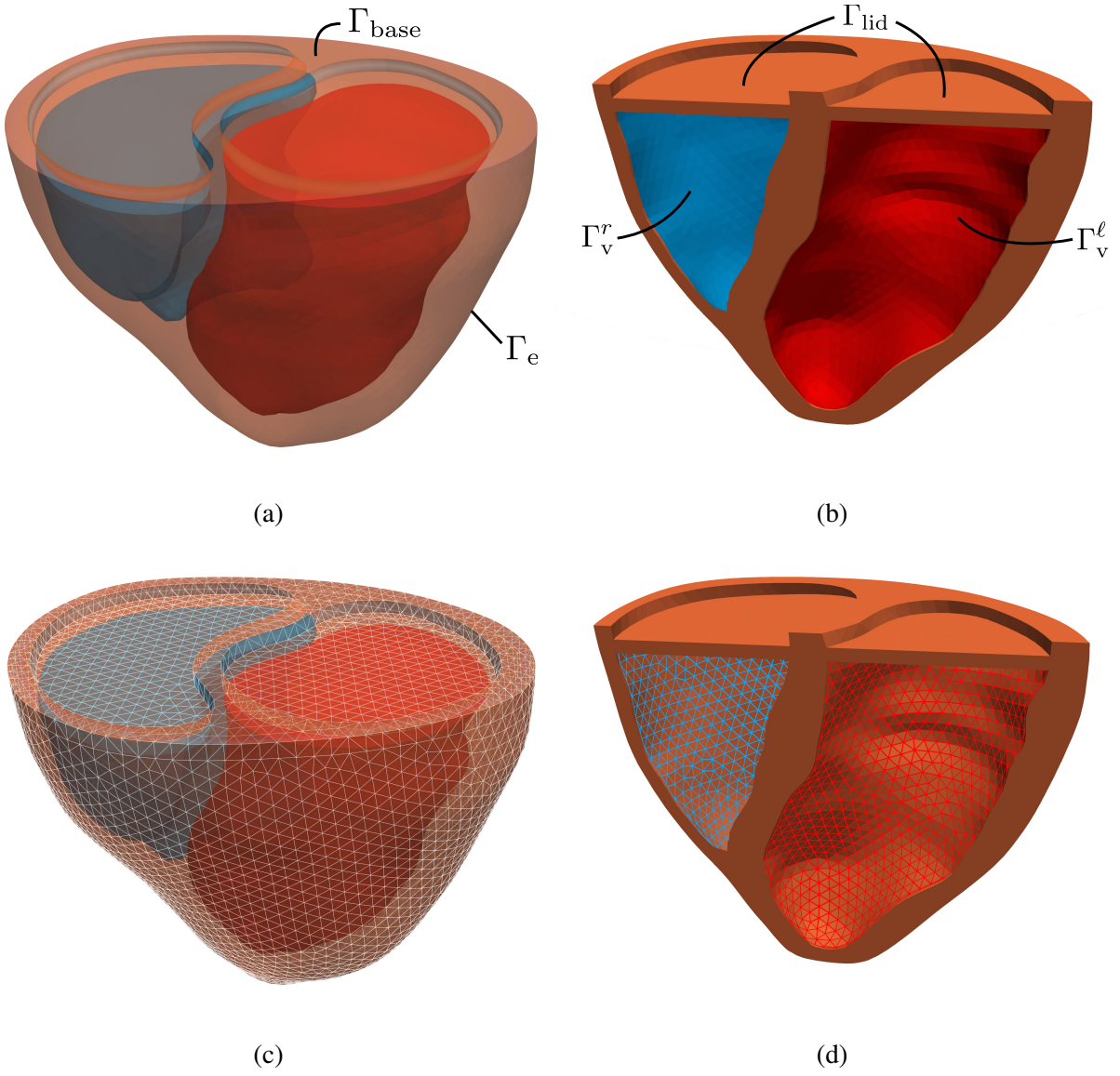

Abbildung 3.3.: Exemplary computational domain of a porcine heart. The epicardium is shown in orange, and the left and right ventricles are represented in red and blue, respectively. In (a), the full computational domain of the heart is shown, whereas in (b), a cut-through of the heart is depicted, exposing the ventricle volumes. In (c), an example mesh of the epicardium is shown, and in (d), an example mesh of the ventricle lumina is depicted.

The strain energy function for the artificial lids is based on a Neo-Hookean material under a volumetric-isochoric split, and it reads

$$\Psi^{\text{lid}} = \frac{\mu_{\text{lid}}}{2}[\bar{I}_1 - 3] + \frac{\kappa_{\text{lid}}}{2}[J-1]^2, \tag{3.3}$$

with Lamé constants μ_{lid} and κ_{lid}. The second part of Eq. (3.1) models the active stress contribution in fiber direction $\boldsymbol{f}_0$. The time dependent active stress $\tau_{\text{a}}(t)$ results from the solution

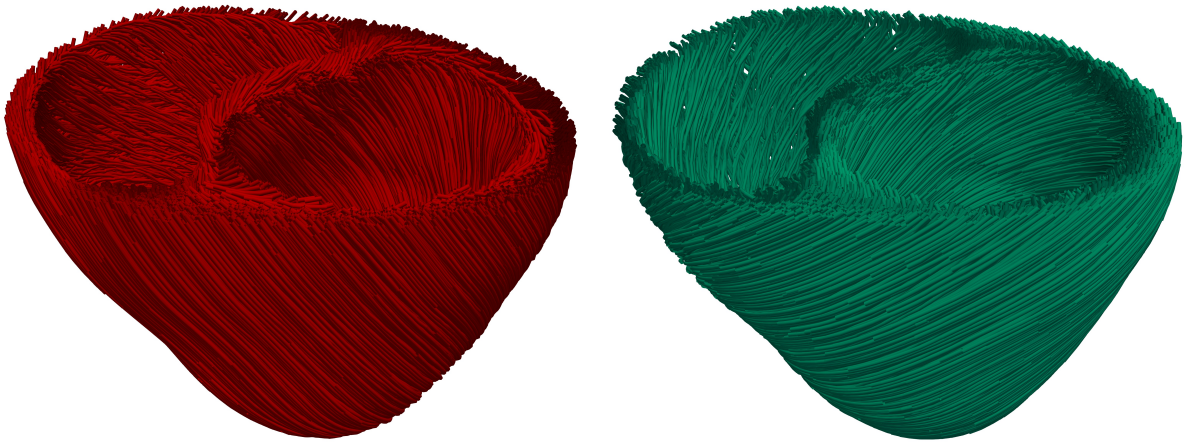

Abbildung 3.4.: Exemplary visualization of fiber and sheet direction on a 3-dimensional ventricular model of a porcine heart with muscle fiber orientation $\boldsymbol{f}_0$ (red) and sheet orientation $\boldsymbol{s}_0$ (green).

of [62]

$$\dot{\tau}_{\mathrm{a}}(t) = -|u(t)|\tau_{\mathrm{a}}(t) + \sigma_0 \max(0, u(t)), \tag{3.4}$$

where σ_0 is called the *contractility*, which adjusts the maximum of the active stress. The scaling function u is defined by

$$u(t) = \hat{f}(t) \cdot \alpha_{\max} + (1 - \hat{f}(t)) \cdot \alpha_{\min}, \tag{3.5}$$

with $\alpha_{\max}$ as the upstroke rate and $\alpha_{\min}$ as the relaxation rate. The activation function $\hat{f}$ reads

$$\begin{aligned} \hat{f}(t) = (K(t-c_1)+1) \cdot \mathcal{H}\left[K(t-c_1)+1\right] - K(t-c_1) \cdot \mathcal{H}\left[K(t-c_1)\right] \\ - K(t-c_2) \cdot \mathcal{H}\left[K(t-c_2)\right] + (K(t-c_2)-1) \cdot \mathcal{H}\left[K(t-c_2)-1\right], \end{aligned} \tag{3.6}$$

where the Heaviside function $\mathcal{H} : \mathbb{R} \mapsto [0, 1]$ is defined as

$$\mathcal{H}\left[(\bullet)\right] := \begin{cases} 0 & \text{for } (\bullet) < 0, \\ 1 & \text{for } (\bullet) \geqslant 0. \end{cases} \tag{3.7}$$

The parameter K is a positive constant and the parameters c_1 and c_2 are defined by the contraction time t_{contr} and the relaxation time t_{relax} as

$$c_1 = t_{\mathrm{contr}} + \frac{\alpha_{\max}}{K(\alpha_{\max} - \alpha_{\min})}, \tag{3.8}$$

$$c_2 = t_{\mathrm{relax}} - \frac{\alpha_{\max}}{K(\alpha_{\max} - \alpha_{\min})}. \tag{3.9}$$

Note that $\partial \tau_{\mathrm{a}} / \partial \boldsymbol{C} = 0$ and thus only the passive material contributes to the material tangent, see Eq. (2.32). In Fig. 3.5, the active stress τ_{a} is depicted using the material parameters from Tab. 3.1. The parameter t_{contr} marks the start of the contraction, and at $t = t_{\mathrm{relax}}$ the relaxation starts. The duration of one cardiac cycle is denoted by T_{cycl}. The ODE (3.4) is solved using the Backward-Euler scheme with initial value $\tau_{\mathrm{a}}(0) = 0$, see Eq. (2.72). An explicit derivation of its solution is given in App. B.1.

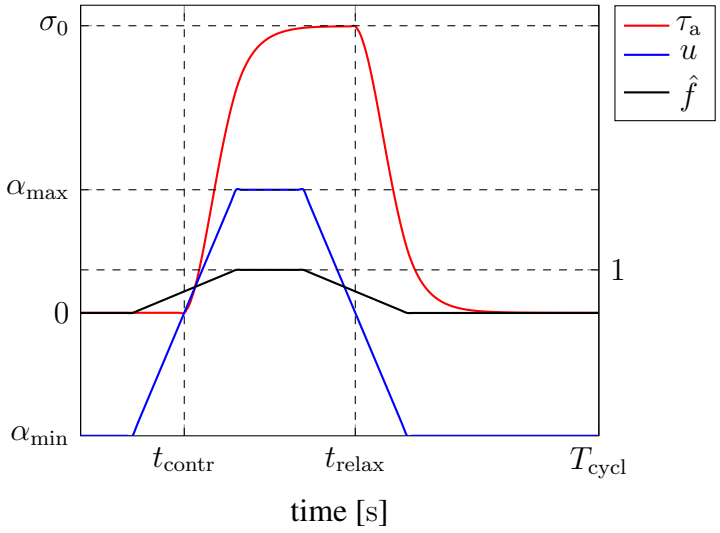

Abbildung 3.5.: Time-dependent active stress evolution τ_{a} (red) over one cardiac cycle T_{cycl}, based on the scaling function u (blue) and the activation function $\hat{f}$ (black). At t_{contr}, the contraction starts, and at t_{relax}, muscle fiber relaxation begins.

3.1.3. Boundary conditions of the embedding tissue

To model the embedding tissue, so-called *Robin boundary conditions* are used [53]. They are employed at the heart base as well as at the covering lids and the epicardial surface. Therefore, two types of boundary conditions are defined.
First, the boundary conditions at the heart base are modeled based on springs and dashpots, which are locally proportional to the displacement and velocity acting in all directions and leading to the following traction force

$$\boldsymbol{t}_{0_{k,c}}^{\text{base}} = -k_{\text{base}}\boldsymbol{u} - c_{\text{base}}\dot{\boldsymbol{u}}. \tag{3.10}$$

Second, springs and dashpots acting in reference surface normal direction are introduced, and they induce the traction force defined as

$$\boldsymbol{t}_{0_{k,c}}^{i,\perp} = -(\boldsymbol{N}\otimes\boldsymbol{N})(k_i^{\perp}\boldsymbol{u} + c_i^{\perp}\dot{\boldsymbol{u}}) = k_i^{\perp}(\boldsymbol{u}\cdot\boldsymbol{N})\boldsymbol{N} - c_i^{\perp}(\dot{\boldsymbol{u}}\cdot\boldsymbol{N})\boldsymbol{N}, \tag{3.11}$$

where the index $i \in \{\text{base}, \text{epi}, \text{lid}\}$ represents the surface on which the boundary condition is acting. The parameters k_{base} and $k_i^{\perp}$ can be interpreted as spring stiffness per reference surface area $[\text{kPa}/\text{mm}]$. In contrast, the constants c_{base} and $c_i^{\perp}$ can be interpreted as dashpot damping per unit reference surface area $[\text{kPa}\,\text{s}/\text{mm}]$. An overview of all baseline parameters is given in Tab. 3.2. Unless stated otherwise, these parameters are chosen for all simulations.

3.1.4. Prestressing

Patient-specific cardiac geometries reconstructed from medical screening are subjected to *in-vivo* blood pressure. This becomes particularly important when employing specific constitutive

Tabelle 3.1.: Baseline constitutive model parameters.

symbol	value	unit	equation
passive myocardial material			
a_0	0.059	[kPa]	(3.2)
a_f	18.472	[kPa]	(3.2)
a_s	2.481	[kPa]	(3.2)
a_{fs}	0.216	[kPa]	(3.2)
b_0	8.023	[-]	(3.2)
b_f	16.026	[-]	(3.2)
b_s	11.120	[-]	(3.2)
b_{fs}	11.436	[-]	(3.2)
κ	10^3	[kPa]	(3.2)
ρ_0	10^{-6}	$[\mathrm{kg/mm^3}]$	(3.39)
lid material			
μ_{lid}	50	[kPa]	(3.3)
κ_{lid}	10	[kPa]	(3.3)
ρ_0	10^{-6}	$[\mathrm{kg/mm^3}]$	(3.39)
active contraction			
σ_0	70	[kPa]	(3.4)
$\alpha_{\min}$	-30	[1/s]	(3.5),(3.8),(3.9)
$\alpha_{\max}$	30	[1/s]	(3.5),(3.8),(3.9)
K	5	[-]	(3.6),(3.8),(3.9)
t_{contr}	$0.2 \cdot T_{\text{cycl}}$	[s]	(3.8)
t_{relax}	$0.53 \cdot T_{\text{cycl}}$	[s]	(3.9)

Tabelle 3.2.: Spring and dashpot boundary condition parameters.

symbol	value	unit	equation
boundary conditions			
k_{base}	0.25	[kPa/mm]	(3.10)
$k^{\perp}_{\text{base}}$	1.25	[kPa/mm]	(3.11)
$k^{\perp}_{\text{epi}}$	0.075	[kPa/mm]	(3.11)
$k^{\perp}_{\text{lid}}$	0.05	[kPa/mm]	(3.11)
c_{base}	0.0005	[kPa s/mm]	(3.10)
$c^{\perp}_{\text{base}}$	0.0005	[kPa s/mm]	(3.11)
$c^{\perp}_{\text{epi}}$	0.0005	[kPa s/mm]	(3.11)
$c^{\perp}_{\text{lid}}$	0.0005	[kPa s/mm]	(3.11)

models based on experimentally derived material parameters. In continuum mechanics, this corresponds to a non-stress-free reference configuration. To address the already acting stresses and strains in the imaged configuration, *prestressing* based on the so-called *Modified Updated Lagrangian Formulation* (MULF) is used [47, 48].
To determine the prestresses acting in the reference configuration, the image configuration is

enforced by keeping it fixed while gradually applying the intended load. The accumulated deformation gradient from all preceding load increments reads

$$\boldsymbol{F}_{\mathrm{p}} = \boldsymbol{F}^{n}\boldsymbol{F}^{n-1}...\boldsymbol{F}^{0}. \tag{3.12}$$

This deformation gradient results in a stress state embedded in the imaged configuration, see Eq. (2.30). This process allows for an estimation of the stress state in a fixed configuration without reconstructing the stress-free configuration. In any follow-up simulation, where deformation occurs (given by $\boldsymbol{F}_{\mathrm{d}}$), the accumulated deformation gradient $\boldsymbol{F}_{\mathrm{p}}$ is additionally considered, such that the total deformation gradient is given by

$$\boldsymbol{F} = \boldsymbol{F}_{\mathrm{d}}\boldsymbol{F}_{\mathrm{p}}. \tag{3.13}$$

The advantage of this method is that it is computationally efficient and reliable. An alternative method for prestressing is to solve an inverse problem to find the stress-free reference configuration, which transforms into the imaged configuration after applying the load under consideration. This method is the so-called *inverse design* or *inverse elastostatics* method [48, 113].

Finally, the IBVP from Sec. 2.1.4 for the prestressing stage is given by

$$\nabla_{\boldsymbol{X}} \cdot \boldsymbol{P} = \boldsymbol{0} \qquad \text{in } \Omega, \tag{3.14}$$

$$\boldsymbol{P} \cdot \boldsymbol{N} = \boldsymbol{t}_{0_p}^{i} \qquad \text{on } \Gamma_{\mathrm{v}}^{i}, i \in \{r, \ell\}, \tag{3.15}$$

$$\boldsymbol{P} \cdot \boldsymbol{N} = \boldsymbol{t}_{0_k}^{\text{base}} + \boldsymbol{t}_{0_k}^{\text{base},\perp} \qquad \text{on } \Gamma_{\text{base}}, \tag{3.16}$$

$$\boldsymbol{P} \cdot \boldsymbol{N} = \boldsymbol{t}_{0_k}^{i,\perp} \qquad \text{on } \Gamma_i, i \in \{\text{epi}, \text{lid}\}. \tag{3.17}$$

The traction $\boldsymbol{t}_{0_p}^{i}$ is prescribed on the endocardial surfaces of the ventricles and is defined by the constant prescribed ventricular pressures $\hat{p}_{\mathrm{v}}^{i}$ as

$$\boldsymbol{t}_{0_p}^{i} = -\hat{p}_{\mathrm{v}}^{i} J \boldsymbol{F}^{-T} \boldsymbol{N}. \tag{3.18}$$

Note that since the prestressing stage is a quasi-static problem, no dashpot components will appear in Eq. (3.10) and Eq. (3.11).

3.1.5. 3D-0D coupled cardiovascular mechanics

The heart and cardiovascular system form a closed loop, where the dynamics of the cardiovascular system influence the contraction pattern of the heart and *vice versa*. Consequently, it is essential to represent this interaction as a two-way coupled problem.
First, the vascular system is introduced as the 0-dimensional (0D) *flow network* using the windkessel elements introduced in Sec. 2.1.5, and it is based on the work in [62]. Fig. 3.6 depicts the flow network consisting of 16 equations. It is described by eight pressure states and eight flow rates, see Tab. 3.3 for a detailed explanation.
In particular, the flow network consists of four windkessel models. The venous systemic and pulmonary systems are represented by 2-element windkessel models, whereas 4-element windkessel models describe the arterial systemic and pulmonary circulation. Furthermore, the four

valves are represented by diode elements, and the two atria are modeled with elastance functions. At the epicardial surface of the heart, the spring and dashpot elements are used to model the embedding tissue.
The equations of the flow network read

left heart

left atrial mass
$$\frac{\mathrm{d}V_{\mathrm{at}}^{\ell}(\boldsymbol{u})}{\mathrm{d}t} - q_{\mathrm{ven}}^{\mathrm{pul}} + q_{\mathrm{v,in}}^{\ell} = 0, \tag{3.19}$$

mitral valve momentum
$$\frac{1}{\tilde{R}_{\mathrm{v,in}}^{\ell}}[p_{\mathrm{at}}^{\ell} - p_{\mathrm{v}}^{\ell}] - q_{\mathrm{v,in}}^{\ell} = 0, \tag{3.20}$$

left ventricular mass
$$\frac{\mathrm{d}V_{\mathrm{v}}^{\ell}(\boldsymbol{u})}{\mathrm{d}t} - q_{\mathrm{v,in}}^{\ell} + q_{\mathrm{v,out}}^{\ell} = 0, \tag{3.21}$$

aortic valve momentum
$$\frac{1}{\tilde{R}_{\mathrm{v,out}}^{\ell}}[p_{\mathrm{v}}^{\ell} - p_{\mathrm{ar}}^{\mathrm{sys}}] - q_{\mathrm{v,out}}^{\ell} = 0, \tag{3.22}$$

systemic circulation

systemic arterial mass
$$C_{\mathrm{ar}}^{\mathrm{sys}}\left[\frac{\mathrm{d}p_{\mathrm{ar}}^{\mathrm{sys}}}{\mathrm{d}t} - Z_{\mathrm{ar}}^{\mathrm{sys}}\frac{\mathrm{d}q_{\mathrm{v,out}}^{\ell}}{\mathrm{d}t}\right] - q_{\mathrm{v,out}}^{\ell} + q_{\mathrm{ar}}^{\mathrm{sys}} = 0, \tag{3.23}$$

systemic arterial momentum
$$\frac{L_{\mathrm{ar}}^{\mathrm{sys}}}{R_{\mathrm{ar}}^{\mathrm{sys}}}\frac{\mathrm{d}q_{\mathrm{ar}}^{\mathrm{sys}}}{\mathrm{d}t} + \frac{1}{R_{\mathrm{ar}}^{\mathrm{sys}}}\left[p_{\mathrm{ven}}^{\mathrm{sys}} - p_{\mathrm{ar}}^{\mathrm{sys}} + Z_{\mathrm{ar}}^{\mathrm{sys}}q_{\mathrm{v,out}}^{\ell}\right] + q_{\mathrm{ar}}^{\mathrm{sys}} = 0, \tag{3.24}$$

systemic venous mass
$$C_{\mathrm{ven}}^{\mathrm{sys}}\frac{\mathrm{d}p_{\mathrm{ven}}^{\mathrm{sys}}}{\mathrm{d}t} - q_{\mathrm{ar}}^{\mathrm{sys}} + q_{\mathrm{ven}}^{\mathrm{sys}} = 0, \tag{3.25}$$

systemic venous momentum
$$\frac{L_{\mathrm{ven}}^{\mathrm{sys}}}{R_{\mathrm{ven}}^{\mathrm{sys}}}\frac{\mathrm{d}q_{\mathrm{ven}}^{\mathrm{sys}}}{\mathrm{d}t} + \frac{1}{R_{\mathrm{ven}}^{\mathrm{sys}}}[p_{\mathrm{ar}}^{r} - p_{\mathrm{ven}}^{\mathrm{sys}}] + q_{\mathrm{ven}}^{\mathrm{sys}} = 0, \tag{3.26}$$

right heart

right atrial mass
$$\frac{\mathrm{d}V_{\mathrm{at}}^{r}(\boldsymbol{u})}{\mathrm{d}t} - q_{\mathrm{ven}}^{\mathrm{sys}} + q_{\mathrm{v,in}}^{r} = 0, \tag{3.27}$$

tricuspid valve momentum
$$\frac{1}{\tilde{R}_{\mathrm{v,in}}^{r}}[p_{\mathrm{at}}^{r} - p_{\mathrm{v}}^{r}] - q_{\mathrm{v,in}}^{r} = 0, \tag{3.28}$$

right ventricular mass
$$\frac{\mathrm{d}V_{\mathrm{v}}^{r}(\boldsymbol{u})}{\mathrm{d}t} - q_{\mathrm{v,in}}^{r} + q_{\mathrm{v,out}}^{r} = 0, \tag{3.29}$$

pulmonary valve momentum
$$\frac{1}{\tilde{R}_{\mathrm{v,out}}^{r}}[p_{\mathrm{v}}^{r} - p_{\mathrm{ar}}^{\mathrm{pul}}] - q_{\mathrm{v,out}}^{r} = 0, \tag{3.30}$$

pulmonary circulation

pulmonary arterial mass
$$C_{\mathrm{ar}}^{\mathrm{pul}}\left[\frac{\mathrm{d}p_{\mathrm{ar}}^{\mathrm{pul}}}{\mathrm{d}t} - Z_{\mathrm{ar}}^{\mathrm{pul}}\frac{\mathrm{d}q_{\mathrm{v,out}}^{r}}{\mathrm{d}t}\right] - q_{\mathrm{v,out}}^{r} + q_{\mathrm{ar}}^{\mathrm{pul}} = 0, \tag{3.31}$$

pulmonary arterial momentum
$$\frac{L_{\mathrm{ar}}^{\mathrm{pul}}}{R_{\mathrm{ar}}^{\mathrm{pul}}}\frac{\mathrm{d}q_{\mathrm{ar}}^{\mathrm{pul}}}{\mathrm{d}t} + \frac{1}{R_{\mathrm{ar}}^{\mathrm{pul}}}\left[p_{\mathrm{ven}}^{\mathrm{pul}} - p_{\mathrm{ar}}^{\mathrm{pul}} + Z_{\mathrm{ar}}^{\mathrm{pul}}q_{\mathrm{v,out}}^{r}\right] + q_{\mathrm{ar}}^{\mathrm{pul}} = 0, \tag{3.32}$$

pulmonary venous mass
$$C_{\mathrm{ven}}^{\mathrm{pul}}\frac{\mathrm{d}p_{\mathrm{ven}}^{\mathrm{pul}}}{\mathrm{d}t} - q_{\mathrm{ar}}^{\mathrm{pul}} + q_{\mathrm{ven}}^{\mathrm{pul}} = 0, \tag{3.33}$$

pulmonary venous momentum
$$\frac{L_{\mathrm{ven}}^{\mathrm{pul}}}{R_{\mathrm{ven}}^{\mathrm{pul}}}\frac{\mathrm{d}q_{\mathrm{ven}}^{\mathrm{pul}}}{\mathrm{d}t} + \frac{1}{R_{\mathrm{ven}}^{\mathrm{pul}}}\left[p_{\mathrm{ar}}^{\ell} - p_{\mathrm{ven}}^{\mathrm{pul}}\right] + q_{\mathrm{ven}}^{\mathrm{pul}} = 0. \tag{3.34}$$

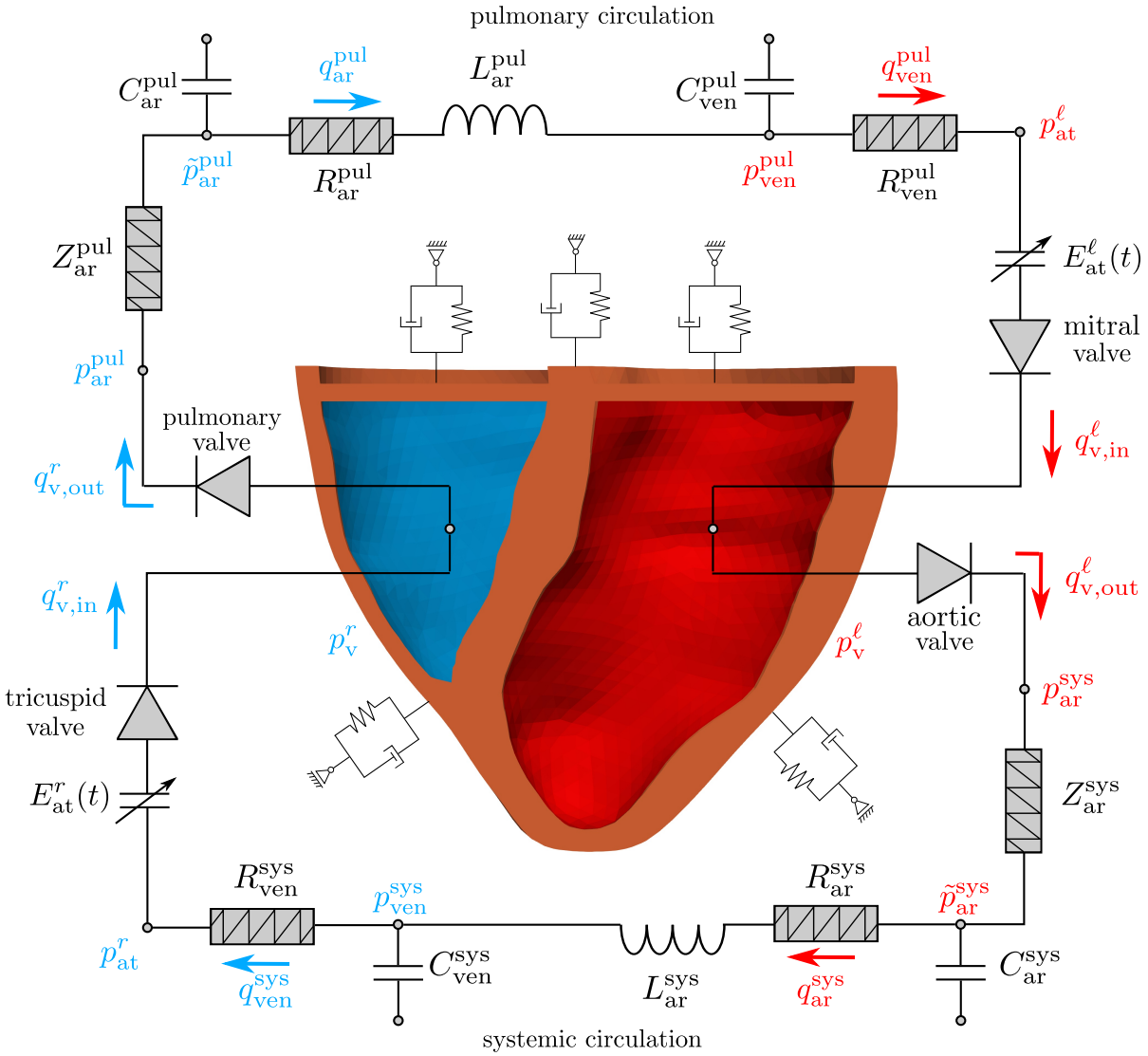

Abbildung 3.6.: Three-dimensional heart model coupled to the dimensionally reduced vascular system network, including pulmonary and systemic circulation. The two ventricular chambers are modeled as a 3D structural mechanics model, and the two atria are modeled within the 0D flow network by the elastance model. Spring and dashpot elements at the epicardial surface of the heart model the embedding tissue.

The time-dependent cavity volumes are V_{at}^{ℓ}, V_{v}^{ℓ}, V_{at}^{r} and V_{v}^{r} for the left atrium, left ventricle, right atrium, and right ventricle cavity volume, respectively. The ventricular volumes are computed from the 3D structure model as the boundary integral over the ventricular surfaces Γ_{v}^{ℓ} and Γ_{v}^{r} and their corresponding inner lid surfaces $\Gamma_{\text{lid}}^{\ell}$ and Γ_{lid}^{r}, see Fig. 3.3. The volume computation reads

$$V_{\text{v}}^{i}(\boldsymbol{u}) = \frac{1}{3}\int_{\Gamma_{\text{v}}^{i}\cup\Gamma_{\text{lid}}^{i}} \boldsymbol{x}\cdot\boldsymbol{n}\,\mathrm{d}a = \frac{1}{3}\int_{\Gamma_{\text{v}}^{i}\cup\Gamma_{\text{lid}}^{i}} (\boldsymbol{X}+\boldsymbol{u})\cdot J\boldsymbol{F}^{-T}\boldsymbol{N}\,\mathrm{d}A, \quad i\in\{r,\ell\}. \tag{3.35}$$

Tabelle 3.3.: Pressure states and flow rates within the flow network.

symbol	state	equation
	pressure states [kPa]	
p_{at}^{ℓ}	left atrial pressure	(3.20)
p_{v}^{ℓ}	left ventricular pressure	(3.20),(3.22)
$p_{\text{ar}}^{\text{sys}}$	systemic arterial pressure	(3.22),(3.23),(3.24)
$p_{\text{ven}}^{\text{sys}}$	systemic venous pressure	(3.24),(3.25),(3.26)
p_{at}^{r}	right atrial pressure	(3.28)
p_{v}^{r}	right ventricular pressure	(3.28),(3.30)
$p_{\text{ar}}^{\text{pul}}$	pulmonary arterial pressure	(3.30),(3.31),(3.32)
$p_{\text{ven}}^{\text{pul}}$	pulmonary venous pressure	(3.32),(3.33),(3.34)
	flow rates [mL/s]	
$q_{\text{v,in}}^{\ell}$	inflow rate left ventricle	(3.19),(3.20),(3.21)
$q_{\text{v,out}}^{\ell}$	outflow rate left ventricle	(3.21),(3.22),(3.23),(3.24)
$q_{\text{ar}}^{\text{sys}}$	systemic arterial flow rate	(3.23),(3.24),(3.25)
$q_{\text{ven}}^{\text{sys}}$	systemic venous flow rate	(3.25),(3.26),(3.27)
$q_{\text{v,in}}^{r}$	inflow rate right ventricle	(3.27),(3.28),(3.29)
$q_{\text{v,out}}^{r}$	outflow rate right ventricle	(3.29),(3.30),(3.31),(3.32)
$q_{\text{ar}}^{\text{pul}}$	pulmonary arterial flow rate	(3.31),(3.32),(3.33)
$q_{\text{ven}}^{\text{pul}}$	pulmonary venous flow rate	(3.19),(3.33),(3.34)

The atria volumes V_{at}^{i} are derived from the elastance models given by

$$p_{\text{at}}^{i} = E_{\text{at}}^{i}(t)\,(V_{\text{at}}^{i} - V_{\text{at,u}}^{i}), \quad i \in \{r, \ell\}, \tag{3.36}$$

where $V_{\text{at,u}}^{i}$ is the unstressed volume of the atria and p_{at}^{i} the atrial pressure. The time-varying elastance function is used to model atrial contraction and relaxation as

$$E_{\text{at}}^{i}(t) = (E_{\text{at,max}}^{i} - E_{\text{at,min}}^{i}) \cdot y_{\text{at}}^{i}(t) + E_{\text{at,min}}^{i}, \quad i \in \{r, \ell\}, \tag{3.37}$$

with $E_{\text{at,max}}^{i}$ and $E_{\text{at,min}}^{i}$ as the maximal and minimal atrial elastances. The atrial activation function is given as

$$y_{\text{at}}^{i}(t) = \begin{cases} \frac{1}{2}\left[1 - \cos\left(\frac{2\pi t}{\Delta t_{\text{act}}}\right)\right], & \text{for } t \leq \Delta t_{\text{act}}, \\ 0, & \text{for } t > \Delta t_{\text{act}}, \end{cases} \quad i \in \{r, \ell\}, \tag{3.38}$$

where Δt_{act} is the duration of atrial activation. An exemplary evolution of atrial elastance is depicted in Fig. 3.7.
All baseline model parameters of the flow network are based on [62, 144, 157] and are listed in Tab. 3.4. Unless stated otherwise, these model parameters are used for all simulations.

Coupling and IBVP

To couple the flow network with the 3D structural model of the heart, coupling boundary conditions are needed. In this work, the structural heart model provides ventricle volumes, which are

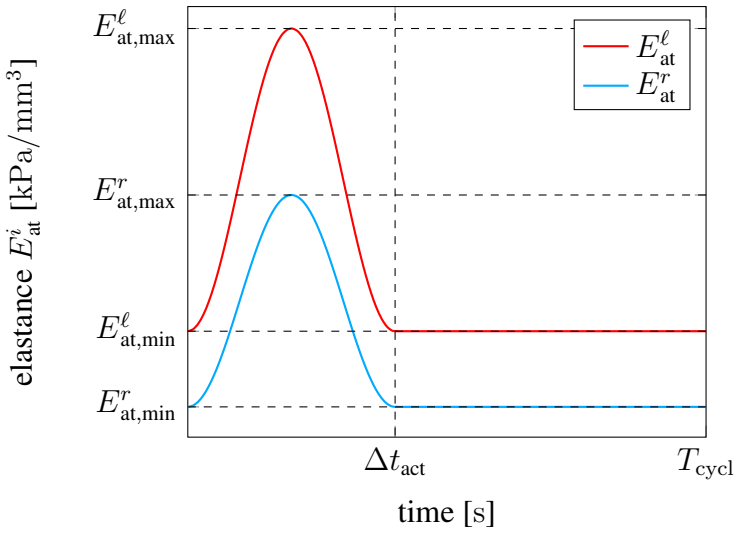

Abbildung 3.7.: Left (red) and right (blue) atrial elastance evolution over a cardiac cycle.

Tabelle 3.4.: Baseline parameters for flow network.

symbol	value	equation
system resistances/ impedances [kPa s/mm^3]		
$R^{\text{sys}}_{\text{ar}}$	$120 \cdot 10^{-6}$	(3.24)
$R^{\text{sys}}_{\text{ven}}$	$\frac{1}{5} R^{\text{sys}}_{\text{ar}}$	(3.26)
$R^{\text{pul}}_{\text{ar}}$	$\frac{1}{8} R^{\text{sys}}_{\text{ar}}$	(3.32)
$R^{\text{pul}}_{\text{ven}}$	$\frac{1}{8} R^{\text{sys}}_{\text{ar}}$	(3.34)
$Z^{\text{sys}}_{\text{ar}}$	$\frac{1}{20} R^{\text{sys}}_{\text{ar}}$	(3.23)
$Z^{\text{pul}}_{\text{ar}}$	$0 \cdot 10^{-6}$	(3.31)
valve resistances (2.48) [kPa s/mm^3]		
$R^{\ell,\text{min}}_{\text{v,in}}$	10^{-6}	(3.20)
$R^{\ell,\text{max}}_{\text{v,in}}$	10	(3.20)
$R^{\ell,\text{min}}_{\text{v,out}}$	10^{-6}	(3.22)
$R^{\ell,\text{max}}_{\text{v,out}}$	10	(3.22)
$R^{r,\text{min}}_{\text{v,in}}$	$5 \cdot 10^{-6}$	(3.28)
$R^{r,\text{max}}_{\text{v,in}}$	10	(3.28)
$R^{r,\text{min}}_{\text{v,out}}$	10^{-6}	(3.30)
$R^{r,\text{max}}_{\text{v,out}}$	10	(3.30)

symbol	value	equation
system capacitances [mm^3/kPa]		
$C^{\text{sys}}_{\text{ar}}$	$1.3770 \cdot 10^{4}$	(3.23)
$C^{\text{sys}}_{\text{ven}}$	$30 C^{\text{sys}}_{\text{ar}}$	(3.25)
$C^{\text{pul}}_{\text{ar}}$	$2 \cdot 10^{4}$	(3.31)
$C^{\text{pul}}_{\text{ven}}$	$2.5 C^{\text{pul}}_{\text{ar}}$	(3.33)
system inertances [kPa s^2/mm^3]		
$L^{\text{sys}}_{\text{ar}}$	$0.667 \cdot 10^{-6}$	(3.24)
$L^{\text{pul}}_{\text{ar}}$	0	(3.32)

symbol	value	unit	equation
atrial elastance			
$E^{\ell}_{\text{at,min}}$	$9 \cdot 10^{-6}$	[kPa/mm^3]	(3.37)
$E^{\ell}_{\text{at,max}}$	$2.9 \cdot 10^{-5}$	[kPa/mm^3]	(3.37)
$E^{r}_{\text{at,min}}$	$8 \cdot 10^{-6}$	[kPa/mm^3]	(3.37)
$E^{r}_{\text{at,max}}$	$1.8 \cdot 10^{-5}$	[kPa/mm^3]	(3.37)
Δt_{act}	$0.4 \cdot T_{\text{cycl}}$	[s]	(3.38)

incorporated into the flow network through the left and right ventricular mass balances (3.21) and (3.29). The ventricle pressure state variables of the flow network are applied as traction boundary conditions on the structural heart model.

Finally, the IBVP from Sec. 2.1.4 for the 3D structural problem reads

$$\nabla_{\boldsymbol{X}} \cdot \boldsymbol{P} = \rho_0 \dot{\boldsymbol{v}} \qquad \text{in } \Omega, \tag{3.39}$$

$$\boldsymbol{P} \cdot \boldsymbol{N} = \boldsymbol{t}_{0_p}^{i} \qquad \text{on } \Gamma_{\text{v}}^{i}, i \in \{r, \ell\}, \tag{3.40}$$

$$\boldsymbol{P} \cdot \boldsymbol{N} = \boldsymbol{t}_{0_k}^{\text{base}} + \boldsymbol{t}_{0_k}^{\text{base},\perp} \qquad \text{on } \Gamma_{\text{base}}, \tag{3.41}$$

$$\boldsymbol{P} \cdot \boldsymbol{N} = \boldsymbol{t}_{0_k}^{i,\perp} \qquad \text{on } \Gamma_i, i \in \{\text{epi}, \text{lid}\}. \tag{3.42}$$

The traction boundary conditions for the embedding tissue remain unchanged, similar to the prestressing stage, and they are given in Eq. (3.10) and Eq. (3.11). The pressure traction boundary condition $\boldsymbol{t}_{0_p}^{i}$ from Eq. (3.18) becomes

$$\boldsymbol{t}_{0_p}^{i} = -p_{\text{v}}^{i} J \boldsymbol{F}^{-T} \boldsymbol{N}, \tag{3.43}$$

where p_{v}^{i} results from the solution of the 0D flow network.

Numerical solution

The full system is solved monolithically using Newton-Raphson iterations, see Sec. 2.2.4. Therefore, the 16 network variables are interpreted as a vector of unknowns at time step n

$$\boldsymbol{q}^n = [p_{\text{at}}^{\ell}, p_{\text{v}}^{\ell}, p_{\text{ar}}^{\text{sys}}, p_{\text{ven}}^{\text{sys}}, p_{\text{at}}^{r}, p_{\text{v}}^{r}, p_{\text{ar}}^{\text{pul}}, p_{\text{ven}}^{\text{pul}}, \tag{3.44}$$

$$q_{\text{v,in}}^{\ell}, q_{\text{v,out}}^{\ell}, q_{\text{ar}}^{\text{sys}}, q_{\text{ven}}^{\text{sys}}, q_{\text{v,in}}^{r}, q_{\text{v,out}}^{r}, q_{\text{ar}}^{\text{pul}}, q_{\text{ven}}^{\text{pul}}]^n. \tag{3.45}$$

Based on this representation, the fully coupled linearized system reads

$$\begin{bmatrix} \boldsymbol{K}^{\text{3D}} & \boldsymbol{K}^{\text{3D,0D}} \\ \boldsymbol{K}^{\text{0D,3D}} & \boldsymbol{K}^{\text{0D}} \end{bmatrix}_i^n \begin{bmatrix} \Delta \boldsymbol{d} \\ \Delta \boldsymbol{q} \end{bmatrix}_{i+1}^n = - \begin{bmatrix} \boldsymbol{r}^{\text{3D}} \\ \boldsymbol{r}^{\text{0D}} \end{bmatrix}_i^n, \tag{3.46}$$

which is solved for $\Delta \boldsymbol{d}_{i+1}^n$ and $\Delta \boldsymbol{q}_{i+1}^n$ to update the solutions

$$\begin{bmatrix} \boldsymbol{d} \\ \boldsymbol{q} \end{bmatrix}_{i+1}^n = \begin{bmatrix} \boldsymbol{d} \\ \boldsymbol{q} \end{bmatrix}_i^n + \begin{bmatrix} \Delta \boldsymbol{d} \\ \Delta \boldsymbol{q} \end{bmatrix}_{i+1}^n. \tag{3.47}$$

Here, the matrix $\boldsymbol{K}^{\text{3D}} \in \mathbb{R}^{n_{\text{dof}} \times n_{\text{dof}}}$ is the effective tangential stiffness matrix from Eq. (2.86). The off-diagonal matrix $\boldsymbol{K}^{\text{3D,0D}} \in \mathbb{R}^{n_{\text{dof}} \times 16}$ describes the dependence of the structural mechanics problem on the vascular model and reads

$$\boldsymbol{K}^{\text{3D,0D}} \Big|_i^n = \frac{\partial \boldsymbol{r}^{\text{3D}}}{\partial \boldsymbol{q}} \Big|_i^n. \tag{3.48}$$

The second off-diagonal matrix $\boldsymbol{K}^{\text{0D,3D}} \in \mathbb{R}^{16\times n_{\text{dof}}}$ governs the dependence of the vascular model on the structural mechanics problem and reads

$$\boldsymbol{K}^{\text{0D,3D}}\Big|_i^n = \frac{\partial \boldsymbol{r}^{\text{0D}}}{\partial \boldsymbol{d}}\bigg|_i^n. \tag{3.49}$$

The stiffness matrix $\boldsymbol{K}^{\text{0D}} \in \mathbb{R}^{16\times 16}$ is given by

$$\boldsymbol{K}^{\text{0D}}\Big|_i^n = \frac{\partial \boldsymbol{r}^{\text{0D}}}{\partial \boldsymbol{q}}\bigg|_i^n. \tag{3.50}$$

For a more detailed derivation, the reader is referred to [62].

The vascular system is described by a system of ODEs, and therefore initial conditions are required, and they are listed in Tab. 3.5.

Tabelle 3.5.: Baseline values for the initial network state variables.

symbol	initial value
pressure states [kPa]	
p_{at}^{ℓ}	0.606
p_{v}^{ℓ}	0.6
$p_{\text{ar}}^{\text{sys}}$	12
$p_{\text{ven}}^{\text{sys}}$	2.266
p_{at}^{r}	0.0606
p_{v}^{r}	0.6
$p_{\text{ar}}^{\text{pul}}$	2.4
$p_{\text{ven}}^{\text{pul}}$	1.6

symbol	initial value
flow rates [mL/s]	
$q_{\text{v,in}}^{\ell}$	0
$q_{\text{v,out}}^{\ell}$	0
$q_{\text{ar}}^{\text{sys}}$	0
$q_{\text{ven}}^{\text{sys}}$	0
$q_{\text{v,in}}^{r}$	0
$q_{\text{v,out}}^{r}$	0
$q_{\text{ar}}^{\text{pul}}$	0
$q_{\text{ven}}^{\text{pul}}$	0

As explained in Sec. 1.2, the cardiovascular system is a closed loop, and hence, the solution of the heartbeat prediction must fulfill some periodicity requirements. Therefore, the so-called *periodic state* is considered as developed if some of the state variables become periodic, i.e., the value at the beginning of the cycle $t = 0$ has to be equal to the value at the end of the cycle $t = T_{\text{cycl}}$. The periodic state is achieved when the so-called *cycle error criterion* (CER), denoted by $\varepsilon_{\text{cycl}}$, is fulfilled

$$\begin{aligned}\varepsilon_{\text{cycl}} = \max\Bigg(&\left|\frac{p_{\text{ar}}^{\text{sys}}(T_{\text{cycl}}) - p_{\text{ar}}^{\text{sys}}(0)}{p_{\text{ar}}^{\text{sys}}(0)}\right|, \left|\frac{p_{\text{ar}}^{\text{pul}}(T_{\text{cycl}}) - p_{\text{ar}}^{\text{pul}}(0)}{p_{\text{ar}}^{\text{pul}}(0)}\right|,\\ &\left|\frac{p_{\text{ven}}^{\text{sys}}(T_{\text{cycl}}) - p_{\text{ven}}^{\text{sys}}(0)}{p_{\text{ven}}^{\text{sys}}(0)}\right|, \left|\frac{p_{\text{ven}}^{\text{pul}}(T_{\text{cycl}}) - p_{\text{ven}}^{\text{pul}}(0)}{p_{\text{ven}}^{\text{pul}}(0)}\right|,\\ &\left|\frac{V_{\text{v}}^{\ell}(T_{\text{cycl}}) - V_{\text{v}}^{\ell}(0)}{V_{\text{v}}^{\ell}(0)}\right|, \left|\frac{V_{\text{v}}^{r}(T_{\text{cycl}}) - V_{\text{v}}^{r}(0)}{V_{\text{v}}^{r}(0)}\right|\Bigg) \leq \varepsilon_{\text{tol}},\end{aligned} \tag{3.51}$$

where ε_{tol} is the prescribed tolerance.

Given the initial values at $t = 0$, all 0D network state quantities evaluated at $t = T_{\text{cycl}}$ result from the evaluation of the cardiac cycle. To fulfill Eq. (3.51), identifying the periodic state can be reformulated as finding a set of initial conditions $\boldsymbol{q}(t = 0)$ for the flow network. To find such initial conditions, multiple cardiac cycles are evaluated, where after each cycle, the initial conditions are updated using the previous results at $t = T_{\text{cycl}}$. The iterative process to evaluate a cardiac cycle until a periodic state is achieved is shown in Alg. 3.

Algorithm 3 periodic state computation

Require: $\boldsymbol{q}(t = 0)$ ▷ initial conditions

while not converged($\varepsilon_{\text{cycl}} > \varepsilon_{\text{tol}}$) **do**
  $\hat{p}_{\text{v}}^{\ell} \leftarrow \boldsymbol{q}(p_{\text{v}}^{\ell}(t = 0))$ ▷ update pressure traction (3.18)
  $\hat{p}_{\text{v}}^{r} \leftarrow \boldsymbol{q}(p_{\text{v}}^{r}(t = 0))$ ▷ update pressure traction (3.18)
  compute prestressing stage Eq. (3.14)-(3.17)
  compute cardiac cycle Eq. (3.39)-(3.42)
  compute cycle error criterion $\varepsilon_{\text{cycl}}$ Eq. (3.51)
  $\boldsymbol{q}(t = 0) \leftarrow \boldsymbol{q}(t = T_{\text{cycl}})$ ▷ update initial conditions
end while

3.2. Computational cardiac growth mechanics

Cardiac growth and remodeling (G&R) refers to the dynamic processes through which the heart adapts its structure and function in response to various physiological and pathological stimuli. These adaptive changes are crucial for maintaining optimal cardiac performance. This section provides an overview of the key aspects of cardiac G&R and summarizes previous research in this field.

Numerous studies have delved into the complex mechanisms of cardiac G&R. For example, in [108], it is investigated how the heart can adapt its geometry and function to diverse stimuli and the underlying molecular processes. In [119] and [146], the adaptation of heart function in response to changes in pumping demand has been discussed. At the cellular level, research in [39] has explored sarcomerogenesis, while studies in [156] have investigated myocardial fibrosis. Cardiac G&R can be triggered by natural factors such as pregnancy and athletic pursuits, which is called *physiological hypertrophy*, or in response to abnormal conditions like valve dysfunction and genetic mutations, called *pathological hypertrophy*. Both types are briefly discussed in the following.

Physiological hypertrophy is considered a compensatory mechanism, leading to an increase in cardiac mass due to the growth of cardiomyocytes in both length and width. A heart displaying physiological hypertrophy maintains or even enhances its systolic function, and it was shown that the left ventricular dimension in trained athletes is significantly larger [42, 105]. Importantly, this improvement in function does not result in alterations to the extracellular matrix or the development of fibrosis [24]. Furthermore, it's worth noting that physiological hypertrophy is entirely reversible [100]. For example, in the case of pregnancy, elevated hormone levels, incre-

ased blood volume, and cardiac output trigger an adaptive hypertrophy in the left ventricle that returns to the normal condition within two weeks [151].
Pathological hypertrophy is characterized as an initial, adaptive, and compensatory reaction to abnormal ventricular loading or the presence of mutant sarcomeric proteins [46]. Nonetheless, this form of hypertrophy can eventually become maladaptive, leading to myocardial fibrosis and disruptions in myocyte function. These changes can detrimentally affect both systolic and diastolic function, ultimately culminating in irreversible cardiac growth and heart failure [59, 138].
There are typically two classical categories of pathological hypertrophy, which are distinguished by the changes in ventricular geometry resulting from the underlying condition.
First, *concentric* hypertrophy involves the thickening of the ventricular wall and an increase in cardiac mass while the chamber volume remains relatively unchanged. This phenomenon occurs due to the parallel deposition of sarcomeres in cardiomyocytes [59].
Second, *eccentric* hypertrophy, also known as *dilated* hypertrophy, is characterized by the dilation of the chamber volume. Unlike concentric hypertrophy, there is only a slight change in the thickness of the ventricular wall. This type of hypertrophy results from the serial addition of sarcomeres and the lengthening of cardiomyocytes [59].
Numerous heart diseases can lead to the development of these two primary forms of pathological cardiac hypertrophy. Three predominant causes are highlighted as follows.

- Pressure overloading refers to an external abnormal mechanical loading condition where the ventricular afterload is increased. To counteract this elevated afterload, the contractile stress in the sarcomeres increases to generate the necessary force for pumping blood out of the left ventricle and into the rest of the body [116].

- Volume overloading represents another type of abnormal ventricular loading. In this scenario, the left or right ventricle becomes filled with an excessive amount of blood during diastole, resulting in an elevated ventricular preload [116].

- Hypertrophic cardiomyopathy stands out as the most common form of genetic heart disease. It arises due to mutations in the sarcomeric proteins found in the myocardium, which is the muscular tissue of the heart. This genetic condition can lead to abnormal cardiac growth and structure [99].

Over the past decades, the focus on computational and mathematical modeling of cardiac G&R has increased. These models offer the potential to deepen the comprehension of the complex behaviors and interactions within living systems. Further, with the help of these models, different hypotheses, as the choice of mechanical stimuli [106, 125] and the reversal of cardiac hypertrophy [95] on the hypertrophic behavior of the heart, were investigated.
The multiplicative split framework from [122] has been used in many different applications. It was initially used to model arterial growth, see for example [90, 123] or to model growth in the developing heart, see [96, 120, 147]. Therein, the growth deformation gradient was defined as a differential equation involving the deviation of a growth stimulus from its periodic value [96] and was applied to a ventricle geometry in [88].
Another research focus has been the development of constitutive growth laws that govern the formulation of the growth deformation gradient. The debate over which stimulus or combination of stimuli drives cardiac growth continues. Still, conventional cardiac growth models have

typically employed stress, strain, or a combination of both to stimulate the evolution of the deformation gradient. There has been a growing emphasis on determining the most effective stimulus or combination of stimuli to reliably induce stable growth, along with an increased focus on integrating multiscale and mechanical aspects. For example, [160] conducted a comparative analysis of eight established growth laws in response to cyclic stretches designed to simulate either volume or pressure overload. However, only two models could reach a steady-state growth in both simulations [83, 96].
Additionally, signaling pathways have been incorporated in modeling heart growth, see for example [41, 162]. They describe the hormonal and mechanical signaling cascades, which are active transcriptional factors that induce heart growth. A more detailed overview is given in Sec. 3.3.
Instead of using the kinematic growth model from [122], cardiac G&R can also be described using the so-called *homogenized constraint mixture model* [71]. Therein, the different constituents of tissue exhibit unique production and turnover rates within a single continuum mixture. An example application is given in [28] for G&R in arteries and vessels.

Within the scope of this thesis, the kinematic growth model presented in [122] is used and is therefore discussed within the following section. For further insights into recent G&R studies, the reader is referred to [103, 136].

3.2.1. Kinematics of growth

The multiplicative split of the deformation gradient, see Eq. (2.6), is introduced as

$$\boldsymbol{F} = \boldsymbol{F}_{\mathrm{e}}\boldsymbol{F}_{\mathrm{g}}, \tag{3.52}$$

where $\boldsymbol{F}_{\mathrm{e}}$ is the elastic deformation and $\boldsymbol{F}_{\mathrm{g}}$ corresponds to the inelastic or growth deformation. In the nonlinear continuum mechanics setting, applying $\boldsymbol{F}_{\mathrm{g}}$ to the reference configuration Ω_0 leads to an intermediate configuration Ω_{g}, see Fig. 3.8.
In this intermediate configuration, local kinematic compatibility conditions are not imposed. Hence, the mapping from Ω_0 to Ω_{g} is not necessarily differentiable in space and can therefore not be described by a mapping function $\boldsymbol{\varphi}_{\mathrm{g}}$ [160]. The mapping from the intermediate configuration Ω_{g} to the current configuration Ω_t is defined by the elastic deformation gradient $\boldsymbol{F}_{\mathrm{e}}$.
As a result of the multiplicative split, the elastic right Cauchy-Green deformation tensor from Eq. (2.14) is defined as

$$\boldsymbol{C}_{\mathrm{e}} = \boldsymbol{F}_{\mathrm{e}}{}^{T}\boldsymbol{F}_{\mathrm{e}} = \boldsymbol{F}_{\mathrm{g}}{}^{-T}\boldsymbol{C}\boldsymbol{F}_{\mathrm{g}}{}^{-1}, \tag{3.53}$$

and the elastic second Piola-Kirchhoff stress tensor from Eq. (2.19) reads

$$\boldsymbol{S}_{\mathrm{e}} = \boldsymbol{F}_{\mathrm{g}}\boldsymbol{S}\boldsymbol{F}_{\mathrm{g}}{}^{T}. \tag{3.54}$$

Furthermore, growth is not supposed to induce stresses directly. Hence, the strain energy function is reformulated in terms of the elastic right Cauchy-Green deformation tensor and is defined as

$$\Psi_{\mathrm{e}}(\boldsymbol{C}) = \Psi(\boldsymbol{C}_{\mathrm{e}}), \tag{3.55}$$

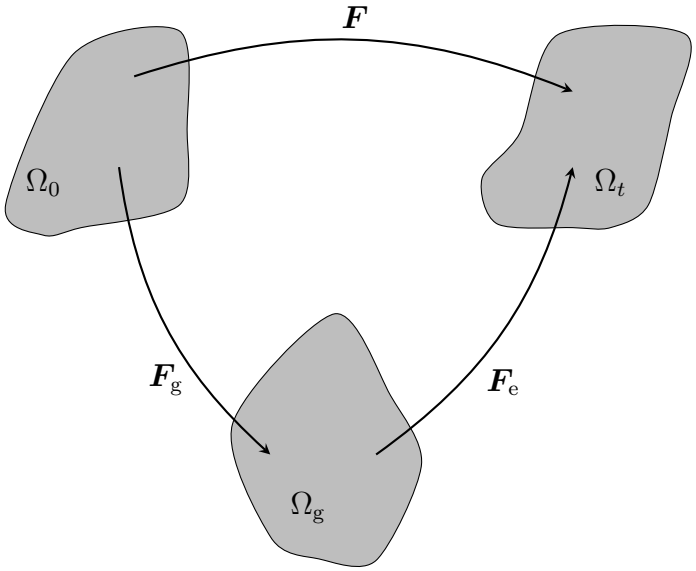

Abbildung 3.8.: Visualization of the multiplicative split of the deformation gradient. The intermediate configuration Ω_g arises from applying the growth deformation gradient $\boldsymbol{F}_\mathrm{g}$ to the reference configuration Ω_0. The mapping from Ω_g to Ω_t is defined by the elastic deformation gradient $\boldsymbol{F}_\mathrm{e}$.

Similar to Eq. (2.31) and Eq. (2.32), the elastic second Piola-Kirchhoff and the elastic material tangent is given by

$$\boldsymbol{S}_\mathrm{e} = 2\frac{\partial \Psi_\mathrm{e}}{\partial \boldsymbol{C}_\mathrm{e}}, \qquad \text{and} \qquad \mathbb{C}_\mathrm{e} = 4\frac{\partial^2 \Psi_\mathrm{e}}{\partial \boldsymbol{C}_\mathrm{e}{}^2}. \tag{3.56}$$

3.2.2. Phenomenological growth model

In this section, the specific growth law suitable for modeling physiological heart growth is presented. The growth deformation gradient $\boldsymbol{F}_\mathrm{g}$ is described by the growth stretch. Specifically, the underlying growth law is chosen based on [83] and reads

$$\boldsymbol{F}_\mathrm{g}(\vartheta) = \vartheta_1 \boldsymbol{f}_0 \otimes \boldsymbol{f}_0 + \vartheta_2(\boldsymbol{s}_0 \otimes \boldsymbol{s}_0 + \boldsymbol{r}_0 \otimes \boldsymbol{r}_0), \tag{3.57}$$

with $\boldsymbol{r}_0$ as the surface normal direction, perpendicular to $\boldsymbol{f}_0$ and $\boldsymbol{s}_0$. Since these three directions form an orthonormal basis, it follows that

$$\boldsymbol{I} = \boldsymbol{f}_0 \otimes \boldsymbol{f}_0 + \boldsymbol{s}_0 \otimes \boldsymbol{s}_0 + \boldsymbol{r}_0 \otimes \boldsymbol{r}_0, \tag{3.58}$$

holds and thus, Eq. (3.57) can be rewritten as

$$\boldsymbol{F}_\mathrm{g}(\vartheta_1, \vartheta_2) = \vartheta_1 \boldsymbol{f}_0 \otimes \boldsymbol{f}_0 + \vartheta_2(\boldsymbol{I} - \boldsymbol{f}_0 \otimes \boldsymbol{f}_0). \tag{3.59}$$

This growth law is motivated by cylindrical growth, where a cylinder is regarded as an approximation of the muscle fiber. Consequently, two growth directions are defined, one in the fiber direction and the other one in the cross-fiber direction. This assumes that sarcomeres are added

equally in parallel in both cross-fiber directions, that is, transversely isotropic growth. As the material needs to be deposited in two directions, the second growth stretch ratio is applied to both cross-fiber directions and has to be lower than the first growth stretch.
Following [83], the relation between the two growth stretches reads

$$\vartheta_1 = \vartheta \tag{3.60}$$

$$\vartheta_2 = \sqrt{\vartheta}. \tag{3.61}$$

This choice simplifies the parameter optimization problem for the growth stretch ϑ described in Sec. 2.3.
Note that the gradient of $\boldsymbol{S}$ with respect to the growth stretch ϑ is needed in case of the parameter estimation framework, see Eq. (2.112). This linearization is given in App. B.2.

IBVP

The growth stretch $\vartheta(\boldsymbol{X}, t)$ is a spatial field, defining growth at point $\boldsymbol{X}$ at time t. In this work, a temporal constant growth rate $c_\vartheta(\boldsymbol{X})$ is assumed due to the lack of available information. Additionally, it is assumed that there is no significant growth acceleration within the considered timeframe of physiological growth. Thus, the evolution equation for $\vartheta(\boldsymbol{X}, t)$ is given by

$$\dot{\vartheta}(\boldsymbol{X}, t) = c_\vartheta(\boldsymbol{X}). \tag{3.62}$$

Its solution reads

$$\vartheta(\boldsymbol{X}, t) = \vartheta(\boldsymbol{X}, t_0) + \int_{t_0}^{T_{\text{growth}}} c_\vartheta(\boldsymbol{X}) \mathrm{d}t = \vartheta(\boldsymbol{X}, t_0) + c_\vartheta(\boldsymbol{X})(T_{\text{growth}} - t_0), \tag{3.63}$$

where $T_{\text{growth}} - t_0$ is the duration of the growth time. The initial condition is chosen to be $\vartheta(\boldsymbol{X}, t_0) = 1$ everywhere.
Finally, the IBVP from Section 2.1.4 for the growth mechanics model reads

$$\nabla_{\boldsymbol{X}} \cdot \boldsymbol{P} = \boldsymbol{0} \qquad \text{in } \Omega, \tag{3.64}$$

$$\boldsymbol{P} \cdot \boldsymbol{N} = \boldsymbol{t}_{0_p}^{i} \qquad \text{on } \Gamma_{\text{v}}^{i}, i \in \{r, \ell\}, \tag{3.65}$$

$$\boldsymbol{P} \cdot \boldsymbol{N} = \boldsymbol{t}_{0_k}^{\text{base}} + \boldsymbol{t}_{0_k}^{\text{base},\perp} \qquad \text{on } \Gamma_{\text{base}}, \tag{3.66}$$

$$\boldsymbol{P} \cdot \boldsymbol{N} = \boldsymbol{t}_{0_k}^{i,\perp} \qquad \text{on } \Gamma_i, i \in \{\text{epi}, \text{lid}\}. \tag{3.67}$$

The traction boundary conditions for the embedding tissue remain unchanged and are given in (3.10) and (3.11). The growth computation is performed after evaluating the cardiac cycle, see Section 3.1.5. Therefore, the end-diastolic configuration is chosen as the reference configuration of the growth model. Hence, the pressure traction boundary condition $\boldsymbol{t}_{0_p}^{i}$ from (3.43) is still applied, where the constant p_{v}^{i} equals the end-diastolic pressure. Note that the same strain energy function as in Eq. (3.2) is used.

3.3. Signaling growth network

As already outlined in Sec. 3.2, cardiac G&R is a complex interplay between biochemical and mechanical stimuli [45, 56]. This interplay across different time and length scales is pivotal to understanding cardiac G&R [55, 153]. In particular, the underlying cellular processes must be considered if one wants to predict the influence of hormones and pharmacologic interventions on growth.
On a cellular level, the hormone *insulin-like growth factor 1* (*IGF1*) plays a central role in G&R. When *IGF1* binds to its receptor *IGF1R*, multiple signaling pathways are triggered, which regulate cell proliferation, differentiation, metabolism, and survival [150]. Primarily synthesized in the liver, *IGF1* travels through the bloodstream to the heart, activating an endocrine effect [93]. However, it can also be locally produced in response to mechanical stretches, leading to an autocrine or paracrine effect [161]. The absence of *IGF1* restricts cardiomyocyte growth in hypertension, ultimately contributing to heart failure. Thus, the local production of *IGF1* emerges as a critical factor for heart growth and has to be considered in the context of G&R [164].
The local cellular processes are often described by various intracellular signaling pathways and growth factors, which can be represented by signaling networks [45, 55, 56, 153]. They consist of a set of species and a set of reactions determining their mutual dependencies. Species refer to the molecular entities involved in the signaling network, such as proteins, small molecules, nucleic acids, and complexes formed by these molecules. Reactions represent the biochemical interactions or transformations that occur between species, e.g., protein-protein binding. Within these signaling networks, the species *CellArea* has been used to describe heart growth [41].
In the past, these signaling networks were based on kinetic models [134], Boolean models [1], fuzzy logic analysis [2], or normalized Hill differential equations [87, 159]. The analysis of these signaling networks is challenging due to the high number of parameters and interactions between species. A detailed overview is given in [94].
Signaling networks were used to predict the effects of hormones and pharmaceutical interventions on cardiac G&R. For example, they were used to model hypertrophic signaling within a single cardiomyocyte and to predict growth in response to both mechanical and hormonal changes in the system [128] and validated against *in-vivo* measurements in [45]. In [41], a signaling network was coupled with a finite element model of the left ventricle by using the network output as input of the computational model to predict cardiac G&R.
In this work, the local *IGF1* production is incorporated into an existing signaling network for cardiac G&R. Thereafter, the resulting signaling network is coupled to the cardiac growth mechanics presented in Sec. 3.2. In the following, the resulting signaling network is presented in Sec. 3.3.1. Subsequently, in Sec. 3.3.2, the mathematical model to evaluate a signaling network is outlined, and in Sec. 3.3.3, an exemplary evaluation is shown. Finally, in Sec. 3.3.4, the coupling to the cardiac growth mechanics is discussed. Parts of the presented work in this section are submitted in [9].

3.3.1. Heart growth network

As a starting point, an established signaling network originally published in [128] and subsequently utilized in other studies [41, 45, 77] was used. For the sake of completeness, this network is shown in the App. Fig. C.1. Throughout this work, it is referred to as the reference (REF) net-

work. The REF network consists of 106 species, 193 reactions with 17 inputs and 7 outputs, and is organized in 19 layers, where all species in a layer depend only on species in previous layers. All species depicted in the first layer are called *input* species, whereas species in the last layer are called *output* species. The input species *Stretch* represents the local mechanical stimulus, whereas the output species *CellArea* can be used to quantify heart growth [41]. All other species are hormonal and biochemical factors. A detailed list of all species within the network can be found in the App. in Tab. C.1.

The REF network is modified in two steps. First, since the goal is to analyze heart growth, the signaling network is simplified such that all species and reactions that do not influence the output quantity of interest *CellArea* are removed.
Second, an additional species, denoted as l-*IGF1*, which accounts for the local *IGF1* production, is incorporated into the second layer of the network. It is connected to *Stretch* and *IGF1R*. Furthermore, the species *IGF1* is renamed as g-*IGF1* and now only represents the global *IGF1* production.

Following the work in [161], the l-*IGF1* production is initiated by a calcium influx through transient receptor potential vanilloid 4 (TRPV4)-calcium channels, which trigger *IGF1* gene expression. Resident cardiac macrophages are in physical contact with cardiomyocytes via focal adhesion complexes and contribute to the l-*IGF1* production process. Furthermore, it has been shown in [164] that locally produced *IGF1* is a crucial requirement for functional heart remodeling processes. Tissue-resident macrophages are also involved in tissue development, remodeling and immune adaption [20].

The resulting signaling network is referred to as the reduced and modified (R&M) network and is shown in Fig. 3.9.

3.3.2. Hill differential equation approach

Let $\mathcal{S}$ represent the set of all species in a signaling network and $\mathcal{I} \subset \mathcal{S}$ denote the set of all input species as the species without ingoing reactions. Each species s $\in \mathcal{S}$ is defined by a concentration $c_\mathrm{s} \in [0, c_\mathrm{s,max}]$. Here, $c_\mathrm{s} = 0$ corresponds to the lowest and $c_\mathrm{s} = c_\mathrm{s,max}$ to the highest possible level of activation. Furthermore, a network evaluation is denoted as $y = f(\boldsymbol{c}_\mathcal{I})$, with $\boldsymbol{c}_\mathcal{I} = \{c_i \in [0, c_{i,\mathrm{max}}] | i \in \mathcal{I}\}$. In the case of the REF and R&M networks, the output y corresponds to the concentration c_CellArea.

Within the Hill differential equation approach, four different reaction types are introduced, and they are shown in Fig. 3.10. They are exemplified for X, Y, Z $\in \mathcal{S}$. In a single *activation*, species X activates species Z, whereas in an *inhibition*, species X inhibits the activation of species Z. In an OR activation, either species X or Y can activate Z, and in an AND activation, both species X and Y must be active to activate species Z. Furthermore, a reaction weight w is assigned to each reaction.

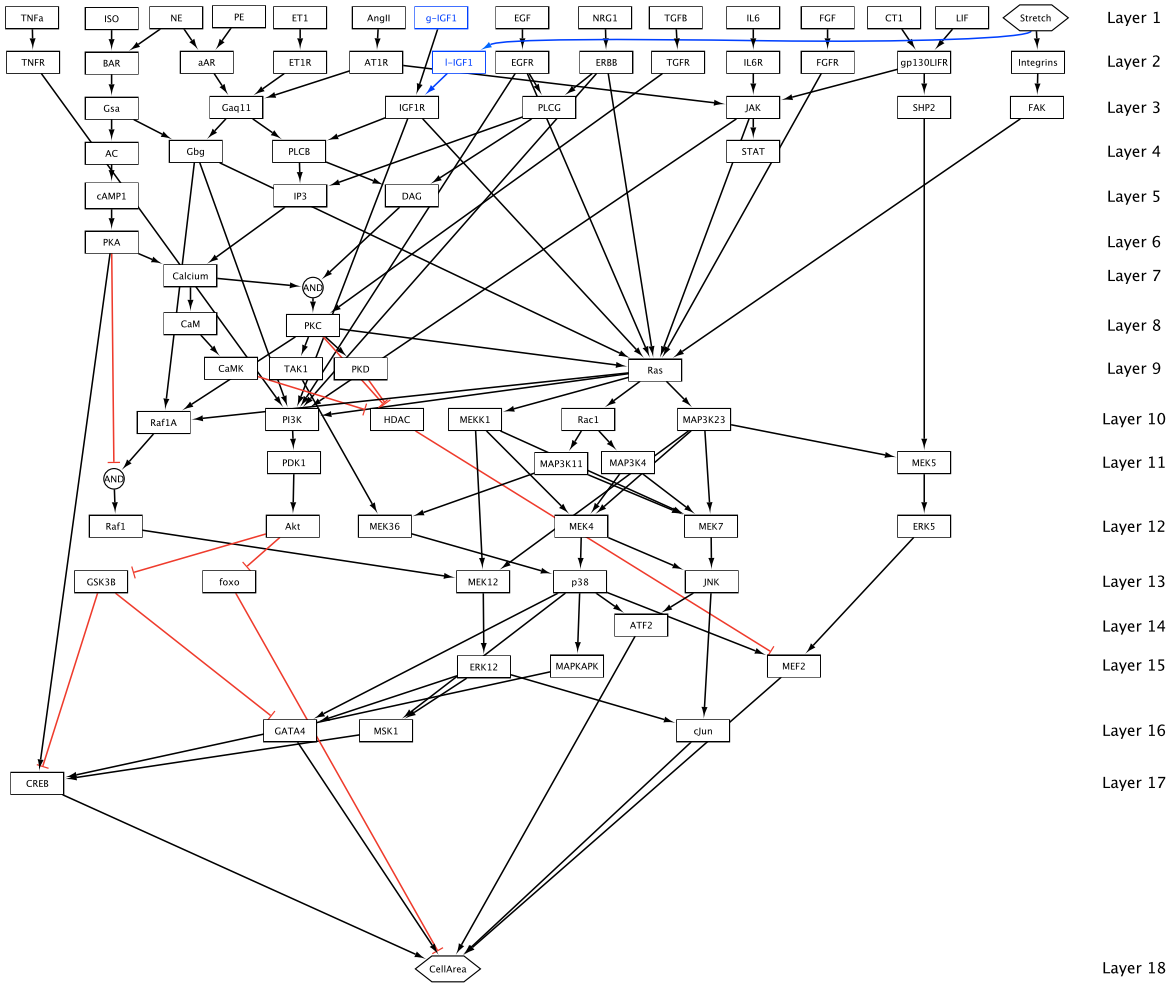

Abbildung 3.9.: Reduced and modified (R&M) signaling network containing 80 species, 140 reactions, and 18 layers. It consists of 15 input species. *CellArea* remains the only output species. The model connection from *Stretch* to *IGF1R* was added (blue), based on [161, 164].

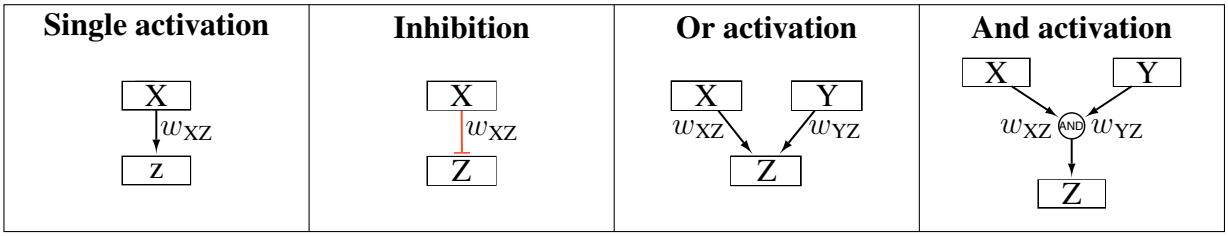

Abbildung 3.10.: Different reaction types within a signaling network reaction weight w [9].

The Hill activation function $f_{\text{act}}^{\to \text{Z}} : [0,1] \mapsto [0,1]$ from species X to Z is defined by

$$f_{\text{act}}^{\to \text{Z}}(c_{\text{X}}) := w_{\text{XZ}} \frac{B c_{\text{X}}^n}{K^n + c_{\text{X}}^n}, \tag{3.68}$$

where $w_{XZ} \in [0,1]$ is the reaction weight, $B = \frac{{EC_{50}}^n - 1}{2{EC_{50}}^n - 1}$ and $K = (B-1)^{\frac{1}{n}}$. The parameter EC_{50} is the input species concentration required to result in half-maximal activation of the corresponding output species. Based on the work in [87], $EC_{50} = 0.5$, $n = 1.4$ and the parameters B and K ensure that

$$f_{\text{act}}(1) = 1, \tag{3.69}$$
$$f_{\text{act}}(EC_{50}) = 0.5. \tag{3.70}$$

The Hill coefficient n determines the steepness of the Hill curve and is depicted in Fig. 3.11.

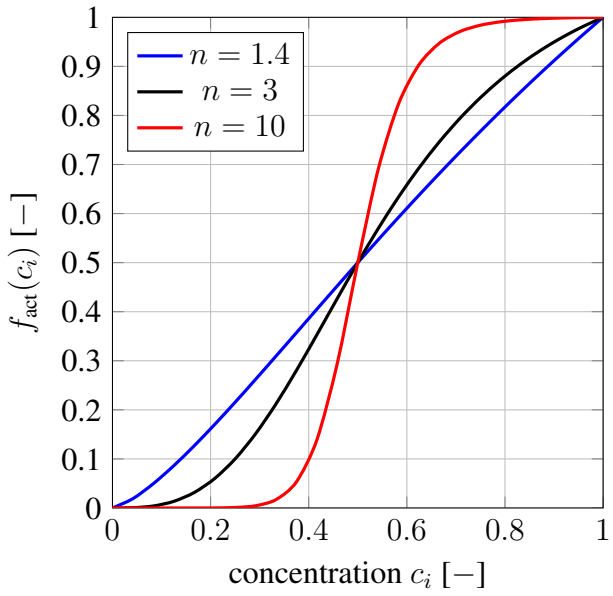

Abbildung 3.11.: Nonlinear Hill activation function with $w = 1$ and $EC_{50} = 0.5$ [9].

The inhibition function $f_{\text{inh}}^{\to Z} : [0,1] \mapsto [0,1]$ from species X to Z is given by

$$f_{\text{inh}}^{\to Z}(c_X) := 1 - f_{\text{act}}^{\to Z}(c_X). \tag{3.71}$$

The logical functions $\text{OR} : [0,1] \times [0,1] \mapsto [0,1]$ and $\text{AND} : [0,1] \times [0,1] \mapsto [0,1]$ between species X, Y and Z read

$$\text{OR}\big(f_{\text{act}}^{\to Z}(c_X), f_{\text{act}}^{\to Z}(c_Y)\big) := f_{\text{act}}^{\to Z}(c_X) + f_{\text{act}}^{\to Z}(c_Y) - f_{\text{act}}^{\to Z}(c_X) f_{\text{act}}^{\to Z}(c_Y), \tag{3.72}$$
$$\text{AND}\big(f_{\text{inh}}^{\to Z}(c_X), f_{\text{act}}^{\to Z}(c_Y)\big) := f_{\text{inh}}^{\to Z}(c_X)\ f_{\text{act}}^{\to Z}(c_Y). \tag{3.73}$$

These AND and OR functions are applied recursively in case of more than two inputs as in the REF and R&M network. Exemplary, for three inputs, they read

$$\text{AND}\big(\bullet,\bullet,\bullet\big) := \text{AND}\big(\bullet, \text{AND}(\bullet,\bullet)\big), \tag{3.74}$$
$$\text{OR}\big(\bullet,\bullet,\bullet\big) := \text{OR}\big(\bullet, \text{OR}(\bullet,\bullet)\big). \tag{3.75}$$

Further, the gradients for all different reaction types are defined as

Single activation from X to Z

$$\frac{\mathrm{d}c_{\mathrm{Z}}}{\mathrm{d}c_{\mathrm{X}}} = c_{\mathrm{Z,max}} \frac{\mathrm{d}f_{\mathrm{act}}^{\rightarrow \mathrm{Z}}(c_{\mathrm{X}})}{\mathrm{d}c_{\mathrm{X}}}, \tag{3.76}$$

AND activation to Z for N inputs

$$\frac{\mathrm{d}c_{\mathrm{Z}}}{\mathrm{d}c_{\mathrm{X}}} = c_{\mathrm{Z,max}} \frac{\mathrm{d}f_{\mathrm{act}}^{\rightarrow \mathrm{Z}}(c_{\mathrm{X}})}{\mathrm{d}c_{\mathrm{X}}} \prod_{\mathcal{I}}^{N} f_{\mathrm{act}}^{\rightarrow \mathrm{Z}}(c_i), \quad \text{with } \mathcal{I} \in \mathcal{S}\backslash\{\mathrm{X}\}, \tag{3.77}$$

OR activation to Z for N inputs

$$\frac{\mathrm{d}c_{\mathrm{Z}}}{\mathrm{d}c_{\mathrm{X}}} = c_{\mathrm{Z,max}} \frac{\mathrm{d}f_{\mathrm{act}}^{\rightarrow \mathrm{Z}}(c_{\mathrm{X}})}{\mathrm{d}c_{\mathrm{X}}} \left[1 - \mathrm{OR}\big(f_{\mathrm{act}}^{\rightarrow \mathrm{Z}}(c_j, 0)\big)\right], \quad \text{with } j \in \mathcal{S}\backslash\{\mathrm{X}\}. \tag{3.78}$$

The derivative of the activation function with respect to an input c_{X} reads

$$\frac{\mathrm{d}f_{\mathrm{act}}^{\rightarrow \mathrm{Z}}(c_{\mathrm{X}})}{\mathrm{d}c_{\mathrm{X}}} = wB\left(\frac{nc_{\mathrm{X}}^{n-1}}{K^n + c_{\mathrm{X}}^n} - \frac{nc_{\mathrm{X}}^{2n-1}}{(K^n + c_{\mathrm{X}}^n)^2}\right). \tag{3.79}$$

The derivative of the inhibition function follows from Eq. (3.71) and results in

$$\frac{\mathrm{d}f_{\mathrm{inh}}^{\rightarrow \mathrm{Z}}(c_{\mathrm{X}})}{\mathrm{d}c_{\mathrm{X}}} = -\frac{\mathrm{d}f_{\mathrm{act}}^{\rightarrow \mathrm{Z}}(c_{\mathrm{X}})}{\mathrm{d}c_{\mathrm{X}}}. \tag{3.80}$$

Within the Hill differential equation approach, the temporal development of the species concentrations is modeled. Therefore, the reaction time constants τ_{s} with $\mathrm{s} \in \mathcal{S}$ are introduced, which influence the reaction dynamics of the corresponding activation. For the sake of simplicity and readability, the arrow in the Hill activation and inhibition functions is omitted. Exemplary, for the REF and R&M network, the Hill ODEs read

$$\frac{\mathrm{d}c_{\mathrm{Calcium}}}{\mathrm{d}t} = \frac{1}{\tau_{\mathrm{Calcium}}}\left[\mathrm{OR}(f_{\mathrm{act}}(c_{\mathrm{IP3}}), f_{\mathrm{act}}(c_{\mathrm{PKA}}))c_{\mathrm{Calcium,max}} - c_{\mathrm{Calcium}}\right], \tag{3.81}$$

$$\frac{\mathrm{d}c_{\mathrm{HDAC}}}{\mathrm{d}t} = \frac{1}{\tau_{\mathrm{HDAC}}}\left[\mathrm{OR}(f_{\mathrm{inh}}(c_{\mathrm{CaMK}}), f_{\mathrm{inh}}(c_{\mathrm{PKC}}), f_{\mathrm{inh}}(c_{\mathrm{PKD}}))c_{\mathrm{HDAC,max}} - c_{\mathrm{HDAC}}\right], \tag{3.82}$$

$$\frac{\mathrm{d}c_{\mathrm{ERK5}}}{\mathrm{d}t} = \frac{1}{\tau_{\mathrm{ERK5}}}\left[f_{\mathrm{act}}(c_{\mathrm{MEK5}})c_{\mathrm{ERK5,max}} - c_{\mathrm{ERK5}}\right], \tag{3.83}$$

$$\frac{\mathrm{d}c_{\mathrm{p38}}}{\mathrm{d}t} = \frac{1}{\tau_{\mathrm{p38}}}\left[\mathrm{OR}(f_{\mathrm{act}}(c_{\mathrm{MEK36}}), f_{\mathrm{act}}(c_{\mathrm{MEK4}}))c_{\mathrm{p38,max}} - c_{\mathrm{p38}}\right], \tag{3.84}$$

$$\frac{\mathrm{d}c_{\mathrm{MEF2}}}{\mathrm{d}t} = \frac{1}{\tau_{\mathrm{MEF2}}}\left[\mathrm{OR}(f_{\mathrm{inh}}(c_{\mathrm{HDAC}}), f_{\mathrm{act}}(c_{\mathrm{ERK5}}), f_{\mathrm{act}}(c_{\mathrm{p38}}))c_{\mathrm{MEF2,max}} - c_{\mathrm{MEF2}}\right], \tag{3.85}$$

$$\begin{aligned}\frac{\mathrm{d}c_{\mathrm{CellArea}}}{\mathrm{d}t} = \frac{1}{\tau_{\mathrm{CellArea}}}[&\mathrm{OR}(f_{\mathrm{inh}}(c_{\mathrm{foxo}}), f_{\mathrm{act}}(c_{\mathrm{ATF2}}), f_{\mathrm{act}}(c_{\mathrm{cJun}}), f_{\mathrm{act}}(c_{\mathrm{CREB}}),\\ &f_{\mathrm{act}}(c_{\mathrm{GATA4}}), f_{\mathrm{act}}(c_{\mathrm{MEF2}}))c_{\mathrm{CellArea,max}} - c_{\mathrm{CellArea}}].\end{aligned} \tag{3.86}$$

The stationary solution of this system of ODEs is characterized by the condition

$$\frac{\mathrm{d}c_s}{\mathrm{d}t} = 0 \quad \forall s \in \mathcal{S}\backslash\mathcal{I}. \tag{3.87}$$

The *direct stationary solutions* (DSS) are obtained by using Eq. (3.87) and they read

$$c^{\text{DSS}}_{\text{Calcium}} = \text{OR}(f_{\text{act}}(c_{\text{IP3}}), f_{\text{act}}(c_{\text{PKA}}))c_{\text{Calcium,max}}, \tag{3.88}$$

$$c^{\text{DSS}}_{\text{HDAC}} = \text{OR}(f_{\text{inh}}(c_{\text{CaMK}}), f_{\text{inh}}(c_{\text{PKC}}), f_{\text{inh}}(c_{\text{PKD}}))c_{\text{HDAC,max}}, \tag{3.89}$$

$$c^{\text{DSS}}_{\text{ERK5}} = f_{\text{act}}(c_{\text{MEK5}})c_{\text{ERK5,max}}, \tag{3.90}$$

$$c^{\text{DSS}}_{\text{p38}} = \text{OR}(f_{\text{act}}(c_{\text{MEK36}}), f_{\text{act}}(c_{\text{MEK4}}))c_{\text{p38,max}}, \tag{3.91}$$

$$c^{\text{DSS}}_{\text{MEF2}} = \text{OR}(f_{\text{inh}}(c_{\text{HDAC}}), f_{\text{act}}(c_{\text{ERK5}}), f_{\text{act}}(c_{\text{p38}}))c_{\text{MEF2,max}}, \tag{3.92}$$

$$\begin{aligned} c^{\text{DSS}}_{\text{CellArea}} = \text{OR}(&f_{\text{inh}}(c_{\text{foxo}}), f_{\text{act}}(c_{\text{ATF2}}), f_{\text{act}}(c_{\text{cJun}}), f_{\text{act}}(c_{\text{CREB}}), \\ &f_{\text{act}}(c_{\text{GATA4}}), f_{\text{act}}(c_{\text{MEF2}}))c_{\text{CellArea,max}}. \end{aligned} \tag{3.93}$$

As all signaling networks in this work are arranged hierarchically in layers, the DSS can be computed using forward substitution consecutively from the first to the last layer. Furthermore, to compute the gradient of a specific species with respect to a previous species, chain rule can be used. For illustration purposes, a demonstrator network is shown in the App. C.2. Additionally, a proof that all signaling networks presented in this work are asymptotically stable is given in App. C.3. Hence, the stationary solutions are independent of the choice of the initial conditions.

3.3.3. Signaling network evaluation

Here, the REF and R&M networks are evaluated using the Hill differential equations approach. For the evaluation, the parameters are set as follows: $c_{s,\max} = 1, \tau_s = 1 \; \forall s \in \mathcal{S}\backslash\mathcal{I}$. All downstream reaction weights w are set to 1 [41] and the pseudo time interval is set to $[0, 40]$. All input nodes, including *Stretch*, are consistently set to a constant value of $c_i = 0.06, i \in \mathcal{I}$ throughout the entire simulation time. This assumption is based on the expectation of low basal activation under normal *in-vivo* conditions [45]. The system of ODEs is numerically solved with a third-order explicit Runge-Kutta method for nonstiff ODEs [11].

In Fig. 3.12, the time-dependent concentrations of the species *Calcium*, *HDAC*, *ERK5*, *p38*, *MEF2*, and *CellArea* are depicted for the REF and R&M network. Furthermore, the DSS are shown for the R&M network.

All shown concentrations approach a stationary value in both networks. Compared to the REF network, within the R&M network, the concentration c_{CellArea} attains a higher stationary value due to the additional pathway from *Stretch* to l-*IGF1*. The concentration c_{Calcium} attains a value close to zero due to the nonlinear behavior of the Hill activation function with a low-level input concentration. Since the concentration of *Calcium* is low, the downstream concentrations of *CaMK*, *PKC*, and *PKD* are also low. These species inhibit the activation of species *HDAC* and resulting from Eq. (3.71), c_{HDAC} attains a value of 1. Similarly to c_{Calcium}, the concentration c_{ERK5} and c_{p38} are low. The species *HDAC*, *ERK5*, and *p38* determine the concentration of species *MEF2*, see Eq. (3.85). The dynamic effects of the system lead to a drastic increase of c_{MEF2} in the beginning until the concentration c_{HDAC} reaches 1. Subsequently, *MEF2* is determined by the behavior of *ERK5* and *p38*. The concentration c_{CellArea} has a similar structure compared to the concentration c_{MEF2}.

In the following, only the stationary solutions of the presented signaling networks are computed due to the following reasons:

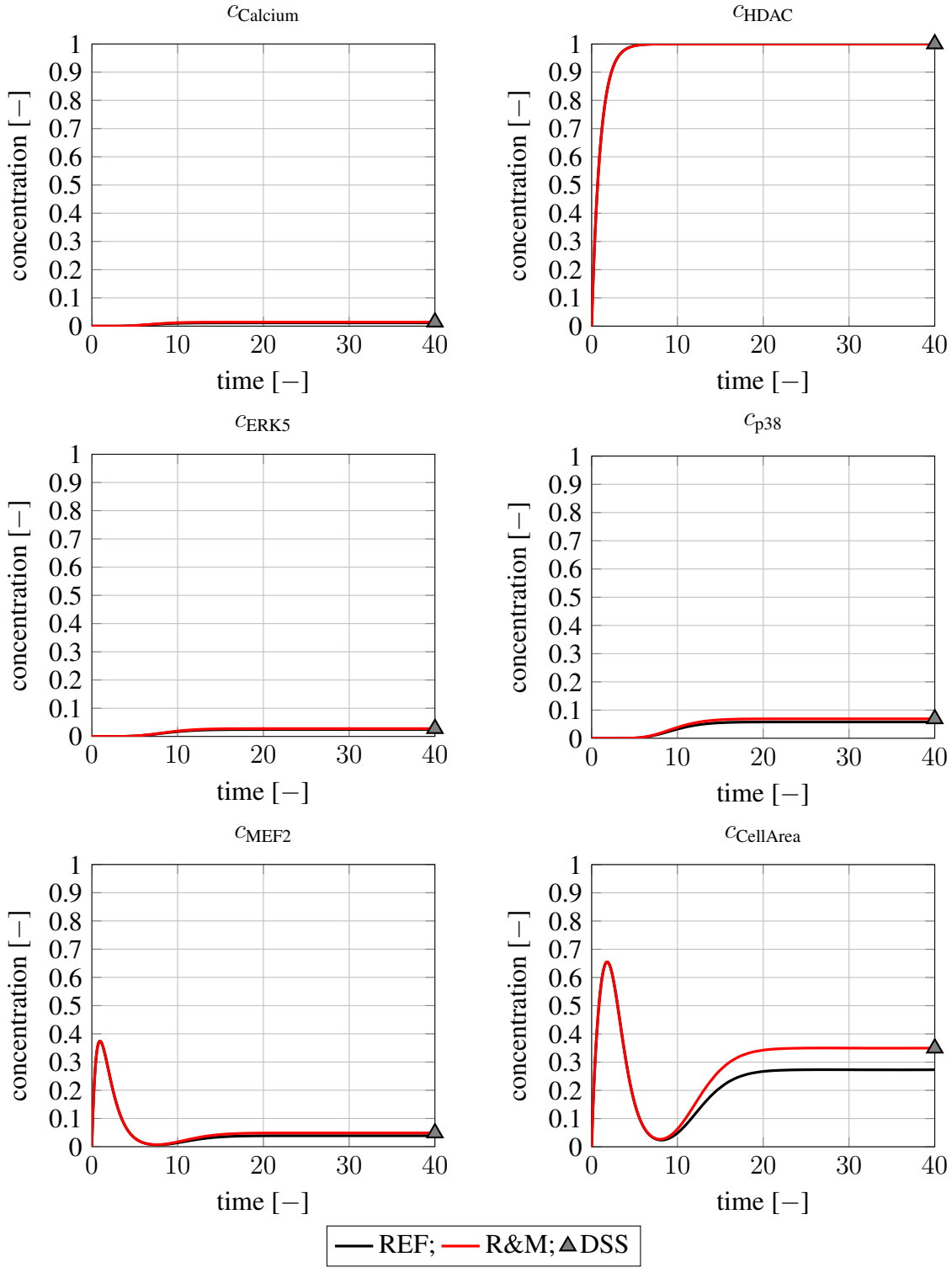

Abbildung 3.12.: Heart growth signaling network ODE solution of the REF and R&M network in comparison. The direct stationary solution (DSS) is shown for the R&M network [9].

- The timescale of heart growth is significantly larger than the timescale of dynamic hormonal changes.
- The initial transient oscillations of the concentrations in Fig. 3.12 arise from the arbitrarily chosen initial values and do not allow a statement on heart growth. Furthermore, no literature data is currently available to improve the choice of the initial conditions.

Physiological input range

Within the REF and R&M network, a strong monotonic behavior between the inputs $\boldsymbol{c}_{\mathcal{I}}$ and the output c_{CellArea} is observed. Further, only inhibitions can introduce a non-monotonic behavior. However, from Eq. (3.71), it can be seen that two consecutive inhibitions cancel each other out. Within the R&M network, only the pathway between *PKA* and *Raf1* includes a single inhibition. However, since *PKA* also activates two other pathways, it still shows a monotonic behavior with respect to *CellArea*. This is depicted in Fig. 3.13, where the concentration c_{CellArea} over the input concentration c_{ISO}, which activates the *PKA* pathways, is shown. Whenever the inputs exceed small threshold values, c_{CellArea} reaches 1. Therefore, the upper limit for physiological input concentrations is $\tilde{c}_{i,\max} \ll 1$. In App. C.4 in Fig. C.4, a heatmap plot is shown which depicts the difference in the DSS between the R&M and REF networks.

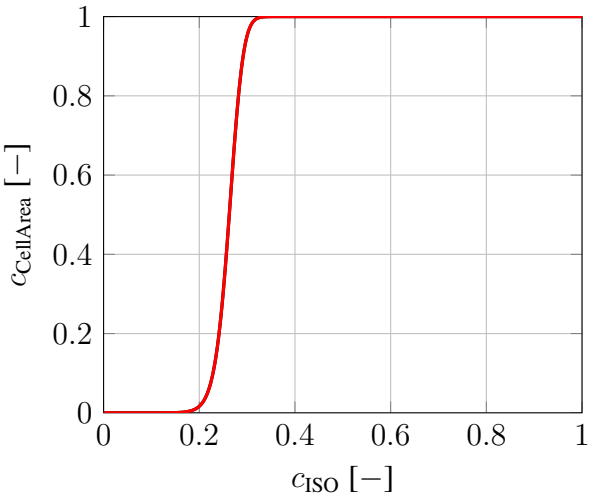

Abbildung 3.13.: R&M signaling network output concentration of species *CellArea* over input concentration c_{ISO}, where all other input concentrations are set to 0. For any concentration $c_{\text{ISO}} > 0.35$, the output concentration c_{CellArea} reaches 1 [9].

3.3.4. Coupling the signaling network and cardiac mechanics

To couple the presented signaling networks to the cardiac mechanics models outlined in Sec. 3.1 and Sec. 3.2, so-called *transfer functions* are needed. A transfer function maps a key output of a model to inputs of the other model. Specifically, in this case, two transfer functions are needed. The first transfer function is designed to map a mechanical quantity obtained from the cardiac

cycle evaluation to the concentration of input species *Stretch* of the signaling networks. The second transfer function is used to map the output concentration of *CellArea* of both networks to a growth rate needed to compute cardiac growth.
Since the signaling networks incorporate a single normalized input concentration for the species *Stretch* that activates stretch-related intracellular pathways, the transfer function is required to compute a single strain metric from the cardiac cycle evaluation. In this work, the maximal fiber strain is used as a strain metric. It is defined as a mapping from the Green-Lagrange strain tensor $\boldsymbol{E}$ in fiber direction $\boldsymbol{f}_0$ and reads [83]

$$E_{ff} = \boldsymbol{f}_0{}^T \boldsymbol{E} \boldsymbol{f}_0. \tag{3.94}$$

A linear transfer function between E_{ff} and c_{Stretch} is used, which reads

$$c_{\text{Stretch}} = c_{\text{Stretch,max}} \max(E_{ff}). \tag{3.95}$$

The value of the maximal concentration $c_{\text{Stretch,max}}$ will be discussed in Sec. 4.6. For simplicity, in the second transfer function, the concentration $c_{\text{CellArea}} \in [0, 1]$ is interpreted as the growth rate c_ϑ and it reads

$$c_\vartheta(\boldsymbol{X}) = c_{\text{CellArea}}. \tag{3.96}$$

4. Application

In this chapter, the patient-specific cardiac mechanics results are presented. In Sec. 4.1, the measurements needed for the patient-specific calibration process are outlined. In Sec. 4.2, the application of the atlas construction is presented. Subsequently, in Sec. 4.3, the calibration of the 3D-0D coupled cardiovascular mechanics model from Sec. 3.1.5 is discussed. In Sec. 4.4, the application of the surface matching framework from Sec. 2.4.1 is presented. Subsequently, in Sec. 4.5, the calibration of the cardiac growth mechanics model from Sec. 3.2 is shown. In Sec. 4.6, a global sensitivity analysis of the signaling networks from Sec. 3.3 is performed. Furthermore, the coupling results to the growth mechanics model are discussed.

4.1. Measurements

The measurements for the patient-specific calibration in this study were conducted on a porcine heart model. This heart model is based on genetically modified donor pigs, which are developed for xenotransplantation [86]. Specifically, the growth hormone receptor (GHR) was deleted in these pigs, resulting in a reduced growth potential. It was shown that these pigs, at age six months, exhibited significant reductions in body weight of around 61% and heart weight of around 63% compared to control pigs. Additionally, the mean minimal diameter of cardiomyocytes in the GHR-deleted pigs was reduced by 28% [60, 61].
The data collection process involved taking motion-CT images of the porcine heart, starting from the day of life 40 and continuing every ten days until the day of life 80. More precisely, six pigs, which will be denoted as P1 to P6 throughout this thesis, were analyzed. In this context, motion-CT is a technique that captures the entire cardiac cycle, showing the heartbeat from R-wave to R-wave in 10% steps, see Fig. 1.2. It's important to note that ethics approval has been granted for this study.
The collected data serve three primary purposes:

- First, the 80% diastolic state is segmented to establish a reference configuration for all cardiac mechanics models, as outlined in Sec. 3.1.1.
- Second, each phase in a motion-CT is segmented to generate a volume over time relationship, which is used to calibrate the cardiac cycle evaluation discussed in Sec. 3.1.5.
- Third, the CT images taken every ten days are segmented at the 80% diastolic state and are used to calibrate the cardiac growth mechanics model explained in Sec. 3.2.

During the data collection process, pig P3 passed away after the initial examination. Additionally, pig P4 encountered challenges during the CT imaging acquisition, resulting in data that cannot be utilized. Consequently, these two subjects are excluded from the dataset presentation. In App. D.1, a detailed overview of the collected data is presented.

An example of a porcine heart segmented at the 80% diastolic state is depicted in Fig. 3.2.
In the following, the calibration data for the cardiac cycle evaluation is presented in Sec. 4.1.1. Subsequently, in Sec. 4.1.2, the calibration data for the cardiac growth mechanics model is shown.

4.1.1. Cardiac cycle calibration data

Fig. 4.1 depicts the volume curve over the heart phase for the left (LV) and right (RV) ventricle for pig P2 obtained from segmenting its motion-CT at day of life 40. The measured heart rate (HR) during this CT data collection was 90 beats per minute.

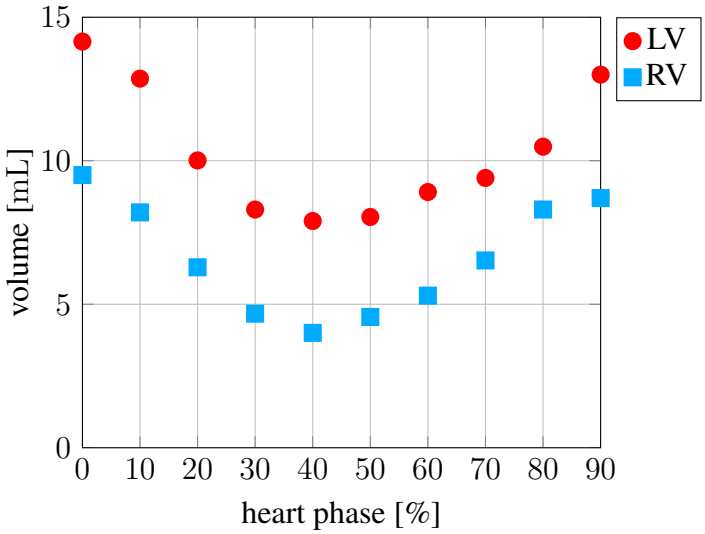

Abbildung 4.1.: Left and right ventricular volume segmented over a cardiac cycle at day of life 40 for pig P2. At 100%, the value equals the volume at 0%.

At 0%, corresponding to the R-wave, the maximal volume, i.e., the EDV, is observed. Subsequently, systole begins, leading to blood ejection and a resulting decrease in volume. At 40%, the minimal volume, i.e., the ESV, is reached. Diastole starts, leading to a gradual increase in volume. Due to the periodic nature of the cardiac cycle, 100% corresponds to 0%.
As explained in Sec. 1.2, the stroke volume (SV) is defined as the difference between the EDV and the ESV, see Eq. (1.1). In this case, the SV of the left ventricle is around $6.67\ \mathrm{mL}$ and for the right ventricle approximately $5.83\ \mathrm{mL}$. Note that these values are slightly different due to variations in the workload and function of each ventricle. In a healthy cardiovascular system, the stroke volume of both ventricles balances out over time to ensure adequate blood flow throughout the body. However, minor differences in stroke volume are normal and compensated for by the body's regulatory mechanisms. Additionally, it's important to consider the segmentation bias, which influences the computed volumes. The SVs for pigs P1-P6 from day of life 40 to 80 are depicted in App. D.1 in Fig. D.1.
To calibrate the cardiac cycle evaluation for these heart geometries, pressure over time curves within the vascular system are necessary. However, in this study no pressure measurements are available. Therefore, the volume data obtained from segmentation are used as a basis to search

for suitable pressure data curves of human children in the literature, which are considered as a substitute. This literature data will then be used to calibrate all presented models. The process to find the according literature is explained below. It's important to note that there might be physiological differences; however, the focus remains on the calibration process methods.
In general, the pressure data is often provided in correlation with age, such that the strategy involves an indirect comparison. First, the volume data is compared to the body surface area (BSA) for human children. A LV EDV value of 14.15 mL corresponds to a BSA value of approximately 0.4617 m^2, while 25 mL is roughly equivalent to a BSA value of 0.6166 m^2. Similarly, an RV EDV value of 9.4 mL corresponds to a BSA of around 0.4820 m^2, and 20 mL to approximately 0.6328 m^2 [17, 52, 92]. Second, the BSA values are compared to corresponding age groups. For a BSA value of 0.4617 m^2, the estimated age is approximately 12 months, and a value of 0.6166 m^2 corresponds to about 24 months [111, 137]. According to [43], at this age, the left ventricular pressure is around 85 to 100 mmHg, and the HR is around 80 to 150 beats per minute. Fig. 4.2 shows the resulting pressure curves with a HR of 90 beats per minute. On the left, the left ventricular pressure $\tilde{p}_{\mathrm{v}}^{\ell}$ and the aortic pressure $\tilde{p}_{\mathrm{ar}}^{\mathrm{sys}}$ are depicted. On the right, the right ventricular pressure $\tilde{p}_{\mathrm{v}}^{r}$ and the pulmonary pressure $\tilde{p}_{\mathrm{ar}}^{\mathrm{pul}}$ is shown. All measured quantities presented in this work are denoted with a tilde ($\tilde{\bullet}$).

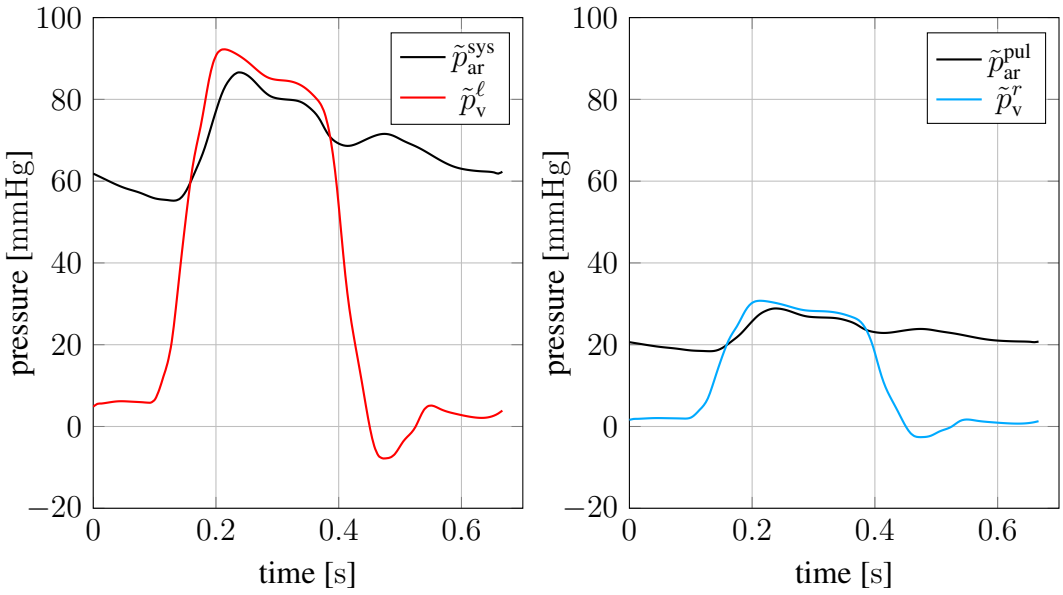

Abbildung 4.2.: Artificial pressure over time curves for the left and right heart.

4.1.2. Growth mechanics calibration data

The left and right ventricular EDVs for pigs P1-P6 from the day of life 40 to 80 are depicted in Fig. 4.3. A value of zero is assigned whenever a measurement is unavailable.
At day of life 40, the mean left ventricular volume is observed to be the lowest at 12 mL with a standard deviation of 2.35 mL. Note that as time progresses, the volumes increase, but the trend is not strictly linear. For instance, from the day of life 40 to 50, the mean left ventricular volume

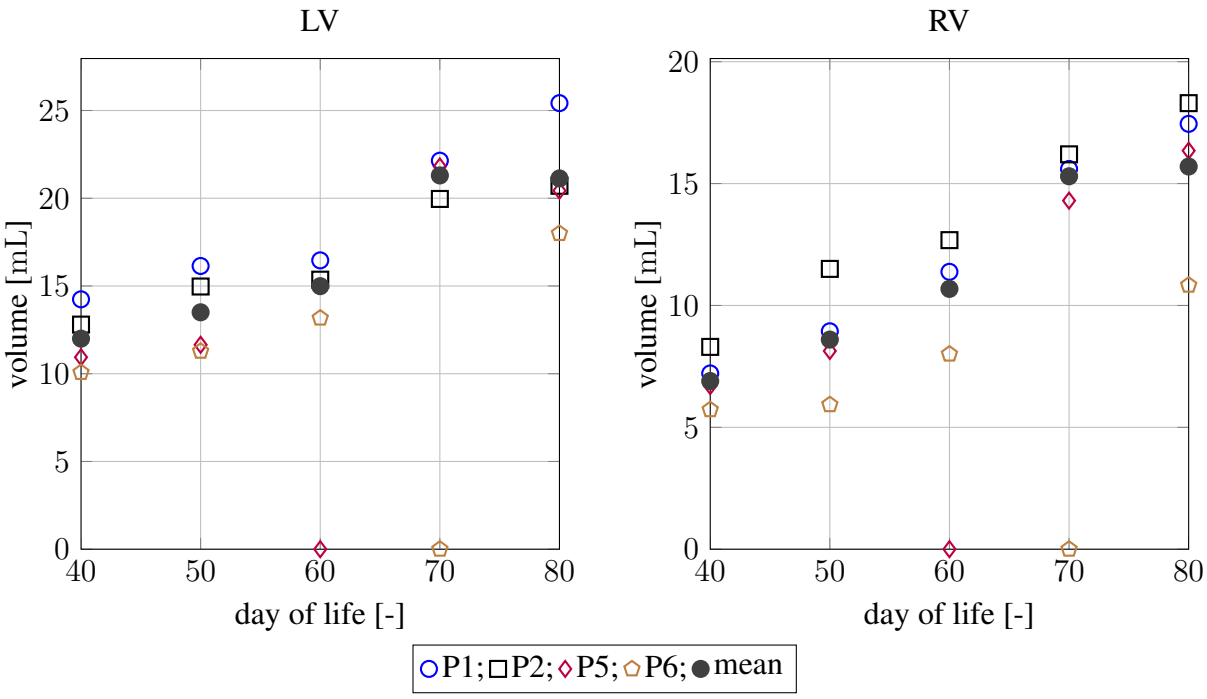

Abbildung 4.3.: Left and right ventricular EDVs over lifetime. A value of zero means that the measurement at that point in time is not available. To calculate the mean value, any values of zero are omitted from the computation.

increases by around $1.5\ \mathrm{mL}$, whereas from the day of life 60 to 70, the growth is around $6.3\ \mathrm{mL}$. A similar behavior is observed for the right ventricle.

In Fig. 4.4, the CT images, the segmentations, and the resulting .stl shapes for pig P2 from the day of life 40 to 80 are shown. Similar to Fig. 4.3, a volume increase from the day of life 40 to 80 is observed.

To calibrate the growth model presented in Sec. 3.2, the first step involves aligning the CT images. However, the alignment of consecutive cardiac images is inherently challenging due to the patient variability in positioning during CT scans, leading to both rotational and translational effects. To address this problem, stable reference points within the CT scans emerge as a potential solution for defining a unique alignment. Anatomical landmarks such as AV, MVP, and LVB, introduced in Sec. 3.1.1, serve as promising candidates for stable reference points. However, identifying these points consistently is challenging due to the image quality and the segmentation process noise, leading to the potential persistence of rigid body mode effects.
Ideally, growth as a biological phenomenon should be characterized without the interference of rigid body motions. To address this concern, the surface matching framework, detailed in Sec. 2.4, is employed to align the resulting geometries. This process is presented in Sec. 4.4. Before patient-specific cardiac growth is discussed, first, the conventional, patient-agnostic approach of computing a representative heart shape with the atlas construction method is presented in the following section.

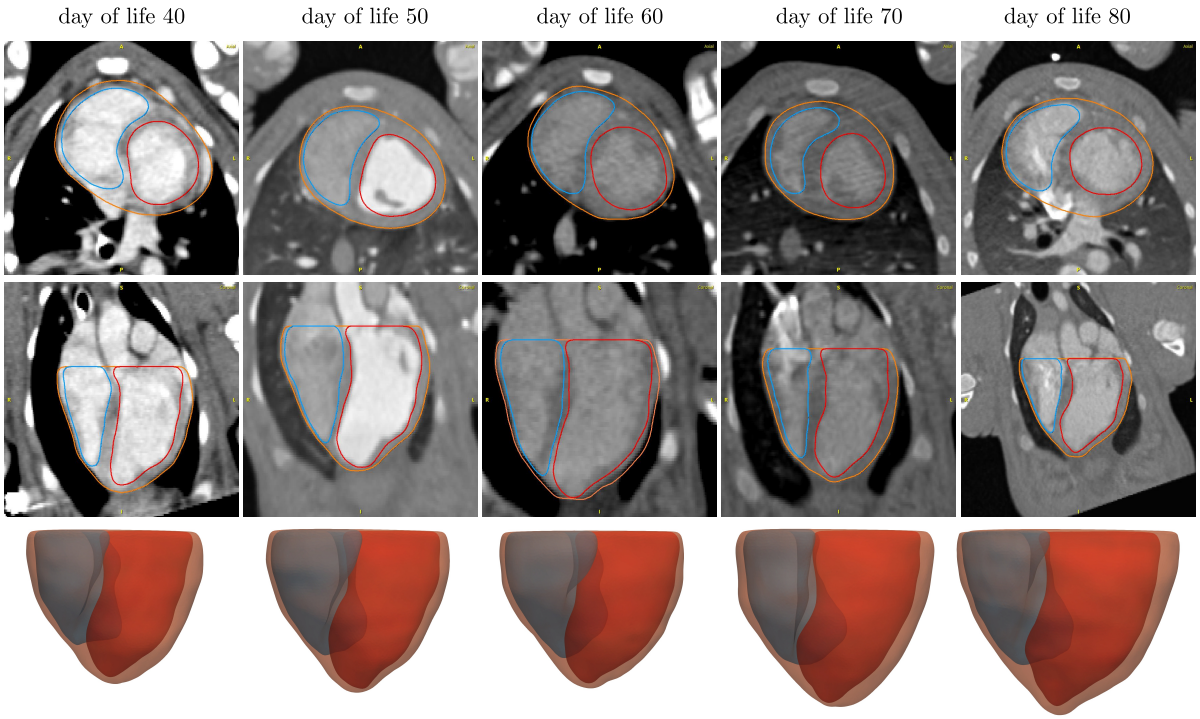

Abbildung 4.4.: Segmented 80% diastolic state of the heart of pig P2 from day of life 40 to 80.

4.2. Atlas computation

In this section, the application of the atlas construction method from Sec. 2.4.2 is presented. The aim is to find a representative heart shape of the epicardial surface of the heart geometries for pigs P1 to P6 at day of life 40. In the following, in Sec. 4.2.1, the problem setup is outlined. Subsequently, in Sec. 4.2.2, the results are shown and discussed in Sec. 4.2.3.

4.2.1. Problem setup and parameter setting

Fig. 4.5 depicts the epicardial surfaces for all six pigs at day of life 40. These shapes are denoted by $\mathcal{S}^i$ with $i \in \{1, ..., n_{\text{Sh}} = 6\}$. The initial alignment is performed using the AV, MVP, and LVB as their individual coordinate system as explained in Sec. 3.1.1. Afterward, the shapes are translated to their center of mass, establishing it as the origin.
The objective is to find an atlas shape $\mathcal{A}$ that captures the key features within the given data set. Additionally, the kinematic energy required to align and transform the atlas shape to match each surface $\mathcal{S}^i$ is minimized, see Eq. (2.143). As outlined in Alg. 2, an initial atlas with surface points $\boldsymbol{x}_0^{\mathcal{A}}$ and control points $\boldsymbol{c}_0^{\mathcal{A}}$ has to be chosen. In this case, the epicardial surface of pig P1 is chosen as initial atlas $\mathcal{A}_0 = \mathcal{S}^{\text{P1}}$. Furthermore, within the atlas construction problem, a surface matching problem is solved starting from the atlas shape to each given surface $\mathcal{S}^i$. Hence, the kernel widths σ_W, σ_V, the regularization parameter σ, and initial conditions for the momenta $\boldsymbol{\alpha}_0$ have to be chosen.
The varifold kernel width σ_W needs to be sufficiently large to maintain sensitivity to variations in the relative position between meshes and to smooth noise. Too small values may lead to

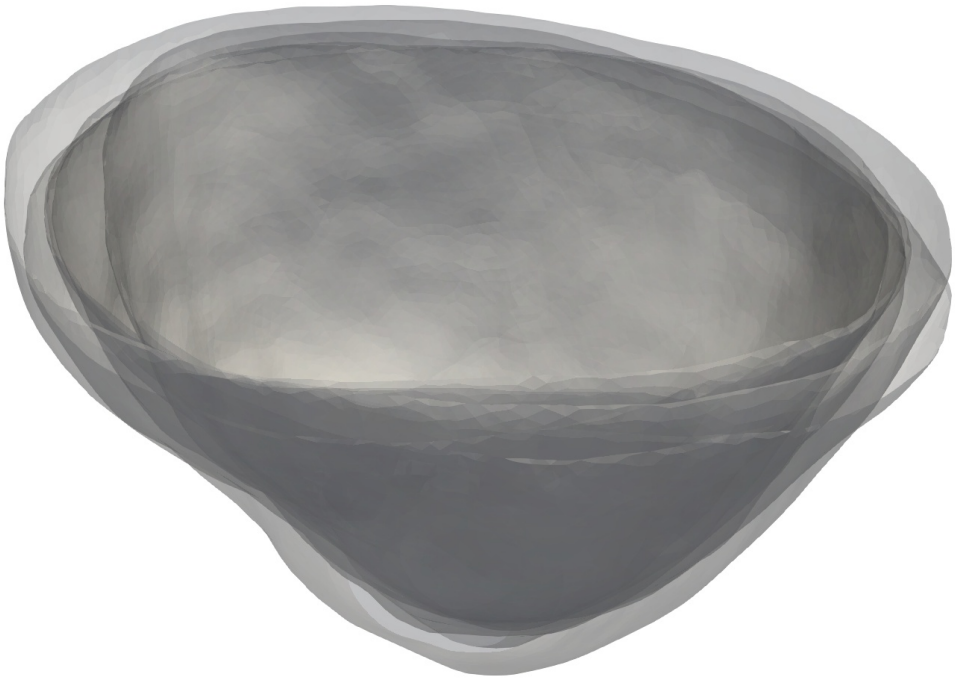

Abbildung 4.5.: Epicardial surfaces for all six pigs at day of life 40.

distorted shapes or artifacts. However, large values are prone to homogenizing all shapes and thereby compromising the accuracy of the matching process [38].
The deformation kernel width σ_V should be comparable with the expected scale of shape variations. Deformations are primarily constructed by integrating translations within neighborhoods characterized by a radius of σ_V. Smaller values causes the model to account for more distinct local variations, resulting in less effective integration of information from larger anatomical regions. Conversely, larger values tend to favor a model that emphasizes minimal deformation or limited local variations [38].
As the initial conditions, the momenta $\boldsymbol{\alpha}_0$ are initialized to zero for each surface matching problem. Additionally, the dense mode is employed, signifying $\boldsymbol{c}(t) = \boldsymbol{x}(t)$.
The adjoint equations Eq. (2.141) and Eq. (2.142) are solved using the one-step-θ method with $\theta = 1$ and five pseudo time steps. The resulting optimization problem is solved using the L-BFGS method, see App. A.5.
All relevant parameters used for this computation are provided in Tab. 4.1 and will be discussed in Sec. 4.2.3.

4.2.2. Numerical results

The atlas shape consists of $14,037$ surface points. The dimensions of the problem span from -26.443 to 24.4686 mm along the x-axis, -22.4883 to 22.1572 mm along the y-axis, and -16.6587 to 18.4174 mm along the z-axis. In each iteration of the atlas construction, six surface matching problems are solved together with the computation of the gradients. Therefore, the implementation is optimized for efficiency and computational performance through parallelization. Each of the six independent surface matching problems is solved on a dedicated core,

Tabelle 4.1.: Overview of the atlas problem parameters.

atlas constructing parameter			
parameter	symbol	value	unit
varifold kernel width	σ_V	3	$[\mathrm{mm}]$
deformation kernel width	σ_W	1	$[\mathrm{mm}]$
regularization	σ	$1.0 \cdot 10^{-3}$	$[\mathrm{mm}^2]$
time step	Δt	0.2	[s]
initial momenta	$\boldsymbol{\alpha}(t=0)$	0	[-]
initial atlas shape	$\mathcal{A}_0$	$\mathcal{S}^{\mathrm{P1}}$	[-]

allowing for simultaneous processing. The optimization stopped after 15 iterations where the relative change in the gradient norm was below 1%, and the obtained result is illustrated in Fig. 4.6. The resulting atlas shape $\mathcal{A}$ is shown in red, and the initial shapes $\mathcal{S}^i$ are depicted in gray. In the beginning, the objective function value was $2.3103 \cdot 10^5$, and after 15 iterations, the value dropped to $4.12 \cdot 10^4$.

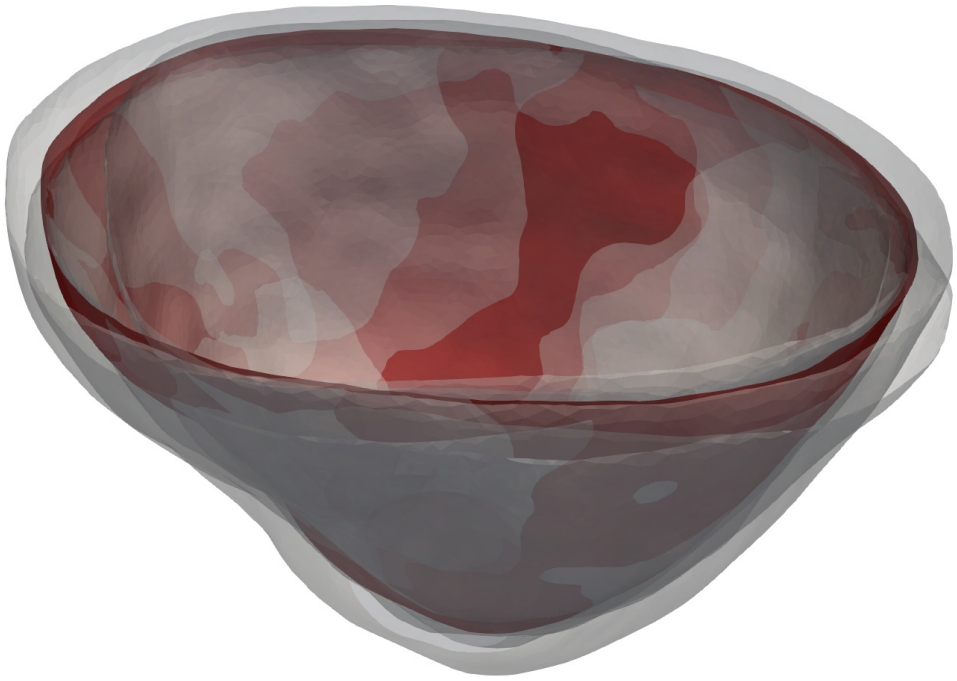

Abbildung 4.6.: Solution of the atlas construction problem. The given epicardial surfaces are depicted in gray, whereas the resulting atlas shape is shown in red.

4.2.3. Discussion

The atlas construction problem is developed to analyze a given data set from medical imaging. The primary objective of this method is to estimate a template shape that serves as a representative model for the anatomical structures under examination. This method is robust to noise and capable of smoothing out imperfections within the anatomical structures.

The specific selection of the parameters can be intricate, particularly the choice of kernel widths. To identify optimal parameters, a recommended approach involves solving a series of surface matching problems to determine suitable kernel widths. While this iterative process can be time-consuming, it is indispensable since the kernel widths determine the accuracy of the model. Notably, the kernel width σ_V is important as with larger values, the template shape captures less variations and gets smoother, whereas, for small values, the template shape captures finer details [38].
To enhance the performance, the independent surface matching problems were solved in parallel. However, the dense mode, where the control points are equal to the surface points, resulted in a high-dimensional feature space, leading to computational inefficiency due to increased dimensionality. This limitation can be addressed through the incorporation of control points. The selection and significance of these control points are extensively discussed in [36].
In this thesis, the given data set consisted of six shapes, and one atlas shape was computed. A promising extension could be to modify the method such that in case of a larger data set, the method estimates n template shapes. These multiple atlas shapes should be different from each other, but all represent distinct subsets of the given data set. The advantage of this approach would be that the user does not have to cluster the data set manually beforehand. This is particularly interesting because users may lack insight into optimal clustering strategies in certain cases.
The atlas shape can be used as a reference heart shape for a generic medical treatment, particularly when a patient-specific treatment is unfeasible. However, the primary goal is patient-specific treatment. Therefore, in the following section, the calibration process for the beating heart model is outlined, serving as the basis for the cardiac growth models.

4.3. 3D-0D heartbeat model calibration

In this section, the patient-specific evaluation of the cardiac cycle mechanical model is presented. Therefore, the parameters of the 3D and 0D models are estimated based on the measurements from Sec. 4.1. In Sec. 4.3.1, the calibration of the flow network parameters is outlined. Since the 3D-0D coupled problem is used as a forward model to calibrate the parameters of the 3D model, its solution process is explained in Sec. 4.3.2. Subsequently, the calibration procedure for the active stress model is presented in Sec. 4.3.3. Finally, the calibrated cardiac cycle evaluation is shown in Sec. 4.3.4 and discussed in Sec. 4.3.5.

4.3.1. Flow network calibration

The flow network, presented in Fig. 3.6, consists of four different windkessel models. The windkessel models are connected in series and measurements have been identified between each windkessel model. Thus, the calibration of the windkessel parameters is performed individually. In contrast to considering the full coupled model as the forward problem to calibrate all relevant parameters, this allows for a dimensionally-reduced, robust, computationally efficient, and well-posed inverse problem formulation. It is important to note, that all flow or volume based measurements are derived from the motion-CT images and the pressure data sets are artificial as

explained in Sec. 4.1.1. Furthermore, all measured quantities presented in the previous section are denoted with a tilde ($\tilde{\bullet}$) and are depicted with dashed lines.
In the following, the calibration process for each windkessel model in the flow network is shown.

4-element windkessel model

Within a 4-element windkessel model, there are four parameters to calibrate, see Eq. (2.46). In the case of the systemic arterial system, the parameters are $L_{\text{ar}}^{\text{sys}}$, $R_{\text{ar}}^{\text{sys}}$, $Z_{\text{ar}}^{\text{sys}}$ and $C_{\text{ar}}^{\text{sys}}$. However, the inertance $L_{\text{ar}}^{\text{sys}}$ and the resistance dependent impedance $Z_{\text{ar}}^{\text{sys}}$ are not optimized. They have only a minor impact on the solution, and according to literature, these parameters exhibit only negligible variations [144, 157]. Their values are listed in Tab. 3.4.
Fig. 4.7 shows the calibration workflow, where on the left side, the measured left ventricular outflow $\tilde{q}_{\text{v,out}}^{\ell}$ enters the windkessel model as input from the segmentation and the aortic pressure $\tilde{p}_{\text{ar}}^{\text{sys}}$, depicted on the right, is the target output quantity.

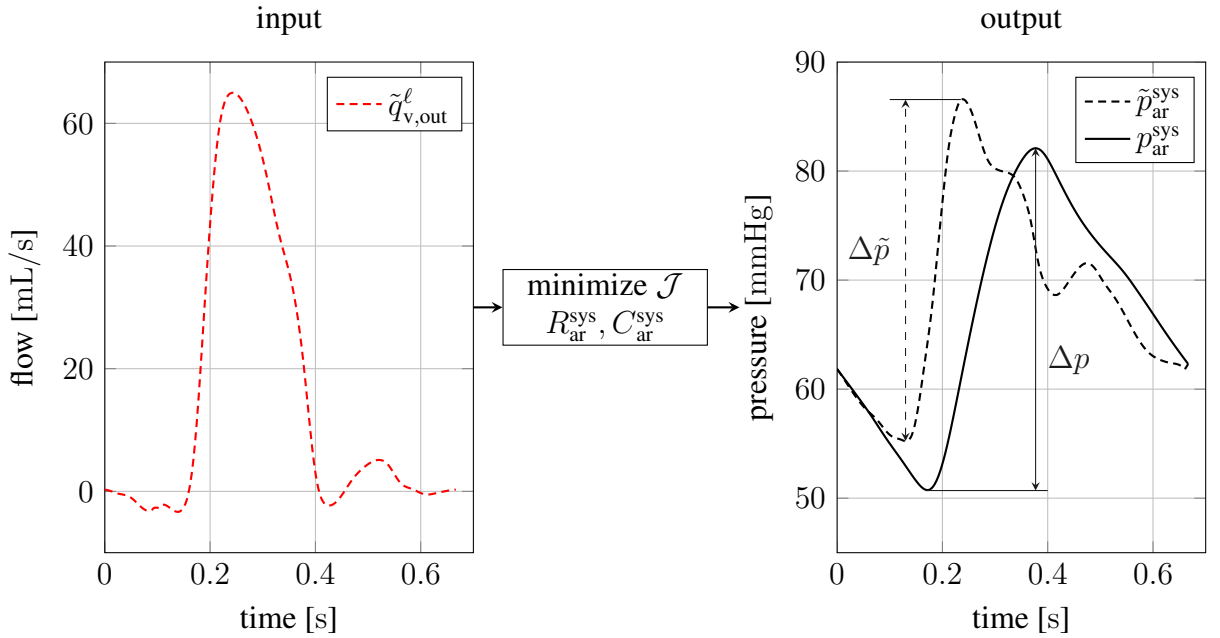

Abbildung 4.7.: Calibration of the systemic arterial windkessel model. The input is the measured left ventricular outflow $\tilde{q}_{\text{v,out}}^{\ell}$. The target output is the measured aortic pressure $\tilde{p}_{\text{ar}}^{\text{sys}}$. The optimization parameters are the resistance $R_{\text{ar}}^{\text{sys}}$ and the capacitance $C_{\text{ar}}^{\text{sys}}$. The optimized pressure curve $p_{\text{ar}}^{\text{sys}}$ is shown on the right.

For the calibration, the pressure pulse is used [143]. Here, the difference between the measured and computed pressure pulse is minimized. The pressure pulse is defined as the difference between the maximal and minimal value of the pressure curve. For example, the measured pressure pulse is given by

$$\Delta\tilde{p} = \max(\tilde{p}_{\text{ar}}^{\text{sys}}) - \min(\tilde{p}_{\text{ar}}^{\text{sys}}). \tag{4.1}$$

Another objective in the cardiac cycle computation is reaching the periodic state. Therefore, the windkessel models require periodicity, i.e., the last value of the computed pressure has to be

equal to its initial value, or in this case, the previous value of the computed pressure has to be similar to the measured pressure value. These two requirements lead to the following scalar-valued objective function

$$\min_{R_{\text{ar}}^{\text{sys}},C_{\text{ar}}^{\text{sys}}} \mathcal{J} = \min_{R_{\text{ar}}^{\text{sys}},C_{\text{ar}}^{\text{sys}}} \left(\underbrace{\left[\frac{|\Delta\tilde{p} - \Delta p|}{\Delta\tilde{p}} \right]}_{\text{pressure pulse}} + \underbrace{\frac{|p_{\text{ar}}^{\text{sys}} - \tilde{p}_{\text{ar}}^{\text{sys}}|}{\tilde{p}_{\text{ar}}^{\text{sys}}}}_{\text{periodicity}} \Bigg|_{T_{\text{cycl}}} \right). \tag{4.2}$$

Note that this objective function does not address differences in extreme values, as it is not crucial for this model. The primary emphasis here is on accurately capturing the pressure pulse, which serves as the main driver. To optimize the resistance and capacitance parameters, an *Interior-Point* optimization method is used [19]. The corresponding ODE of the 4-element windkessel model is solved using an explicit Runge-Kutta method for nonstiff ODEs [34].
The optimized systemic parameters are listed in Tab. 4.2 and the resulting curve is shown in Fig. 4.7 on the right. Note that a time shift between the measured and computed curve is observed. This time discrepancy results from the challenge to align the measurements from the segmentation with the artificial pressure data. However, the focus is on approximating the pressure pulse together with the periodicity, and hence, the time shift between the curves is negligible.
The same optimization method is used for the pulmonary arterial system. Here, the right ventricular outflow $\tilde{q}_{\text{v,out}}^{r}$ is used as input, whereas the pulmonary pressure $\tilde{p}_{\text{ar}}^{\text{pul}}$ is set as target output quantity. Similar to the systemic arterial system, the inertance $L_{\text{ar}}^{\text{pul}}$ and the resistance dependent impedance $Z_{\text{ar}}^{\text{pul}}$ are not optimized. Their values are listed in Tab. 3.4. The optimization results for the pulmonary arterial system parameters are listed in Tab. 4.2.

2-element windkessel model

Within a 2-element windkessel model, there are two parameters to calibrate, see Eq. (2.45). In the case of systemic venous circulation, these parameters are $R_{\text{ven}}^{\text{sys}}$ and $C_{\text{ven}}^{\text{sys}}$. The estimation of these parameters relies on the dependencies identified in [157], as presented in Tab. 3.4. The results for the systemic venous circulation and the pulmonary venous circulation are listed in Tab. 4.2.

Valve model

Within the valve model, there are two parameters to calibrate, see Eq. (2.48). In the case of the aortic valve, these parameters are $R_{\text{v,out}}^{\ell,\text{min}}$ and $R_{\text{v,out}}^{\ell,\text{max}}$. The maximal resistance value serves as a lower boundary, regulating the backflow through the valve. Assuming a healthy valve with no backflow, this value is set to a high value based on the work in [62] and remains uncalibrated. The resistance values for the mitral and tricuspid valves remain uncalibrated due to the absence of available measurements. These values are listed in Tab. 3.4.
The calibration workflow for the minimal resistance parameter is depicted in Fig. 4.8. Here, the measured left ventricular pressure $\tilde{p}_{\text{v}}^{\ell}$ and the measured aortic pressure $\tilde{p}_{\text{ar}}^{\text{sys}}$ are used as inputs, whereas the measured left ventricular outflow $\tilde{q}_{\text{v,out}}^{\ell}$ is used as target output quantity.

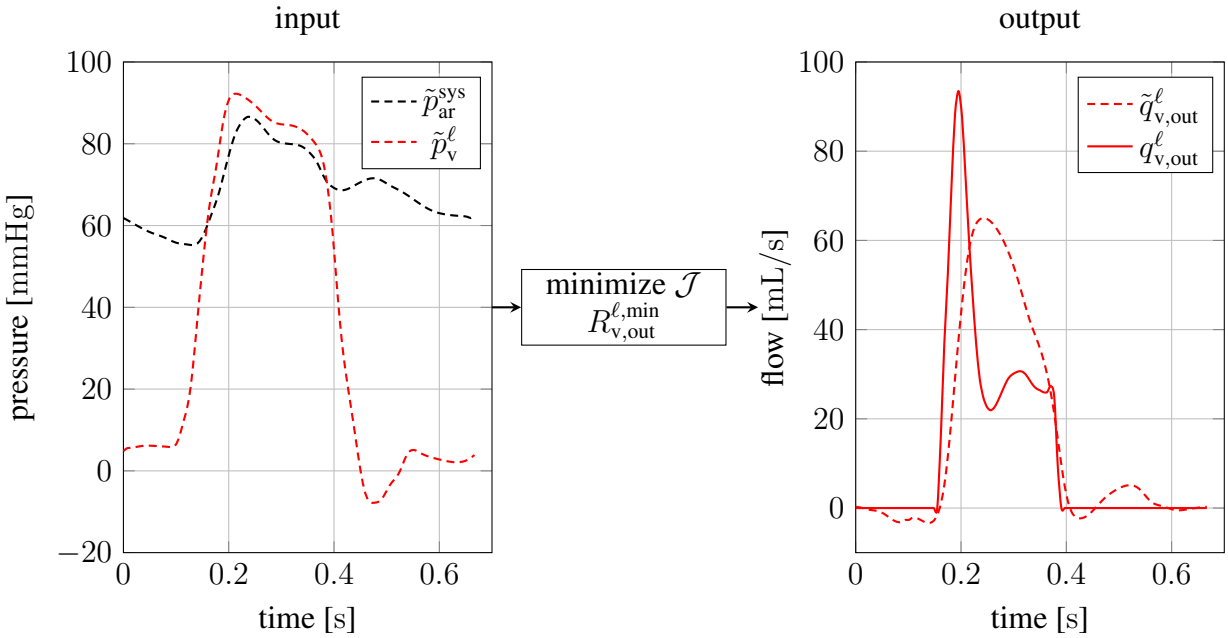

Abbildung 4.8.: Calibration of the aortic valve model. The input are the measured left ventricular pressure $\tilde{p}^{\ell}_{\mathrm{v}}$ and the aortic pressure $\tilde{p}^{\mathrm{sys}}_{\mathrm{ar}}$. The target output is left ventricular outflow $\tilde{q}^{\ell}_{\mathrm{v,out}}$. The optimization parameter is the minimal valve resistance $R^{\ell,\min}_{\mathrm{v,out}}$. The optimized flow curve $q^{\ell}_{\mathrm{v,out}}$ with respect to the area under the curve is shown on the right.

The calibration objective ensures that the computed flow through the valve is equal to the measured flow. The resulting scalar-valued objective function reads

$$\min_{R^{\ell,\min}_{\mathrm{v,out}}} \mathcal{J} = \min_{R^{\ell,\min}_{\mathrm{v,out}}} \left(\int_0^{T_{\mathrm{cycl}}} \frac{\left| \tilde{q}^{\ell}_{\mathrm{v,out}} - q^{\ell}_{\mathrm{v,out}} \right|}{q^{\ell}_{\mathrm{v,out}}} \, \mathrm{d}t \right). \tag{4.3}$$

Similar to the 4-element windkessel model, this objective function does not consider differences in extreme values, as only the integral value is considered important. The optimization is performed using an Interior-Point optimization and the result is listed in Tab. 4.2. The same optimization method is used for the pulmonary valve. Here, the right ventricular pressure $\tilde{p}^{r}_{\mathrm{v}}$ and the measured pulmonary pressure $\tilde{p}^{\mathrm{out}}_{\mathrm{ar}}$ are used as inputs, whereas the measured right ventricular outflow $\tilde{q}^{r}_{\mathrm{v,out}}$ is used as target output quantity. This optimization result is listed in Tab. 4.2.

Elastance model

Within the elastance model, there are three parameters to calibrate, see Eq. (2.50). In the case of the left atrium, these parameters are $V^{\ell}_{\mathrm{at,u}}$, $E^{\ell}_{\mathrm{at,min}}$ and $E^{\ell}_{\mathrm{at,max}}$.
According to the literature [29], the pressure within the left atrium typically ranges from 5 to 9 mmHg, while in the right atrium, it varies between 0 to 4 mmHg. Eq. (3.37) at minimal

activation, i.e., $y(t) = 0$ and at maximal atria activation, i.e., $y(t) = 1$, yields

$$p_{\text{at,min}} = E_{\max}(V_{\text{at,min}} - V_{\text{at,u}}), \tag{4.4}$$
$$p_{\text{at,max}} = E_{\min}(V_{\text{at,max}} - V_{\text{at,u}}), \tag{4.5}$$

where the minimal and maximal atrial volume results from segmentation. For the left atrium these values are $V^{\ell}_{\text{at,min}} = 4.99\,\text{mL}$ and $V^{\ell}_{\text{at,max}} = 5.4\,\text{mL}$, whereas for the right atrium the values result in $V^{r}_{\text{at,min}} = 6.2\,\text{mL}$ and $V^{r}_{\text{at,max}} = 9.5\,\text{mL}$. Note that at a maximal atria activation, the volume reaches its minimum. The unstressed volumes are estimated based on [62] and are set to $V^{\ell}_{\text{at,u}} = 4.5\,\text{mL}$ and $V^{r}_{\text{at,u}} = 5.5\,\text{mL}$ for the left and right atrium, respectively.
With these values and Eq. (4.4) and Eq. (4.5), the elastance values for the left and right atria can be estimated and the results are listed in Tab. 4.2.

Tabelle 4.2.: Optimized flow network parameters.

symbol	value	unit
4-element windkessel model		
$R^{\text{sys}}_{\text{ar}}$	$9.255 \cdot 10^{-4}$	$[\text{kPa s/mm}^3]$
$C^{\text{sys}}_{\text{ar}}$	700	$[\text{mm}^3/\text{kPa}]$
$R^{\text{pul}}_{\text{ar}}$	$8.228 \cdot 10^{-5}$	$[\text{kPa s/mm}^3]$
$C^{\text{pul}}_{\text{ar}}$	800	$[\text{mm}^3/\text{kPa}]$
2-element windkessel model		
$R^{\text{sys}}_{\text{ven}}$	$1.6456 \cdot 10^{-4}$	$[\text{kPa s/mm}^3]$
$C^{\text{sys}}_{\text{ven}}$	21000	$[\text{mm}^3/\text{kPa}]$
$R^{\text{pul}}_{\text{ven}}$	$8.228 \cdot 10^{-5}$	$[\text{kPa s/mm}^3]$
$C^{\text{pul}}_{\text{ven}}$	2000	$[\text{mm}^3/\text{kPa}]$
valve model		
$R^{\ell,\text{min}}_{\text{v,out}}$	$2.014 \cdot 10^{-5}$	$[\text{kPa s/mm}^3]$
$R^{r,\text{min}}_{\text{v,out}}$	$3.02 \cdot 10^{-5}$	$[\text{kPa s/mm}^3]$
elastance model		
$E^{\ell}_{\text{at,min}}$	$1.5 \cdot 10^{-4}$	$[\text{kPa/mm}^3]$
$E^{\ell}_{\text{at,max}}$	$3 \cdot 10^{-4}$	$[\text{kPa/mm}^3]$
$E^{r}_{\text{at,min}}$	$7 \cdot 10^{-6}$	$[\text{kPa/mm}^3]$
$E^{r}_{\text{at,max}}$	$9 \cdot 10^{-5}$	$[\text{kPa/mm}^3]$

4.3.2. Numerical parameters

The heart model is discretized using 4-node linear displacement-based tetrahedral finite elements with an edge length of approximately $1.5\,\text{mm}$. This results in $50,642$ finite elements with $11,501$ nodes and $14,503$ DOFs. A graphical representation of the finite element, together with a spatial resolution study, is given in the App. D.2 in Fig. D.2. As described in Alg. 3, the first step is prestressing the reference configuration. The ventricular pressure load is applied in 10 steps using a PTC enhanced Newton-Raphson nonlinear solver with initial value $k_0^{\text{ptc}} = 3.33$,

see Sec. 2.2.4. Subsequently, the computation of the cardiac cycle starts. As a model assumption, the heart rate is set to 90 beats per minute, and thus, the duration of the cardiac cycle is $T_{\text{cycl}} = \frac{2}{3}$ s. This results in an atrial activation time of $\Delta t_{\text{act}} = 0.4 \cdot T_{\text{cycl}} = 0.266$ s, see Tab. 3.4. The ventricular contraction starts at $t_{\text{contr}} = 0.2 \cdot T_{\text{cycl}} = 0.133$ s and ventricular relaxation starts at $t_{\text{relax}} = 0.53 \cdot T_{\text{cycl}} = 0.35$ s, see Tab. 3.1. The temporal discretization of the flow network is done using the one-step-θ scheme with $\theta = 0.5$, see Sec. 2.2.3. Temporal discretization of the structural model is performed by the generalized-α scheme using 1000 time steps of size $\frac{2}{3000}$ s and $\rho_\infty = 0.8$. The resulting linear block systems, see Eq. (3.46), are solved iteratively using a parallel GMRES method implemented in the software Trilinos [57]. To further improve convergence, a SIMPLE type preconditioning [40] is added for the full block system, while algebraic multigrid preconditioning [127] is applied to the structural block. The model parameters for the flow network are taken from Tab. 3.4 unless redefined in Sec. 4.3.1. The parameters for boundary conditions are taken from Tab. 3.2. The active stress model parameters are listed in Tab. 3.1. The tolerance of the cycle error criterion (CER) is set to $\varepsilon_{\text{tol}} = 0.01$, see Eq. (3.51). This value is primarily chosen based on experience, as a 1% relative change is sufficient to consider the state as periodic.
Relevant parameters are provided in Tab. 4.3.

Tabelle 4.3.: Overview of the numerical parameters for the 3D-0D coupled problem.

cardiac cycle evaluation parameter			
parameter	symbol	value	unit
cardiac cycle duration	T_{cycl}	$\frac{2}{3}$	[s]
atrial activation time	Δt_{act}	0.266	[s]
ventricular contraction time	t_{contr}	0.133	[s]
ventricular relaxation time	t_{relax}	0.35	[s]
time step size	Δt	$\frac{2}{3000}$	[s]
first-order time discretization	θ	0.5	[-]
time discretization dissipation factor	ρ_∞	0.8	[-]
cycle error criterion	ε_{tol}	0.01	[-]

4.3.3. Active stress calibration

Within the active stress model, there are three parameters to calibrate for each ventricle, see Eq. (3.4). These parameters are the contractility σ_0 and upstroke rate $\alpha_{\max}$ and relaxation rate $\alpha_{\min}$. The active stress functions for the left and right ventricles are calibrated by minimizing the difference between the measured and computed volumes. The upstroke rate $\alpha_{\max}$ solely affects the active stress curve between t_{contr} and t_{relax}. In contrast, the relaxation rate $\alpha_{\min}$ influences the curve from t_{relax} until the end of the cardiac cycle. The contractility σ_0 affects the maximal contraction, and thus, the minimal volume, see Fig. 3.5.
To calibrate these parameters, three measured volumes are used here. The first measured volume is obtained at $t_{\text{contr}}^{\text{mid}} = 0.24$ s, defined as the midpoints between t_{contr} and t_{relax}. The second volume corresponds to the ESV at $t_{\text{contr}}^{\max} = 0.4$ s. The third volume is obtained during mid-

relaxation at $t^{\text{mid}}_{\text{relax}} = 0.55$ s. Based on these points, the scalar-valued objective function reads

$$\min_{\sigma_0^\ell, \alpha^\ell_{\max}, \alpha^\ell_{\min}} \mathcal{J} = \min_{\sigma_0^\ell, \alpha^\ell_{\max}, \alpha^\ell_{\min}} \left(\sum_i \frac{\left| \tilde{V}^\ell_{\text{v}} - V^\ell_{\text{v}} \right|}{\tilde{V}^\ell_{\text{v}}} \Big|_{t_i} \right), \qquad \text{with } t_i \in \{t^{\text{mid}}_{\text{contr}}, t^{\text{max}}_{\text{contr}}, t^{\text{mid}}_{\text{relax}}\}. \tag{4.6}$$

To optimize the parameters, a gradient descent algorithm is used in combination with a finite differences approach. Fig. 4.9 depicts the measured volumes as well as the final computed volume curve with optimized parameters for the left and right ventricles. Note that in the beginning, atrial contraction causes the volumes to increase before the contraction of the ventricles starts. The resulting parameters for the left and right ventricle are listed in Tab. 4.4.
Furthermore, the measured stroke volumes of $\tilde{\text{SV}}^\ell = 6.2$ mL and $\tilde{\text{SV}}^r = 5.5$ mL agree with the computed stroke volumes of $\text{SV}^\ell = 5.84$ mL and $\text{SV}^r = 5.23$ mL.

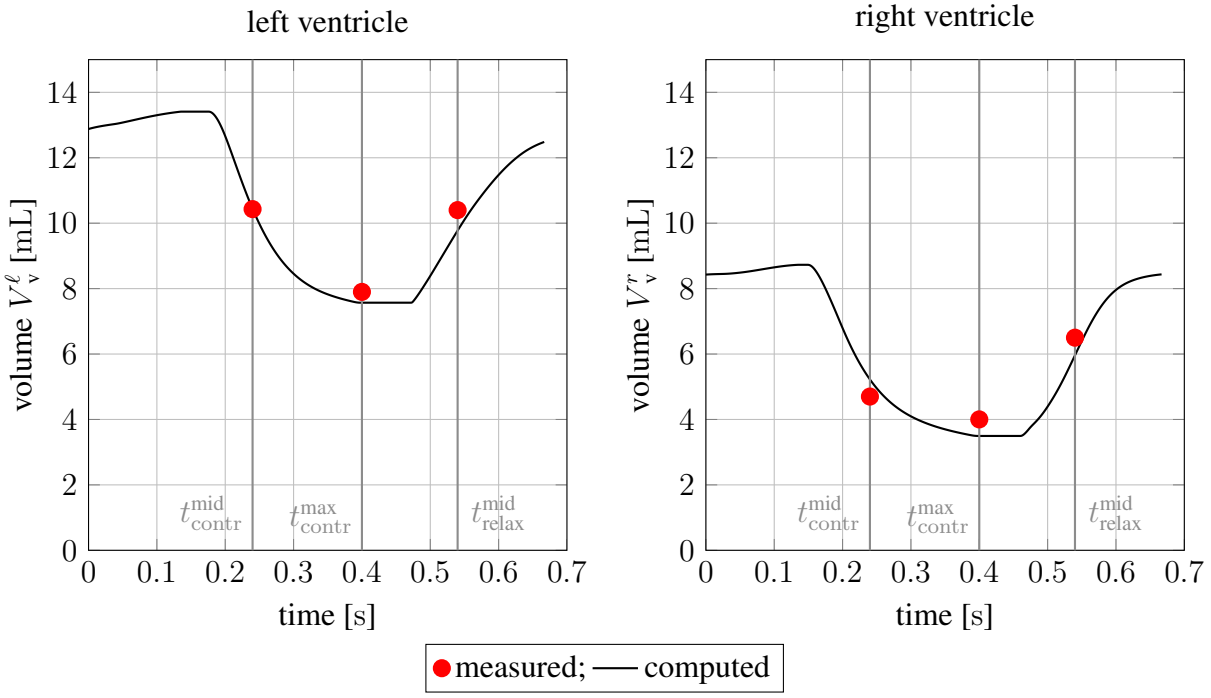

Abbildung 4.9.: Calibration of the active stress functions for the left and right ventricle.

Tabelle 4.4.: Optimized active stress parameters for the 3D-0D coupled problem.

symbol	value	unit
left ventricle		
σ^ℓ_0	60	[kPa]
$\alpha^\ell_{\min}$	-25	[1/s]
$\alpha^\ell_{\max}$	25	[1/s]

symbol	value	unit
right ventricle		
σ^r_0	55	[kPa]
$\alpha^r_{\min}$	-29	[1/s]
$\alpha^r_{\max}$	29	[1/s]

4.3.4. Patient-specific numerical results

The periodic state is computed using all stated parameters above, and it is reached after eight cardiac cycles, resulting in a CER $= 0.008406$.

The patient-specific periodic state flow network variables are depicted in Fig. 4.10. At time $t = 0$ s atrial contraction starts causing the atrial pressure to increase, see Fig. 4.10 (a) and (b). During this period, blood flows from the atria into the ventricles, see Fig. 4.10 (b) and (c). Atrial contraction ends at time $t = 0.133$ s and the atrioventricular valves close. Thereafter, isovolumetric contraction begins until the ventricular pressures surpass the aortic and pulmonary pressures, initiating ventricular ejection, see Fig. 4.10 (a) and (b). The ejected ventricular blood flow is depicted in Fig. 4.10 (c) and (d). At time $t = 0.4$ s, ventricular ejection ends, and the semilunar valves close since the ventricular pressure is below the aortic or pulmonary pressure. Subsequently, isovolumetric relaxation continues until time $t = 0.46$ s, where the ventricular pressure aligns with the atrial pressure again. The rest of the cardiac cycle is passive ventricular filling, see Fig. 4.10 (c) and (d).

Fig. 4.10 (e) depicts the volume-pressure curves over one cardiac cycle for the left and right ventricle. The integral of the area in a volume-pressure loop corresponds to the accomplished mechanical work of the ventricles.

Fig. 4.11 depicts the 3D structural model of the ventricular heart during one cardiac cycle. The initial configuration is shown at time $t = 0$ s. Thereafter, the mid ventricular contraction at time $t^{\text{mid}}_{\text{contr}} = 0.24$ s, the maximal contraction at time $t^{\text{max}}_{\text{contr}} = 0.4$ s and the mid relaxation at time $t^{\text{mid}}_{\text{relax}} = 0.55$ s configurations are depicted. Note that at time $t = T_{\text{cycl}}$, the final configuration resembles the initial configuration.

4.3.5. Discussion

The presented model was utilized to estimate a periodic state within a cardiac cycle. It couples a 3D structural model of the ventricular heart with a flow network accounting for the vascular system. The primary objective of this section was to calibrate the periodic state in a patient-specific setting. Therefore, various parameters need calibration.

The flow network consists of four windkessel models, which are connected in series. The arterial systemic and pulmonary circulation are represented by 4-element windkessel models, and the venous systemic and pulmonary systems are described by 2-element windkessel models. Heart valves are modeled using a diode element, and the behavior of the atria is approximated using an elastance model. As outlined in Sec. 4.1.1, the volume and flow based measurements are derives from the motion-CT images and the pressure data sets are identified from literature [17, 52, 92, 111, 137]. Hence, the parameters within each windkessel model were calibrated individually.

The calibration method was based on scalar-valued optimization, which is computationally efficient and robust. An Interior-Point optimization method, together with an explicit Runge-Kutta method for nonstiff ODEs, was used to optimize the parameters. The windkessel models are simple approximations of the vascular system and therefore, they cannot precisely replicate the prescribed pressure and flow curves, see Fig. 4.7 and Fig. 4.8. As the focus of this thesis was solely on the overall integral behavior of the vascular system, the used windkessel models yield accurate results such that this approximation is suitable. In cases where no measurements were

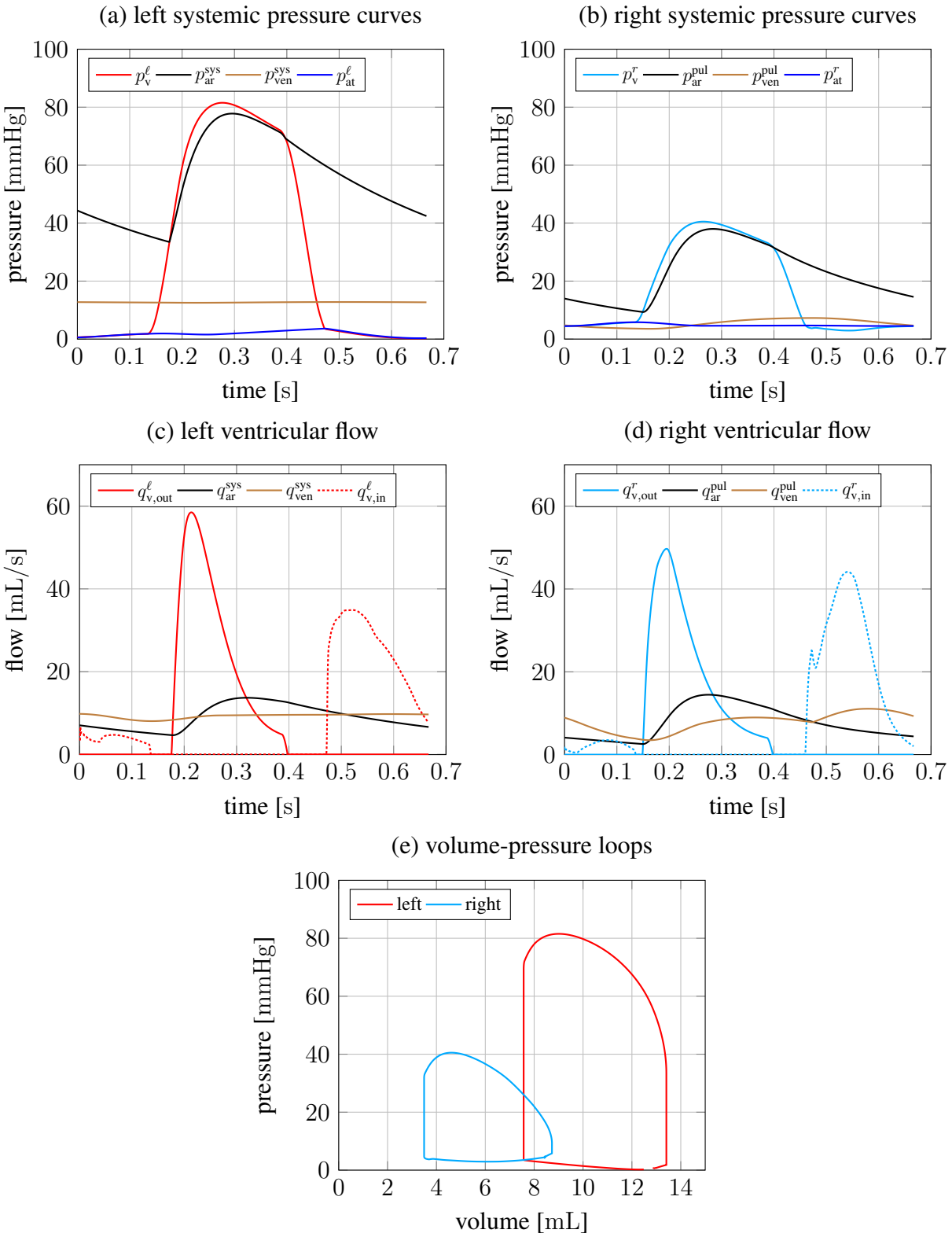

Abbildung 4.10.: Flow network state variables over one cardiac cycle.

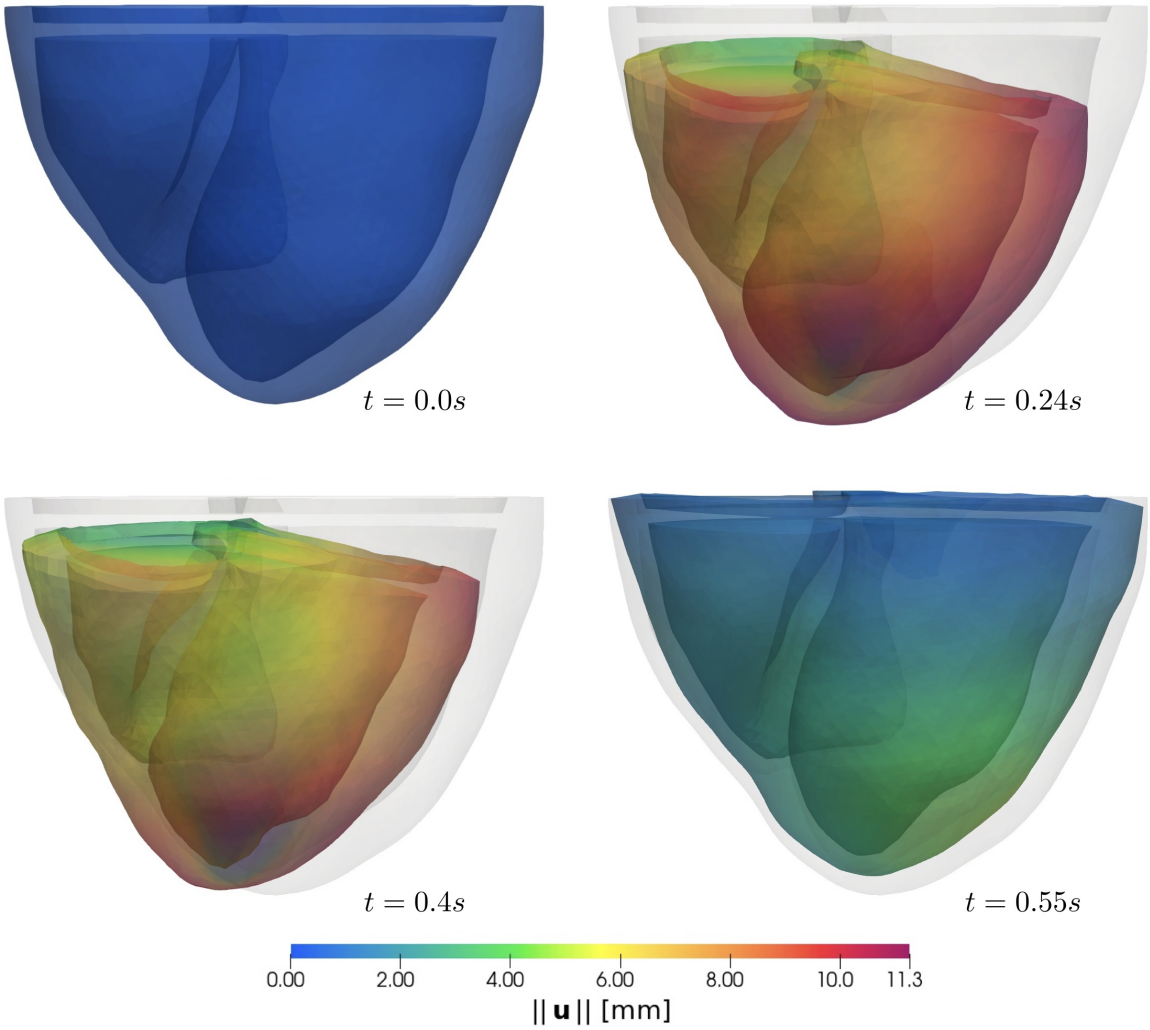

Abbildung 4.11.: Deformation of the heart over one cardiac cycle.

available, the parameters were estimated based on literature data [144, 157]. Generally, a higher quantity of measurements leads to improved calibration and more accurate results.

The 3D structural model of the ventricular heart was generated from CT images, as outlined in Sec. 3.1.1. Since this work focuses on ventricular contraction and ventricular growth, the atria and valves were not segmented but were approximated by the flow network. The fiber and sheet directions are established through generic and rule-based models and do not rely on patient-specific measurements. To improve accuracy and to attain a more physiologically accurate representation, methods presented in [8, 115] could be employed. The embedding tissue boundary conditions were also not calibrated but taken based on previous work in [62], as no measurements were available.

To approximate the already acting stresses and strains in the imaged configuration, prestressing based on the Modified Updated Lagrangian Formulation (MULF) was used, see Sec. 3.1.4. This method is computationally efficient and robust. An alternative approach for prestressing is inverse design analysis, which involves solving an inverse problem to determine the stress-free

reference configuration. This configuration transforms into the imaged configuration after applying the load under consideration [48, 113]. The advantage of this method is a more accurate stress-state representation in the imaged configuration. However, it suffers from computational inefficiency due to the fact that this problem is highly nonlinear and has a non-unique solution space.
The constitutive model consisted of a passive material model and an active stress model. The passive material was based on [65] and was not calibrated due to the absence of available data for calibration. Within the active stress model, there were three parameters to calibrate for each ventricle, namely the contractility, upstroke rate, and relaxation rate. These parameters were calibrated using the cardiac cycle evaluation as a forward model and objectives based on the segmented volumes in Fig. 4.1. The forward model was evaluated until a periodic state was achieved. To optimize the parameters a gradient-based optimization was used, where the gradient was approximated using finite differences.
One limitation of this model is that the activation of the contraction is temporally prescribed and spatially constant. One advantage of spatially constant activation is that it is easy to calibrate. Additionally, it effectively captures the overall integral behavior, such as the stroke volume. However, a disadvantage is that it does not capture spatial resolution. To address this constraint, cardiac electrophysiology offers a potential solution where the propagation of the electromechanical activation is studied and temporally and spatially resolved [149].
In conclusion, the methodologies presented in this section demonstrate the capability to effectively calibrate the computational 3D-0D model based on the patient-specific data outlined in Sec. 4.1.1. This calibration process can be repeated for all motion-CT data sets from day of life 40 to 80. The resulting configuration serves as a starting point for the subsequent cardiac growth simulations, which are discussed in Sec. 4.5 and Sec. 4.6. The calibration process of the cardiac growth model requires precisely aligned images, which can be ensured by solving the surface matching problem discussed in the next section.

4.4. Surface matching problem for growth

As discussed in Sec. 4.1.2, the alignment of consecutive images is not straightforward. Therefore, the surface matching framework presented in Sec. 2.4.1 is used to overcome this problem. In the following, in Sec. 4.4.1, the problem setup is outlined. After that, in Sec. 4.4.2, the results are shown and discussed in Sec. 4.4.3.

4.4.1. Problem setup and parameter setting

The surface matching is shown for Pig 2 between CT1 and CT2, taken at day of life 40 and 50, respectively. The geometry from CT1 is denoted by $\mathcal{S}_0$, and the geometry from CT2 acts as the target shape, denoted by $\mathcal{T}$. Similar to the atlas construction method in Sec. 4.2, the initial alignment is performed by using AV, MVP, and LVB as a coordinate system. Thereafter, the shapes are translated to their center of mass. The initial configuration of the surface matching problem is illustrated in Fig. 4.12, where the geometry $\mathcal{S}_0$ is represented in grey with the surface mesh, and the target geometry $\mathcal{T}$ is depicted in red.

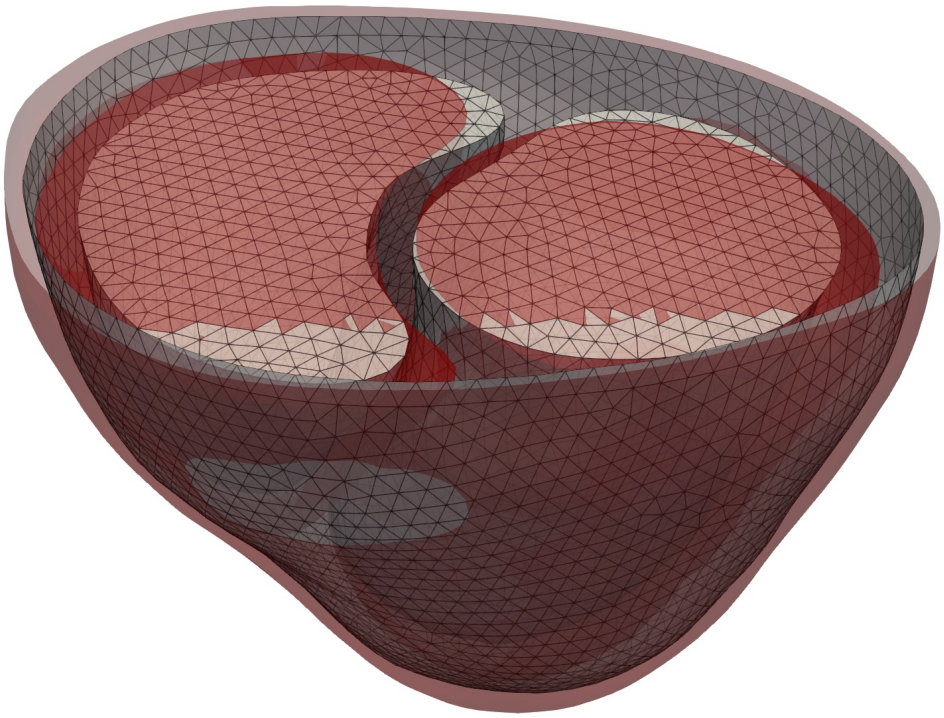

Abbildung 4.12.: Initial configuration of the surface matching problem. The initial geometry $\mathcal{S}_0$ is represented in gray, and the target geometry $\mathcal{T}$ is depicted in red.

The objective is to find the initial momenta $\boldsymbol{\alpha}_0$ such that the resulting shape $\mathcal{S}_1$ represents the target shape $\mathcal{T}$. Similar to the atlas construction, the surface matching quality is measured using the surface currents similarity measure, where the kernel widths σ_W and σ_V have to be chosen.

As the initial conditions, the momenta $\boldsymbol{\alpha}_0$ are initialized to zero. Additionally, the dense mode is employed, signifying $\boldsymbol{c}(t) = \boldsymbol{x}(t)$. The adjoint equations Eq. (2.141) and Eq. (2.142) are solved using the one-step-θ method with $\theta = 1$ and ten pseudo time steps. The resulting optimization problem, see Alg. 1, is solved using the L-BFGS method, see App. A.5.

All relevant parameters are provided in Tab. 4.5.

Tabelle 4.5.: Overview of the surface matching parameters.

surface matching parameter			
parameter	symbol	value	unit
varifold kernel width	σ_V	5	$[\mathrm{mm}]$
deformation kernel width	σ_W	2	$[\mathrm{mm}]$
regularization	σ	$1.0 \cdot 10^{-3}$	$[\mathrm{mm}^2]$
time step	Δt	0.1	[s]
initial momenta	$\boldsymbol{\alpha}(t=0)$	0	[-]

4.4.2. Numerical results

The numerical model for the surface matching problem in Fig. 4.12 consists of $5,430$ surface nodes for initial shape $\mathcal{S}_0$ and $6,139$ surface nodes for target shape $\mathcal{T}$. Hence, the meshes do not coincide topologically. The optimization ended after 100 iterations. The obtained results are illustrated in Fig. 4.13. The resulting shape $\mathcal{S}_1$ is shown in gray, and the target shape $\mathcal{T}$ is depicted in red. The results of the surface matching problem reveal a significant similarity between the two shapes. In the beginning, the surface norm between $\mathcal{S}_0$ and $\mathcal{T}$ is $65,428.19$. After 100 iterations, the surface norm results in 136.76. To better understand the results, for every surface point of $\mathcal{S}_1$, the closest point distance to $\mathcal{T}$ is computed and yields a mean value of 0.55 mm and a maximum value of 1.36 mm.

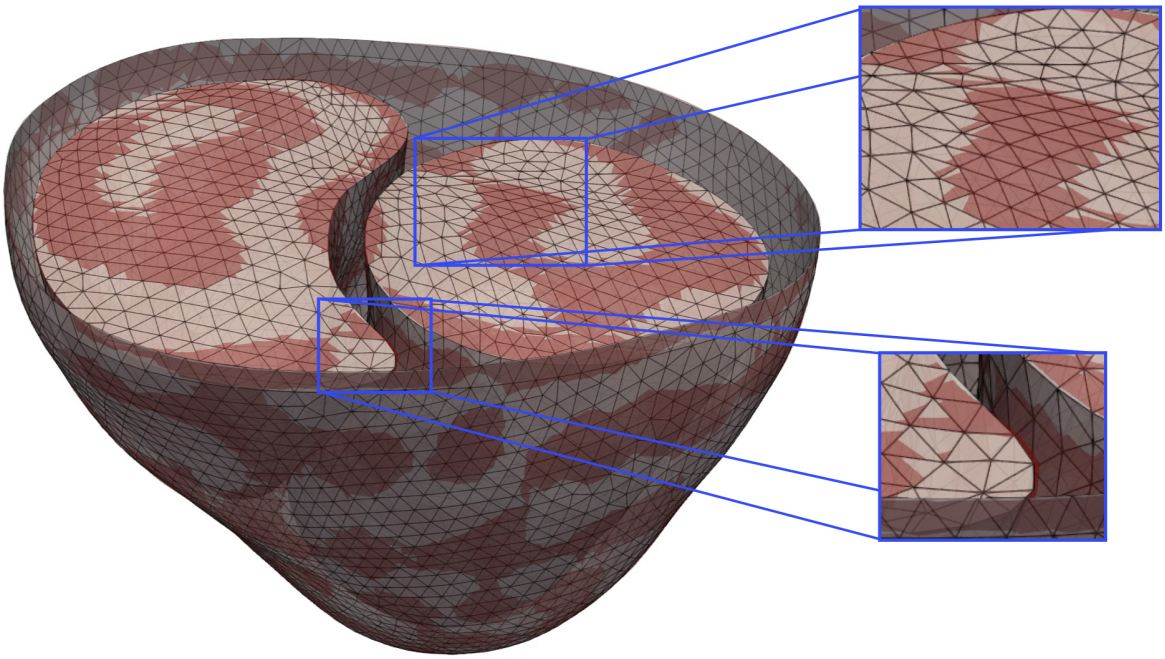

Abbildung 4.13.: Final configuration of the surface matching problem. The resulting shape $\mathcal{S}_1$ is shown in gray, and the target shape $\mathcal{T}$ is depicted in red.

Despite the similarity between the two shapes, a significant mesh distortion is evident in the results. These distortions are primarily attributed to the rigid body modes of translation and rotation. To achieve a rigid body mode-free transformation from $\mathcal{S}_0$ to $\mathcal{S}_1$, a subspace projection is applied. The used projector removes translation and rotation components in the solution of the momenta $\boldsymbol{\alpha}(t)$ and is based on a so-called subspace projection [7, 21]. Applying these projected momenta to the initial shape $\mathcal{S}_0$ results in a new shape $\tilde{\mathcal{S}}_1$, which is orthogonal to the space of rigid body modes.

Fig. 4.14 depicts the resultant shape $\tilde{\mathcal{S}}_1$ compared to the target shape $\mathcal{T}$. It can be observed that the image does not fit the target shape $\mathcal{T}$ as well as the result shown in Fig. 4.13. However, there is no mesh distortion anymore, making the shape $\tilde{\mathcal{S}}_1$ an optimal choice as a target geometry for the growth model as outlined in Sec. 4.1.2. The surface norm between $\tilde{\mathcal{S}}_1$ and $\mathcal{T}$ results in

$1,420.57$. The mean value of the closest point distances is 0.612 mm, and the maximal value results in 3.284 mm.

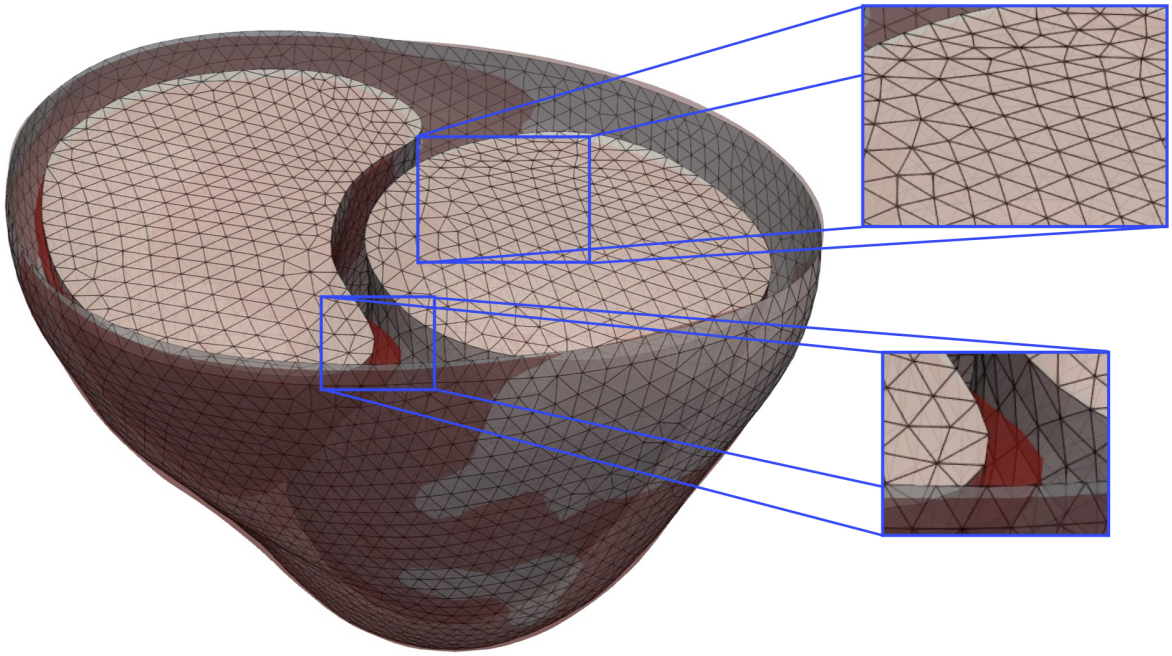

Abbildung 4.14.: Projected solution of the surface matching problem.

4.4.3. Discussion

The surface matching framework is designed for the statistical analysis of complex 3D anatomical shapes, and it is versatile enough to deal with generated surfaces from various segmentation methods. The primary objective of this method is to estimate a transformation path from one shape to another. It is robust to noise and mesh imperfections.
However, similar to the atlas construction method, the selection of the parameters can be intricate, particularly the choice of kernel widths. The accuracy of the model is influenced by the selection of the kernel widths and regularization parameter [38]. Too large values result in an overly smoothed solution, where geometrical features vanish. Conversely, too small values contribute to capturing undesirable noise. One potential extension could involve the development of methods for automatically tuning these hyperparameters.
The employed dense mode, where the control points are equal to the surface points, resulted in a high-dimensional feature space, leading to a computationally costly formulation due to the increased dimensionality. To overcome this constraint, control points could be used. Control points are a minimal set of points representing the most important features of the geometry. The choice of control points is a critical aspect of the surface matching framework and is extensively discussed in [36].
As a postprocessing step to the surface matching problem, a projector was employed to eliminate the rigid body modes of translation and rotation within the momenta. This resulted in a new shape. While this shape exhibited a larger deviation from the target shape compared to the original

result, there was no mesh distortion. While the use of a projector was a viable solution, an alternative and potentially more effective approach would be the reformulation of the optimization problem by directly optimizing for rigid-body-mode-free momenta.
It is important to note that within the scope of this thesis, surface matching serves as a preprocessing step to the growth identification problem. Therefore, computational efficiency was not a primary concern, and the focus remained on the accuracy and reliability of the transformation path estimation. Given the absence of rigid body modes, the new shape proves to be a favorable choice as a target for the growth identification problem, see Sec. 4.5.

4.5. Cardiac growth model calibration

In this section, the calibration of the growth parameter based on the Bayesian inverse problem from Sec. 2.3 is presented. Therefore, in Sec. 4.5.1, the problem setup is outlined. Subsequently, in Sec. 4.5.2, the results are presented and discussed in Sec. 4.5.3.

4.5.1. Growth prediction for two consecutive images

The growth calibration is focused on pig P2 from day of life 40 to 50. The initial configuration $\mathcal{S}_0$ at time instance t_0 is derived after evaluating the cardiac cycle computation from Sec. 4.3 at day of life 40. This step ensures the establishment of a physiological stress state within the heart. The grown configuration at time instance T_{growth} is obtained by evaluating the forward model $\mathcal{S}_1 = F(\boldsymbol{u}(\boldsymbol{\theta}), \boldsymbol{\theta})$ presented in Sec. 3.2.2. The target geometry is the grown configuration at day of life 50, representing the observation $\boldsymbol{Z}$. The alignment between the initial and target shapes is achieved through the surface matching application, as detailed in Sec. 4.4.
The objective in the calibration process is to determine a spatial distribution of the growth rate parameter $c_\vartheta(\boldsymbol{X})$ such that the grown configuration $\mathcal{S}_1$ closely resembles the target shape $\boldsymbol{Z}$. Surface currents serve as a similarity measure to quantify the quality of the match. The comparison focuses on the left and right ventricles, as well as the epicardial surface.
The associated kernel widths are set similarly to the surface matching application: The varifold kernel width $\sigma_V = 5\ \text{mm}$ and the distance measure width $\sigma = 1.0 \cdot 10^{-3}\ \text{mm}^2$.
As regularization, the total variation functional is chosen. Therein, the parameters are set to $\varepsilon_{\text{tv}} = 1.0 \cdot 10^{-3}\ \text{mm/s}$ and the overall regularization weight is set to $\alpha = 1\ \text{s/mm}$.
In summary, all relevant parameters are listed in Tab. 4.6.

Tabelle 4.6.: Overview of the growth identification problem parameters.

growth calibration parameter			
parameter	symbol	value	unit
varifold kernel width	σ_V	5	$[\text{mm}]$
distance measure width	σ	$1.0 \cdot 10^{-3}$	$[\text{mm}^2]$
TV regularization weight	α	1	$[\text{s/mm}]$
TV regularization prior	ε_{tv}	$1.0 \cdot 10^{-3}$	$[\text{mm/s}]$
initial condition	c_ϑ	0	$[1/\text{s}]$

4.5.2. Numerical results

Similar to the cardiac cycle evaluation, the numerical model consists of $50,642$ finite elements with an edge length of approximately $1.5\ \mathrm{mm}$ and $239,619$ DOFs for the displacement field. In each iteration, one forward problem is solved to evaluate the objective function $\mathcal{L}(\boldsymbol{u}(\boldsymbol{\theta}), \boldsymbol{\lambda}, \boldsymbol{\theta})$ and compute its gradient. The optimization problem is solved using the L-BFGS method and it ended after 150 iterations. The numerical costs for solving one step within the adjoint problem consist of the solution to one forward problem, along with the calculation costs for the gradients, which only increase by an additional linear system solve. Fig. 4.15 depicts the evolution of the objective function value over the number of iterations. A noticeable pattern emerges, characterized by an initial decrease followed by subsequent small oscillations. Notably, beyond the $70-$th iteration, the development of further progress becomes increasingly challenging.

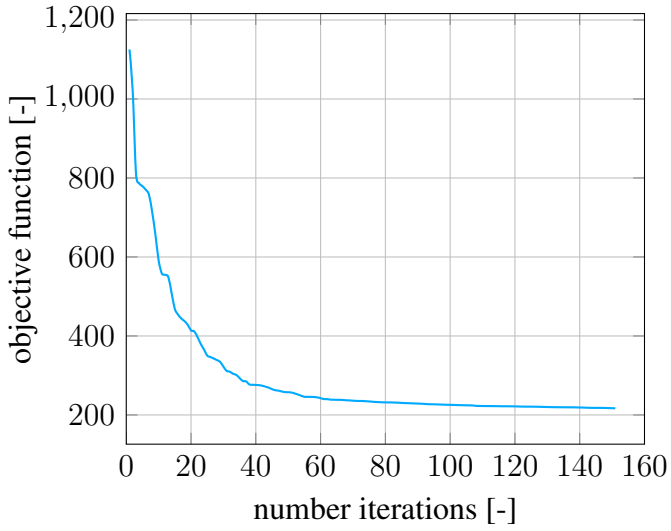

Abbildung 4.15.: Objective function value during the growth calibration process over the number of iterations.

In Fig. 4.16, the spatial distribution of the growth rate parameter c_ϑ across the heart is presented. Notably, distinct patterns emerge, with elevated growth rate values observed in the ventricular regions. Conversely, the septal area exhibits lower growth rate values.

In Fig. 4.17, the resulting grown configuration $\mathcal{S}_1$ is compared in six slices to the observation $\boldsymbol{Z}$. In each slice, the outline of the observation is shown in black, and the grown configuration is colored. Qualitatively, a notable resemblance is observed between the grown configuration and the observation, although a perfect alignment is not achieved.

The initial and final volumes of the grown configurations and the volumes measured for the target shape, resulting from the surface matching application are listed in Tab. 4.7 for the left and right ventricle. In comparison to the initial volumes, this yields a 14.7% increase for the right ventricle and a 17.8% increase for the left ventricle.

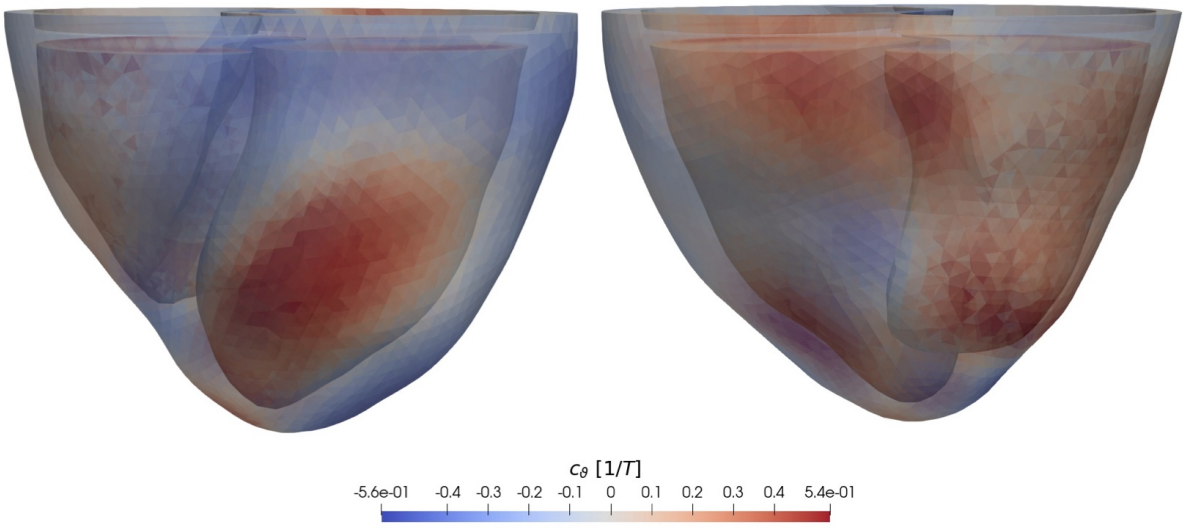

Abbildung 4.16.: Frontal and back view of the final distribution of the optimized growth parameter c_ϑ over the heart.

Tabelle 4.7.: Initial, grown and measured volumes of the left and right ventricles.

	symbol	value	unit
initial configuration	$V_{\mathrm{v}}^{\ell}(t_0)$	8.39	[mL]
	$V_{\mathrm{v}}^{r}(t_0)$	12.81	[mL]
grown configuration	$V_{\mathrm{v}}^{\ell}(T_{\mathrm{growth}})$	9.89	[mL]
	$V_{\mathrm{v}}^{r}(T_{\mathrm{growth}})$	14.70	[mL]
measured target	$\tilde{V}_{\mathrm{v}}^{\ell}(T_{\mathrm{growth}})$	10.3	[mL]
	$\tilde{V}_{\mathrm{v}}^{r}(T_{\mathrm{growth}})$	15.1	[mL]

4.5.3. Discussion

The identification problem presented in this section focused on calibrating the growth rate parameter for the reference geometry derived from pig P2 at day of life 40 to the target geometry obtained at day of life 50. Thereby, the target geometry was obtained as a result of the surface matching problem, see Sec. 4.4.

The results revealed a qualitative resemblance between the grown geometry, obtained by the calibrated growth rate parameter, and the target geometry. However, a perfect match was not achieved, and several factors contributed to this discrepancy.

First, finding optimal parameters is crucial and similar to the surface matching problem, finding optimal parameters can be intricate. The selection of kernel widths, regularization, and noise parameters influences the spatial distribution. Ensuring that kernel width parameters are sufficiently large is essential to maintain sensitivity to variations in the relative position between meshes and to smooth noise. However, excessively small values can lead to geometrically distinct shapes.

Abbildung 4.17.: Comparison of the grown configuration $\mathcal{S}_1$ with the observation $\boldsymbol{Z}$. In each slice, the grown configuration is depicted in colors, and the outline of the observation is shown in black.

The regularization parameter further smoothes the solution and has to be chosen large enough to prevent unphysiological jumps in the spatial distribution of the growth rate. On the other hand, excessively large values of the regularization parameter can influence the outcome, leading to less accurate surface matching.

Furthermore, the computational effort required is substantial, given that the number of unknowns corresponds to the number of elements utilized. In this case, a single iteration took around $15\,\mathrm{min}$ on an Intel Xeon W-2235 CPU (3.80GHz) processor using 12 cores. The expense of 150 iterations makes the process for finding optimal parameters both costly and time-consuming. To address this challenge, a potential solution was proposed in [80], where Principal Component Analysis was employed to reduce the number of parameters for calibration purposes. While this approach proved to be more efficient than sampling the entire parameter space, the numerical

costs remained substantial, and accurately assessing the approximation accuracy poses a difficulty.
Another challenge lies in the definition of the target shape. Although the target shape was obtained through a rigid body mode-free projection from the surface matching problem, the resulting displacement field may not be entirely physiological. Certain elements underwent substantial compression, while others experienced high stretches. This can be seen in Fig. 4.16, where some elements have to shrink by the same factor as neighboring elements have to grow. These scenarios are not covered by physiological growth mechanics. One potential solution to overcome this challenge and to obtain a more homogenized growth rate distribution is the implementation of a new mesh regularization, which could enhance the definition of a more physiologically accurate target shape. More specifically, the implementation of a method could focus on reducing abrupt transitions between compressed and stretched elements.
In conclusion, a trade-off exists between accuracy and practicality in the calibration of the growth rate parameter. The application of this model focuses on predicting heart growth. The presented calibration process can be repeated every ten days for all measurements outlined in Sec. 4.1.2. To achieve this, the 3D-0D model has to be re-calibrated every ten days, as explained in Sec. 4.3. Additionally, a new target shape has to be defined for each of these identification problems, as detailed in Sec. 4.4. With this, a time extrapolation method based on the acquired growth pattern can be used to predict future cardiac growth. Potential time extrapolation methods could involve the use of a spline approximation or a neural network. This prediction could provide valuable insights for doctors in developing effective therapeutic approaches, making informed treatment decisions, and selecting appropriate implants and prostheses, thus enhancing patient care strategies.

4.6. Signaling network

In this section, the cardiac growth model is coupled to the reference (REF) and reduced and modified (R&M) signaling networks. In contrast to the previous section, the growth rate is now determined as a result of the solution of the signaling network. First, a global sensitivity analysis for the REF and R&M networks is performed to identify the most influential input species on *CellArea* and is presented in Sec. 4.6.1. Subsequently, in Sec. 4.6.2, both signaling networks are coupled to the kinematic growth framework to evaluate a cardiac growth simulation. Finally, in Sec. 4.6.3, the presented results are discussed.

4.6.1. Global sensitivity analysis of signaling networks

The results presented in this section are submitted in [9]. As discussed in Sec. 3.3.3, the REF and R&M signaling networks show strong monotonic behavior between the input concentrations and the output concentration of the species *CellArea*. For too large input concentrations the output concentrations results in $c_{\text{CellArea}} = 1$. Therefore, a physiological input range is identified at $\tilde{c}_{i,\text{max}} = 0.12$ for all input species in both signaling networks.
The base sample matrices $\boldsymbol{A}$ and $\boldsymbol{B}$ are filled using Latin Hypercube sampling [101] on the interval $[0, 0.12]$ with number of samples $n_S = 1 \cdot 10^6$. Both networks are evaluated using the

DSS. In Fig. 4.18, the sensitivity estimators S^{Sat} and T^{Jan} of *CellArea* with respect to all input species are depicted.

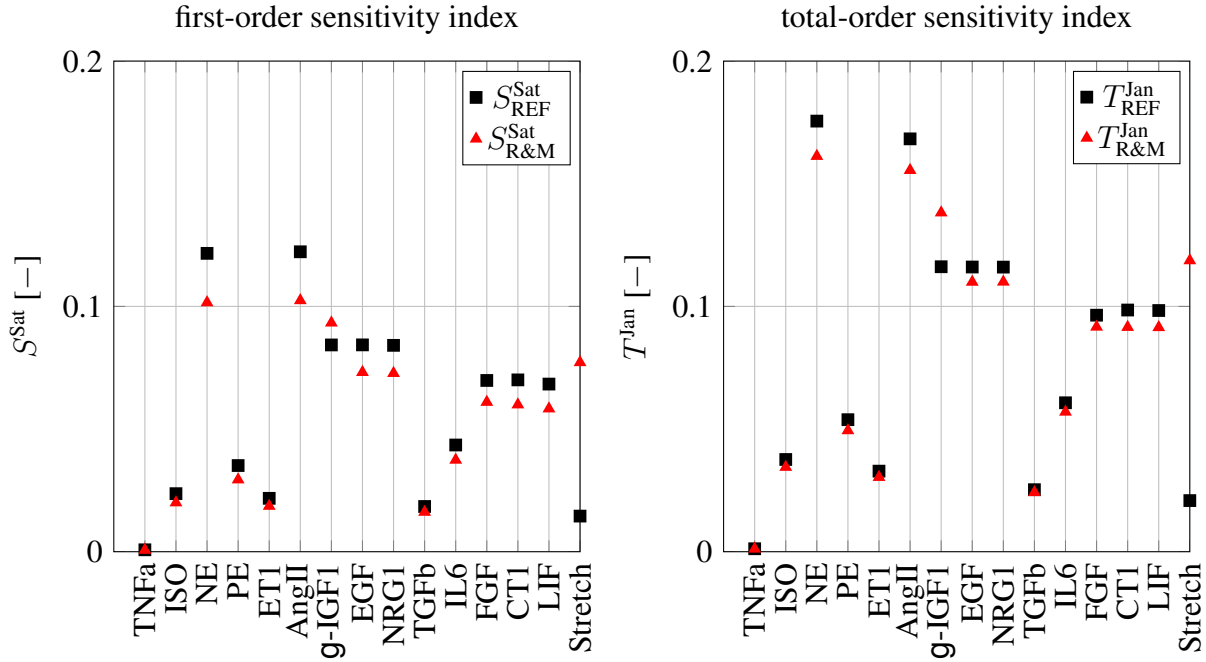

Abbildung 4.18.: First- and total-order sensitivities for c_{CellArea} for all input species in both networks [9].

Within the REF network, *Stretch* has a very low influence on *CellArea*, which changes in the R&M network significantly. Both sensitivity indices for *Stretch* increase approximately by a factor of five in the R&M network. In the R&M network, *Stretch* becomes one of the most influential factors on *CellArea*, together with g-*IGF1*, *NE*, and *ANGII*. Further, due to the increased sensitivity of *Stretch*, the remaining sensitivities decrease.
The total-order sensitivity of g-*IGF1* increases in the R&M network. This increase is based on the interaction between the pathway from g-*IGF1* to *IGF1R* and the novel pathway from *Stretch* to l-*IGF1* to *IGF1R*. The sensitivities of the species *TNFa* are small since it only enters one OR-activation with six other species. Moreover, the sensitivities of *CT1* and *LIF* are similar as they are only connected to *gp130LIFR*.
To conclude the convergence of the sensitivity analysis, Fig. 4.19 shows the first- and total-order estimators for both networks for the input node *Stretch* over the number of samples used for their computation. Additionally, all six presented estimators from Tab. 2.1 are shown in the App. D.3 in Fig. D.5 and induce convergence since the sensitivities for all estimators are similar. A numeric representation of the sensitivities can be found in Tab. D.4 and Tab. D.5.

4.6.2. Coupling results

To couple the signaling network with the cardiac mechanics models, transfer functions are needed, as outlined in Sec. 3.3.4. The first transfer function from Eq. (3.95) is used to map the

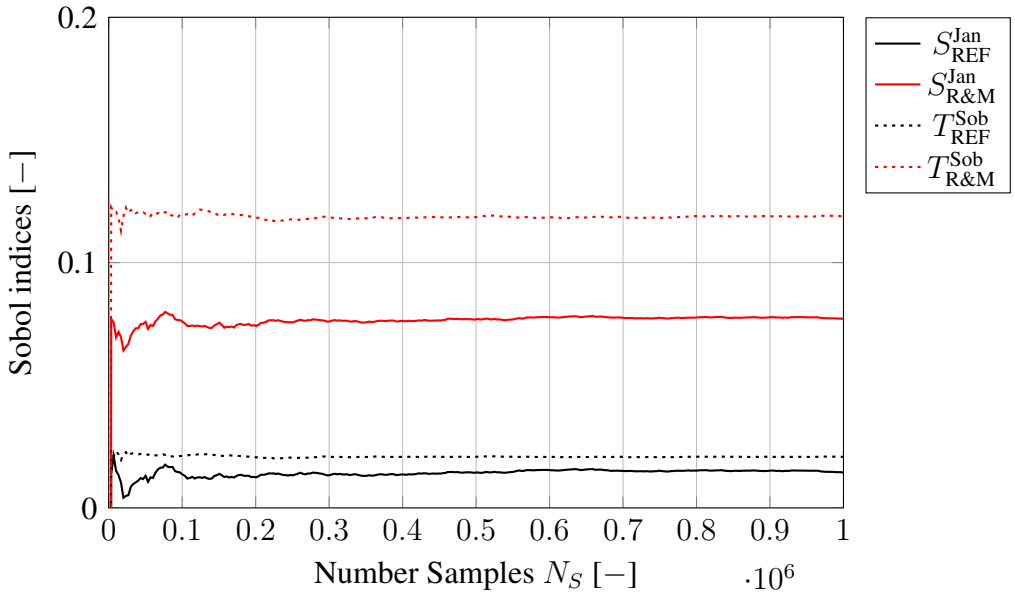

Abbildung 4.19.: Convergence of the Sobol indices for *CellArea* with respect to *Stretch* in both networks over a varying number of samples [9].

maximal fiber strain, defined in Eq. (3.94), from the solution of the cardiac cycle evaluation presented in Sec. 4.3.4 to the input concentration c_{Stretch}. Using the results from the previous section, the maximal physiological range for the species *Stretch* is set to $\tilde{c}_{\text{Stretch,max}} = 0.12$. In Fig. 4.20, the concentration c_{Stretch} over the computational heart domain is depicted.

Using this spatial distribution of the concentration c_{Stretch}, both signaling networks are evaluated for each element. Similar to Sec. 3.3.3, the input concentrations for all other input species are set to $c_i = 0.06$, except the input concentration for the species g-IGF1. As presented in Sec. 4.1, the data collection in this work was based on a porcine heart model, in which the growth hormone receptor was deleted. The normal physiological sequence involves growth hormone binding to its receptor in the liver and subsequently stimulating the synthesis of g-*IGF1* [93]. However, due to the GHR knockout, the global *IGF1* concentration is reduced. Hence, the input concentration is set to a value of $c_{g-\text{IGF1}} = 0$.

Both signaling networks are evaluated using the DSS. The resulting concentrations of the species *CellArea* over the computational heart domain for the REF and R&M network are depicted in Fig. 4.21.

The second transfer function from Eq. (3.96) associates the concentration c_{CellArea} of the species *CellArea* with the growth rate parameter c_ϑ, as detailed in Section 3.3.4. Subsequently, the computational cardiac growth model is evaluated over the time span of ten days. The resulting growth configurations for the REF and R&M networks are illustrated in Figure 4.21.

For the REF network, the growth configuration results in a final volume of $13.3\ \text{mL}$ for the left ventricle and $9.0\ \text{mL}$ for the right ventricle. In comparison, for the R&M network, the growth configuration results in a final volume of $13.7421\ \text{mL}$ for the left ventricle and $9.11105\ \text{mL}$ for the right ventricle.

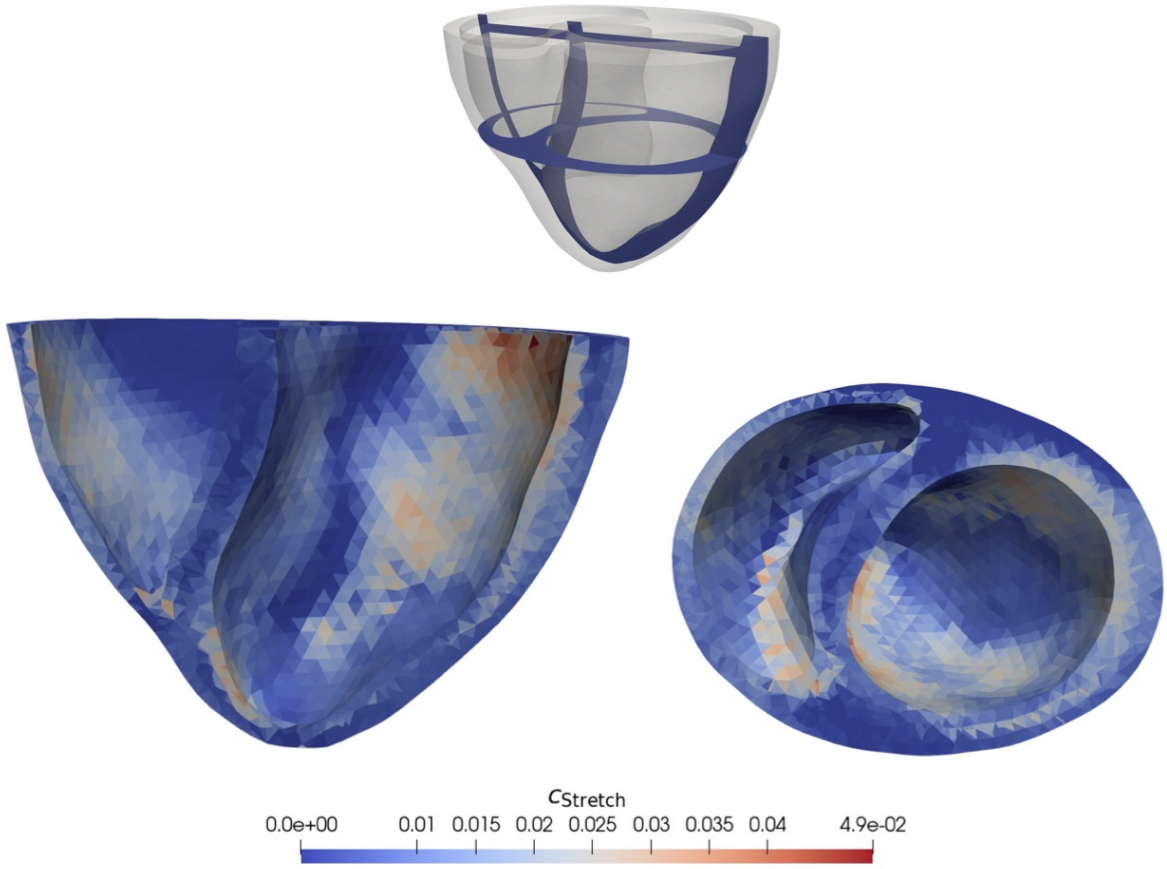

Abbildung 4.20.: Concentration c_{Stretch} of the species *Stretch* over the computational heart domain.

4.6.3. Discussion

Based on research in [161] and [164], the local mechanically induced *IGF1* was incorporated into an existing signaling network for heart growth [128]. Therefore, a new species l-*IGF1*was added into the network and connected to *Stretch* and *IGF1R*. Furthermore, all species and reactions that do not influence *CellArea*, the quantity of the interest with respect to heart growth, were removed to make the analysis of the network cheaper.
The presented sensitivity analysis for the species *CellArea* with respect to the input species, see Fig. 4.18, shows that within the original REF network, the species *Stretch* has only a minor contribution to heart growth compared to other influential quantities. However, it has been shown in [69] that *Stretch* is a crucial factor for cardiomyocytes in heart growth. Within the R&M network, *Stretch* became one of the most influential factors for growth and the sensitivities of *CellArea* with respect to *Stretch* are approximately five times higher than in the REF network.
When evaluating the REF and R&M networks with the Hill-differential equation approach, the transient effects due to arbitrary initial conditions are not physiologically interpretable, see Fig. 3.12. Furthermore, both networks converge to their stationary solution. Moreover, the selection of suitable initial conditions and reaction time constants poses a challenge, primarily attributed

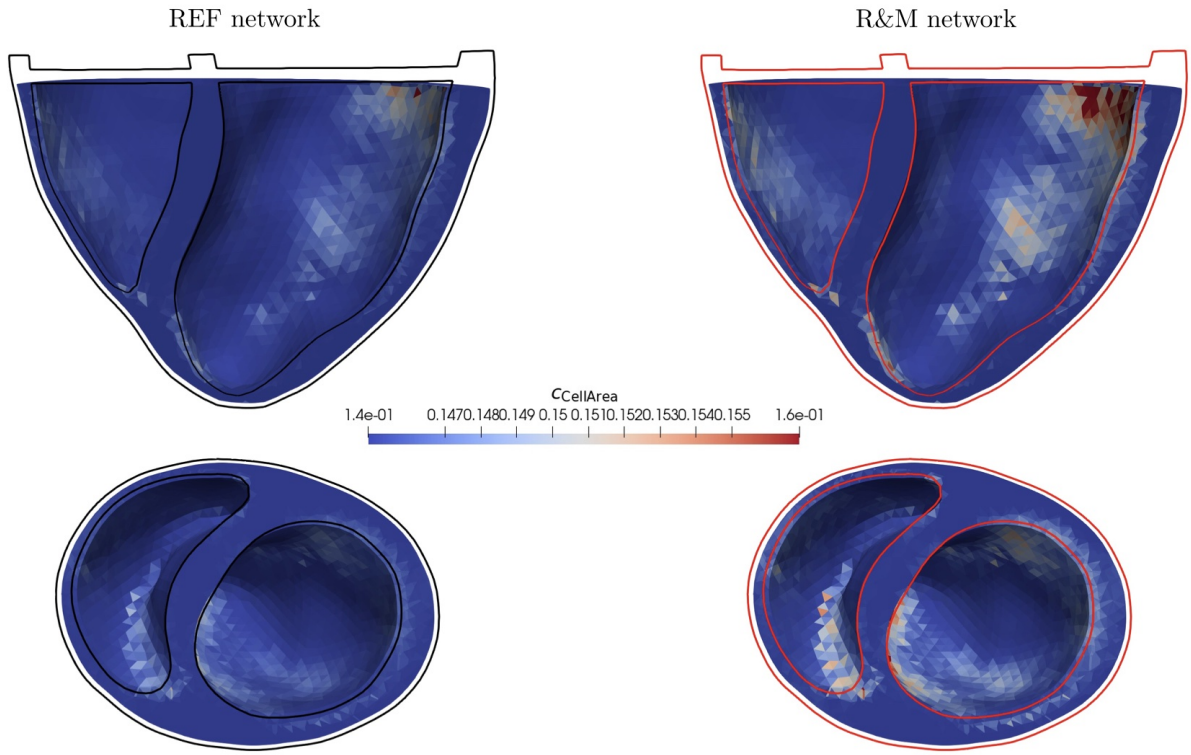

Abbildung 4.21.: Concentration c_{CellArea} of the species *CellArea* over the computational heart domain resulting from the REF and R&M signaling network. The grown configurations are shown as slices in black for the REF and in red for the R&M network.

to the complexities associated with data acquisition. The timescale of dynamic hormonal and biochemical changes is much smaller compared to the timescale of heart growth. This led to the formulation of the direct stationary solutions (DSS), where reaction time constants and initial conditions are no longer required.

Considering the nonlinear nature of the signaling networks with numerous interactions, a global sensitivity analysis was conducted to identify the most influential factors on *CellArea*. The computational cost for many model evaluations was reduced by the DSS approach. First- and total-order sensitivities were estimated using a variance-based Monte Carlo approach, and a physiological input range was identified for sampling the input concentrations.

Within the R&M network, the first-order sensitivity index revealed an increased sensitivity of *Stretch* and decreased sensitivities of all other species. The total-order sensitivity, accounting for interactions between the species, increased for *Stretch* and g-*IGF1* while decreasing for all other species.

As the most influential factors on *CellArea*, the species *Stretch*, *NE*, *AngII*, and g-*IGF1*were identified. Research in [150, 161, 164] shows that locally produced *IGF1* is necessary for physiological heart growth. Moreover, the species *NE* is pivotal in regulating fundamental biological properties such as growth in myocytes and other cell types within the heart [27, 84]. The species *AngII* plays a role in the regulation of cardiac contractility, cell coupling, and impulse propagation, being implicated in cardiac growth and remodeling [6, 31].

Additionally, the species *TNFa* has the lowest sensitivity and, therefore, the lowest influence on heart growth. In physiological heart growth, it has been shown that the *TNFa* signaling cascade is not required for normal cardiogenesis or that this pathway is redundant and compensated for by alternate signaling pathways [129]. Conversely, in pathological cases, the concentration of circulating *TNFa* is elevated [89] and can induce hypertrophy [85]. These findings are consistent with the estimated sensitivity results.

Coupling the signaling network to the cardiac mechanics models presented in Sec. 3.1 and Sec. 3.2 involves defining two transfer functions. For the first transfer function, which couples the cardiac cycle evaluation with the input concentration of *Stretch*, a linear mapping using the identified physiological range was chosen. The choice of different mechanical stimuli is discussed in [83, 160]. The second transfer function was based on a linear mapping between the output concentration of *CellArea* and the growth rate c_ϑ. In general, the definition of these transfer functions is not straightforward as they map a physical quantity into a space of normalized concentrations and then back to a physically interpretable quantity.

In Fig. 4.20, the concentration of the species *Stretch* is depicted based on the maximal fiber strain resulting from the cardiac cycle evaluation. Notably, the concentration value was lower in the septum region, aligning with the expected physiological behavior where the septum undergoes less contraction compared to the rest of the heart. The high concentration value within the left ventricle results from the large left ventricular deformation during the cardiac cycle, which can be observed in Fig. 4.11 at $t = 0.24$.

Both networks were evaluated in each element using the local concentration of *Stretch* as input. The resulting distribution of the concentration of *CellArea* over the heart is illustrated in Fig. 4.21. This distribution exhibited a similar structure to the concentration distribution of *Stretch* due to the monotonic behavior of the signaling networks. Compared to the REF network, within the R&M network, the overall concentration was higher, and thus, the growth response was increased.

Another set of transfer functions was proposed in [41]. Therein, the minimum of the maximal cross-fiber strain was used to derive a transfer function for *Stretch* by fitting the output of the growth prediction to their measurements. However, this approach does not allow a general definition of transfer functions.

Calibrating the signaling network is challenging due to the high number of inputs and model parameters. However, in a so-called *factor fixing* [118] approach, the sensitivity analysis results can be used to reduce the dimensionality of the input space and calibrate the signaling networks. In particular, the estimated growth rates from Sec. 4.5 could be used to define a mapping between the models and calibrate the input concentrations. However, within the presented model approach, the concentration of *CellArea* is always positive, i.e., shrinkage of elements cannot be represented. Therefore, the obtained results from the identification problem in Sec. 4.5 cannot be used to calibrate this model.

A possible extension could be to modify the model to allow for shrinking as well. Currently, the growth response is always between 0 and 1, indicating a mass increase. However, as described in [100], physiological hypertrophy is entirely reversible. Therefore, incorporating the possibility of shrinking into the model would provide a more comprehensive representation of the dynamic processes involved in cardiac growth and remodeling. This extension could involve introducing mechanisms or parameters that allow for negative growth responses, reflecting the reversible nature of hypertrophy.

5. Summary and outlook

In modern health care, the most common causes of death are cardiovascular diseases associated with heart failure (HF). In HF therapy, heart transplantation is considered to be the gold standard. However, the limited availability of donor hearts restricts its accessibility to all patients in need. This critical limitation can be addressed by the early identification of patients progressing towards HF. However, early identification requires a detailed understanding of many HF-associated mechanisms. Therefore, this thesis was motivated by the need to enhance the understanding of cardiac growth and remodeling by developing computational models of cardiac mechanics. These computational models have the potential to support clinical decision making and predict long-term treatment responses *in-silico*.

The acquired data used for the patient-specific calibration of the cardiac mechanics models was based on a growth hormone receptor knockout pig model due to its resemblance to the heart size of children. Motion-CT images of the heart of six pigs were captured, ranging from day of life 40 to 80. A single CT scan calibrated the cardiac cycle evaluation, while a series of long-term CT scans was used to calibrate the cardiac growth model.

The atlas construction method was employed to identify a representative heart shape of the acquired data set for all six pigs at the day of life 40. The resulting shape acted as a generic heart shape, which represents the key geometrical features of all other heart shapes. This heart shape can be used for generic treatment methods when patient-specific treatments are unfeasible.

The cardiac cycle evaluation in this study relies on a 3D-0D model, combining a 3D structural model of the ventricular heart with a 0D vascular flow network comprising four windkessel models. To calibrate the 3D-0D model, motion-CT and the pressure over time relationship were utilized. Thereby, each windkessel model was calibrated individually. This approach allowed for a well-posed and computationally efficient scalar-valued optimization. Whenever measurements of pressure and flow were unavailable, artificial data was used to calibrate the corresponding parameters. Additionally, the active stress model was calibrated using the cardiac cycle evaluation as the forward model. The objective function was based on three volumes obtained from the segmentation of the motion-CT. The overall calibration results demonstrated promising agreement between the model predictions and the observed data.

The growth model employed in this thesis was based on the kinematic growth framework, utilizing a growth law that approximates muscle fibers using a cylindrical model, focusing on radial and circumferential growth. The calibration of this model required two consecutive CT images segmented at the same heart phase. However, aligning two heart geometries from consecutive images is not straightforward due to the patient's variability in positioning within the CT scan. Furthermore, physiological landmarks proved inadequate for the alignment task as they are chal-

lenging to identify consistently for all images. Therefore, the surface matching framework was used together with a rigid-body-mode-free projection as a post-processing step to define the newly grown target shape.

The resulting heart shape was then used to calibrate the kinematic growth model. The calibration process employed a Bayesian inverse problem formulation using surface currents as a similarity measure. While a perfect match between the two shapes was not achieved, the results demonstrated a sufficiently accurate overall resemblance.

A novel signaling network was proposed based on an existing network to model biochemical, hormonal, and mechanical signaling pathways that can trigger heart growth. The novel network incorporates the local *IGF1* production based on mechanical stretch. To identify the most influential factors on heart growth, a global sensitivity analysis was performed for both the existing and the novel networks. Therefore, the modeling approach was simplified by solving for the stationary solution. The results of the global sensitivity analysis based on Monte Carlo estimation showed that within the novel signaling network, the influence of the mechanical stimuli *Stretch* has a much higher influence on heart growth. Furthermore, the species g-*IGF1*, *NE*, and *ANGII* are identified to be the most influential factors on heart growth.

Both presented signaling networks were coupled to the computational cardiac growth model. Therefore, a transfer function was defined to map the maximal fiber strain from the cardiac cycle evaluation to the signaling network normalized input concentration of the mechanical species *Stretch*. Subsequently, the network was evaluated, and the resulting concentration of the species *CellArea* was used to drive the cardiac growth model. The results showed that the proposed novel network resulted in an increased growth response.

Potential future investigations for the presented models have been discussed in the relevant sections of the results in Chapter 4. Further investigations could include

- the development of an automatic segmentation tool: Manual segmentation of CT images of the heart requires a trained expert and can be time-consuming. Therefore, machine learning methods could be used to automate this process.
- the incorporation of pathological data: Including the data from pathological cases could improve the models' predictive capabilities.
- the usage of model order reduction: As the presented model evaluations are computationally expensive, model order reduction approaches could be used for acceleration.

A. Mathematical model details

A.1. Tensor notation and mathematical operators

In this section, a brief overview of the mathematical operations is given. Therefore, index notation is introduced. In this notation, each term can feature indices at most twice, with the condition that identical indices are unrepeated. Unrepeated indices increase the tensorial order of expressions, while, according to Einstein's summation convention, repeated indices imply summation over that index. Furthermore, temporal and spatial derivatives are indicated by a comma, followed by t and/or spatial indices, respectively.
Given the following vectors and matrices $\boldsymbol{a}, \boldsymbol{b} \in \mathbb{R}^3$, $\boldsymbol{A}, \boldsymbol{B} \in \mathbb{R}^{3\times3}$.
The dot product or contraction of two vectors is given by

$$\boldsymbol{a} \cdot \boldsymbol{b} = a_i b_i. \tag{A.1}$$

The double-dot or double contraction is defined as

$$\boldsymbol{A} : \boldsymbol{B} = A_{ij} B_{ij}. \tag{A.2}$$

The dot product or inner product between a matrix and a vector is defined as

$$\boldsymbol{A} \cdot \boldsymbol{b} = A_{ij} b_j. \tag{A.3}$$

The trace of a matrix reads

$$tr(\boldsymbol{A}) = A_{ii}. \tag{A.4}$$

The gradient of a tensor is defined as

$$\nabla \boldsymbol{A} = A_{ij,k}. \tag{A.5}$$

The divergence is given by

$$\nabla \cdot \boldsymbol{A} = A_{ij,i}. \tag{A.6}$$

A.2. Windkessel model details

In this section, all 0D flow network components and Windkessel models are presented, and their corresponding equations are derived based on work in [62, 158].

Resistance The resistance is proportional to the flow rate, and its equation reads

$$R\,q = p_{\text{in}} - p_{\text{out}}. \tag{A.7}$$

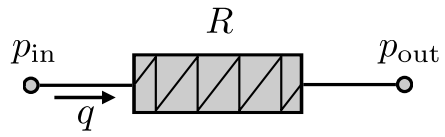

Abbildung A.1.: Resistance element.

Compliance The compliance can accumulate and release fluid in response to pressure changes, and its equation is given by

$$C\frac{\mathrm{d}p}{\mathrm{d}t} = q_{\text{in}} - q_{\text{out}} = q_C. \tag{A.8}$$

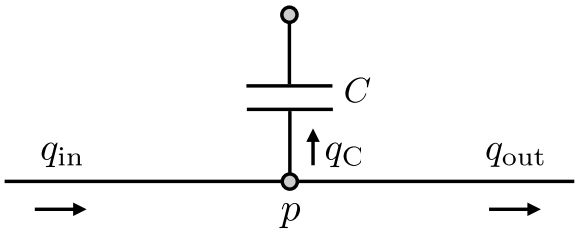

Abbildung A.2.: Compliance element.

Inertance The inertance generates a pressure reduction that is directly proportional to the change in flow rate, and its equation reads

$$L\frac{\mathrm{d}q}{\mathrm{d}t} = p_{\text{in}} - p_{\text{out}}. \tag{A.9}$$

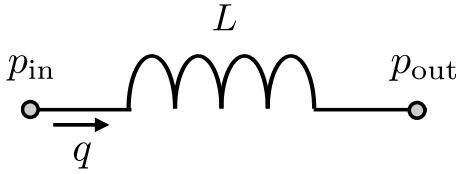

Abbildung A.3.: Inertance element.

Derivation of windkessel equations

2-element windkessel The equation for a 2-element windkessel model is derived using Eq. (A.7) and Eq. (A.8). Using the terminology from Fig. 2.2, they read

$$C\frac{\mathrm{d}p_{\text{in}}}{\mathrm{d}t} = q_{\text{in}} - q_{\text{out}}, \tag{A.10}$$

$$q_{\text{out}} = \frac{p_{\text{in}} - p_{\text{out}}}{R}. \tag{A.11}$$

Inserting Eq. (A.11) into Eq. (A.10) yields Eq. (2.45).

3-element windkessel The 3-element windkessel model is depicted in Fig. A.4.

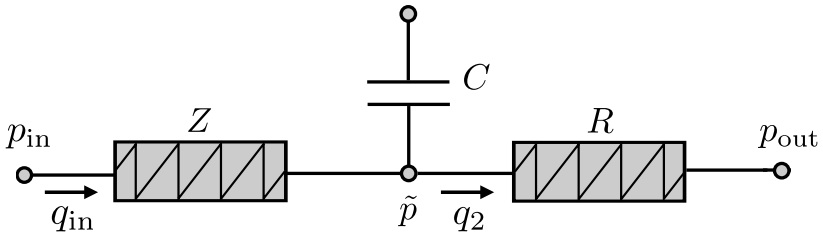

Abbildung A.4.: 3-element windkessel model.

The model equation is derived using the 2-element windkessel Eq. (2.45) and Eq. (A.7). The system reads

$$C\frac{\mathrm{d}p_{\text{in}}}{\mathrm{d}t} + \frac{\tilde{p} - p_{\text{out}}}{R} = q_2, \tag{A.12}$$

$$q_2 = \frac{p_{\text{in}} - \tilde{p}}{Z}. \tag{A.13}$$

Reformulating Eq. (A.13) yields

$$\tilde{p} = p_{\text{in}} - Zq_2. \tag{A.14}$$

Inserting Eq. (A.14) in Eq. (A.12) leads to

$$C\frac{\mathrm{d}p_{\text{in}}}{\mathrm{d}t} + \frac{p_{\text{in}} - p_{\text{out}}}{R} = CZ\frac{\mathrm{d}q_{\text{in}}}{\mathrm{d}t} + q_{\text{in}} + \frac{Z}{R}q_{\text{in}}. \tag{A.15}$$

4-element windkessel The equations for the 4-element windkessel model are depicted in Fig. 2.3. Its model equation is derived using Eq. (A.15), Eq. (A.8) and Eq. (A.9). Using the terminology from Fig. 2.3, they read

$$C\frac{\mathrm{d}p_{\text{in}}}{\mathrm{d}t} + \frac{p_{\text{in}} - p_2}{R} = \left(1 + \frac{Z}{R}\right) q_{\text{in}} + CZ\frac{\mathrm{d}q_{\text{in}}}{\mathrm{d}t}, \tag{A.16}$$

$$L\frac{\mathrm{d}q_2}{\mathrm{d}t} = p_2 - p_{\text{out}}, \tag{A.17}$$

$$C\frac{\mathrm{d}p_{\text{in}}}{\mathrm{d}t} = q_{\text{in}} - q_2. \tag{A.18}$$

Reformulating Eq. (A.17) and Eq. (A.18) yield

$$p_2 = L\frac{\mathrm{d}q_2}{\mathrm{d}t} + p_{\text{out}}, \tag{A.19}$$

$$q_2 = q_{\text{in}} - C\frac{\mathrm{d}p_{\text{in}}}{\mathrm{d}t}. \tag{A.20}$$

Inserting Eq. (A.20) into Eq. (A.19) leads to

$$p_2 = L\frac{\mathrm{d}q_{\text{in}}}{\mathrm{d}t} - LC\frac{\mathrm{d}^2 p_{\text{in}}}{\mathrm{d}t^2} + p_{\text{out}}. \tag{A.21}$$

Finally, inserting Eq. (A.21) into Eq. (A.16) leads to

$$C\frac{\mathrm{d}p_{\text{in}}}{\mathrm{d}t} + \frac{p_{\text{in}} - p_{\text{out}}}{R} = \left(1 + \frac{Z}{R}\right) q_{\text{in}} + \left(CZ + \frac{L}{R}\right)\frac{\mathrm{d}q_{\text{in}}}{\mathrm{d}t} - \frac{LC}{R}\frac{\mathrm{d}^2 p_{\text{in}}}{\mathrm{d}t^2} + \frac{LCZ}{R}\frac{\mathrm{d}^2 q_{\text{in}}}{\mathrm{d}t^2}. \tag{A.22}$$

A.3. Derivation of the weak form

In this section, the weak form in reference configuration is derived. Starting with the balance law from Eq. (2.40) and multiplying it with a test function $\delta\boldsymbol{u}$ and then integrating it over the reference domain Ω_0. This yields

$$\int_{\Omega_0} \left[\rho_0 \ddot{\boldsymbol{u}} - \nabla_{\boldsymbol{X}} \cdot \boldsymbol{P} - \boldsymbol{b}_0\right] \delta\boldsymbol{u} \, \mathrm{d}V = 0 \quad \forall \delta\boldsymbol{u} \in \mathcal{V}. \tag{A.23}$$

Using the identity

$$\nabla \cdot (\boldsymbol{A}^T \cdot \boldsymbol{b}) = \boldsymbol{b} \cdot (\nabla \cdot \boldsymbol{A}) - \boldsymbol{A} : (\nabla \boldsymbol{b}), \tag{A.24}$$

it follows that

$$\int_{\Omega_0} \nabla_{\boldsymbol{X}} \cdot \boldsymbol{P} \cdot \delta\boldsymbol{u} \, \mathrm{d}V = \int_{\Omega_0} \nabla_{\boldsymbol{X}} \cdot (\boldsymbol{P}\delta\boldsymbol{u}) \, \mathrm{d}V - \int_{\Omega_0} \boldsymbol{P} : \nabla_{\boldsymbol{X}} \delta\boldsymbol{u} \, \mathrm{d}V. \tag{A.25}$$

The divergence theorem (or Gauß theorem) relates the divergence of a vector field in an enclosed volume to the *flux* of the vector field through a closed surface. Thereby, it transforms the volume integral into a surface integral. Applied to the first term of Eq. (A.25), it yields

$$\int_{\Omega_0} \nabla_{\boldsymbol{X}} \cdot (\boldsymbol{P}\delta\boldsymbol{u}) \, \mathrm{d}V = \int_{\Gamma_{\text{n}}} \boldsymbol{P}\boldsymbol{N} \, \mathrm{d}A = \int_{\Gamma_{\text{n}}} \boldsymbol{t}_0 \, \mathrm{d}A. \tag{A.26}$$

Furthermore, using Eq. (2.6), the following holds

$$\boldsymbol{P} : \nabla_{\boldsymbol{X}} \delta\boldsymbol{u} = \boldsymbol{P} : \delta\boldsymbol{F}. \tag{A.27}$$

Inserting Eq. (A.26) and Eq. (A.27) into Eq. (A.25) yields

$$\int_{\Omega_0} \nabla_{\boldsymbol{X}} \cdot \boldsymbol{P} \cdot \delta\boldsymbol{u} \, \mathrm{d}V = \int_{\Gamma_{\text{n}}} \boldsymbol{t}_0 \, \mathrm{d}A - \int_{\Omega_0} \boldsymbol{P} : \delta\boldsymbol{F} \, \mathrm{d}V. \tag{A.28}$$

Inserting Eq. (A.28) into Eq. (A.23) yields

$$\int_{\Omega_0} \rho_0 \ddot{\boldsymbol{u}} \cdot \delta \boldsymbol{u} \, \mathrm{d}V - \int_{\Gamma_\mathrm{n}} \boldsymbol{t}_0 \, \mathrm{d}A + \int_{\Omega_0} \boldsymbol{P} : \delta \boldsymbol{F} \, \mathrm{d}V - \int_{\Omega_0} \boldsymbol{b}_0 \delta \boldsymbol{u} \, \mathrm{d}V = 0 \quad \forall \delta \boldsymbol{u} \in \mathcal{V}. \tag{A.29}$$

Using the definition of the Green-Lagrange strain tensor in Eq.(2.12), it follows that

$$\delta \boldsymbol{E} = \frac{1}{2} \left(\delta \boldsymbol{F}^T \boldsymbol{F} + \boldsymbol{F}^T \delta \boldsymbol{F} \right) = \frac{1}{2} \left(\boldsymbol{F}^T \delta \boldsymbol{F}^T \boldsymbol{F} + \boldsymbol{F}^T \delta \boldsymbol{F} \right) = \boldsymbol{F}^T \delta \boldsymbol{F}. \tag{A.30}$$

Furthermore, it holds that

$$\boldsymbol{P} : \delta \boldsymbol{F} = \underbrace{\boldsymbol{F} \boldsymbol{F}^{-1}}_{=\boldsymbol{I}} \boldsymbol{P} : \delta \boldsymbol{F} = \boldsymbol{F} \underbrace{\boldsymbol{F}^{-1} \boldsymbol{P}}_{\substack{=\boldsymbol{S} \\ \text{see } Eq. \text{ (2.19)}}} : \delta \boldsymbol{F} = \underbrace{\boldsymbol{S}^T}_{\substack{=\boldsymbol{S} \\ \text{see } Eq. \text{ (2.39)}}} : \underbrace{\boldsymbol{F}^T \delta \boldsymbol{F}}_{\substack{=\delta \boldsymbol{E} \\ \text{see } Eq. \text{ (A.30)}}} = \boldsymbol{S} : \delta \boldsymbol{E}. \tag{A.31}$$

Inserting Eq. (A.31) into Eq. (A.29) yields the final form of the weak form in reference configuration

$$\int_{\Omega_0} \rho_0 \ddot{\boldsymbol{u}} \cdot \delta \boldsymbol{u} \, \mathrm{d}V - \int_{\Gamma_\mathrm{n}} \boldsymbol{t}_0 \, \mathrm{d}A + \int_{\Omega_0} \boldsymbol{S} : \delta \boldsymbol{E} \, \mathrm{d}V - \int_{\Omega_0} \boldsymbol{b}_0 \delta \boldsymbol{u} \, \mathrm{d}V = 0 \quad \forall \delta \boldsymbol{u} \in \mathcal{V}. \tag{A.32}$$

A.4. Probability space and random variables

Given a probability space $(\Omega, \mathcal{F}, P)$, the sample space Ω is the set of all possible outcomes, $\mathcal{F}$ the associated σ-algebra and P a probability measure, which satisfies

$$0 \leq P(A) \leq 1, \tag{A.33}$$

$$P(\Omega) = 1, \tag{A.34}$$

$$P(\bigcup_{i=1}^{\infty} A_i) = \sum_{i=1}^{\infty} P(A_i), \tag{A.35}$$

where $A_i \in \mathcal{F}$ accounts for a specific event.
Conditional probability can then be defined by

$$P(A|B) = \frac{P(A \bigcap B)}{P(B)}, \tag{A.36}$$

where $A, B \in \mathcal{F}$ and $P(B) > 0$. Using that $P(A \bigcap B) = P(B \bigcap A)$ is symmetric, the so-called *Bayes' theorem* follows as

$$P(B|A) = \frac{P(A|B)P(B)}{P(A)}. \tag{A.37}$$

Let X be a random variable defined as a measurable function on the sample space Ω. In the continuous case, the probability $P(X = x)$ can be expressed in terms of the Lebesgue integral, which reads

$$P(X) = \int_{\mathcal{B}} P(dx) = \int_{\mathcal{B}} p_X(x) \, dx. \tag{A.38}$$

In this case, $x \in \mathbb{R}^n$ is a real value, $\mathcal{B}$ is the Borel set on $\mathbb{R}^n$ and $p_X : \Omega \mapsto [0, \infty[$ is the so-called *probability density function* (PDF).

The *expected value* or *mean value* of a random variable is defined as

$$E_{p_X}[X] = \int x \, p_X(x) \, dx. \tag{A.39}$$

The variance of the random variable reads

$$V_{p_X}[X] = \int (x - E_{p_X}[Y])^2 p(x) \, dx = E_{p_X}\left[X^2\right] - E_{p_X}[X]^2 . \tag{A.40}$$

The joint PDF $p_{X,Y} : X \times Y \mapsto [0, \infty[$ describes the joint probability for random variable $X \in \mathcal{B}_X$ and $Y \in \mathcal{B}_Y$ and is given by

$$P(X, Y) = \int_{\mathcal{B}_X} \int_{\mathcal{B}_Y} p_{X,Y}(x, y) \, dxdy. \tag{A.41}$$

The conditional probability for X knowing $Y = y$ is defined as

$$P(X|Y = y) = \int_{\mathcal{B}_X} p_X(x|y) \, dx. \tag{A.42}$$

Therein, the conditional PDF reads

$$p_X(x|y) = \frac{p_{X,Y}(x, y)}{p_Y(y)}. \tag{A.43}$$

Using Eq. (A.37) leads to Bayes' theorem as

$$p_X(x|y) = \frac{p_Y(y|x)p_X(x)}{p_Y(y)}, \tag{A.44}$$

where $p_X(x|y)$ is the posterior PDF, $p_Y(y|x)$ is the likelihood, $p_X(x)$ is the prior PDF and $p_Y(y)$ the model evidence.

A.5. L-BFGS and optimization framework

In this section, a brief overview of the limited-memory BFGS (L-BFGS) algorithm and the optimization framework is given. Here, $\boldsymbol{\theta}$ is the parameter to be optimized and $\mathcal{J}$ acts as the objective function. Within the L-BFGS method, the Hessian is not computed directly. Starting with initial guess $\boldsymbol{H}_0 = \boldsymbol{I}$ of the Hessian matrix and $g(\boldsymbol{\theta}) = \frac{\mathrm{d}\mathcal{J}}{\mathrm{d}\boldsymbol{\theta}}$, the update rule for the Hessian at the n-th iteration reads

$$\boldsymbol{s}_n = \boldsymbol{\theta}_{n+1} - \boldsymbol{\theta}_n, \tag{A.45}$$

$$\boldsymbol{y}_n = g(\boldsymbol{\theta}_{n+1}) - g(\boldsymbol{\theta}_n), \tag{A.46}$$

$$\boldsymbol{H}_{n+1} \cdot \boldsymbol{s}_n = \boldsymbol{y}_n. \tag{A.47}$$

To determine a unique $\boldsymbol{H}_{n+1}$, Eq. (A.47) is reformulated as an optimization problem, to which the solution is given by the inverse Hessian, which reads

$$\boldsymbol{H}_{n+1}^{-1} = (\boldsymbol{I} + \frac{\boldsymbol{s}_n \boldsymbol{y}_n}{\boldsymbol{y}_n \cdot \boldsymbol{s}_n}) \boldsymbol{H}_n^{-1} (\boldsymbol{I} + \frac{\boldsymbol{y}_n \boldsymbol{s}_n}{\boldsymbol{y}_n \cdot \boldsymbol{s}_n}) + \frac{\boldsymbol{s}_n \boldsymbol{s}_n}{\boldsymbol{s}_n \cdot \boldsymbol{s}_n}, \tag{A.48}$$

where

$$\boldsymbol{y}_n \cdot \boldsymbol{s}_n > 0, \tag{A.49}$$

has to be fulfilled to guarantee that the matrix $\boldsymbol{H}_{n+1}^{-1}$ is symmetric positive definite. This is achieved using a line search strategy based on the Armijo-Goldstein condition [81].
The storage cost of the non-sparse inverse Hessian is considerably high. Therefore, within the limited-memory BFGS, this matrix is never explicitly constructed. Only the m most recent increments of $\boldsymbol{s}_n$ and $\boldsymbol{y}_n$ are used.
In A.1, the pseudo-code to solve the optimization problem is presented.

```
vector theta_0 = getInitialGuess();
vector F = callForwardProblem(theta_0);
double J_n = evaluateObjectiveFunction(F, theta_0);
vector Grad_n = evaluateObjectiveFunctionGradient(F, theta_0);

vector p = computeSearchDirection(Grad_n);

while(norm(Grad_n) > tol)   // L-BFGS optimization loop
{
    vector s_n = updateStep(s_0, p);

    while(s_n > s_min) // line search
    {
        vector D = callForwardProblem(theta);
        double J_np = evaluateObjectiveFunction(F, theta);
        vector Grad_np = evaluateObjectiveFunctionGradient(F, theta);

        if (J_np - J_n < tol)   // check for sufficient decrease
        {
            J_n = J_np;
            Grad_n = Grad_np;
            break;
        }
        else
        {
            s_n = updateStep(s_n, p);
        }
    }
    p = computeSearchDirection(Grad_n);
}
```

Listing A.1: Optimization framework pseudo code

A.6. Surface matching linearization

In this section, the gradient of the Lagrangian formulation of the objective function from Eq. (2.138) is presented.

Here, the time dependencies are denoted in index notation, e.g., $\theta(t=0)=\theta_0$ and $\theta(t=1)=\theta_1$. First, the gradient of $\mathcal{L}$ with respect to $\boldsymbol{x}_0$ is derived, which reads

$$\frac{\partial \mathcal{L}}{\partial \boldsymbol{x}_0} = \frac{1}{\sigma^2}\frac{\partial D(\mathcal{T},\mathcal{S}_1)}{\partial \boldsymbol{x}_1}\frac{\partial \boldsymbol{x}_1}{\partial \boldsymbol{x}_0} + \int_0^1 \left(\frac{\partial G(\boldsymbol{x},\boldsymbol{S})}{\partial \boldsymbol{x}}\frac{\partial \boldsymbol{x}}{\partial \boldsymbol{x}_0} - \frac{\partial \dot{\boldsymbol{x}}}{\partial \boldsymbol{x}_0}\right)\theta \,\mathrm{d}t. \tag{A.50}$$

Using partial integration, the last part of the integral becomes

$$-\int_0^1 \left(\frac{\partial \dot{\boldsymbol{x}}}{\partial \boldsymbol{x}_0}\right)\theta \,\mathrm{d}t = -\int_0^1 \frac{\partial \boldsymbol{x}}{\partial \boldsymbol{x}_0}\dot{\theta}\,\mathrm{d}t + \theta_0 \underbrace{\frac{\partial \boldsymbol{x}_0}{\partial \boldsymbol{x}_0}}_{=1} - \theta_1 \frac{\partial \boldsymbol{x}_1}{\partial \boldsymbol{x}_0}. \tag{A.51}$$

Inserting Eq. (A.51) into Eq. (A.50) and rearranging yields

$$\frac{\partial \mathcal{L}}{\partial \boldsymbol{x}_0} = \underbrace{\left(\frac{1}{\sigma^2}\frac{\partial D(\mathcal{T},\mathcal{S}_1)}{\partial \boldsymbol{x}_1} - \theta_1\right)}_{\stackrel{!}{=}0,\text{ constraint}}\frac{\partial \boldsymbol{x}_1}{\partial \boldsymbol{x}_0} + \int_0^1 \underbrace{\left(\frac{\partial G(\boldsymbol{x},\boldsymbol{S})}{\partial \boldsymbol{x}}\theta - \dot{\theta}\right)}_{\text{adjoint equation}}\frac{\partial \boldsymbol{x}}{\partial \boldsymbol{x}_0}\,\mathrm{d}t + \theta_0. \tag{A.52}$$

The first adjoint equation and its initial condition are given by

$$\frac{\partial G(\boldsymbol{x},\boldsymbol{S})}{\partial \boldsymbol{x}}\theta - \dot{\theta} = 0, \quad \text{with } \frac{1}{\sigma^2}\frac{\partial D(\mathcal{T},\mathcal{S}_1)}{\partial \boldsymbol{x}_1} = \theta_1. \tag{A.53}$$

The final gradient results in

$$\frac{\partial \mathcal{L}}{\partial \boldsymbol{x}_0} = \theta_0. \tag{A.54}$$

Second, the gradient of $\mathcal{L}$ with respect to $\boldsymbol{S}_0$ is derived, which reads

$$\begin{aligned}\frac{\partial \mathcal{L}}{\partial \boldsymbol{S}_0} = \frac{1}{\sigma^2}\frac{\partial D(\mathcal{T},\mathcal{S}_1)}{\partial \boldsymbol{x}_1}\frac{\partial \boldsymbol{x}_1}{\partial \boldsymbol{S}_0} + \left.\frac{\partial E_{\text{kin}}}{\partial \boldsymbol{S}_0}\right|_{t=0} + \int_0^1 \left(\frac{\partial F(\boldsymbol{S})}{\partial \boldsymbol{S}}\frac{\partial \boldsymbol{S}}{\partial \boldsymbol{S}_0} - \frac{\partial \dot{\boldsymbol{S}}}{\partial \boldsymbol{S}_0}\right)\xi \,\mathrm{d}t \\ + \int_0^1 \left(\frac{\partial G(\boldsymbol{x},\boldsymbol{S})}{\partial \boldsymbol{S}}\frac{\partial \boldsymbol{S}}{\partial \boldsymbol{S}_0} + \frac{\partial G(\boldsymbol{x},\boldsymbol{S})}{\partial \boldsymbol{x}}\frac{\partial \boldsymbol{x}}{\partial \boldsymbol{S}_0} - \frac{\partial \dot{\boldsymbol{x}}}{\partial \boldsymbol{S}_0}\right)\theta \,\mathrm{d}t.\end{aligned} \tag{A.55}$$

Using partial integration, the temporal derivatives become

$$-\int_0^1 \left(\frac{\partial \dot{\boldsymbol{S}}}{\partial \boldsymbol{S}_0}\right)\xi \,\mathrm{d}t = -\int_0^1 \frac{\partial \boldsymbol{S}}{\partial \boldsymbol{S}_0}\dot{\xi}\,\mathrm{d}t + \xi_0 \underbrace{\frac{\partial \boldsymbol{S}_0}{\partial \boldsymbol{S}_0}}_{=1} - \xi_1 \frac{\partial \boldsymbol{S}_1}{\partial \boldsymbol{S}_0}, \tag{A.56}$$

$$-\int_0^1 \left(\frac{\partial \dot{\boldsymbol{x}}}{\partial \boldsymbol{S}_0}\right)\theta \,\mathrm{d}t = -\int_0^1 \frac{\partial \boldsymbol{x}}{\partial \boldsymbol{S}_0}\dot{\theta}\,\mathrm{d}t + \theta_0 \underbrace{\frac{\partial \boldsymbol{x}_0}{\partial \boldsymbol{S}_0}}_{=0} - \theta_1 \frac{\partial \boldsymbol{x}_1}{\partial \boldsymbol{S}_0}. \tag{A.57}$$

Inserting Eq. (A.56) and Eq. (A.57) into Eq. (A.55) and rearranging yields

$$\begin{aligned}\frac{\partial \mathcal{L}}{\partial \boldsymbol{S}_0} = &\underbrace{\left(\frac{1}{\sigma^2}\frac{\partial D(\mathcal{T},\mathcal{S}_1)}{\partial \boldsymbol{x}_1} - \theta_1\right)}_{=0,\text{ see (A.53)}}\frac{\partial \boldsymbol{x}_1}{\partial \boldsymbol{S}_0} + \left.\frac{\partial E_{\text{kin}}}{\partial \boldsymbol{S}_0}\right|_{t=0} \\ &+ \int_0^1 \underbrace{\left(\frac{\partial F(\boldsymbol{S})}{\partial \boldsymbol{S}}\xi - \dot{\xi} + \frac{\partial G(\boldsymbol{x},\boldsymbol{S})}{\partial \boldsymbol{S}}\theta\right)}_{\text{adjoint equation}}\frac{\partial \boldsymbol{S}}{\partial \boldsymbol{S}_0}\,\mathrm{d}t + \xi_0 - \underbrace{\xi_1}_{\substack{\overset{!}{=}0\\ \text{constraint}}}\frac{\partial \boldsymbol{S}_1}{\partial \boldsymbol{S}_0} \\ &+ \int_0^1 \underbrace{\left(\frac{\partial G(\boldsymbol{x},\boldsymbol{S})}{\partial \boldsymbol{x}} - \dot{\theta}\right)}_{=0,\text{ see (A.53)}}\frac{\partial \boldsymbol{x}}{\partial \boldsymbol{S}_0}\,\mathrm{d}t.\end{aligned} \tag{A.58}$$

The second adjoint equation and its initial condition are given by

$$\frac{\partial F(\boldsymbol{S})}{\partial \boldsymbol{S}}\xi - \dot{\xi} + \frac{\partial G(\boldsymbol{x},\boldsymbol{S})}{\partial \boldsymbol{S}}\theta = 0, \quad \text{with } \xi_1 = 0. \tag{A.59}$$

The final gradient results in

$$\frac{\partial \mathcal{L}}{\partial \boldsymbol{S}_0} = \xi_0 + \left.\frac{\partial E_{\text{kin}}}{\partial \boldsymbol{S}_0}\right|_{t=0}. \tag{A.60}$$

The evaluation of the gradient starts with solving the first adjoint equation (A.53) for θ_0. Thereafter, the solution is inserted into the second adjoint equation (A.59), which is solved for ξ_0. Finally, the gradients in Eq. (A.54) and Eq. (A.60) are computed.
However, for their evaluation, the partial derivatives are needed, and they are derived in the following section.

Partial derivatives

The partial derivative of the surface measurement D is given in Eq. (2.124). For the sake of simplicity, the Kronecker-delta function is used, see Eq. (2.128). Further, the different gradients of the kernel function are given by

$$\frac{\partial k(\boldsymbol{x}_i,\boldsymbol{c}_k)}{\partial \boldsymbol{x}_j} = \frac{-2}{{\sigma_W}^2}\delta_{ij}\; k(\boldsymbol{x}_i,\boldsymbol{c}_k)(\boldsymbol{x}_i - \boldsymbol{c}_k), \tag{A.61}$$

$$\frac{\partial k(\boldsymbol{x}_i,\boldsymbol{c}_k)}{\partial \boldsymbol{c}_j} = \frac{2}{{\sigma_W}^2}\delta_{jk}\; k(\boldsymbol{x}_i,\boldsymbol{c}_k)(\boldsymbol{x}_i - \boldsymbol{c}_k), \tag{A.62}$$

$$\frac{\partial k(\boldsymbol{c}_i,\boldsymbol{c}_k)}{\partial \boldsymbol{c}_j} = \frac{-2}{{\sigma_W}^2}(\delta_{ij} - \delta_{jk})\; k(\boldsymbol{c}_i,\boldsymbol{c}_k)(\boldsymbol{c}_i - \boldsymbol{c}_k). \tag{A.63}$$

The kinetic energy at time $t = 0$ is given by

$$E_{\text{kin}}\Big|_{t=0} = \frac{1}{2}\sum_{k=1}^{n_{\text{cp}}}\sum_{p=1}^{n_{\text{cp}}}\boldsymbol{\alpha}_{0k}^T k(\boldsymbol{c}_{0k},\boldsymbol{c}_{0p})\boldsymbol{\alpha}_{0p}. \tag{A.64}$$

The derivative with respect to the initial control points $\boldsymbol{c}_0$ using Eq. (A.63) reads

$$\begin{aligned}\left.\frac{\partial E_{\text{kin}}}{\partial \boldsymbol{c}_{0j}}\right|_{t=0} &= \frac{1}{2}\sum_{k=1}^{n_{\text{cp}}}\sum_{p=1}^{n_{\text{cp}}} \boldsymbol{\alpha}_{0k}^T \frac{\partial k(\boldsymbol{c}_{0k},\boldsymbol{c}_{0p})}{\partial \boldsymbol{c}_{0j}}\boldsymbol{\alpha}_{0p}, \\ &= \frac{-1}{{\sigma_W}^2}\sum_{k=1}^{n_{\text{cp}}}\sum_{p=1}^{n_{\text{cp}}} \boldsymbol{\alpha}_{0k}^T(\delta_{jk}-\delta_{jp})\; k(\boldsymbol{c}_{0k},\boldsymbol{c}_{0p})(\boldsymbol{c}_{0k}-\boldsymbol{c}_{0p})\boldsymbol{\alpha}_{0p}.\end{aligned} \tag{A.65}$$

The derivative with respect to the initial momenta $\boldsymbol{\alpha}_0$ results in

$$\begin{aligned}\left.\frac{\partial E_{\text{kin}}}{\partial \boldsymbol{\alpha}_{0j}}\right|_{t=0} &= \frac{1}{2}\sum_{k=1}^{n_{\text{cp}}}\sum_{p=1}^{n_{\text{cp}}} k(\boldsymbol{c}_{0k},\boldsymbol{c}_{0p})\frac{\partial \boldsymbol{\alpha}_{0k}^T\boldsymbol{\alpha}_{0p}}{\partial \boldsymbol{\alpha}_{0j}}, \\ &= \frac{1}{2}\sum_{k=1}^{n_{\text{cp}}}\sum_{p=1}^{n_{\text{cp}}} k(\boldsymbol{c}_{0k},\boldsymbol{c}_{0p})\left[\frac{\partial \boldsymbol{\alpha}_{0k}^T}{\partial \boldsymbol{\alpha}_{0j}}\boldsymbol{\alpha}_{0p} + \boldsymbol{\alpha}_{0k}^T\frac{\partial \boldsymbol{\alpha}_{0p}}{\partial \boldsymbol{\alpha}_{0j}}\right], \\ &= \frac{1}{2}\sum_{k=1}^{n_{\text{cp}}}\sum_{p=1}^{n_{\text{cp}}} k(\boldsymbol{c}_{0k},\boldsymbol{c}_{0p})\left[\delta_{jk}\boldsymbol{\alpha}_{0p} + \boldsymbol{\alpha}_{0k}^T\delta_{jp}\right].\end{aligned} \tag{A.66}$$

The flow function for a surface point i is given by

$$G(\boldsymbol{x}_i,\boldsymbol{S}) = \dot{\boldsymbol{x}}_i = \sum_{k=1}^{n_{\text{cp}}} k(\boldsymbol{x}_i,\boldsymbol{c}_k)\boldsymbol{\alpha}_k. \tag{A.67}$$

Its derivative with respect to the position $\boldsymbol{x}$ using Eq. (A.61) reads

$$\begin{aligned}\frac{\partial G(\boldsymbol{x}_i,\boldsymbol{S})}{\partial \boldsymbol{x}_j} &= \sum_{k=1}^{n_{\text{cp}}} \frac{\partial k(\boldsymbol{x}_i,\boldsymbol{c}_k)}{\partial \boldsymbol{x}_j}\boldsymbol{\alpha}_k, \\ &= \frac{-2}{{\sigma_W}^2}\delta_{ij}\sum_{k=1}^{n_{\text{cp}}} k(\boldsymbol{x}_i,\boldsymbol{c}_k)(\boldsymbol{x}_i-\boldsymbol{c}_k)\boldsymbol{\alpha}_k.\end{aligned} \tag{A.68}$$

The derivative with respect to the control points $\boldsymbol{c}$ using Eq. (A.62) is given by

$$\begin{aligned}\frac{\partial G(\boldsymbol{x}_i,\boldsymbol{S})}{\partial \boldsymbol{c}_j} &= \sum_{k=1}^{n_{\text{cp}}} \frac{\partial k(\boldsymbol{x}_i,\boldsymbol{c}_k)}{\partial \boldsymbol{c}_j}\boldsymbol{\alpha}_k, \\ &= \frac{2}{{\sigma_W}^2}\sum_{k=1}^{n_{\text{cp}}} \delta_{jk}\; k(\boldsymbol{x}_i,\boldsymbol{c}_k)(\boldsymbol{x}_i-\boldsymbol{c}_k)\boldsymbol{\alpha}_k, \\ &= \frac{2}{{\sigma_W}^2}k(\boldsymbol{x}_i,\boldsymbol{c}_j)(\boldsymbol{x}_i-\boldsymbol{c}_j)\boldsymbol{\alpha}_j.\end{aligned} \tag{A.69}$$

The derivative with respect to the momenta $\boldsymbol{\alpha}$ results in

$$\begin{aligned}\frac{\partial G(\boldsymbol{x}_i,\boldsymbol{S})}{\partial \boldsymbol{\alpha}_j} &= \sum_{k=1}^{n_{\text{cp}}} k(\boldsymbol{x}_i,\boldsymbol{c}_k)\frac{\partial \boldsymbol{\alpha}_k}{\partial \boldsymbol{\alpha}_j}, \\ &= \sum_{k=1}^{n_{\text{cp}}} k(\boldsymbol{x}_i,\boldsymbol{c}_k)\delta_{jk}\boldsymbol{I}_3, \\ &= k(\boldsymbol{x}_i,\boldsymbol{c}_j)\boldsymbol{I}_3.\end{aligned} \tag{A.70}$$

The shoot function for the control points is given by

$$F_k^c(\boldsymbol{S}) = \dot{\boldsymbol{c}}_k = \sum_{p=1}^{n_{\text{cp}}} k(\boldsymbol{c}_k, \boldsymbol{c}_p)\boldsymbol{\alpha}_p. \tag{A.71}$$

Its derivative with respect to the control points $\boldsymbol{c}$ using Eq. (A.63) reads

$$\begin{aligned}
\frac{\partial F_k^c}{\partial \boldsymbol{c}_j} &= \sum_{p=1}^{n_{\text{cp}}} \frac{\partial k(\boldsymbol{c}_k, \boldsymbol{c}_p)}{\partial \boldsymbol{c}_j}\boldsymbol{\alpha}_p, \\
&= \frac{-2}{{\sigma_W}^2} \sum_{p=1}^{n_{\text{cp}}} (\delta_{jk} - \delta_{jp})\; k(\boldsymbol{c}_k, \boldsymbol{c}_p)(\boldsymbol{c}_k - \boldsymbol{c}_p)\boldsymbol{\alpha}_p, \\
&= \frac{-2}{{\sigma_W}^2}\delta_{jk} \left[\sum_{p=1}^{n_{\text{cp}}} k(\boldsymbol{c}_k, \boldsymbol{c}_p)(\boldsymbol{c}_k - \boldsymbol{c}_p)\boldsymbol{\alpha}_p\right] \\
&\quad + \frac{2}{{\sigma_W}^2} \left[\sum_{p=1}^{n_{\text{cp}}} \delta_{jp}\; k(\boldsymbol{c}_k, \boldsymbol{c}_p)(\boldsymbol{c}_k - \boldsymbol{c}_p)\boldsymbol{\alpha}_p\right], \\
&= \frac{-2}{{\sigma_W}^2}\delta_{jk} \left[\sum_{p=1}^{n_{\text{cp}}} k(\boldsymbol{c}_k, \boldsymbol{c}_p)(\boldsymbol{c}_k - \boldsymbol{c}_p)\boldsymbol{\alpha}_p\right] + \frac{2}{{\sigma_W}^2} k(\boldsymbol{c}_k, \boldsymbol{c}_j)(\boldsymbol{c}_k - \boldsymbol{c}_j(\boldsymbol{\alpha}_j.
\end{aligned} \tag{A.72}$$

The derivative with respect to the momenta $\boldsymbol{\alpha}$ is given by

$$\begin{aligned}
\frac{\partial F_k^c}{\partial \boldsymbol{\alpha}_j} &= \sum_{p=1}^{n_{\text{cp}}} k(\boldsymbol{c}_k, \boldsymbol{c}_p)\frac{\partial \boldsymbol{\alpha}_p}{\partial \boldsymbol{\alpha}_j}, \\
&= \sum_{p=1}^{n_{\text{cp}}} k(\boldsymbol{c}_k, \boldsymbol{c}_p)\delta_{jp}\; \boldsymbol{I}_3, \\
&= k(\boldsymbol{c}_k, \boldsymbol{c}_j)\boldsymbol{I}_3.
\end{aligned} \tag{A.73}$$

The shoot function for the momenta is given by

$$\begin{aligned}
F_k^\alpha(\boldsymbol{S}) = \dot{\boldsymbol{\alpha}}_k &= -\sum_{p=1}^{n_{\text{cp}}} \boldsymbol{\alpha}_k^T \boldsymbol{\alpha}_p \nabla_1 k(\boldsymbol{c}_k, \boldsymbol{c}_p), \\
&= \frac{2}{{\sigma_W}^2} \sum_{p=1}^{n_{\text{cp}}} \boldsymbol{\alpha}_k^T \boldsymbol{\alpha}_p k(\boldsymbol{c}_k, \boldsymbol{c}_p)(\boldsymbol{c}_k - \boldsymbol{c}_p).
\end{aligned} \tag{A.74}$$

The derivative with respect to the control points $\boldsymbol{c}$ using Eq. (A.63) results in

$$
\begin{aligned}
\frac{\partial F_k^\alpha}{\partial \boldsymbol{c}_j} &= \frac{2}{{\sigma_W}^2} \sum_{p=1}^{n_{\mathrm{cp}}} \boldsymbol{\alpha}_k^T \boldsymbol{\alpha}_p \left[\frac{\partial k(\boldsymbol{c}_k, \boldsymbol{c}_p)}{\partial \boldsymbol{c}_j} (\boldsymbol{c}_k - \boldsymbol{c}_p) + k(\boldsymbol{c}_k, \boldsymbol{c}_p) \frac{\partial (\boldsymbol{c}_k - \boldsymbol{c}_p)}{\partial \boldsymbol{c}_j} \right], \\
&= \frac{2}{{\sigma_W}^2} \left[\sum_{p=1}^{n_{\mathrm{cp}}} \boldsymbol{\alpha}_k^T \boldsymbol{\alpha}_p \frac{-2}{{\sigma_W}^2} (\delta_{jk} - \delta_{jp})\, k(\boldsymbol{c}_k, \boldsymbol{c}_p) (\boldsymbol{c}_k - \boldsymbol{c}_p)^2 \right] \\
&\quad + \frac{2}{{\sigma_W}^2} \left[\sum_{p=1}^{n_{\mathrm{cp}}} \boldsymbol{\alpha}_k^T \boldsymbol{\alpha}_p k(\boldsymbol{c}_k, \boldsymbol{c}_p) (\delta_{jk} - \delta_{jp}) \right], \\
&= \frac{-4}{{\sigma_W}^4} \delta_{jk} \left[\sum_{p=1}^{n_{\mathrm{cp}}} \boldsymbol{\alpha}_k^T \boldsymbol{\alpha}_p k(\boldsymbol{c}_k, \boldsymbol{c}_p) (\boldsymbol{c}_k - \boldsymbol{c}_p)^2 \right] \\
&\quad + \frac{4}{{\sigma_W}^4} \left[\sum_{p=1}^{n_{\mathrm{cp}}} \boldsymbol{\alpha}_k^T \boldsymbol{\alpha}_p \delta_{jp}\, k(\boldsymbol{c}_k, \boldsymbol{c}_p) (\boldsymbol{c}_k - \boldsymbol{c}_p)^2 \right] \\
&\quad + \frac{2}{{\sigma_W}^2} \delta_{jk} \left[\sum_{p=1}^{n_{\mathrm{cp}}} \boldsymbol{\alpha}_k^T \boldsymbol{\alpha}_p k(\boldsymbol{c}_k, \boldsymbol{c}_p) \right] - \frac{2}{{\sigma_W}^2} \left[\sum_{p=1}^{n_{\mathrm{cp}}} \boldsymbol{\alpha}_k^T \boldsymbol{\alpha}_p k(\boldsymbol{c}_k, \boldsymbol{c}_p) \delta_{jp} \right], \\
&= \frac{-4}{{\sigma_W}^4} \delta_{jk} \left[\sum_{p=1}^{n_{\mathrm{cp}}} \boldsymbol{\alpha}_k^T \boldsymbol{\alpha}_p k(\boldsymbol{c}_k, \boldsymbol{c}_p) (\boldsymbol{c}_k - \boldsymbol{c}_p)^2 \right] + \frac{4}{{\sigma_W}^4} \boldsymbol{\alpha}_k^T \boldsymbol{\alpha}_j k(\boldsymbol{c}_k, \boldsymbol{c}_j) (\boldsymbol{c}_k - \boldsymbol{c}_j)^2 \\
&\quad + \frac{2}{{\sigma_W}^2} \delta_{jk} \left[\sum_{p=1}^{n_{\mathrm{cp}}} \boldsymbol{\alpha}_k^T \boldsymbol{\alpha}_p k(\boldsymbol{c}_k, \boldsymbol{c}_p) \right] - \frac{2}{{\sigma_W}^2} \boldsymbol{\alpha}_k^T \boldsymbol{\alpha}_j k(\boldsymbol{c}_k, \boldsymbol{c}_j).
\end{aligned}
\tag{A.75}
$$

The derivative with respect to the momenta $\boldsymbol{\alpha}$ reads

$$
\begin{aligned}
\frac{\partial F_k^\alpha}{\partial \boldsymbol{\alpha}_j} &= \frac{2}{{\sigma_W}^2} \sum_{p=1}^{n_{\mathrm{cp}}} \frac{\partial \boldsymbol{\alpha}_k^T \boldsymbol{\alpha}_p}{\partial \boldsymbol{\alpha}_j} k(\boldsymbol{c}_k, \boldsymbol{c}_p) (\boldsymbol{c}_k - \boldsymbol{c}_p), \\
&= \frac{2}{{\sigma_W}^2} \sum_{p=1}^{n_{\mathrm{cp}}} \left[\frac{\partial \boldsymbol{\alpha}_k^T}{\partial \boldsymbol{\alpha}_j} \boldsymbol{\alpha}_p + \boldsymbol{\alpha}_k^T \frac{\partial \boldsymbol{\alpha}_p}{\partial \boldsymbol{\alpha}_j} \right] k(\boldsymbol{c}_k, \boldsymbol{c}_p) (\boldsymbol{c}_k - \boldsymbol{c}_p), \\
&= \frac{2}{{\sigma_W}^2} \sum_{p=1}^{n_{\mathrm{cp}}} \left[\delta_{jk} \boldsymbol{\alpha}_p + \boldsymbol{\alpha}_k^T \delta_{jp} \right] k(\boldsymbol{c}_k, \boldsymbol{c}_p) (\boldsymbol{c}_k - \boldsymbol{c}_p), \\
&= \frac{2}{{\sigma_W}^2} \delta_{jk} \left[\sum_{p=1}^{n_{\mathrm{cp}}} \boldsymbol{\alpha}_p k(\boldsymbol{c}_k, \boldsymbol{c}_p) (\boldsymbol{c}_k - \boldsymbol{c}_p) \right] \\
&\quad + \frac{2}{{\sigma_W}^2} \left[\sum_{p=1}^{n_{\mathrm{cp}}} \boldsymbol{\alpha}_k^T \delta_{jp}\, k(\boldsymbol{c}_k, \boldsymbol{c}_p) (\boldsymbol{c}_k - \boldsymbol{c}_p) \right], \\
&= \frac{2}{{\sigma_W}^2} \delta_{jk} \left[\sum_{p=1}^{n_{\mathrm{cp}}} \boldsymbol{\alpha}_p k(\boldsymbol{c}_k, \boldsymbol{c}_p) (\boldsymbol{c}_k - \boldsymbol{c}_p) \right] + \frac{2}{{\sigma_W}^2} \boldsymbol{\alpha}_k^T k(\boldsymbol{c}_k, \boldsymbol{c}_j) (\boldsymbol{c}_k - \boldsymbol{c}_j).
\end{aligned}
\tag{A.76}
$$

B. Cardiac mechanics model

B.1. Active stress discretization

To solve the time-dependent ODE (3.4), the Backward-Euler scheme is used. The initial value is set to be $\tau_{\mathrm{a}}(0) = 0$. The Backward-Euler scheme is obtained by using the one-step-θ method with $\theta = 1$, see Eq. (2.72). The solution of the active stress model reads

$$\begin{aligned} \frac{{\tau_{\mathrm{a}}}^{n} - {\tau_{\mathrm{a}}}^{n-1}}{\Delta t} &= f({\tau_{\mathrm{a}}}^{n}), \\ \frac{{\tau_{\mathrm{a}}}^{n} - {\tau_{\mathrm{a}}}^{n-1}}{\Delta t} &= -|u^n|{\tau_{\mathrm{a}}}^{n} + \sigma_0 \max(0, u^n), \\ {\tau_{\mathrm{a}}}^{n} + \Delta t\, |u^n|{\tau_{\mathrm{a}}}^{n} &= {\tau_{\mathrm{a}}}^{n-1} + \Delta t\, \sigma_0 \max(0, u^n), \\ {\tau_{\mathrm{a}}}^{n} &= \frac{{\tau_{\mathrm{a}}}^{n-1} + \Delta t\, \sigma_0 \max(0, u^n)}{1 + \Delta t\, |u^n|}. \end{aligned} \tag{B.1}$$

Here, n denotes the current time step, and thus, the new active stress value is entirely defined by its previous values.

B.2. Growth material linearization

In order to solve the identification problem Eq. (2.96), the gradient of $\boldsymbol{S}$ with respect to the growth stretch ϑ is needed, see Eq. (2.112). Using the chain rule, the gradient becomes

$$\frac{\partial \boldsymbol{S}}{\partial \vartheta} = \frac{\partial \boldsymbol{S}}{\partial \boldsymbol{F}_{\mathrm{g}}} : \frac{\partial \boldsymbol{F}_{\mathrm{g}}}{\partial \vartheta}. \tag{B.2}$$

Using Eq. (3.52), the following holds

$$\boldsymbol{F}^T = {\boldsymbol{F}_{\mathrm{g}}}^T {\boldsymbol{F}_{\mathrm{e}}}^T, \tag{B.3}$$

$$\boldsymbol{F}^{-1} = {\boldsymbol{F}_{\mathrm{g}}}^{-1} {\boldsymbol{F}_{\mathrm{e}}}^{-1}, \tag{B.4}$$

$$\boldsymbol{F}^{-T} = {\boldsymbol{F}_{\mathrm{e}}}^{-T} {\boldsymbol{F}_{\mathrm{g}}}^{-T}. \tag{B.5}$$

Following Eq. (2.14), it holds

$$\boldsymbol{C} = \boldsymbol{F}^T \boldsymbol{F} = {\boldsymbol{F}_{\mathrm{g}}}^T \underbrace{{\boldsymbol{F}_{\mathrm{e}}}^T \boldsymbol{F}_{\mathrm{e}}}_{=\boldsymbol{C}_{\mathrm{e}}} \boldsymbol{F}_{\mathrm{g}} = {\boldsymbol{F}_{\mathrm{g}}}^T \boldsymbol{C}_{\mathrm{e}} \boldsymbol{F}_{\mathrm{g}}. \tag{B.6}$$

From Eq. (2.18) and Eq. (2.19), it follows that

$$\boldsymbol{S} = J\boldsymbol{F}^{-1}\boldsymbol{\sigma}\boldsymbol{F}^{-T} = J{\boldsymbol{F}_{\mathrm{g}}}^{-1} \underbrace{J{\boldsymbol{F}_{\mathrm{e}}}^{-1}\boldsymbol{\sigma}{\boldsymbol{F}_{\mathrm{e}}}^{-T}}_{=\boldsymbol{S}_{\mathrm{e}}} {\boldsymbol{F}_{\mathrm{g}}}^{-T} = {\boldsymbol{F}_{\mathrm{g}}}^{-1} \boldsymbol{S}_{\mathrm{e}} {\boldsymbol{F}_{\mathrm{g}}}^{-T}. \tag{B.7}$$

The first derivative in Eq. (B.2) can be computed using chain rule, and Eq. (B.7), leading to

$$\begin{aligned}\frac{\partial \boldsymbol{S}}{\partial \boldsymbol{F}_\mathrm{g}} &= \frac{\partial}{\partial \boldsymbol{F}_\mathrm{g}}(\boldsymbol{F}_\mathrm{g}{}^{-1}\boldsymbol{S}_\mathrm{e}\boldsymbol{F}_\mathrm{g}{}^{-T}),\\ &= \frac{\partial \boldsymbol{F}_\mathrm{g}{}^{-1}}{\partial \boldsymbol{F}_\mathrm{g}}\underbrace{\boldsymbol{S}_\mathrm{e}\boldsymbol{F}_\mathrm{g}{}^{-T}}_{\substack{=\boldsymbol{F}_\mathrm{g}\boldsymbol{S}\\ \text{see (B.7)}}} + \boldsymbol{F}_\mathrm{g}{}^{-1}\frac{\partial \boldsymbol{S}_\mathrm{e}}{\partial \boldsymbol{F}_\mathrm{g}}\boldsymbol{F}_\mathrm{g}{}^{-T} + \underbrace{\boldsymbol{F}_\mathrm{g}{}^{-1}\boldsymbol{S}_\mathrm{e}}_{\substack{=\boldsymbol{S}\boldsymbol{F}_\mathrm{g}{}^{T}\\ \text{see (B.7)}}}\frac{\partial \boldsymbol{F}_\mathrm{g}{}^{-T}}{\partial \boldsymbol{F}_\mathrm{g}}.\end{aligned} \tag{B.8}$$

Using that

$$\frac{\partial \boldsymbol{F}_\mathrm{g}{}^{-1}}{\partial \boldsymbol{F}_\mathrm{g}} = -\boldsymbol{F}_\mathrm{g}{}^{-2}, \tag{B.9}$$

$$\frac{\partial \boldsymbol{F}_\mathrm{g}{}^{-T}}{\partial \boldsymbol{F}_\mathrm{g}} = -\boldsymbol{F}_\mathrm{g}{}^{-2T}, \tag{B.10}$$

Eq. (B.8) becomes

$$\frac{\partial \boldsymbol{S}}{\partial \boldsymbol{F}_\mathrm{g}} = -\boldsymbol{F}_\mathrm{g}{}^{-1}\boldsymbol{S} + \boldsymbol{F}_\mathrm{g}{}^{-1}\frac{\partial \boldsymbol{S}_\mathrm{e}}{\partial \boldsymbol{F}_\mathrm{g}}\boldsymbol{F}_\mathrm{g}{}^{-T} - \boldsymbol{S}\boldsymbol{F}_\mathrm{g}{}^{-T}. \tag{B.11}$$

The partial derivative of $\boldsymbol{S}_\mathrm{e}$ with respect to $\boldsymbol{F}_\mathrm{g}$ is given by

$$\frac{\partial \boldsymbol{S}_\mathrm{e}}{\partial \boldsymbol{F}_\mathrm{g}} = \underbrace{\frac{\partial \boldsymbol{S}_\mathrm{e}}{\partial \boldsymbol{C}_\mathrm{e}}}_{\substack{=\frac{1}{2}\mathbb{C}_\mathrm{e}\\ \text{see (2.32)}}} : \frac{\partial \boldsymbol{C}_\mathrm{e}}{\partial \boldsymbol{C}}\frac{\partial \boldsymbol{C}}{\partial \boldsymbol{F}_\mathrm{g}} \tag{B.12}$$

Using Eq. (B.6), it follows that

$$\begin{aligned}\frac{\partial \boldsymbol{C}_\mathrm{e}}{\partial \boldsymbol{C}} &= \frac{\partial}{\partial \boldsymbol{C}}(\boldsymbol{F}_\mathrm{g}{}^{-T}\boldsymbol{C}\boldsymbol{F}_\mathrm{g}{}^{-1}),\\ &= \boldsymbol{F}_\mathrm{g}{}^{-T}\boldsymbol{F}_\mathrm{g}{}^{-1},\\ &= \boldsymbol{I},\end{aligned} \tag{B.13}$$

and

$$\begin{aligned}\frac{\partial \boldsymbol{C}}{\partial \boldsymbol{F}_\mathrm{g}} &= \frac{\partial}{\partial \boldsymbol{F}_\mathrm{g}}(\boldsymbol{F}_\mathrm{g}{}^{T}\boldsymbol{C}_\mathrm{e}\boldsymbol{F}_\mathrm{g}),\\ &= \frac{\partial \boldsymbol{F}_\mathrm{g}{}^{T}}{\partial \boldsymbol{F}_\mathrm{g}}\underbrace{\boldsymbol{C}_\mathrm{e}\boldsymbol{F}_\mathrm{g}}_{\substack{=\boldsymbol{F}_\mathrm{g}{}^{-T}\boldsymbol{C}\\ \text{see (B.6)}}} + \boldsymbol{F}_\mathrm{g}{}^{T}\frac{\partial \boldsymbol{C}_\mathrm{e}}{\partial \boldsymbol{F}_\mathrm{g}}\boldsymbol{F}_\mathrm{g} + \underbrace{\boldsymbol{F}_\mathrm{g}{}^{T}\boldsymbol{C}_\mathrm{e}}_{\substack{=\boldsymbol{C}\boldsymbol{F}_\mathrm{g}{}^{-1}\\ \text{see (B.6)}}}\frac{\partial \boldsymbol{F}_\mathrm{g}}{\partial \boldsymbol{F}_\mathrm{g}},\\ &= \boldsymbol{F}_\mathrm{g}{}^{-T}\boldsymbol{C} + \boldsymbol{C}\boldsymbol{F}_\mathrm{g}{}^{-1}.\end{aligned} \tag{B.14}$$

Following Eq. (B.13) and Eq. (B.14), the partial derivative of $\boldsymbol{S}_\mathrm{e}$ with respect to $\boldsymbol{F}_\mathrm{g}$ becomes

$$\frac{\partial \boldsymbol{S}_\mathrm{e}}{\partial \boldsymbol{F}_\mathrm{g}} = \frac{1}{2}\mathbb{C}_\mathrm{e} : \left[\boldsymbol{F}_\mathrm{g}{}^{-T}\boldsymbol{C} + \boldsymbol{C}\boldsymbol{F}_\mathrm{g}{}^{-1}\right]. \tag{B.15}$$

Inserting Eq. (B.15) into Eq. (B.11), the partial derivative of $\boldsymbol{S}$ with respect to $\boldsymbol{F}_{\mathrm{g}}$ becomes

$$\frac{\partial \boldsymbol{S}}{\partial \boldsymbol{F}_{\mathrm{g}}} = -\boldsymbol{F}_{\mathrm{g}}{}^{-1}\boldsymbol{S} + \boldsymbol{F}_{\mathrm{g}}{}^{-1}\left[\frac{1}{2}\mathbb{C}_{\mathrm{e}} : \left[\boldsymbol{F}_{\mathrm{g}}{}^{-T}\boldsymbol{C} + \boldsymbol{C}\boldsymbol{F}_{\mathrm{g}}{}^{-1}\right]\right]\boldsymbol{F}_{\mathrm{g}}{}^{-T} - \boldsymbol{S}\boldsymbol{F}_{\mathrm{g}}{}^{-T}. \tag{B.16}$$

The second derivative from Eq. (B.2) can be computed using the growth law from Eq. (3.57) and it reads

$$\frac{\partial \boldsymbol{F}_{\mathrm{g}}}{\partial \vartheta} = \boldsymbol{f}_0 \otimes \boldsymbol{f}_0 - \frac{1}{2}\vartheta^{-1/2}(\boldsymbol{s}_0 \otimes \boldsymbol{s}_0 + \boldsymbol{r}_0 \otimes \boldsymbol{r}_0). \tag{B.17}$$

Using Eq. (B.16) and Eq. (B.17), the gradient of $\boldsymbol{S}$ with respect to the growth stretch ϑ can be computed, see Eq. (B.2).
Another way to compute this gradient is using a FD approximation, which reads

$$\frac{\partial \boldsymbol{S}}{\partial \vartheta} = \frac{\boldsymbol{S}(\vartheta + \varepsilon) + \boldsymbol{S}(\vartheta)}{\varepsilon}, \tag{B.18}$$

with $\varepsilon \to 0$. Since in the context of the finite element method, $\boldsymbol{S}$ is a 3×3 matrix, the computational cost compared to the analytical linearization is low. However, this approach is only a feasible choice for a low number of parameters ϑ.

C. Signaling network

C.1. Heart growth signaling network

The reference (REF) network is depicted in Fig. C.1. A detailed list of all species within the REF and R&M networks is presented in Tab. C.1.

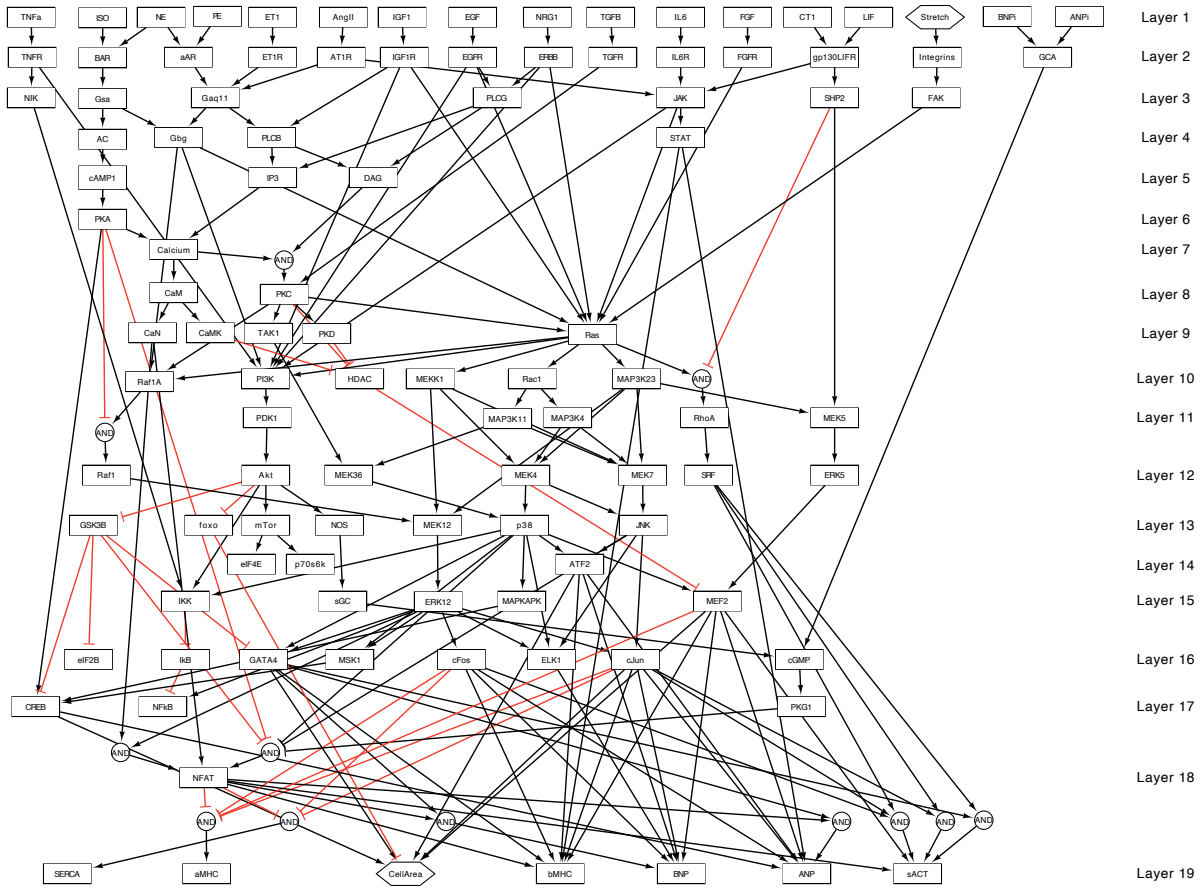

Abbildung C.1.: Reference (REF) network containing 106 species and 193 reactions [41, 45, 77, 128]. It consists of 17 inputs and 7 outputs and is arranged in 19 layers, where all species in a layer depend only on species in previous layers. The species *Stretch* and *CellArea* are represented as hexagons as they are related to mechanical quantities. A black connection denotes a species activation, whereas a red color represents an inhibition [9].

Tabelle C.1.: List of all species within the REF and R&M network. Nodes that do not interact with CellArea are marked with a *

abb.	species	layer
TNFa	tumor necrosis factor	Layer 1
ISO	isoproterenol	
NE	norepinephrine	
PE	phycoerythrin	
ET1	endothelin-1	
AngII	angiotensin II	
IGF1* (g-IGF1)	(global) insulin-like growth factor	
EGF	epidermal growth factor	
NRG1	neuregulin 1	
TGFb	transforming growth factor beta	
IL6	interleukin 6	
FGF	fibroblast growth factor	
CT1	cardiotrophin 1	
LIF	eukemia inhibitory factor	
Stretch	mechanical input	
BNPi*	brain natriuretic peptide input	
ANPi*	atrial natriuretic factor input	
TNFR	tumor necrosis factor receptor	Layer 2
bAR	β-adrenergic receptor	
aAR	α adrenergic receptor	
ET1R	endothelin-1 receptor	
AT1R	angiotensin II receptor	
l-*IGF1*	local insulin-like growth factor	
EGFR	epidermal growth factor receptor	
ERBB	erythroblastic leukemia viral oncogene homolog 2 and 3 or 4	
TGFR	transforming growth factor teceptors	
IL6R	interleukin 6 receptor and interleukin 6 signal transducer gp130	
FGFR	fibroblast growth factor receptor	
gp130LIFR	leukemia inhibitory receptor alpha and interleukin 6 signal transducer	
Integrins	integrins	
GCA*	guanylate cyclase A	
NIK*	NFkB inducing kinase	Layer 3
Gsa	G protein alpha s	
Gaq11	G protein alpha subunit q or 11	
IGF1R	insulin-like growth factor receptor	
PLCg	phopholipase C gamma 1	
JAK	janus kinase 1 or 2	
SHP2	protein tyrosine phosphatase, non-receptor type 11	

FAK	focal adhesion kinase	
AC	adenylyl cyclase	Layer 4
Gbg	G protein beta and gamma subunits	
PLCb	phospholipase C beta	
STAT*	STAT	
cAMP	cyclic AMP	Layer 5
IP3	inositol triphosphate	
DAG	diacylglycerol	
PKA	protein kinase A	Layer 6
Calcium	calcium	Layer 7
CAM	calmodulin	Layer 8
PKC	protein kinase C	
CaN*	calcineurin	Layer 9
CaMK	CaM kinase	
TAK1	TGF-beta activated kinase 1	
PKD	protein kinase D	
Ras	rat sarcoma viral oncogene homolog	
Raf1A	activated raf1	Layer 10
PI3K	phosphatidyl inositol 3 kinase	
HDAC	histone deacetylase	
MEKK1	MAPK kinase kinase 1	
Rac1	Ras-related C3 botulinum toxin substrate 1	
MAP3K23	MAPK kinase kinase 2 or 3	
PDK1	3-phosphoinositide dependent protein kinase-1	Layer 11
MAP3K11	MAPK kinase kinase 11	
MAP3K4	MAPK kinase kinase 4	
RhoA*	Ras homolog gene family, member A	
MEK5	MAPK kinase 5	
Raf1	Raf1	Layer 12
Akt	protein kinase B	
MEK36	MAPK kinase 3 or MAPK kinase 6	
MEK4	MAPK kinase 4	
MEK7	MAPK kinase 7	
SRF*	serum response factor	
ERK5	ERK5	
GSK3b	glycogen synthase kinase 3 beta	Layer 13
foxo	forkhead box O	
mTor*	mechanistic target of rapamycin	
NOS*	endothelial nitric oxide synthase	
MEK12	MAPK kinase 1 or MAPK kinase 2	
p38	p38 mitogen-activated protein kinase	
JNK	c-Jun N-terminal kinase	

elF4E*	eukaryotic translation initiation factor 4E	Layer 14
p70s6k*	70 kDa ribosomal protein S6 kinase I	
ATF2	activating transcription factor 2	
IKK*	inhibitor of kappa light polypeptide gene enhancer B-cells, kinase beta	Layer 15
sGC*	soluble guanylyl cyclase	
ERK12	extracellular signal-regulated kinases 1 or 2	
MAPKAPK	MAPK-activated protein kinase	
MEF2	myocyte enhancer factor-2	
elF2B*	eukaryotic initiation factor 2	Layer 16
IkB*	nuclear factor of kappa light polypeptide gene enhancer B-cells inhibitor	
GATA4	protein GATA	
MSK1	ribosomal protein S6 kinase, 90kDa, polypeptide 5	
cFos*	protein c-Fos	
ELK1*	ELK1	
cJun	protein cJun	
cGMP*	cyclic guanosine monophosphate	
CREB	cAMP response element binding	Layer 17
NFkB*	nuclear factor kappa-light-chain-enhancer of activated B cells	
PKG1*	cGMP-dependent protein kinase 1	
NFAT*	nuclear factor of activated T-cells	Layer 18
SERCA*	sarcoplasmic reticulum	Layer 19
αMHC*	α-myosin heavy chain	
CellArea	growth target node	
βMHC*	β-myosin heavy chain	
BNP*	brain natriuretic peptide	
ANP*	atrial naturetic peptide	
sACT*	skeletal α-actin	

C.2. Demonstrator network

For illustration purposes, a demonstrator network is introduced containing all four reaction types and is depicted in Fig. C.2.
Based on [87], the Hill differential equations for the demonstrator network can be written as

$$\frac{\mathrm{d}c_\mathrm{C}}{\mathrm{d}t} = \frac{1}{\tau_\mathrm{C}}\Big(f_\mathrm{act}^{\to\mathrm{C}}(c_\mathrm{A})\; c_\mathrm{C,max} - c_\mathrm{C}\Big), \tag{C.1}$$

$$\frac{\mathrm{d}c_\mathrm{D}}{\mathrm{d}t} = \frac{1}{\tau_\mathrm{D}}\Big(\mathrm{OR}\big(f_\mathrm{act}^{\to\mathrm{D}}(c_\mathrm{A}), f_\mathrm{act}^{\to\mathrm{D}}(c_\mathrm{B})\big)\; c_\mathrm{D,max} - c_\mathrm{D}\Big), \tag{C.2}$$

$$\frac{\mathrm{d}c_\mathrm{E}}{\mathrm{d}t} = \frac{1}{\tau_\mathrm{E}}\Big(\mathrm{AND}\big(f_\mathrm{inh}^{\to\mathrm{E}}(c_\mathrm{C}),\; f_\mathrm{act}^{\to\mathrm{E}}(c_\mathrm{D})\big)\; c_\mathrm{E,max} - c_\mathrm{E}\Big). \tag{C.3}$$

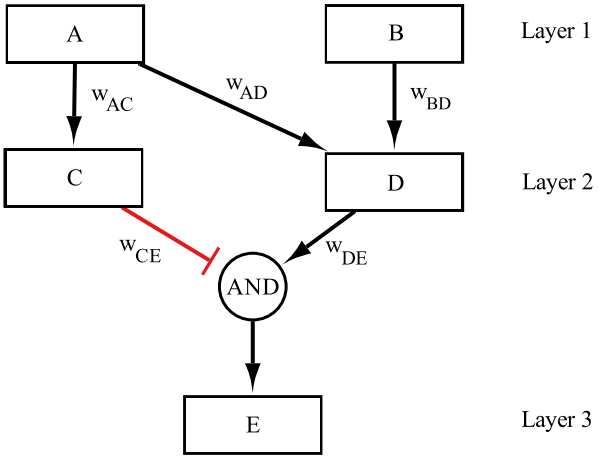

Abbildung C.2.: Demonstrator network containing all reaction types. It consists of five species $\mathcal{S} = \{\text{A, B, C, D, E}\}$ with two input species $\mathcal{I} = \{A, B\}$ and one output species E [9].

To solve the initial value problem for the demonstrator network, constant input concentrations $c_{\text{A}} = 0.5$ and $c_{\text{B}} = 0.6$ are chosen. The remaining species are initialized to $c_s = 0 \; \forall \; s \in \mathcal{S} \backslash \mathcal{I}$. The maximal activation $c_{s,\text{max}}$ is set to 1 for all species $s \in \mathcal{S}$, the reaction time parameter $\tau_s = 1 \, \forall s \in \{\text{C}, \text{D}, \text{E}\}$ and all reaction weights are set to 1. The system of ODEs in Eq. (C.1)-Eq. (C.3) is numerically solved with a third-order explicit Runge-Kutta method for nonstiff ODEs [11] on the pseudo time interval $t \in [0, 20]$. The numerical solution of the system is shown in Fig. C.3.

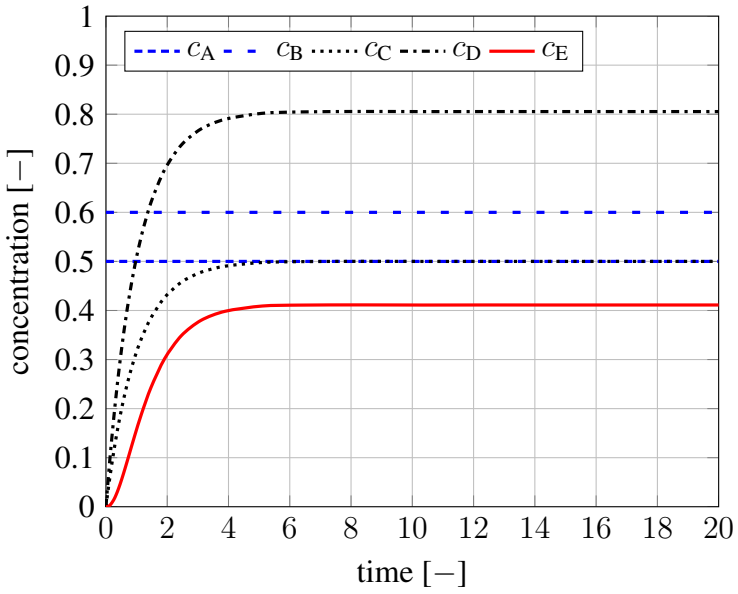

Abbildung C.3.: Numerical solution of the demonstrator network [9].

It can be observed that all species in the network converge to a stationary solution. The species C and D are activated, and their concentrations rise until they reach a stationary value. Following that, the species E, which is inhibited by C, attains a stationary solution of $c_{\mathrm{E}} = 0.411$.
The direct stationary solutions (DSS) for the demonstrator network read

$$c_{\mathrm{C}}^{\mathrm{DSS}} = f_{\mathrm{act}}(c_{\mathrm{A}})c_{\mathrm{C,max}}, \tag{C.4}$$

$$c_{\mathrm{D}}^{\mathrm{DSS}} = \mathrm{OR}(f_{\mathrm{act}}(c_{\mathrm{A}}), f_{\mathrm{act}}(c_{\mathrm{B}}))c_{\mathrm{D,max}}, \tag{C.5}$$

$$c_{\mathrm{E}}^{\mathrm{DSS}} = \mathrm{AND}(f_{\mathrm{inh}}(c_{\mathrm{C}}), f_{\mathrm{act}}(c_{\mathrm{D}}))c_{\mathrm{E,max}}. \tag{C.6}$$

To examine the gradients of the network output concentration c_E with respect to the inputs A and B, chain rule and backward propagation through the network is used and lead to

$$\frac{\mathrm{d}c_{\mathrm{E}}}{\mathrm{d}c_{\mathrm{A}}} = \underbrace{\frac{\mathrm{d}c_{\mathrm{E}}}{\mathrm{d}c_{\mathrm{C}}}\frac{\mathrm{d}c_{\mathrm{C}}}{\mathrm{d}c_{\mathrm{A}}}}_{\text{path 1}} + \underbrace{\frac{\mathrm{d}c_{\mathrm{E}}}{\mathrm{d}c_{\mathrm{D}}}\frac{\mathrm{d}c_{\mathrm{D}}}{\mathrm{d}c_{\mathrm{A}}}}_{\text{path 2}} = -0.832, \tag{C.7}$$

$$\frac{\mathrm{d}c_{\mathrm{E}}}{\mathrm{d}c_{\mathrm{B}}} = \underbrace{\frac{\mathrm{d}c_{\mathrm{E}}}{\mathrm{d}c_{\mathrm{D}}}\frac{\mathrm{d}c_{\mathrm{D}}}{\mathrm{d}c_{\mathrm{B}}}}_{\text{path 3}} = 0.264. \tag{C.8}$$

This indicates that an increase of c_{A} decreases the concentration c_{E} as the inhibition before the AND connection dominates. But if c_{B} is increased, c_{E} also increases.

C.3. Asymptotical stability

Given an autonomous system $\dot{\boldsymbol{c}} = f(\boldsymbol{c})$ with Jacobian $(Df)_{ij} = \frac{\partial f_i}{\partial c_j}$. Its solution is asymptotically stable if the real parts of all eigenvalues of the Jacobian are negative ([33]). For the demonstrator network, $\boldsymbol{D}f$ reads

$$\boldsymbol{D}f = \begin{bmatrix} -\frac{1}{\tau_{\mathrm{C}}} & 0 & 0 \\ 0 & -\frac{1}{\tau_{\mathrm{D}}} & 0 \\ \frac{1}{\tau_E}\frac{d\mathrm{AND}\left(f_{\mathrm{inh}}^{\to \mathrm{E}}(c_{\mathrm{C}}),\ f_{\mathrm{act}}^{\to \mathrm{E}}(c_{\mathrm{D}})\right)}{dc_{\mathrm{C}}} & \frac{1}{\tau_E}\frac{d\mathrm{AND}\left(f_{\mathrm{inh}}^{\to \mathrm{E}}(c_{\mathrm{C}}),\ f_{\mathrm{act}}^{\to \mathrm{E}}(c_{\mathrm{D}})\right)}{dc_{\mathrm{D}}} & -\frac{1}{\tau_{\mathrm{E}}} \end{bmatrix}. \tag{C.9}$$

The eigenvalues of a lower triangular matrix are its diagonal entries [3]. Here, the demonstrator network has only negative eigenvalues and is therefore asymptotically stable. Since all presented signaling networks in this work are acyclic and hierarchically arranged in layers, the Jacobian always has a lower triangular structure. Hence, the REF or R&M networks are also asymptotically stable.

C.4. Signaling network model evaluation

Fig. C.4 depicts a heatmap plot of the difference between the DSS of the R&M and the REF networks. Here, all input concentrations are set to a value of $c_i = 0.06, i \in \mathcal{I}$, except for for the

concentration c_{Stretch}, which varies from 0 to 1. On the y-axis all species in both networks are shown. A positive value indicates and elevated concentration in the R&M network, whereas a negative values denotes a higher concentration in the REF network.

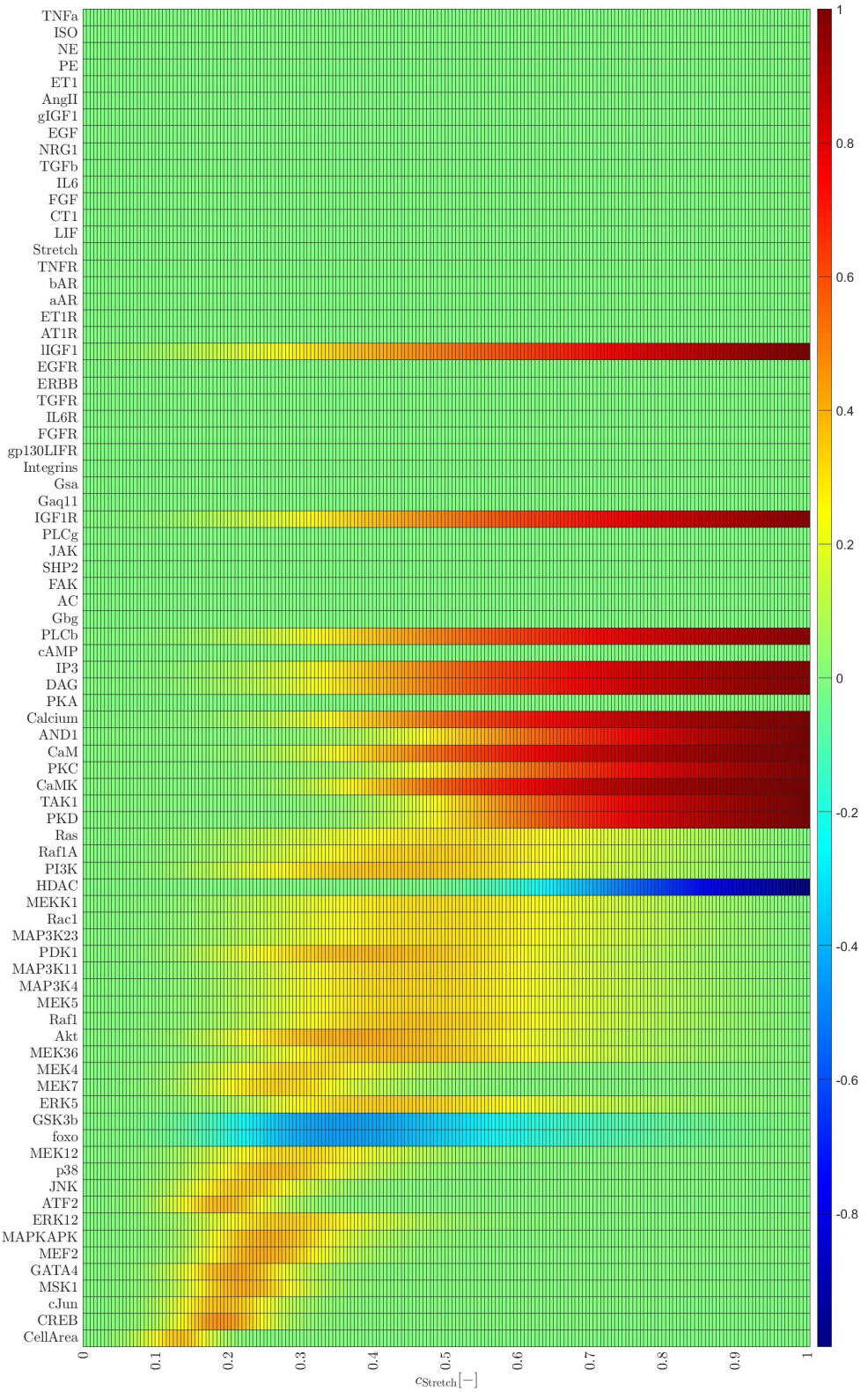

Abbildung C.4.: Difference of DSS between the R&M and REF network over a varying input concentration c_{Stretch}. All other input concentrations are set to a fixed value of $c_i = 0.06$.

D. Numerical results

D.1. Measurements

In Tab. D.1 and Tab. D.2, the end-diastolic and end-systolic volumes are presented for all six pigs P1 to P6. The volumes are obtained after the segmentation and before cutting the surfaces at the atrioventricular plane. Pig P4 faced difficulties during the CT imaging acquisition, resulting in data available only for the 70% end-diastolic state, making it notably smaller in comparison to the rest of the data set.

Tabelle D.1.: End-diastolic volumes for all pigs P1-P6.

		CT1 life day 40	CT2 life day 50	CT3 life day 60	CT4 life day 70	CT5 life day 80
P1	LV volume	20.6	20.3	23.1	30.1	32.9
	RV volume	16.1	18.9	19.2	23.2	27.2
P2	LV volume	18.1	20.4	18.7	29.1	32.7
	RV volume	14.1	18.5	16.6	21.1 24.5	
P3	LV volume	18,5	-	-	-	-
	RV volume	14,6	-	-	-	-
P4	LV volume	7.1	11.2	11.5	13.2	19.7
	RV volume	8.4	8.4	9.1	11.3	13.1
P5	LV volume	14.1	18.1	-	31.1	26.1
	RV volume	9.8	15.5	-	22.9	24.1
P6	LV volume	14.4	16.7	19.4	-	27.5
	RV volume	11.6	12.0	14.2	22.3	

The stroke volume (SV) defined as the difference between the end-diastolic volume (EDV) and the end-systolic volume (ESV) of the left or right ventricle are depicted for all pigs from the day of life 40 to 80 in Fig. D.1.

Tabelle D.2.: End-systolic volumes for all pigs P1-P6.

		CT1 life day 40	CT2 life day 50	CT3 life day 60	CT4 life day 70	CT5 life day 80
P1	LV volume	8.124	7.76	13.48	11.45	14.20
	RV volume	13.06	8.435	7.82	8.97	10.42
P2	LV volume	7.99	7.64	5.79	12.34	15.19
	RV volume	8.80	8.58	8.62	13.25	12.94
P3	LV volume	-	-	-	-	-
	RV volume	-	-	-	-	-
P4	LV volume	-	6.96	7.36	10.69	17.14
	RV volume	-	8.09	8.44	11.18	14.97
P5	LV volume	7.33	8.05	-	13.28	12.38
	RV volume	4.59	7.49	-	7.54	11.57
P6	LV volume	7.67	6.64	8.89	-	13.53
	RV volume	6.74	5.27	6.89	-	10.97

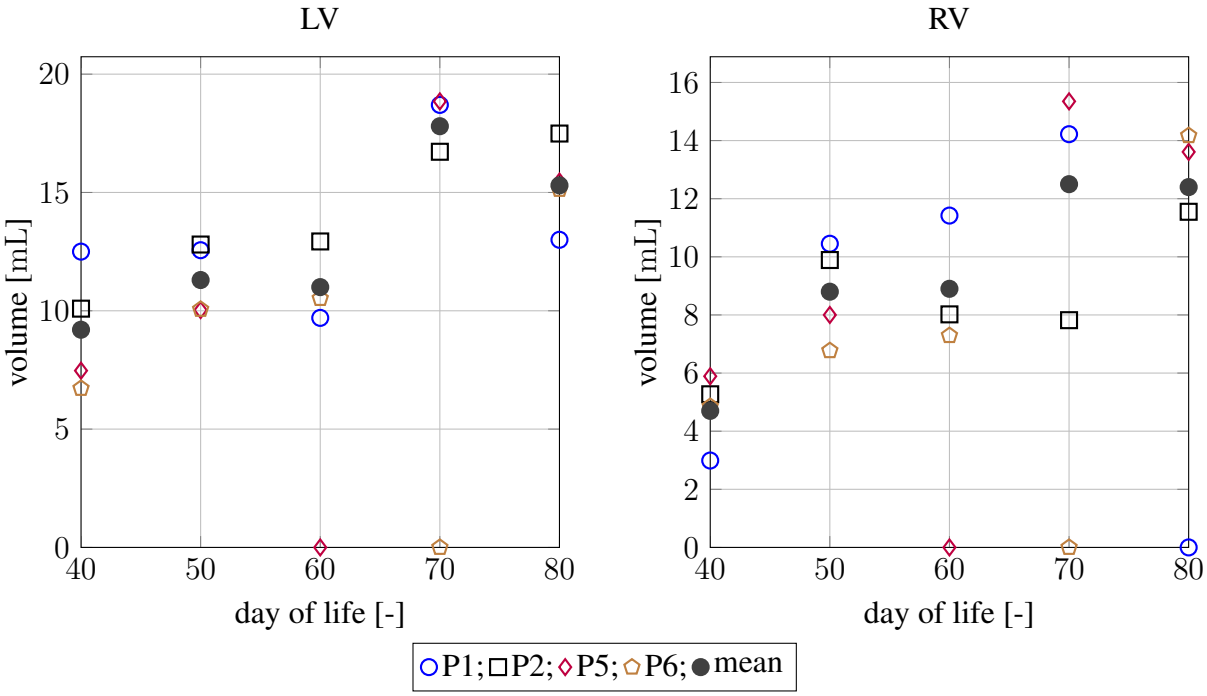

Abbildung D.1.: Left (top) and right (bottom) ventricular stroke volumes (SV) over time. A value of zero means that the measurement at that point in time is not available. To calculate the mean value, any values of zero are omitted from the computation.

D.2. Computational domain

In this section, the spatial resolution of the finite element mesh of the computational heart domain is studied. The computational heart domain is discretized using a $1\,\mathrm{mm}$ and a $1.5\mathrm{mm}$ tetrahedral

mesh, and they are depicted in Fig. D.2. Using these discretizations, three finite element meshes are generated. The first mesh is the $1\ \mathrm{mm}$ mesh, consisting of linear tetrahedral elements (linear, $1\ \mathrm{mm}$). The second mesh is the $1.5\ \mathrm{mm}$ mesh, also composed of linear tetrahedral elements (linear, $1.5\ \mathrm{mm}$). The third mesh is the refined $1.5\ \mathrm{mm}$ mesh, incorporating quadratic tetrahedral elements (quadratic, $1.5\ \mathrm{mm}$).

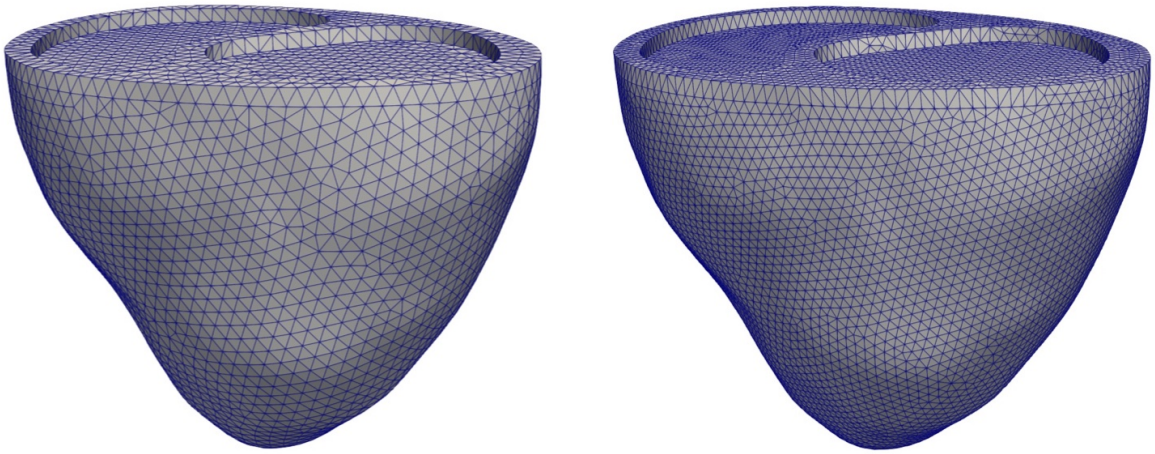

Abbildung D.2.: Visualization of the $1.5\ \mathrm{mm}$ (left) and $1\ \mathrm{mm}$ (right) finite element computational heart domain.

To analyze the spatial resolution, the following example is considered: At the heart base, a zero-value Dirichlet boundary condition is chosen, and within the ventricles, an ortho-pressure boundary condition is used, see Fig. D.3.
The corresponding IBVP reads

$$\nabla_{\boldsymbol{X}} \cdot \boldsymbol{P} = \rho_0 \dot{\boldsymbol{v}} \qquad \text{in } \Omega, \tag{D.1}$$

$$\boldsymbol{P} \cdot \boldsymbol{N} = \boldsymbol{t}_{0_p}^i \qquad \text{on } \Gamma_{\mathrm{v}}^i, i \in \{r, \ell\}, \tag{D.2}$$

$$\boldsymbol{u} = 0 \qquad \text{on } \Gamma_{\text{base}}, \tag{D.3}$$

where the pressure traction $\boldsymbol{t}_{0_p}^i$ is computed using Eq. (3.43) with a linearly increasing pressure applied until it reaches $100\ \mathrm{mmHg}$.
This system of equations is solved for all three tetrahedral meshes using the Newton method presented in Sec. 2.2.4. The solution to this problem is depicted in Fig .D.4 and the final volumes are listed in Tab. D.3. It can be seen that all three meshes converge to a similar solution. Therefore, the linear tetrahedral finite element mesh with an edge length of approximately $1.5\ \mathrm{mm}$ is chosen for all simulations throughout this thesis.

D.3. Global sensitivity analysis of signaling network

In Fig. D.5, the first- and total-order sensitivity estimators for the REF and R&M network are depicted. It can be seen that for the chosen sample size of $N_S = 1 \cdot 10^6$, all estimators converge to the same solution.

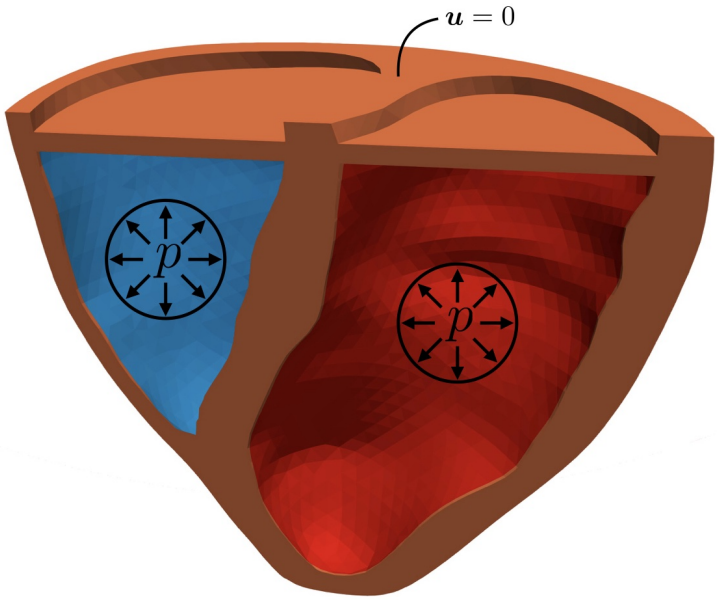

Abbildung D.3.: Visualization of the boundary value problem, with a zero-value Dirichlet boundary condition at the heart base and an ortho-pressure boundary condition within the ventricles.

Tabelle D.3.: Initial and final volumes of the left and right ventricles.

	volumes [mL]	
mesh	left ventricle	right ventricle
initial configuration	12.81	8.46
linear, 1 mm	20.25	15.597
linear, 1.5 mm	20.0028	15.3314
quadratic, 1.5 mm	20.63	16.11

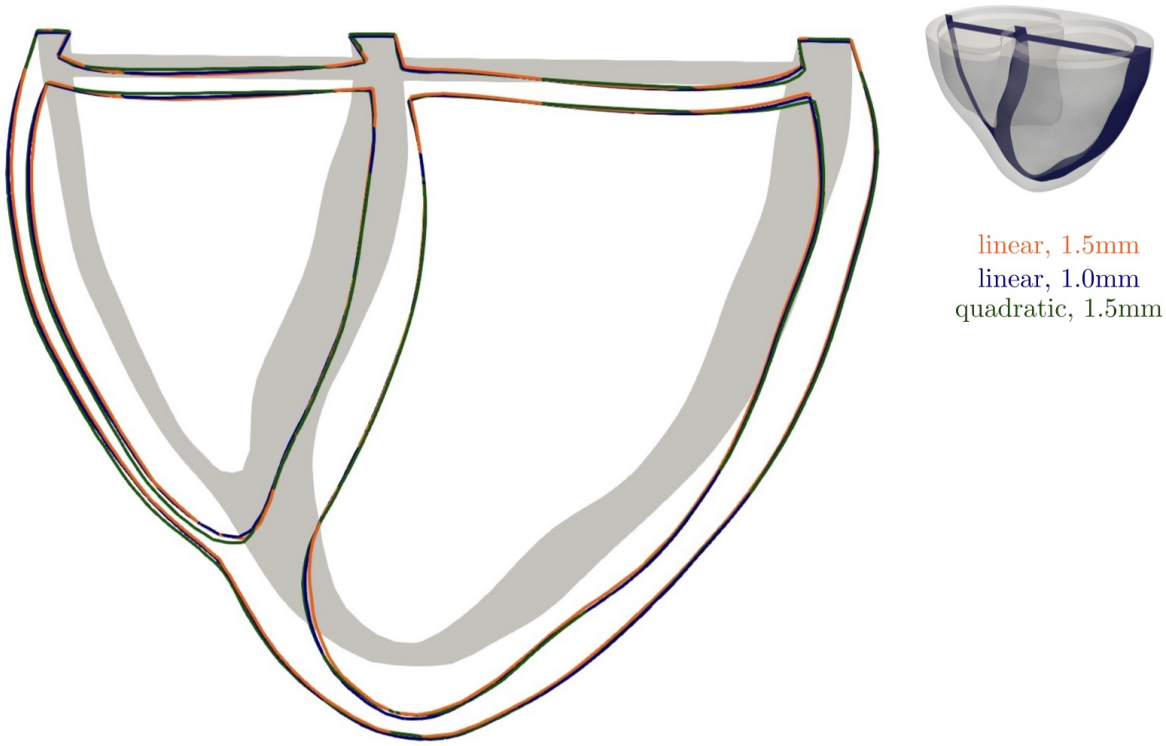

Abbildung D.4.: Numerical solution of the spatial resolution study. The deformation at the pressure value of $100\ \mathrm{mmHg}$ is shown for all three computational meshes. Furthermore, the initial configuration is shown as a slice in gray.

Tabelle D.4.: Global sensitivity estimators for *CellArea* with respect to the input species in the REF network [9].

Species	$S_{\mathbf{jan}}$	$S_{\mathbf{sob}}$	$S_{\mathbf{sat}}$	$T_{\mathbf{jan}}$	$T_{\mathbf{sob}}$	$T_{\mathbf{hom}}$
TNFa	0.0008	0.0007	0.0020	0.0012	0.0013	0.0013
ISO	0.0237	0.0237	0.0250	0.0376	0.0372	0.0372
NE	0.1216	0.1225	0.1240	0.1755	0.1760	0.1760
PE	0.0351	0.0352	0.0367	0.0538	0.0543	0.0543
ET1	0.0218	0.0220	0.0233	0.0329	0.0330	0.0330
AngII	0.1223	0.1225	0.1241	0.1683	0.1681	0.1681
IGF1	0.0843	0.0841	0.0848	0.1162	0.1159	0.1159
EGF	0.0843	0.0838	0.0846	0.1161	0.1156	0.1156
NRG1	0.0841	0.0849	0.0867	0.1160	0.1159	0.1159
TGFb	0.0184	0.0179	0.0196	0.0253	0.0250	0.0250
IL6	0.0435	0.0435	0.0443	0.0607	0.0605	0.0605
FGF	0.0698	0.0701	0.0712	0.0964	0.0964	0.0964
CT1	0.0700	0.0696	0.0699	0.0985	0.0977	0.0977
LIF	0.0683	0.0686	0.0699	0.0983	0.0986	0.0986
Stretch	0.0145	0.0144	0.0159	0.0209	0.0208	0.0208

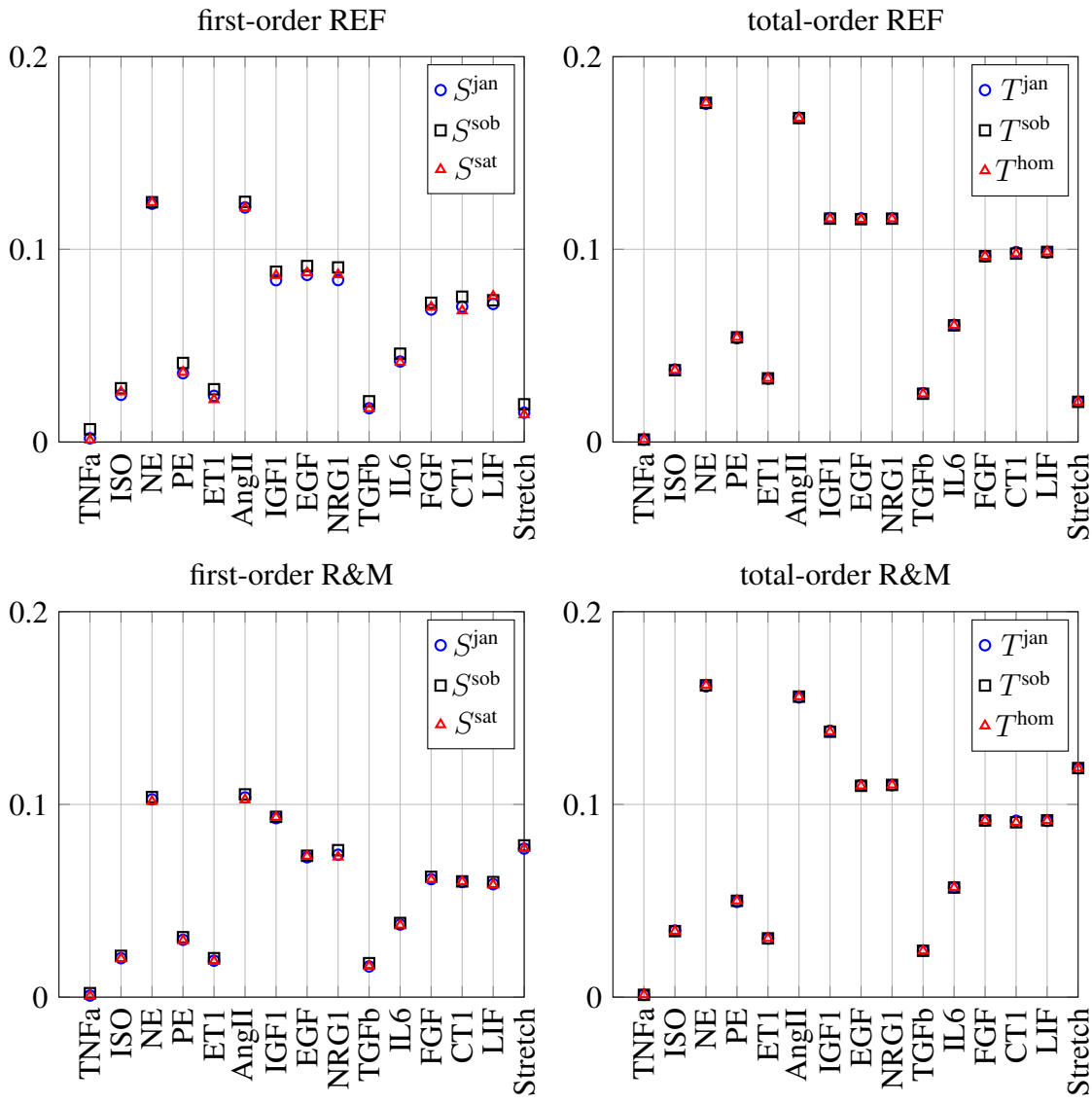

Abbildung D.5.: Sensitivity indices of *CellArea* with respect to the input concentrations for the REF and R&M network. The sensitivity analysis results for the REF network are displayed in the top row, while the bottom row showcases the sensitivities for the R&M network [9].

Tabelle D.5.: Global sensitivity estimators for *CellArea* with respect to the input species in the R&M network [9].

Species	$S_{\textbf{jan}}$	$S_{\textbf{sob}}$	$S_{\textbf{sat}}$	$T_{\textbf{jan}}$	$T_{\textbf{sob}}$	$T_{\textbf{hom}}$
TNFa	0.0007	0.0008	0.0021	0.0012	0.0012	0.0012
ISO	0.0200	0.0202	0.0214	0.0345	0.0342	0.0342
NE	0.1016	0.1026	0.1038	0.1612	0.1618	0.1618
PE	0.0294	0.0297	0.0311	0.0494	0.0500	0.0500
ET1	0.0186	0.0189	0.0202	0.0304	0.0305	0.0305
AngII	0.1024	0.1036	0.1052	0.1555	0.1559	0.1559
IGF1	0.0933	0.0929	0.0935	0.1382	0.1377	0.1377
EGF	0.0731	0.0726	0.0733	0.1099	0.1097	0.1097
NRG1	0.0728	0.0739	0.0763	0.1100	0.1101	0.1101
TGFb	0.0162	0.0159	0.0176	0.0242	0.0240	0.0240
IL6	0.0374	0.0377	0.0385	0.0570	0.0569	0.0569
FGF	0.0610	0.0612	0.0624	0.0916	0.0917	0.0917
CT1	0.0599	0.0597	0.0601	0.0915	0.0907	0.0907
LIF	0.0583	0.0586	0.0597	0.0914	0.0917	0.0917
Stretch	0.0772	0.0771	0.0787	0.1187	0.1189	0.1189

Literaturverzeichnis

[1] I. Albert, J. Thakar, S. Li, R. Zhang, and R. Albert. Boolean network simulations for life scientists. Source code for biology and medicine, 2008.

[2] B. B. Aldridge, J. Saez-Rodriguez, J. L. Muhlich, P. K. Sorger, and D. A. Lauffenburger. Fuzzy logic analysis of kinase pathway crosstalk in tnf/egf/insulin-induced signaling. PLoS computational biology, 2009.

[3] G. Allaire, S. M. Kaber, K. Trabelsi, and G. Allaire, *Numerical linear algebra*, Volume 55, Springer, 2008.

[4] D. Ambrosi and S. Pezzuto. Active stress vs. active strain in mechanobiology: constitutive issues. Journal of Elasticity, 2012.

[5] N. Aronszajn. Theory of reproducing kernels. Transactions of the American mathematical society, 1950.

[6] K. M. Baker and J. F. Aceto. Angiotensin ii stimulation of protein synthesis and cell growth in chick heart cells. American Journal of Physiology-Heart and Circulatory Physiology, 1990.

[7] S. Banerjee and A. Roy, *Linear algebra and matrix analysis for statistics*, Crc Press, 2014.

[8] J. D. Bayer, R. C. Blake, G. Plank, and N. A. Trayanova. A novel rule-based algorithm for assigning myocardial fiber orientation to computational heart models. Annals of biomedical engineering, 2012.

[9] C. Bilas, C. Kratzer, A. Hinrichs, A. Maier, S. Wildhirt, W. Eckhard, and M. W. Gee. Global sensitivity analysis of a novel signaling network for heart growth with local igf1 production. submitted to International journal for numerical methods in biomedical engineering, 2024.

[10] P. Billingsley, *Probability and measure*, John Wiley & Sons, 2017.

[11] P. Bogacki and L. F. Shampine. A 3 (2) pair of runge-kutta formulas. Applied Mathematics Letters, 1989.

[12] J. Bonet and R. D. Wood, *Nonlinear continuum mechanics for finite element analysis*, Cambridge university press, 1997.

[13] R. O. Bonow, D. L. Mann, D. P. Zipes, and P. Libby, *Braunwald's heart disease e-book: A textbook of cardiovascular medicine*, Elsevier Health Sciences, 2011.

[14] G. E. Box, W. H. Hunter, S. Hunter, et al., *Statistics for experimenters*, Volume 664, John Wiley and sons New York, 1978.

[15] C. G. Broyden. A class of methods for solving nonlinear simultaneous equations. Mathematics of computation, 1965.

[16] L. Bruder, *Biomechanical assessment of abdominal aortic aneurysm rupture risk and growth using clinical data: a probabilistic approach*, PhD thesis, Technische Universität München, 2022.

[17] E. V. Buechel, T. Kaiser, C. Jackson, A. Schmitz, and C. J. Kellenberger. Normal right- and left ventricular volumes and myocardial mass in children measured by steady state free precession cardiovascular magnetic resonance. Journal of Cardiovascular Magnetic Resonance, 2009.

[18] By adh30 revised work by DanielChangMD who revised original work of DestinyQx; Redrawn as SVG by xavax. Wiggers diagram.svg. CC BY-SA 4.0, https://commons.wikimedia.org/w/index.php?curid=50317988, 2020. URL https://commons.wikimedia.org/wiki/File:Wiggers_Diagram_de.svg. Accessed: November 05, 2023.

[19] R. H. Byrd, M. E. Hribar, and J. Nocedal. An interior point algorithm for large-scale nonlinear programming. SIAM Journal on Optimization, 1999.

[20] M. Cao, Z. Wang, W. Lan, B. Xiang, W. Liao, J. Zhou, X. Liu, Y. Wang, S. Zhang, S. Lu, et al. The roles of tissue resident macrophages in health and cancer. Experimental Hematology & Oncology, 2024.

[21] D. M. Carl. Matrix analysis and applied linear algebra, 2000.

[22] Center for Disease Control and Prevention. Heart disease facts, 2023. URL https://www.cdc.gov/heartdisease/facts.htm. Accessed: November 08, 2023.

[23] K. Chen, *Matrix preconditioning techniques and applications*, Volume 19, Cambridge University Press, 2005.

[24] E. Chung and L. A. Leinwand. Pregnancy as a cardiac stress model. Cardiovascular research, 2014.

[25] J. Chung and G. Hulbert. A time integration algorithm for structural dynamics with improved numerical dissipation: the generalized-α method. The American Society of Mechanical Engineers, 1993.

[26] Colorado Community College System. 42 cardiovascular structures and functions. CC BY-SA 4.0 DEED https://creativecommons.org/licenses/by-sa/4.0/, 2023. URL https://pressbooks.ccconline.org/bio106/chapter/cardiovascular-structures-and-functions/. Accessed: November 05, 2023.

[27] W. S. Colucci. The effects of norepinephrine on myocardial biology: implications for the therapy of heart failure. Clinical cardiology, 1998.

[28] C. Cyron, R. Aydin, and J. Humphrey. A homogenized constrained mixture (and mechanical analog) model for growth and remodeling of soft tissue. Biomechanics and modeling in mechanobiology, 2016.

[29] S. R. Daniels, S. A. Witt, B. Glascock, P. R. Khoury, and T. R. Kimball. Left atrial size in children with hypertension: the influence of obesity, blood pressure, and left ventricular mass. The Journal of pediatrics, 2002.

[30] B. B. Das. Current state of pediatric heart failure. Children, 2018.

[31] W. C. De Mello and A. J. Danser. Angiotensin ii and the heart: on the intracrine renin-angiotensin system. Hypertension, 2000.

[32] G. de Simone, R. B. Devereux, S. R. Daniels, G. Mureddu, M. J. Roman, T. R. Kimball, R. Greco, S. Witt, and F. Contaldo. Stroke volume and cardiac output in normotensive children and adults: assessment of relations with body size and impact of overweight. Circulation, 1997.

[33] P. Deuflhard and F. Bornemann, *Gewöhnliche Differentialgleichungen*, Walter de Gruyter, 2013.

[34] J. R. Dormand and P. J. Prince. A family of embedded runge-kutta formulae. Journal of computational and applied mathematics, 1980.

[35] P. Dupuis, U. Grenander, and M. I. Miller. Variational problems on flows of diffeomorphisms for image matching. Quarterly of applied mathematics, 1998.

[36] S. Durrleman, *Statistical models of currents for measuring the variability of anatomical curves, surfaces and their evolution*, PhD thesis, Université Nice Sophia Antipolis, 2010.

[37] S. Durrleman, P. Fillard, X. Pennec, A. Trouvé, and N. Ayache. Registration, atlas estimation and variability analysis of white matter fiber bundles modeled as currents. NeuroImage, 2011.

[38] S. Durrleman, M. Prastawa, N. Charon, J. R. Korenberg, S. Joshi, G. Gerig, and A. Trouvé. Morphometry of anatomical shape complexes with dense deformations and sparse parameters. NeuroImage, 2014.

[39] E. Ehler and M. Gautel, The sarcomere and sarcomerogenesis, In *The sarcomere and skeletal muscle disease*, pages 1–14, Springer, 2008.

[40] H. Elman, V. E. Howle, J. Shadid, R. Shuttleworth, and R. Tuminaro. A taxonomy and comparison of parallel block multi-level preconditioners for the incompressible navier–stokes equations. Journal of Computational Physics, 2008.

[41] A. C. Estrada, K. Yoshida, J. J. Saucerman, and J. W. Holmes. A multiscale model of cardiac concentric hypertrophy incorporating both mechanical and hormonal drivers of growth. Biomechanics and modeling in mechanobiology, 2021.

[42] R. Fagard. Athlete's heart. Heart, 2003.

[43] B. Falkner, S. R. Daniels, J. T. Flynn, S. Gidding, L. Green, J. Ingelfinger, R. Lauer, B. Morgenstern, R. Portman, R. Prineas, et al. National high blood pressure education program working group on high blood pressure in children and adolescents. The fourth report on the diagnosis, evaluation, and treatment of high blood pressure in children and adolescents. Pediatrics, 2004.

[44] K. R. Fowler and C. T. Kelley. Pseudo-transient continuation for nonsmooth nonlinear equations. SIAM journal on numerical analysis, 2005.

[45] D. U. Frank, M. D. Sutcliffe, and J. J. Saucerman. Network-based predictions of in vivo cardiac hypertrophy. Journal of molecular and cellular cardiology, 2018.

[46] N. Frey and E. Olson. Cardiac hypertrophy: the good, the bad, and the ugly. Annual review of physiology, 2003.

[47] M. W. Gee, C. Reeps, H. Eckstein, and W. Wall. Prestressing in finite deformation abdominal aortic aneurysm simulation. Journal of biomechanics, 2009.

[48] M. W. Gee, C. Förster, and W. Wall. A computational strategy for prestressing patient-specific biomechanical problems under finite deformation. International Journal for Numerical Methods in Biomedical Engineering, 2010.

[49] D. Givoli. A tutorial on the adjoint method for inverse problems. Computer Methods in Applied Mechanics and Engineering, 2021.

[50] J. Glaunes. Transport par difféomorphismes de points, de mesures et de courants pour la comparaison de formes et l'anatomie numérique. These de sciences, Université Paris, 2005.

[51] J. Glaunes, A. Trouvé, and L. Younes, Diffeomorphic matching of distributions: A new approach for unlabelled point-sets and sub-manifolds matching, In *Proceedings of the 2004 IEEE Computer Society Conference on Computer Vision and Pattern Recognition, 2004. CVPR 2004.*, Volume 2, pages II–II. IEEE, 2004.

[52] T. P. GRAHAM JR, M. Jarmakani, R. V. CANENT JR, M. P. CAPP, and M. S. SPACH. Characterization of left heart volumes and mass in normal children and in ifants with intrinsic myocardial disease. Circulation, 1968.

[53] K. Gustafson and T. Abe. The third boundary condition—was it robin's? The Mathematical Intelligencer, 1998.

[54] J. E. Hall, *Guyton and Hall Textbook of Medical Physiology, Jordanian Edition E-Book*, Elsevier Health Sciences, 2016.

[55] T. R. Heallen, Z. A. Kadow, J. Wang, and J. F. Martin. Determinants of cardiac growth and size. Cold Spring Harbor Perspectives in Biology, 2020.

[56] J. Heineke and J. D. Molkentin. Regulation of cardiac hypertrophy by intracellular signalling pathways. Nature reviews Molecular cell biology, 2006.

[57] M. A. Heroux and J. M. Willenbring. Trilinos users guide, 2003.

[58] M. Hidane, O. Lézoray, and A. Elmoataz. Nonlinear multilayered representation of graph-signals. Journal of mathematical imaging and vision, 2013.

[59] J. A. Hill and E. N. Olson. Cardiac plasticity. New England Journal of Medicine, 2008.

[60] A. Hinrichs, B. Kessler, M. Kurome, A. Blutke, E. Kemter, M. Bernau, A. M. Scholz, B. Rathkolb, S. Renner, S. Bultmann, et al. Growth hormone receptor-deficient pigs resemble the pathophysiology of human laron syndrome and reveal altered activation of signaling cascades in the liver. Molecular metabolism, 2018.

[61] A. Hinrichs, E. O. Riedel, N. Klymiuk, A. Blutke, E. Kemter, M. Längin, M. Dahlhoff, B. Keßler, M. Kurome, V. Zakhartchenko, et al. Growth hormone receptor knockout to reduce the size of donor pigs for preclinical xenotransplantation studies. Xenotransplantation, 2021.

[62] M. Hirschvogel, *Computational modeling of patient-specific cardiac mechanics with model reduction-based parameter estimation and applications to novel heart assist technologies*, PhD thesis, Technische Universität München, 2018.

[63] M. Hirschvogel, M. Bassilious, L. Jagschies, S. M. Wildhirt, and M. W. Gee. A monolithic 3d-0d coupled closed-loop model of the heart and the vascular system: experiment-based parameter estimation for patient-specific cardiac mechanics. International journal for numerical methods in biomedical engineering, 2017.

[64] G. A. Holzapfel. Nonlinear solid mechanics: a continuum approach for engineering science. Kluwer Academic Publishers Dordrecht, 2002.

[65] G. A. Holzapfel and R. W. Ogden. Constitutive modelling of passive myocardium: a structurally based framework for material characterization. Philosophical Transactions of the Royal Society A: Mathematical, Physical and Engineering Sciences, 2009.

[66] T. Homma and A. Saltelli. Importance measures in global sensitivity analysis of nonlinear models. Reliability Engineering & System Safety, 1996.

[67] D. T. Hsu and G. D. Pearson. Heart failure in children: part i: history, etiology, and pathophysiology. Circulation: Heart Failure, 2009.

[68] D. T. Hsu and G. D. Pearson. Heart failure in children: part ii: diagnosis, treatment, and future directions. Circulation: Heart Failure, 2009.

[69] O. Hudlicka and M. Brown. Postnatal growth of the heart and its blood vessels. Journal of vascular research, 1996.

[70] T. J. Hughes, *The finite element method: linear static and dynamic finite element analysis*, Courier Corporation, 2012.

[71] J. D. Humphrey and K. Rajagopal. A constrained mixture model for growth and remodeling of soft tissues. Mathematical models and methods in applied sciences, 2002.

[72] P. A. Iaizzo, *Handbook of cardiac anatomy, physiology, and devices*, Springer Science & Business Media, 2010.

[73] S. IM. Global sensitivity analysis indices for the investigation of nonlinear mathematical models. Matematicheskoe Modelirovanie, 2007.

[74] M. J. Jansen. Analysis of variance designs for model output. Computer Physics Communications, 1999.

[75] S. Joshi, B. Davis, M. Jomier, and G. Gerig. Unbiased diffeomorphic atlas construction for computational anatomy. NeuroImage, 2004.

[76] S. C. Joshi and M. I. Miller. Landmark matching via large deformation diffeomorphisms. IEEE transactions on image processing, 2000.

[77] J. H. Kang, H.-S. Lee, Y.-W. Kang, and K.-H. Cho. Systems biological approaches to the cardiac signaling network. Briefings in bioinformatics, 2016.

[78] J. Keener and J. Sneyd. Mathematical physiology 1: Cellular physiology, 2009.

[79] S. Kehl, *Bayesian Calibration of Nonlinear Cardiovascular Models for the Predictive Simulation of Arterial Growth*, PhD thesis, Technische Universität München, 2017.

[80] S. Kehl and M. W. Gee. Calibration of parameters for cardiovascular models with application to arterial growth. International Journal for Numerical Methods in Biomedical Engineering, 2017.

[81] C. T. Kelley, *Iterative methods for optimization*, SIAM, 1999.

[82] C. D. Kemp and J. V. Conte. The pathophysiology of heart failure. Cardiovascular Pathology, 2012.

[83] R. Kerckhoffs, J. Omens, and A. McCulloch. A single strain-based growth law predicts concentric and eccentric cardiac growth during pressure and volume overload. Biophysical Journal, 2012.

[84] K. Kimura, H. Kanazawa, M. Ieda, H. Kawaguchi-Manabe, Y. Miyake, T. Yagi, T. Arai, M. Sano, and K. Fukuda. Norepinephrine-induced nerve growth factor depletion causes cardiac sympathetic denervation in severe heart failure. Autonomic Neuroscience, 2010.

[85] P. Kleinbongard, R. Schulz, and G. Heusch. Tnfα in myocardial ischemia/reperfusion, remodeling and heart failure. Heart failure reviews, 2011.

[86] N. Klymiuk, B. Aigner, G. Brem, and E. Wolf. Genetic modification of pigs as organ donors for xenotransplantation. Molecular Reproduction and Development: Incorporating Gamete Research, 2010.

[87] M. J. Kraeutler, A. R. Soltis, and J. J. Saucerman. Modeling cardiac β-adrenergic signaling with normalized-hill differential equations: comparison with a biochemical model. BMC systems biology, 2010.

[88] W. Kroon, T. Delhaas, T. Arts, and P. Bovendeerd. Computational modeling of volumetric soft tissue growth: application to the cardiac left ventricle. Biomechanics and modeling in mechanobiology, 2009.

[89] T. Kubota, D. M. McNamara, J. J. Wang, M. Trost, C. F. McTiernan, D. L. Mann, and A. M. Feldman. Effects of tumor necrosis factor gene polymorphisms on patients with congestive heart failure. Circulation, 1998.

[90] E. Kuhl, R. Maas, G. Himpel, and A. Menzel. Computational modeling of arterial wall growth: Attempts towards patient-specific simulations based on computer tomography. Biomechanics and modeling in mechanobiology, 2007.

[91] A. Laadhari, R. Ruiz-Baier, and A. Quarteroni. Fully eulerian finite element approximation of a fluid-structure interaction problem in cardiac cells. International journal for numerical methods in engineering, 2013.

[92] P. E. Lange, D. G. Onnasch, G. H. Schaupp, C. Zill, and P. H. Heintzen. Size and function of the human left and right ventricles during growth: normative angiographic data. Pediatric Cardiology, 1982.

[93] Z. Laron. Insulin-like growth factor 1 (igf-1): a growth hormone. Molecular Pathology, 2001.

[94] N. Le Novere. Quantitative and logic modelling of molecular and gene networks. Nature Reviews Genetics, 2015.

[95] L. C. Lee, M. Genet, G. Acevedo-Bolton, K. Ordovas, J. M. Guccione, and E. Kuhl. A computational model that predicts reverse growth in response to mechanical unloading. Biomechanics and modeling in mechanobiology, 2015.

[96] I.-E. Lin and L. Taber. A model for stress-induced growth in the developing heart, 1995.

[97] S. E. Lipshultz, L. A. Sleeper, J. A. Towbin, A. M. Lowe, E. J. Orav, G. F. Cox, P. R. Lurie, K. L. McCoy, M. A. McDonald, J. E. Messere, et al. The incidence of pediatric cardiomyopathy in two regions of the united states. New England Journal of Medicine, 2003.

[98] T. Mansi, I. Voigt, B. Leonardi, X. Pennec, S. Durrleman, M. Sermesant, H. Delingette, A. M. Taylor, Y. Boudjemline, G. Pongiglione, et al. A statistical model for quantification and prediction of cardiac remodelling: Application to tetralogy of fallot. IEEE transactions on medical imaging, 2011.

[99] B. J. Maron and M. S. Maron. Hypertrophic cardiomyopathy. The Lancet, 2013.

[100] B. J. Maron and A. Pelliccia. The heart of trained athletes: cardiac remodeling and the risks of sports, including sudden death. Circulation, 2006.

[101] M. D. McKay, R. J. Beckman, and W. J. Conover. A comparison of three methods for selecting values of input variables in the analysis of output from a computer code. Technometrics, 2000.

[102] R. McLachlan and S. Marsland. Discrete mechanics and optimal control for image registration. Anziam Journal, 2006.

[103] A. Menzel and E. Kuhl. Frontiers in growth and remodeling. Mechanics research communications, 2012.

[104] M. I. Miller, A. Trouvé, and L. Younes. Geodesic shooting for computational anatomy. Journal of mathematical imaging and vision, 2006.

[105] M. C. Milliken, J. Stray-Gundersen, R. M. Peshock, J. Katz, and J. H. Mitchell. Left ventricular mass as determined by magnetic resonance imaging in male endurance athletes. The American journal of cardiology, 1988.

[106] J. Mojumder, J. Choy, S. Leng, L. Zhong, G. Kassab, and L. Lee. Mechanical stimuli for left ventricular growth during pressure overload. Experimental mechanics, 2021.

[107] A. Nagler, C. Bertoglio, M. W. Gee, and W. A. Wall, Personalization of cardiac fiber orientations from image data using the unscented kalman filter, In *Functional Imaging and Modeling of the Heart: 7th International Conference, FIMH 2013, London, UK, June 20-22, 2013. Proceedings 7*, pages 132–140. Springer, 2013.

[108] M. Nakamura and J. Sadoshima. Mechanisms of physiological and pathological cardiac hypertrophy. Nature Reviews Cardiology, 2018.

[109] J. Nocedal. Updating quasi-newton matrices with limited storage. Mathematics of computation, 1980.

[110] C. Ohlmeier, R. Mikolajczyk, J. Frick, F. Prütz, W. Haverkamp, and E. Garbe. Incidence, prevalence and 1-year all-cause mortality of heart failure in germany: a study based on electronic healthcare data of more than six million persons. Clinical Research in Cardiology, 2015.

[111] M. d. Onis et al. The who child growth standards. Pediatric nutrition in practice, 2008.

[112] S. K. Pasquali, M. Hall, A. D. Slonim, K. J. Jenkins, B. S. Marino, M. S. Cohen, and S. S. Shah. Off-label use of cardiovascular medications in children hospitalized with congenital and acquired heart disease. Circulation: Cardiovascular Quality and Outcomes, 2008.

[113] M. Peirlinck, M. De Beule, P. Segers, and N. Rebelo. A modular inverse elastostatics approach to resolve the pressure-induced stress state for in vivo imaging based cardiovascular modeling. Journal of the mechanical behavior of biomedical materials, 2018.

[114] M. Pfisterer, A. Battler, and B. Zaret. Range of normal values for left and right ventricular ejection fraction at rest and during exercise assessed by radionuclide angiocardiography. European heart journal, 1985.

[115] R. Piersanti, P. C. Africa, M. Fedele, C. Vergara, L. Dedè, A. F. Corno, and A. Quarteroni. Modeling cardiac muscle fibers in ventricular and atrial electrophysiology simulations. Computer Methods in Applied Mechanics and Engineering, 2021.

[116] F. G. Pitoulis and C. M. Terracciano. Heart plasticity in response to pressure-and volume-overload: a review of findings in compensated and decompensated phenotypes. Frontiers in physiology, 2020.

[117] P. Ponikowski, S. D. Anker, K. F. AlHabib, M. R. Cowie, T. L. Force, S. Hu, T. Jaarsma, H. Krum, V. Rastogi, L. E. Rohde, et al. Heart failure: preventing disease and death worldwide. ESC heart failure, 2014.

[118] A. Puy, W. Becker, S. L. Piano, and A. Saltelli. A comprehensive comparison of total-order estimators for global sensitivity analysis. International Journal for Uncertainty Quantification, 2022.

[119] U. Rajendra Acharya, K. Paul Joseph, N. Kannathal, C. M. Lim, and J. S. Suri. Heart rate variability: a review. Medical and biological engineering and computing, 2006.

[120] A. Ramasubramanian and L. A. Taber. Computational modeling of morphogenesis regulated by mechanical feedback. Biomechanics and modeling in mechanobiology, 2008.

[121] T. Razi, M. Niknami, and F. A. Ghazani. Relationship between hounsfield unit in ct scan and gray scale in cbct. Journal of dental research, dental clinics, dental prospects, 2014.

[122] E. K. Rodriguez, A. Hoger, and A. D. McCulloch. Stress-dependent finite growth in soft elastic tissues. Journal of biomechanics, 1994.

[123] J. Rodríguez, J. M. Goicolea, and F. Gabaldon. A volumetric model for growth of arterial walls with arbitrary geometry and loads. Journal of biomechanics, 2007.

[124] V. L. Roger. Epidemiology of heart failure. Circulation research, 2013.

[125] E. Rondanina and P. H. Bovendeerd. Evaluation of stimulus-effect relations in left ventricular growth using a simple multiscale model. Biomechanics and Modeling in Mechanobiology, 2020.

[126] L. I. Rudin, S. Osher, and E. Fatemi. Nonlinear total variation based noise removal algorithms. Physica D: nonlinear phenomena, 1992.

[127] J. W. Ruge and K. Stüben, Algebraic multigrid, In *Multigrid methods*, pages 73–130, SIAM, 1987.

[128] K. A. Ryall, D. O. Holland, K. A. Delaney, M. J. Kraeutler, A. J. Parker, and J. J. Saucerman. Network reconstruction and systems analysis of cardiac myocyte hypertrophy signaling. Journal of Biological Chemistry, 2012.

[129] M. N. Sack, R. M. Smith, and L. H. Opie. Tumor necrosis factor in myocardial hypertrophy and ischaemia—an anti-apoptotic perspective. Cardiovascular research, 2000.

[130] A. Saltelli, S. Tarantola, and K.-S. Chan. A quantitative model-independent method for global sensitivity analysis of model output. Technometrics, 1999.

[131] A. Saltelli, M. Ratto, T. Andres, F. Campolongo, J. Cariboni, D. Gatelli, M. Saisana, and S. Tarantola, *Global sensitivity analysis: the primer*, John Wiley & Sons, 2008.

[132] A. Saltelli, P. Annoni, I. Azzini, F. Campolongo, M. Ratto, and S. Tarantola. Variance based sensitivity analysis of model output. design and estimator for the total sensitivity index. Computer physics communications, 2010.

[133] A. Saltelli, K. Aleksankina, W. Becker, P. Fennell, F. Ferretti, N. Holst, S. Li, and Q. Wu. Why so many published sensitivity analyses are false: A systematic review of sensitivity analysis practices. Environmental modelling & software, 2019.

[134] J. J. Saucerman, L. L. Brunton, A. P. Michailova, and A. D. McCulloch. Modeling β-adrenergic control of cardiac myocyte contractility in silico. Journal of Biological Chemistry, 2003.

[135] G. Savarese and L. H. Lund. Global public health burden of heart failure. Cardiac failure review, 2017.

[136] H. Sharifi, C. K. Mann, A. L. Rockward, M. Mehri, J. Mojumder, L.-C. Lee, K. S. Campbell, and J. F. Wenk. Multiscale simulations of left ventricular growth and remodeling, 2021.

[137] I. Sharkey, A. Boddy, H. Wallace, J. Mycroft, R. Hollis, and S. Picton. Body surface area estimation in children using weight alone: application in paediatric oncology. British journal of cancer, 2001.

[138] I. Shimizu and T. Minamino. Physiological and pathological cardiac hypertrophy. Journal of molecular and cellular cardiology, 2016.

[139] I. M. Sobol. Uniformly distributed sequences with an additional uniform property. USSR Computational Mathematics and Mathematical Physics, 1976.

[140] I. M. Sobol. Sensitivity analysis for non-linear mathematical models. Mathematical modelling and computational experiment, 1993.

[141] I. M. Sobol. Global sensitivity indices for nonlinear mathematical models and their monte carlo estimates. Mathematics and computers in simulation, 2001.

[142] I. M. Sobol'. On the distribution of points in a cube and the approximate evaluation of integrals. Zhurnal Vychislitel'noi Matematiki i Matematicheskoi Fiziki, 1967.

[143] N. Stergiopulos, J. J. Meister, and N. Westerhof. Simple and accurate way for estimating total and segmental arterial compliance: the pulse pressure method. Annals of biomedical engineering, 1994.

[144] N. Stergiopulos, B. E. Westerhof, and N. Westerhof. Total arterial inertance as the fourth element of the windkessel model. American Journal of Physiology-Heart and Circulatory Physiology, 1999.

[145] B. Sudret. Global sensitivity analysis using polynomial chaos expansions. Reliability engineering & system safety, 2008.

[146] B. Swynghedauw. Developmental and functional adaptation of contractile proteins in cardiac and skeletal muscles. Physiological reviews, 1986.

[147] L. Taber and S. Chabert. Theoretical and experimental study of growth and remodeling in the developing heart. Biomechanics and modeling in mechanobiology, 2002.

[148] V. Thomée, *Galerkin finite element methods for parabolic problems*, Volume 25, Springer Science & Business Media, 2007.

[149] N. A. Trayanova. Whole-heart modeling: applications to cardiac electrophysiology and electromechanics. Circulation research, 2011.

[150] R. Troncoso, C. Ibarra, J. M. Vicencio, E. Jaimovich, and S. Lavandero. New insights into igf-1 signaling in the heart. Trends in Endocrinology & Metabolism, 2014.

[151] S. Umar, R. Nadadur, A. Iorga, M. Amjedi, H. Matori, and M. Eghbali. Cardiac structural and hemodynamic changes associated with physiological heart hypertrophy of pregnancy are reversed postpartum. Journal of applied physiology, 2012.

[152] M. Vaillant and J. Glaunes, Surface matching via currents, In *Biennial international conference on information processing in medical imaging*, pages 381–392. Springer, 2005.

[153] J. H. Van Berlo, M. Maillet, J. D. Molkentin, et al. Signaling effectors underlying pathologic growth and remodeling of the heart. The Journal of clinical investigation, 2013.

[154] S. S. Virani, A. Alonso, H. J. Aparicio, E. J. Benjamin, M. S. Bittencourt, C. W. Callaway, A. P. Carson, A. M. Chamberlain, S. Cheng, F. N. Delling, et al. Heart disease and stroke statistics-2021 update: a report from the american heart association. Circulation, 2021.

[155] C. R. Vogel, *Computational methods for inverse problems*, SIAM, 2002.

[156] K. T. Weber and C. G. Brilla. Pathological hypertrophy and cardiac interstitium. fibrosis and renin-angiotensin-aldosterone system. Circulation, 1991.

[157] N. Westerhof and G. Elzinga. Normalized input impedance and arterial decay time over heart period are independent of animal size. American Journal of Physiology-Regulatory, Integrative and Comparative Physiology, 1991.

[158] N. Westerhof, J.-W. Lankhaar, and B. E. Westerhof. The arterial windkessel. Medical & biological engineering & computing, 2009.

[159] D. M. Wittmann, J. Krumsiek, J. Saez-Rodriguez, D. A. Lauffenburger, S. Klamt, and F. J. Theis. Transforming boolean models to continuous models: methodology and application to t-cell receptor signaling. BMC systems biology, 2009.

[160] C. M. Witzenburg and J. W. Holmes. A comparison of phenomenologic growth laws for myocardial hypertrophy. Journal of Elasticity, 2017.

[161] N. R. Wong, J. Mohan, B. J. Kopecky, S. Guo, L. Du, J. Leid, G. Feng, I. Lokshina, O. Dmytrenko, H. Luehmann, et al. Resident cardiac macrophages mediate adaptive myocardial remodeling. Immunity, 2021.

[162] K. Yoshida, J. J. Saucerman, and J. W. Holmes. Multiscale model of heart growth during pregnancy: Integrating mechanical and hormonal signaling. bioRxiv, 2020.

[163] T. J. Ypma. Historical development of the newton–raphson method. SIAM review, 1995.

[164] R. Zaman, H. Hamidzada, C. Kantores, A. Wong, S. A. Dick, Y. Wang, A. Momen, L. Aronoff, J. Lin, B. Razani, et al. Selective loss of resident macrophage-derived insulin-like growth factor-1 abolishes adaptive cardiac growth to stress. Immunity, 2021.

[165] O. C. Zienkiewicz and R. L. Taylor, *The finite element method for solid and structural mechanics*, Elsevier, 2005.